Phase Field Simulation of
Martensite Transformation in Steels

vom Fachbereich Maschinenbau und Verfahrenstechnik
der Technischen Universität Kaiserslautern
zur Verleihung des akademischen Grades
Doktor-Ingenieur (Dr.-Ing.)
genehmigte Dissertation

von
Marius Graf, M.Sc.
aus Ostfildern/Ruit

Hauptreferent:	Prof. Dr.-Ing. Ralf Müller
Korreferent:	Prof. Dr.-Ing. Dennis Michael Kochmann
Vorsitzender:	Prof. Dr.-Ing. Eberhard Kerscher
Dekan:	Prof. Dr.-Ing. Tilmann Beck

Tag der Einreichung:	01.09.21
Tag der mündlichen Prüfung:	22.03.2022

Kaiserslautern, 2022

D 386

Vorwort

Die vorliegende Arbeit ist das Ergebnis von drei unvergesslichen Jahren als Doktorand bei der Robert Bosch GmbH in der Gruppe Werkstoffentwicklung und Wärmebehandlung Metalle am Zentrum für Forschung und Vorausentwicklung in Renningen zusammen mit dem Lehrstuhl für Technische Mechanik der Technischen Universität Kaiserslautern. Viele haben zum Gelingen dieser Arbeit beigetragen, wofür ich sehr dankbar bin.

Mein besonderer Dank gilt meinem Betreuer Herrn Professor Dr. Ralf Müller für die in jeder Hinsicht hervorragende Betreuung und Unterstützung sowie das Vertrauen in diese Arbeit. Ich danke Herrn Professor Dr. Dennis Kochmann für die bereitwillige Übernahme des Korreferates und das damit verbundene Interesse an meiner Arbeit. Weiterhin bedanke ich mich bei Herrn Professor Dr. Eberhard Kerscher für die Übernahme des Vorsitzes.

Mein herzlicher Dank gilt weiterhin allen Kolleginnen und Kollegen meiner Gruppe und Abteilung bei Bosch für das großartige Arbeitsklima und die hervorragenden Forschungsbedingungen. Herrn Dr. Ralf Westerheide sowie Herrn Dr. Hermann Autenrieth möchte ich zusätzlich für die Ermöglichung dieser Arbeit und das mir entgegengebrachte Vertrauen danken. Herrn Dr. Matthias Kuntz danke ich für die stets großartige Betreuung und die Aufmunterung bei Rückschlägen. Ebenfalls möchte ich meinem Sitznachbar Herrn Dr. Patrick Fayek für die vielen Diskussionen, auch zu später Stunde, danken. Für seine Unterstützung und Inspiration seit meinem ersten Tag bei Bosch danke ich Herrn Dr. Udo Hartel. Ein besonderer Dank geht an meine Doktorandenkollegen Dr. Benjamin Schäfer, Dr. Nikolai Arnaudov, Dr. Alexandar Eric, Jannick Kuhn und Erik Natkowski, welche immer ein offenes Ohr für alle möglichen fachlichen und außerfachlichen Themen hatten und haben, ihre Unterstützung und ihre Freundschaft.

Meinen Kollegen am Lehrstuhl danke ich für die angenehme und fruchtvolle Arbeitsatmosphäre, insbesondere während meiner Zeit in Kaiserslautern. Besonders hervorheben möchte ich Dr. Felix Diewald für seine fachliche Unterstützung und wissenschaftlichen Rat sowie Julia Hettesheimer, Dr. Alexander Schlüter und Dr. Christian Sator für die Unterstützung und Übernahme etlicher organisatorischer Angelegenheiten. Herrn Felix Steinmetz danke ich für seine studentische Arbeit.

Mein aufrichtiger Dank gilt Herrn Christoph Otterbach für die Förderung während und nach meiner Ausbildung sowie das Wecken meiner Leidenschaft für Simulation. Herrn Dr. Sebastian Sikora danke ich für seinen wissenschaftlichen Rat und sein Mentoring während meines Studiums. Von beiden habe ich vieles gelernt, wovon diese Arbeit sehr profitiert hat.

Meinen Freunden und meiner Familie danke ich für die Bereicherung meiner Freizeit sowie die bedingungslose Liebe und Unterstützung auf meinem Lebensweg!

Weil der Stadt, im September 2022 *Marius Graf*

Abstract

Important properties for the design of dynamically loaded components are strongly influenced by microstructural features. With regard to steel materials, the martensitic microstructure is of great importance due to its outstanding strength. In this context, the mechanisms involved in the formation of the complex microstructure are still subject of current experimental research, whereby simulations at the microstructure level may contribute to a further understanding.

One focus of this work are experimental investigations in which the influence of the cooling rate on the martensite transformation and the resulting microstructure in a low-alloy steel is examined. From this, a possible transformation mechanism is derived. Another focus of this work is the development of a simulation model which describes the martensitic morphology and its evolution. In this context, a phase field model is presented. Here, order parameters are introduced which describe the material state, in this case austenite and martensite. The evolution of the order parameters is assumed to follow the time-dependent Ginzburg-Landau equation. A major extension to previous models is the consideration of twelve crystallographic martensite variants corresponding to the Nishiyama-Wassermann orientation relationship. To describe the ordered displacement of atoms during transformation and to account for the martensitic substructure, the well-known phenomenological theory of martensite crystallography is employed. The presented experiments as well as thermodynamic calculations are used as a basis in the identification of model parameters.

The presented model simulates the evolution of a thermally induced martensitic microstructure in monocrystals as well as polycrystals by means of the finite element method, whereby in the polycrystalline structures the predominant nucleation at lattice defects (grain boundaries) is considered. Furthermore, the model is able to represent the stress-induced autocatalytic nucleation. Basic features of the martensitic transformation can be reproduced. These include the martensite start temperature and the hierarchical microstructure consisting of blocks and packets. The sizes of the blocks are in good agreement with the real sizes of the experimental database.

Kurzfassung

Wichtige Eigenschaften für die Auslegung dynamisch belasteter Bauteile werden stark von den mikrostrukturellen Eigenschaften beeinflusst. Im Hinblick auf Stahlwerkstoffe ist die martensitische Mikrostruktur aufgrund ihrer herausragenden Festigkeit von großer Bedeutung. Dabei sind die Mechanismen bei der Entstehung des komplexen Gefüges immer noch Gegenstand aktueller experimenteller Forschungsarbeiten, wobei Simulationen auf Mikrostrukturebene zum Verständnis beitragen können.

Ein Schwerpunkt dieser Arbeit sind experimentelle Untersuchungen, bei denen der Einfluss der Abkühlrate auf die Martensittransformation beziehungsweise der resultieren Mikrostruktur in einem niedriglegierten Stahl untersucht wird. Hieraus wird ein möglicher Transformationsmechanismus abgeleitet. Ein weiterer Schwerpunkt dieser Arbeit ist die Erarbeitung eines Simulationsmodells, welches die martensitische Morphologie und deren Entwicklung beschreibt. In diesem Zusammenhang wird ein Phasenfeldmodell vorgestellt. Hierbei werden Ordnungsparameter eingeführt, welche den Materialzustand, in diesem Fall Austenit und Martensit, beschreiben. Bezüglich der Evolution der Ordnungsparameter wird angenommen, dass sie der zeitabhängigen Ginzburg-Landau Gleichung folgt. Eine wesentliche Erweiterung zu bisherigen Modellen ist die Berücksichtigung von zwölf kristallographischen Martensitvarianten entsprechend der Nishiyama-Wassermann-Orientierungsbeziehung. Um die geordnete Verschiebung der Atome während der Transformation zu beschreiben und die martensitische Sub-Struktur zu berücksichtigen, wird die bekannte phänomenologische Theorie der Martensitkristallographie eingesetzt. Die vorgestellten Experimente sowie thermodynamische Berechnungen dienen bei der Identifizierung der Modellparameter als Grundlage.

Mit dem vorgestellten Modell wird die Entwicklung eines thermisch induzierten martensitischen Gefüges in Monokristalllen sowie Polykristallen mittels der Finite-Elemente Methode simuliert, wobei in den polykristallinen Strukturen die vornehmliche Nukleation an Gitterdeffekten (Korngrenzen) berücksichtigt wird. Weiterhin ist das Modell in der Lage, die spannungsinduzierte autokatalytische Nukleation abzubilden. Grundsätzliche Merkmale der martensitischen Transformation können reproduziert werden. Dazu gehören unter anderem die Martensitstarttemperatur sowie die hierarchische Mikrostruktur bestehend aus Blöcken und Paketen. Die Größen der Blöcke werden mit den realen Größen der experimentellen Datenbasis abgeglichen, wobei eine gute Übereinstimmung gefunden wird.

Contents

List of Symbols and Abbreviations

Greek Letters

α^*	Weighting constant
α_{th}	Coefficient of thermal expansion
β	Generic mobility modulus
β^*	Weighting constant
$\boldsymbol{\chi}_t$	Placement in current configuration
$\boldsymbol{\chi}_0$	Placement in reference configuration
$\boldsymbol{\varepsilon}^0$	Eigenstrain tensor
$\boldsymbol{\varepsilon}^{\mathrm{el}}$	Elastic strain
ϵ_{irr}	Tolerance for irreversibility
$\tilde{\boldsymbol{\varepsilon}}$	Martensite transformation strain tensor
$\boldsymbol{\varepsilon}^{\mathrm{pl}}$	Plastic strain
ϵ	Principal strain
$\boldsymbol{\varepsilon}$	(Linearized) strain tensor
$\delta\boldsymbol{\varepsilon}$	Test function
$\tilde{\varepsilon}_{\mathrm{x}}$	Transformation strain parameter
η_1	Scalar component of Bain deformation tensor
η_2	Scalar component of Bain deformation tensor
η_3	Scalar component of Bain deformation tensor
η_{v}	Viscosity
$\tilde{\gamma}$	Effective interface energy
δ_{ij}	Kronecker delta
γ	Interface energy parameter
γ_{c}	Viscoplastic consistency parameter
ν	Poisson's ratio
ϕ_1^{Eul}	Euler angle of rotation around the z-axis
Φ^{Eul}	Euler angle of rotation around the x-axis
ϕ_2^{Eul}	Euler angle of rotation around the z-axis
$\boldsymbol{\phi}$	Reference description of the entire motion
$\boldsymbol{\phi_X}$	Path of particle
$\boldsymbol{\phi}_t$	Configuration at a certain time
ϖ	Internal body force in a micro-force system

ϖ_{dis}	Dissipative contribution of internal body force in a micro-force system
ψ^{el}	Elastic energy potential in the phase field context
ψ^{grad}	Gradient potential
ψ^{sep}	Phase separation potential
Ψ^{int}	Global interface energy
ψ	Helmholtz free energy density or phase field potential
ψ^{int}	Interface part of free energy density or phase field potential
ψ^{*}	Helmholtz free energy per unit mass
ϱ	Volumetric mass density
$\boldsymbol{\sigma}$	Cauchy stress tensor
μ_{r}	Logarithmic mean of r
σ_{r}	Logarithmic standard deviation of r
ς	External body force in a micro-force system
$\tilde{\boldsymbol{\sigma}}$	Stress tensor
σ_{vM}	von Mises stress
σ_{y}	Yield stress
θ_{crit}	Angle threshold for grain reconstruction
ϑ	Generic material field density
θ	Generic material field quantity
φ	Order parameter
$\underline{\varphi}$	Prescribed order parameter
$\delta\varphi$	Test function
$\boldsymbol{\xi}$	Micro-force vector stress
$\underline{\xi}$	Prescribed micro-force
ξ	Natural coordinate
ξ_p	Natural coordinate of Gauss point p
η	Natural coordinate
η_p	Natural coordinate of Gauss point p

Latin Letters

$\boldsymbol{a}$	Vector in the PTMC context
$\boldsymbol{a}$	Acceleration field
A	Area
$\mathbf{a}_1$	Basis vector
$\mathbf{a}_2$	Basis vector

$\mathbf{a}_3$	Basis vector
A^{2D}	Cross-section area
$A^{\mathrm{2D}}_{\mathrm{B}}$	Cross-section area of martensite blocks
$A^{\mathrm{2D}}_{\mathrm{CPP}}$	Cross-section area of close packed plane packets
$A^{\mathrm{2D}}_{\mathrm{PAG}}$	Cross-section area of prior austenite grains
a_α	Lattice constant
a_γ	Lattice constant
$\boldsymbol{B}^{\varphi_i}_I$	B-matrix for φ_i and node I
$\boldsymbol{B}^{\boldsymbol{u}}_I$	B-matrix for $\boldsymbol{u}$ and node I
$\boldsymbol{b}$	Vector in the PTMC context
$\mathbf{b}_1$	Basis vector
$\mathbf{b}_2$	Basis vector
$\mathbf{b}_3$	Basis vector
$\boldsymbol{b}^*$	Force density per unit mass
B	Generic continuum or material body
c_1	Constant
c_2	Constant
c_3	Constant
c_{a}	Constant
c_{b}	Constant
c_{c}	Constant
c_{d}	Constant
C	Component of elasticity tensor
c_α	Lattice constant
$\tilde{\boldsymbol{D}}$	Damping matrix
$\hat{\boldsymbol{d}}$	Vector containing the degrees of freedom at the nodes
d_{eq}	Equivalent diameter
d	Grain diameter
$\boldsymbol{d}_\varphi$	Vector containing the order parameter values
$\hat{\boldsymbol{d}}_\varphi$	Vector containing the order parameter values at the nodes
e^{pl}	Equivalent plastic strain
e	Error norm
$\boldsymbol{E}$	Green-Lagrange strain tensor
E	Young's modulus
$\boldsymbol{f}_{\mathcal{L}}$	Flux of angular momentum

$\boldsymbol{f}_{\mathcal{E}}$	Flux of energy
$\boldsymbol{f}_{\mathcal{H}}$	Flux of entropy
$\tilde{\boldsymbol{F}}$	External force (vector)
f^{bulk}	Dimensionless polynomial for bulk energy
f^{int}	Dimensionless polynomial for interface energy
$\boldsymbol{f}_{\theta}$	Flux of field quantity
$\boldsymbol{f}_{\mathrm{m}}$	Flux of mass
$\boldsymbol{f}_{\mathcal{I}}$	Flux of linear momentum
f_{r}	Probability density function of r
f_{y}	Yield condition
$\boldsymbol{F}$	Deformation gradient
ΔG_{chem}	Chemical driving force
$\Delta G_{\mathrm{chem}}^{\mathrm{MS}}$	Chemical driving force at martensite start temperature
g	Generic fit function
$\tilde{g}$	Chemical energy barrier parameter
Δg	Chemical energy difference per unit volume
Δg_{MS}	Critical chemical energy difference per unit volume at martensite start temperature
$\boldsymbol{H}$	Displacement gradient
H	Hardening modulus
h	Interpolation function
$h_{\sigma_{\mathrm{y}}}$	Interpolation function for yield stress
$\boldsymbol{I}$	Identity tensor
J	Jacobian
$\boldsymbol{J}$	Jacobian matrix
$\boldsymbol{J}$	Rigid body rotation matrix
k_{HP}	Hall–Petch constant
$\tilde{\boldsymbol{K}}$	Stiffness (matrix)
l	Interface width parameter
$\boldsymbol{L}$	Velocity gradient
l_{γ}	Edge length of square austenite grain
l_{el}	Element edge length of square element
l_{x}	Simulation domain size in x-Direction
l_{y}	Simulation domain size in y-Direction
m	Magnitude of the deformations in the PTMC context

m	Mass
M	Mobility constant
n_{int}	Total number of Gauss integration points
n_{if}	Number of nodes in interface (regarding a specific direction)
n_{mart}	Number of martensite variants
n_{fe}	Number of finite elements
n_{n}	Number of nodes per finite element
$\boldsymbol{n}$	Normal of outer boundary in current configuration
n	Magnitude of the deformations in the PTMC context
$\boldsymbol{N}$	Normal of outer boundary in reference configuration
N	Bilinear shape function
O	Origin
$\boldsymbol{P}$	Invariant plane deformation matrix
$p_{\mathcal{L}}$	Production of angular momentum
$p_{\mathcal{E}}$	Production of energy
$p_{\mathcal{H}}$	Production of entropy
p_{θ}	Production of field quantity
$\boldsymbol{p}^{\mathrm{m}}$	Invariant line vector
$\tilde{\boldsymbol{p}}^{\mathrm{m}}$	Normalized invariant line vector
$\tilde{\boldsymbol{P}}$	Internal force (vector)
$\boldsymbol{p}^{\mathrm{n}}$	Invariant plane normal
$\tilde{\boldsymbol{p}}^{\mathrm{n}}$	Normalized invariant plane normal
p_{m}	Production of mass
$p_{\mathcal{J}}$	Production of linear momentum
P	Generic continuum particle or material point
p^{2D}	Cross-section perimeter of grain
$p_{\mathrm{s}^{*}}$	Production of entropy per unit mass
$\boldsymbol{Q}$	Invariant plane deformation matrix
$\boldsymbol{q}_{\mathrm{th}}$	Heat flux
$\boldsymbol{q}^{\mathrm{m}}$	Invariant line vector
$\tilde{\boldsymbol{q}}^{\mathrm{m}}$	Normalized invariant line vector
$\boldsymbol{q}^{\mathrm{n}}$	Invariant plane normal
$\tilde{\boldsymbol{q}}^{\mathrm{n}}$	Normalized invariant plane normal
q	Generic function
r	Generic scalar quantity

r	Scalar heat radiation
$\boldsymbol{R}$	Residual (vector)
$\boldsymbol{S}$	Invariant plane deformation matrix
$s_{\mathcal{L}}$	Supply of angular momentum
s^{2D}	Form factor (circularity)
$\boldsymbol{s}$	Deviatoric stress
$s_{\mathcal{E}}$	Supply of energy
s	Entropy per unit volume
$s_{\mathcal{H}}$	Supply of entropy
s_{θ}	Supply of field quantity
$\boldsymbol{s}^{\text{m}}$	Invariant line vector
$\bar{\boldsymbol{s}}^{\text{m}}$	Bain transformed of invariant line vector
$\boldsymbol{s}^{\text{h}}$	Invariant plane normal
$\bar{\boldsymbol{s}}^{\text{h}}$	Bain transformed of invariant plane normal
s_{m}	Supply of mass
$s_{\mathcal{J}}$	Supply of linear momentum
s^*	Entropy per unit mass
$\tilde{\boldsymbol{S}}$	System matrix
T	(Absolute) temperature
$\boldsymbol{t}$	Traction vector
$\underline{\boldsymbol{t}}$	Prescribed traction
$\dot{\tilde{T}}_{81}$	Aproximated cooling rate from $800\,^{\circ}\text{C}$ to $100\,^{\circ}\text{C}$
t_{81}	Time from $800\,^{\circ}\text{C}$ to $100\,^{\circ}\text{C}$
$\dot{\tilde{T}}_{85}$	Aproximated cooling rate from $800\,^{\circ}\text{C}$ to $500\,^{\circ}\text{C}$
t_{85}	Time from $800\,^{\circ}\text{C}$ to $500\,^{\circ}\text{C}$
t	Time
t_0	Initial time
T_0	Equilibrium temperature
T_{MS}	Martensite start temperature
$t_{T_{\text{MS}}\rightarrow 100\,^{\circ}\text{C}}$	Time from martensite start temperature to $100\,^{\circ}\text{C}$
$\dot{\tilde{T}}_{T_{\text{MS}}\rightarrow 100\,^{\circ}\text{C}}$	Aproximated cooling rate from martensite start temperature to $100\,^{\circ}\text{C}$
T_{q}	Quenching temperature
$\boldsymbol{u}$	Displacement field
$\delta\boldsymbol{u}$	Test function
$\underline{\boldsymbol{u}}$	Prescribed displacement

$\boldsymbol{v}$	Velocity field
V	Volume
w^*	Internal energy per unit mass
w_q	Weight for quadrature point q
x	Coordinate
$\boldsymbol{x}$	Position vector or place in current configuration
$\boldsymbol{X}$	Position vector or place in reference configuration
y	Coordinate

Letter-like Symbols

$\boldsymbol{\mathcal{B}}$	Bain deformation tensor
$\mathcal{B}$	Geometric region
$\partial\mathcal{B}$	Boundary of geometric region
$\partial\mathcal{B}_\xi$	Boundary of geometric region, where prescibed external micro-force works
$\partial\mathcal{B}_{\varphi_i}$	Boundary of geometric region, where prescribed order parameter works
$\partial\mathcal{B}_\sigma$	Boundary of geometric region, where prescibed external traction works
$\partial\mathcal{B}_{\boldsymbol{u}}$	Boundary of geometric region, where prescribed displacement works
$\mathcal{B}_t$	Geometric region in current configuration
$\partial\mathcal{B}_t$	Boundary of geometric region in current configuration
$\mathcal{B}_0$	Geometric region in reference configuration
$\partial\mathcal{B}_0$	Boundary of geometric region in reference configuration
$\boldsymbol{\mathcal{C}}$	Fourth order elasticity tensor
$\boldsymbol{\mathcal{C}}^\gamma$	Fourth order elasticity tensor of austenite
$\boldsymbol{\mathcal{C}}^\alpha$	Fourth order elasticity tensor of martensite
$\mathcal{E}$	Total energy
$\mathcal{H}$	Total entropy
$\mathcal{L}$	Angular momentum
$\boldsymbol{\mathcal{I}}$	Linear momentum
$\mathcal{P}_{\text{ext}}$	External mechanical power
$\mathcal{Q}_{\text{ext}}$	External thermal power
$\mathcal{R}^3$	Three-dimensional Euclidean space
$\mathcal{R}_+$	Set of real positive numbers
$\boldsymbol{\mathcal{R}}$	Rotation matrix
$\boldsymbol{\mathcal{T}}$	Bain correspondence matric
$\mathcal{T}$	Generic time interval

Other Denotations

$\times$	Cross product
$(\bullet)'$	First derivate of $(\bullet)$
$\cdot$	Dot product
$:$	Double contraction
$\otimes$	Dyadic product
$\boldsymbol{\nabla}(\bullet)$	Gradient of $(\bullet)$
$\hat{(\bullet)}$	Denotes nodal quantities in the finite element context
$\lvert \bullet \rvert$	Euclidean norm of $(\bullet)$
$\langle\langle \bullet \rangle\rangle$	Ramp function $((\bullet) + \lvert \bullet \rvert)/2$
$\dot{(\bullet)}$	Time derivate of $(\bullet)$
$(\bullet)^{-1}$	Inverse of $(\bullet)$
$(\bullet)_{\mathrm{at.\%}}$	Atomic percent of chemical element $(\bullet)$
$\det(\bullet)$	Determinant of $(\bullet)$
$\mathrm{dev}(\bullet)$	Deviatoric part of $(\bullet)$
$\mathrm{div}(\bullet)$	Divergence of $(\bullet)$
$\mathrm{grad}(\bullet)$	Gradient of $(\bullet)$
$(\bullet)_I$	Value of $(\bullet)$ at node I
$(\bullet)_J$	Value of $(\bullet)$ at node J
$(\bullet)^T$	Transpose of $(\bullet)$
$(\bullet)^{\mathrm{V}}$	Voigt notation of $(\bullet)$
$(\bullet)_{\mathrm{wt.\%}}$	Weight percent of chemical element $(\bullet)$
$\Delta(\bullet)$	Increment of $(\bullet)$
$\underline{\Delta}(\bullet)$	Laplacian $\mathrm{div}(\mathrm{grad}(\bullet))$

Abbreviations

at.	Atomic
BCC	Body centered cubic
BCT	Body centered tetragonal
const.	Constant
CPP	Close packed plane
EBSD	Electron backscatter diffraction
ECDF	Empirical cumulative distribution function
FCC	Face centered cubic
GT	Greninger-Troiano

|	
IPF	Inverse pole figure
irr.	Irreversible
KS	Kurdjumov-Sachs
max.	Maximum
mic.	Microstructure
min.	Minimum
NW	Nishiyama-Wassermann
PAG	Prior austenite grain
PTMC	Phenomenological theory of martensite crystallography
synth.	Synthetic
wt.	Weight

1. Introduction

The microstructure of materials is decisive for the macroscopic material and component behavior, cf. Schäfer et al. (2019a); Welschinger et al. (2019). This also applies to the microstructure phase martensite, which can basically occur in metals, but also in non-metals, e.g. ceramics. With this allotrope phase, highest strengths of steels can be achieved with a given chemical composition, which leads to an enormous technical importance of martensite. Due to e.g. wear resistance requirements of technical components, the particularly hard martensite is a frequently desired microstructure. Usually, martensite is produced with an appropriate heat treatment process. In this process, the steel must be cooled (usually quenched) from the temperature of high-temperature phase austenite to the temperature of low-temperature phase ferrite (α-phase). If the super-cooling below the equilibrium temperature of these two phases and thus the driving force is large enough and at the same time built up fast enough so that no diffusion takes place, then martensite is formed.

1.1. Motivation and State of the Art

Despite extensive experimental research on martensite and its formation in steels, the underlying mechanisms are still not fully understood. Many complex mechanisms interact in martensite transformation, and the extreme speed under conditions that are difficult to control experimentally makes in-situ observation of nucleation and subsequent growth difficult. In principle, several size scales are relevant for a holistic view of martensite transformation, cf. Fig. 1.1. The nucleation takes place on the nanoscale and with further growth of the martensite crystals the mesoscale is reached, on which the characteristic martensitic microstructure can be observed. The dramatic changes in the microstructure lead to shape changes and stresses, which at the macro scale lead to relevant effects for the design as well as the process control in the manufacturing (heat treatment) of components.

In order to simulate heat treatment processes at the component level, a phenomenological relationship based on the well-known Koistinen-Marburger equation (Koistinen & Marburger (1959)) is classically used to model the austenite-martensite transformation. Such formulations are used to determine the fraction of martensite that forms from high-temperature austenite during monotonic cooling below the martensite start temperature.
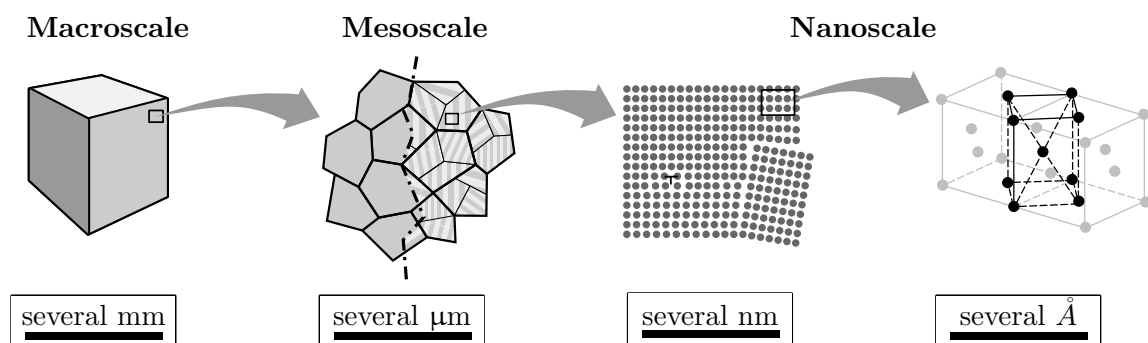
Figure 1.1: Different length scales relevant for martensite transformation

Heat treatment simulations on component level coupling corresponding physical aspects and describing the austenite-martensite transformation by a phenomenological relationship were performed in the context of induction hardening (Schwenk (2014)), quenching (Huiping et al. (2007)) and selective laser melting (Schänzel et al. (2019)), to mention only a few. Since the change in mechanical behavior as well as undesirable effects are accompanied by a dramatic change in microstructure, it is of interest to resolve the microstructure and physical mechanisms on the microstructure length scale. A two-scale coupling of bulk microstructural evolution and macroscopic material behavior was recently developed by Kochmann et al. (2016). However, a modeling technique that couples the macroscopic component behavior with the resolved microstructure during a heat treatment process, taking into account the various physical fields that occur, remains a major challenge. A few key aspects to work on are mentioned by Kochmann et al. (2016): (i) the microstructure model, (ii) multiple length- and timescales (iii) and the computational approach. While Kochmann et al. (2016) refers to points (ii) and (iii), this work is devoted to point (i).

One possibility of modeling microstructures is based on the minimization of the energy with respect to microstructural parameters describing sequential laminates. With neglecting the interface energy and the dissipative interface motion this approach allows a prediction of sequential laminates, which is a characteristic feature of martensite microstructures. Regarding the simulation of martensite microstructures, applications are given by Luskin (1996); Aubry et al. (2003); Kružík et al. (2005). In addition, modifications of this approach are known that consider dissipative effects. In such models, a dissipative evolution of certain microstructural parameters and a minimization with respect to the rest takes place (partial relaxation). Applications to martensite transformations are given by Bartel & Hackl (2008); Bartel (2009); Bartel & Hackl (2009); Bartel et al. (2011). Extensions to incorporate size effects by including interface energy and dissipation are given, for example, by Petryk & Stupkiewicz (2010); Petryk et al. (2010). As a drawback of these relaxation-based approaches remains their limitation to idealized sequential microstructures, while in reality more complex martensitic microstructures occur, minimizing the misfit energy.

Prediction of more realistic martensite morphologies requires models capable of resolving and predicting the evolving spatial morphology of the microstructure without a priori assumptions. With such models it is possible to contribute to the understanding of the martensite transformation. This requires the postulation of additional constitutive relations to describe the kinetics of interfaces, which can be realized in the framework of the continuum mechanical theory of sharp interfaces, see e.g. Abeyaratne & Knowles (1990, 2006); Hildebrand (2013). The main challenge here is the explicit description of the time-dependent topology of sharp interfaces as discontinuity surfaces. Concerning the simulation of martensite evolution on the mesoscale and in accordance to Hildebrand & Miehe (2012b), the known procedures may be divided into two classes based on continuum mechanics of interfaces.

The first class represents sharp interface approaches, where interfaces are modeled as actual discontinuity surfaces. The extended finite element method (XFEM) is a prominent numerical implementation of the sharp interface approach, see e.g. Ji et al. (2002) for application to phase transformations. However, this approach is unsuitable for complex interface topologies, especially if more than two phases are considered. Furthermore,

complex mechanisms such as the formation, unification and dissolution of interfaces must be defined by special criteria.

The second class represents regularized sharp interface approaches, which approximate the sharp interface by a smooth approximation of the discontinuity. These approaches lead to the phase field models, where the sharp discontinuities between different phases are approximated by smooth transitions with appropriate order parameters describing the presence of the respective phase. In a general continuum-thermodynamic context, the theoretic considerations of Fried & Gurtin (1993, 1994); Fried & Grach (1997) provide the basis for such models. The final resulting formulations are generally extensions of the classical Ginzburg-Landau equation to coupled problems of phase transformation and elastic deformation (Hildebrand & Miehe (2012b)). The phase field approach allows formation of unrestricted martensite evolution. It also incorporates interface energy and dissipative effects. Further, it can be shown that suitable phase field formulations achieve sharp interface limit, cf. Fried & Gurtin (1993); Garcke (2000); Alber & Zhu (2008). In contrast to sharp interface approaches, no additional computational effort to track multiple interfaces is required, cf. Chen & Khachaturyan (1991); Levitas et al. (2010). A general overview on phase field modeling is given by Moelans et al. (2008), while Mamivand et al. (2013) focus on phase field models concerning martensite transformations.

Numerous phase field models to describe martensitic phase transformation have been developed. Chen et al. (1992); Wang & Khachaturyan (1997) introduced the first (elastic) phase field models for martensitic transformations, by integrating the micro-elasticity theory according to Khachaturyan & Shatalov (1969). Many others followed, see e.g. Artemev et al. (2000, 2001); Jin et al. (2001), with application to different material systems and different boundary conditions. In recent years, the focus has been on extending phase field models by certain physical mechanisms to improve the prediction of martensite microstructures and its evolution, e.g. by considering elasto-plastic materials (Yamanaka et al. (2008); Malik et al. (2012); Yeddu et al. (2012a,b); Schmitt et al. (2013b)), crystal-plasticity (Yamanaka et al. (2009); Schmitt et al. (2014, 2017)) and dislocation dynamics (Kundin et al. (2011)). In 2015, Schmitt et al. (2015) proposed a phase field model for martensitic transformation coupled with a phase field model for microcracks. A phase field model coupled with the heat equation is proposed by Schmidt et al. (2017); Schmidt & Müller (2017). Furthermore, the phase field method was applied with regard to martensite evolution in dual-phase steels (Schoof et al. (2018b,a)), heterogeneous austenite-graphite structures (Schoof et al. (2019)) as well as shape memory alloys (Ahluwalia et al. (2004); Zhong & Zhu (2014); Cui et al. (2017, 2018)). Effects of prior austenite grain (PAG) sizes were investigated in Fe-Ni alloys (Cui et al. (2016)), shape memory alloys (Ahluwalia et al. (2015)) and recently by considering plasticity (Yeddu (2018)). Partitioning following the martensite transformation after quenching was considered by Mecozzi et al. (2016); Amos et al. (2019); Zhang et al. (2019) with phase field models. The microstructural evolution due to nano-indentation was simulated by Rezaee-Hajidehi & Stupkiewicz (2020). One size scale lower, at the nanoscale scale, the interaction between martensite transformation and dislocations could be modeled and simulated using the phase field method (Levitas & Javanbakht (2015); Javanbakht & Levitas (2015)).

Many publications on phase field modeling of martensite transformation are based on a Fourier transformation formalism with regard to numerical implementation. This is due to the efficiency of the method. Others use finite differences, which is probably motivated

by the simple and flexible implementation, see e.g. Yamanaka et al. (2009); Du (2017); Schoof et al. (2018b,a). In order to consider complicated boundary conditions as well as complex material models, Müller (2016) argues that the finite element method is the most effective for such cases. Examples of phase field models for martensitic transformations with the finite element method are given by Levitas et al. (2010); Hildebrand & Miehe (2010); Roumi (2010); Hildebrand & Miehe (2012a); Yeddu et al. (2012b); Schmitt et al. (2012); Levitas et al. (2013); Malik et al. (2013); Schmitt et al. (2013a).

In addition to continuum approaches, atomistic simulations were also performed. The first studies on martensitic transformations using molecular dynamics (MD) simulations were based on a NiAl system by Rubini & Ballone (1993, 1994). Later, studies were also carried out on ferrous alloys by Entel et al. (2000) and pure Fe by Engin & Urbassek (2008). Both strain- and temperature-induced transformations could be analyzed. Since the Fe-C system is the basis of steel, Wang et al. (2014) investigated a bulk with different carbon contents in order to study the temperature induced austenite-martensite (and vice versa) transition. With simulations of this length scale (nanoscale), details of the transformation path become accessible, see Sandoval & Urbassek (2009). In addition, the energetics and dynamics of the transformation are included and can be analyzed, see e.g. Wang & Urbassek (2013). A detailed review of the previous research in this field is given by Urbassek & Sandoval (2012); Ou (2017). However, when the mesoscale is of interest, the use of MD simulations is of limited utility because length scales beyond 10^2 nanometers and time scales beyond a few nanoseconds are difficult to access with current computer architectures. Phase field models, however, can serve as a scale-bridge tool in this regard, cf. Diewald (2020). By regarding simulations of a smaller length scale, it would be possible to identify reliable model parameters without complex experiments. Investigations that use MD simulations for the parameter identification of phase field simulations concerning martensite transformations are presented by Schmitt et al. (2013c), where the parameters for pure Fe have been identified.

1.2. Objectives and Overview

Based on the numerous publications, the phase field method seems to be a valid tool for simulating martensite transformation. Nevertheless, many publications do not provide a quantitative comparison with experimental results. The aim of this work is to develop a phase field model which allows to simulate thermally induced martensitic microstructures of low-alloy steels on the mesoscale in a quantitative way. Thus, the focus is on the formation of lath martensite morphology. To achieve this, experimental investigations are carried out with the low-alloy steel 50CrMo4 (SAE 4150). The goal of these investigations is to provide an understanding of the underlying martensite transformation mechanism that will be modeled. Further, experimental data is used to identify model parameters and in order to compare simulation results with reality. The work is structured as follows:

Section 2 collects foundations of martensite in steels, with a focus on lath martensite. First, general aspects of martensite transformation, such as the resulting shape change and thermodynamics with respect to driving forces, are covered. In order to introduce some terminology important for the explanation of martensite evolution, subsequently essential features of the resulting martensitic microstructure are explained. Thereafter, the focus is on the theoretical considerations describing martensite crystallography and shape change. The last important point discussed is the martensite mechanisms at initiation and growth.

In **Section 3**, the most important continuum mechanical fundamentals are introduced. This includes the kinematic relationship in the context of small strains and the balance equations.

Section 4 presents the experimental results, whereby at first some background information is provided and the specific motivation of the experimental design is clarified. The setup and the methodology are presented afterwards. Subsequently, the results from the different heat treatments and the resulting material hardnesses are presented. Focusing on the martensite sizes, the microstructure is then characterized. The results are discussed and evaluated on the basis of literature results. Based on this, a possible underlying martensite transformation mechanism is elaborated.

Section 5 takes up the findings from Sec. 4 and Sec. 2 with regard to modeling. First, the phase field model for the mesoscopic martensite transformation is presented. The numerical implementation is described in detail hereafter, referring to the two-dimensional plane strain case for the sake of simplicity. The three-dimensional extension is straightforward. The procedure for generating polycrystalline austenite structures, which serve as input for martensite simulation in polycrystals, is then presented. Based on this, it is described how the initial athermal nucleation in polycrystalline structures and the important mechanism of autocatalytic nucleation are modeled. Furthermore, an extension to viscoplastic material behavior is carried out in this work. The choice of boundary conditions is discussed in the next step. The last important point is the detailed description of how the transformation strain and the martensite variant orientations are determined. This is done based on a crystallographic theory (e.g. the phenomenological theory of martensite crystallography, PTMC), which allows to take into account the substructure of the martensite crystals.

Section 6 presents numerous numerical studies. First, simple model setups are calculated in order to understand the basic model behavior and to review it with regard to relevant mechanisms. The complexity of the models is constantly increased. Effects of plasticity and martensite transformation in polycrystals are investigated. As the highest level of complexity, three-dimensional simulations with twelve martensite variants are performed. A quantitative comparison of the simulated martensite sizes with the real martensite sizes is also made.

Section 7 concludes this thesis and provides an outlook on future tasks and challenges that can be addressed.

Some of the elaborations and results of this work have already been published in international journals or conference proceedings: Graf et al. (2020), Graf et al. (2021a), Graf et al. (2021b), Graf et al. (2021c). Furthermore, a student thesis supported the present work: Steinmetz (2020). They are cited where appropriate.

2. Martensite in Steels

This section describes the foundations of martensite as a product of a transformation. The focus is on martensite in steels, although it is known that martensite can occur in many other metallic, non-ferrous alloys and ceramics, cf. Nishiyama (2012). The formation of body centered cubic or tetragonal (BCC or BCT) α'-martensite from face centered cubic (FCC) γ-austenite in ferrous alloys is the most common transformation path. Relevant monographs or publications that deal with martensite and its transformation are, for example, given by Bhattacharya et al. (2003), Khachaturyan (2013), Nishiyama (2012), Pereloma & Edmonds (2012) and Zhang & Kelly (2009). These works form the basis of this section. In addition, the extensive works of Villa (2013) and Löwy (2015) are used as references. Supplementary findings from recent publications and other aspects relevant to this work are added accordingly.

2.1. General Aspects

Generally, martensite transformation is defined as diffusionless, lattice-distortive, shear-dominant transformation, which occurs by nucleation and growth, cf. Olson & Cohen (1981); Sinha (2003). Diffusionless means that there is no rearrangement and thus no change of the composition due to a movement of atoms larger than the inter-atomic distance. However, a coordinated movement of the atoms is allowed. In contrast to shuffle displacement, a lattice-distortive transformation is accompanied by a relative movement of atoms that converts the initial austenite lattice into the product martensite lattice, implying a transformation strain.

2.1.1. Shape Change

In non-clamped cases, the effect of transformation strain is accompanied with an observable mesoscopic deformation, which is plane-invariant, meaning that the interfaces between parent and product phase is an undistorted and unrotated plane. In Fig. 2.1(a), the unconstrained shape change resulting from invariant plane strain is shown. While there is a slight dilatation strain it is dominated by the shear component, cf. Bhadeshia (2001a,b).

In clamped cases, where the free deformation is counteracted by surrounding material, the strain minimization introduces some curvature in the interface, cf. Fig. 2.1(b). Satisfying
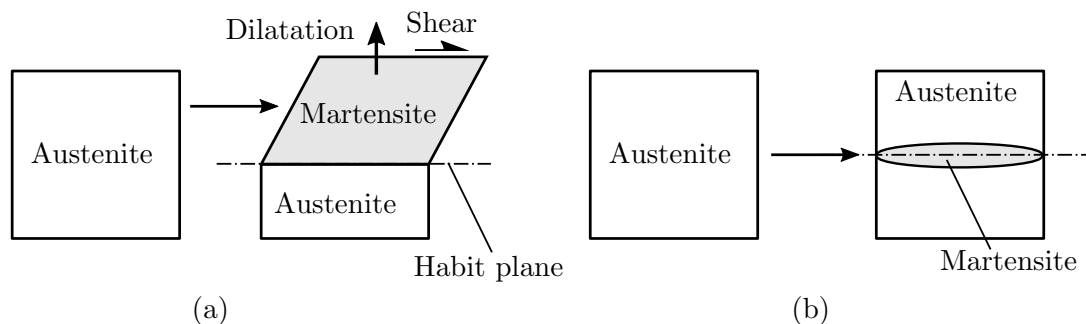
Figure 2.1: Schematic illustration according to Bhadeshia (2001a,b) of an invariant-plane strain shape deformation accompanying martensitic transformation in a non-clamped system in (a), and cross-sectional plate-like martensite formation in a clamped system in (b)
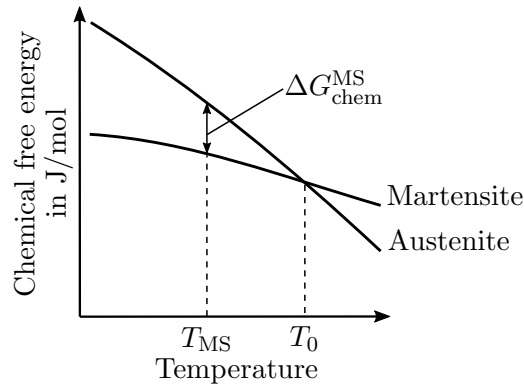
Figure 2.2: Schematic representation of chemical free energies of austenite and martensite as a function of temperature, cf. Wayman & Bhadeshia (1996)

the conditions of invariant plane strain, it has been shown by Eshelby (1957) that the strain energy associated with martensite transformation can be reduced to zero in the form of an infinitesimally thin oblate, see Christian (1976). In reality narrow strips, called laths or plates are formed. Either the interface plane between austenite and martensite or the middle plane of the martensite unit is referred to as habit plane, cf. Klostermann (1972); Villa (2013). Thus, for both cases the habit plane is identical.

2.1.2. Thermodynamics and Driving Forces

The thermodynamics of martensite transformation is typically described in terms of molar Gibbs free energy (free enthalpy), although in martensite transformation the Gibbs free energy can be used interchangeably with the Helmholtz free energy (or simply free energy). To produce martensite, the parent phase is not allowed to be the most stable energy configuration of the system. An excess of Gibbs free energy in the system and thus a driving force must be present in order to initiate a phase transition.

Fig. 2.2 illustrates the chemical Gibbs free energy of austenite and martensite as function of temperature. At an equilibrium temperature T_0 the energies of both phases are identical. At temperatures higher than T_0, austenite is the energetic more favorable phase and below that temperature ($T < T_0$) it is martensite. The difference between those energetic levels is the chemical driving force, which is denoted as ΔG_{chem}. If the chemical driving reaches a certain value $\Delta G_{\text{chem}} = \Delta G_{\text{chem}}^{\text{MS}}$ by supercooling, the martensite starts to grow at the martensite start temperature T_{MS}. For temperatures between T_0 and T_{MS} the chemical driving is not sufficient to trigger the transformation mainly due accompanying elastic stress. In general, it is possible to provide the necessary activation energy by the mechanical energy due to an applied stress. However, this case will not be considered further in this work.

Note that during the transformation into martensite, a partitioning of the atoms cannot take place fast enough. Thus, martensite is a non-equilibrium structure, which is energetically more favorable than austenite, but represents not the most energetically favorable structure of the system.

2.2. Characteristics of Martensite Microstructures

In order to introduce some terminology important for the explanation of martensite evolution, this section explains the essential features of the resulting martensitic microstructure. It should be mentioned in advance that martensite occurs in different variants with different crystal orientations. These variants can be divided into groups of different transformation strains. The properties of the martensite variants lead to characteristic martensite morphologies (shape of the martensite units). First, Sec. 2.2.1 discusses the martensite morphology, focusing on the lath morphology. Subsequently, in Sec. 2.2.3, the characteristic orientation relationships between the parent and product phases are explained.

2.2.1. Microstructural Morphology

In general, there are five morphology types of α-martensite[1] reported, see Maki (1990): lath, butterfly, $(225)_\gamma$ plate type, lenticular and thin plate. These different morphologies arise in dependence of the chemical composition and the martensite start temperature T_{MS}. The aforementioned martensite types tend to occur with decreasing T_{MS} in the mentioned order. Besides T_{MS}, the strength of parent austenite and product martensite, the critical resolved shear stress for slipping and twinning, and the stacking fault energy of austenite seem to be determining factors for the resulting morphology, see e.g. Davies & Magee (1971), Krauss & Marder (1971), Maki et al. (1972), and Carr et al. (1978). Otherwise, the factors are rather poorly defined, see Maki (2012). This work focuses on the lath morphology, which is reported in Fe-C ($\leq 0.6\%$ C), Fe-Ni ($< 28\%$ Ni), and Fe-Mn ($< 10\%$ Ni) alloys, cf. Maki (2012).

The crystallography of lath martensite has been examined by Morito et al. (2003, 2006a) using Kikuchi patterns and electron backscatter diffraction (EBSD) analysis at mesoscopic length scale. In these works, Fe-C alloys with different carbon contents are analyzed and schematic illustrations of structures with high and low carbon contents are given in Morito et al. (2003), see Fig. 2.3(a+b). Accordingly, typical structures consist of a three-level hierarchy, see also Krauss (1990): martensite laths, blocks and packets. In low carbon alloys ($0.1\,C - 0.4\,C$), well developed blocks with parallel boundaries are found. Each block consists of laths from two martensite variants with small misorientation angle. Typically they are referred to as sub-blocks, cf. Kitahara et al. (2006). In high carbon alloys (≈ 0.6 C) packets consist of six variants of blocks with laths from a single variant. As Fig. 2.3 indicates, it has been observed that packet and blocks are of smaller size in the high carbon alloy.

2.2.2. Substructure of Martensite

The substructure of the transformation product martensite refers to the structure within a martensite unit and is an important strain accommodation mode. In lath martensite, a martensite unit is considered as martensite crystal of the lowest hierarchical level, namely a lath. In the case of plate martensite, the plate is considered as one martensite unit. There are two types of substructures: internal twins and arrays of dislocations. Internal twins are mainly observed in thin plate martensite at low transformation temperatures, while dislocations as substructure are dominantly observed in lath martensite with high

---

[1]martensite is often denoted with α' to distinguish it from other α-phases, cf. Nishiyama (2012). For the sake of compactness, the apostrophe is omitted in the further course of this work.

(a)   (b)
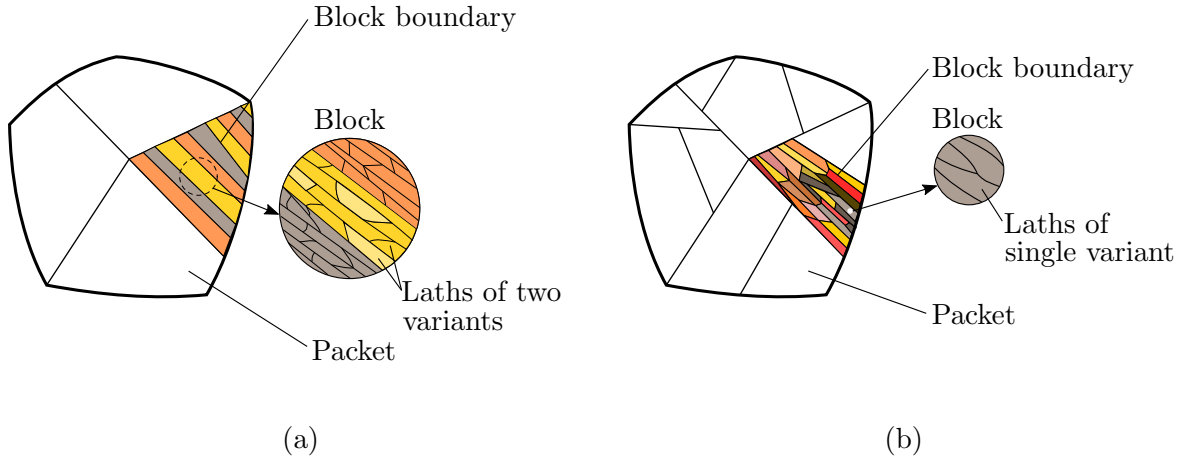
Figure 2.3: Schematic illustrations of hierarchical structure of lath martensite in Fe-C alloys with different carbon contents according to Morito et al. (2003), (a) $0 - 0.4\,\%$ C, (b) $0.6\,\%$ C

transformation temperatures, cf. Maki (2012). However, the partial presence of internal twins in lath martensite is not excluded, cf. Ping et al. (2018).

2.2.3. Orientation Relationships

In terms of crystallographic orientations, there is a clear relationship between the crystal structure of the parent phase austenite and the product phase martensite. This is accompanied by the fact that the growth of a martensite unit is limited to a single grain of the austenite phase. In steels, the orientation relationships according to Kurdjumov & Sachs (1930), Nishiyama (1934), Wassermann (1935) and Greninger & Troiano (1949) are frequently a good description of the experimentally observed orientation relationships, see e.g. Kitahara et al. (2005, 2006) and Kelly et al. (1990). They can be expressed with reference to parallel crystal planes and parallel crystal directions within those planes. Accordingly, the mentioned orientation relationships are typically reported as:

$$\text{Kurdjumov-Sachs (KS):} \qquad (111)_\gamma \,||\, (011)_\alpha \,,\, [\bar{1}01]_\gamma \,||\, [\bar{1}\bar{1}1]_\alpha \,, \tag{2.1}$$

$$\text{Nishiyama-Wassermann (NW):} \; (111)_\gamma \,||\, (110)_\alpha \,,\, [11\bar{2}]_\gamma \,||\, [\bar{1}\bar{1}0]_\alpha \,, \tag{2.2}$$

$$\text{Greninger-Troiano (GT):} \qquad (111)_\gamma \; 1° \text{ from } (001) \,,\, [\bar{1}01]_\gamma \; 2.5° \text{ from } [\bar{1}\bar{1}1] \,, \tag{2.3}$$

where the respective first specification defines the relation between the planes and the respective second specification the relation between the directions.

Due to the cubic symmetry there are in total four equivalent planes to the $(111)_\gamma$ plane[2], with six variants living on such a plane in case of the KS orientation relationship. Overall, there are 24 variants in this orientation relationship, which also applies to the GT orientation relationship. The NW orientation relationship results in twelve variants, since there are three variants per invariant plane.

The three or six variants on a $(111)_\gamma$-plane, or on one of its equivalent planes, form a crystallographic packet corresponding to the illustration in Fig. 2.3. Since these planes are the four close packed planes (CPPs) in a FCC, the variants share the same CPPs. These

---

[2] $(111)_\gamma$, $(\bar{1}11)_\gamma$, $(1\bar{1}1)_\gamma$, $(11\bar{1})$
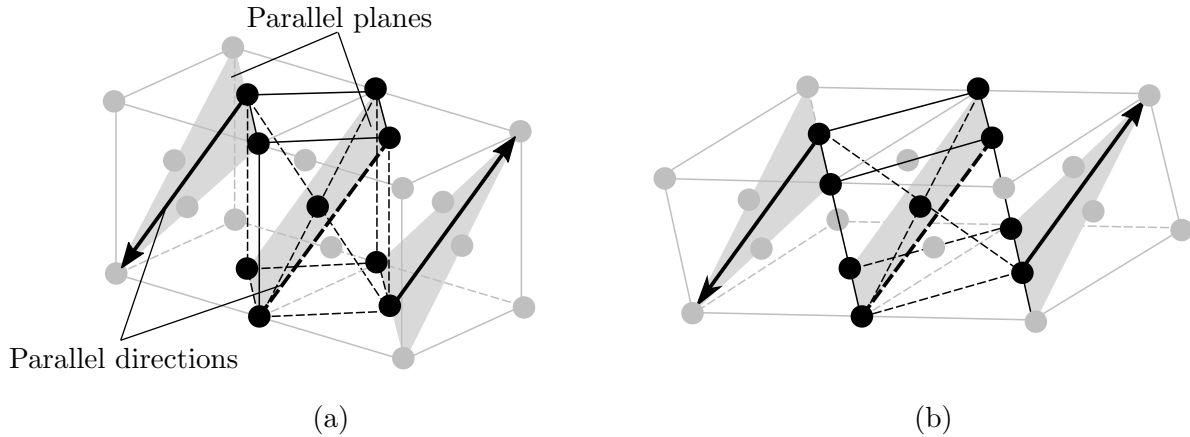
Figure 2.4: Visualization of the NW orientation relationship, (a) parent FCC phase (austenite), (b) product BCC phase (martensite), black arrows indicate possible accompanying movements during the transformation parallel to the invariant direction on the invariant plane

variants also have the same habit planes. Concerning the KS orientation relationship observed in low carbon steel, the variants are not randomly distributed in a packet. Instead, they frequently appear in specific pairs (sub-blocks), cf. Sec. 2.2.1. These pairs tend to have low misorientation angles of about 10°, see Morito et al. (2006a). With the NW orientation relationship, there are only high misorientations of 60° between the three variants forming a packet, see e.g. Morito et al. (2006a) and Suikkanen et al. (2011). An analogous analysis of the misorientations occurring for GT is currently not known. Since this relationship lies between KS and NW, it is often not considered in literature, see e.g. Morito et al. (2006a) and Maki (2012).

In Fig. 2.4(a+b) an attempt is made to visualize the NW transformation path. In addition, the parallel planes $(111)_\gamma$ and $(011)_\alpha$ (gray shaded) and the parallel directions $[11\bar{2}]_\gamma$ and $(01\bar{1})_\alpha$ (black vectors/dashed lines) on that planes are depicted. In order to transfer the austenite FCC system into an BCC martensite system, a shear is indicated in which the specific planes and directions are kept parallel (invariant). A possible snapshot after this shear is illustrated in Fig. 2.4(b). A second step, which is not shown, would be an expansion or contraction of the BCC structure to obtain the corresponding atomic density. It should be noted that this sequence of movements does not have to take place in such a way, but serves here merely as an illustration in order to transform the known initial state to the known final state.

2.3. Crystallographic Concepts for Shape Change Modeling

An essential advance in the theoretical consideration of martensite crystallography is the PTMC, independently developed by Wechsler et al. (1953) and Bowles & Mackenzie (1954). With this theory, the atomic displacements accompanied by the martensite transformation is described in terms of basic matrix algebra. In this section, the basic idea of PTMC will be presented, partially referencing to the explanations by Graf et al. (2021c). As an important basis, the Bain correspondence is explained beforehand.

Bain variant 1 (b=1)   **Remaining Bain variants**
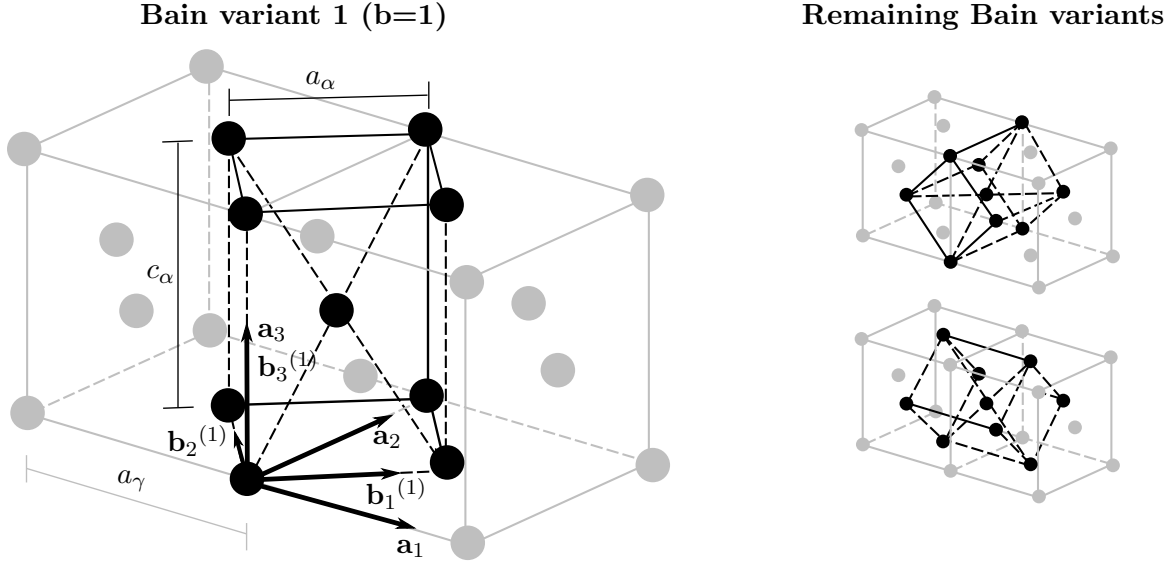
Figure 2.5: Schematic illustration of Bain correspondence for martensite in steels. Two unit cells of austenite (gray) and a unit cell of martensite (black) are depicted. Interstitial carbon atoms are not shown for simplicity's sake.

2.3.1. Bain Correspondence

An essential concept to describe martensitic transformations in steels is the lattice correspondence between the FCC austenite and the BCC martensite. For steels the Bain correspondence, see Bain & Dunkirk (1924), shown schematically in Fig. 2.5 can be verified experimentally, cf. Kelly (2012). To obtain a unit cubic cell of martensite, it is necessary to deform the parent phase austenite by one of three possible deformations. The corresponding deformation gradients are known as the Bain deformations $\boldsymbol{\mathcal{B}}^{(b)}$, e.g.

$$\boldsymbol{\mathcal{B}}^{(1)} = \begin{pmatrix} \eta_1 & 0 & 0 \\ 0 & \eta_2 & 0 \\ 0 & 0 & \eta_3 \end{pmatrix}, \boldsymbol{\mathcal{B}}^{(2)} = \begin{pmatrix} \eta_3 & 0 & 0 \\ 0 & \eta_1 & 0 \\ 0 & 0 & \eta_2 \end{pmatrix},$$

$$\boldsymbol{\mathcal{B}}^{(3)} = \begin{pmatrix} \eta_2 & 0 & 0 \\ 0 & \eta_3 & 0 \\ 0 & 0 & \eta_1 \end{pmatrix} \quad \text{with} \quad \eta_1 = \eta_2 = \sqrt{2}\,\frac{a_\alpha}{a_\gamma}, \quad \eta_3 = \frac{c_\alpha}{a_\gamma}, \tag{2.4}$$

where a_α, c_α and a_γ are the lattice constants shown in Fig. 2.5. According to Fig. 2.5 there are three Bain variants $\boldsymbol{\mathcal{B}}^{(b)}$. For ferrous materials, $\eta_1, \eta_2 > 1$ and $\eta_3 < 1$ usually applies. The total volume change is given by $\eta_1\,\eta_2\,\eta_3 - 1$. Note that for steels containing significant amounts of carbon, the martensite deviates from the ideal cubic BCC shape. Depending on the carbon content, the lattice is tetragonally distorted to BCT, see Nishiyama (2012). The Bain correspondence follows the most intuitive transformation path to transfer the FCC to the BCC crystal. However, the resulting orientation relationship expressed as

$$(001)_\gamma \,||\, (001)_\alpha\,, \, [\bar{1}01]_\gamma \,||\, [\bar{1}\bar{1}1]_\alpha \tag{2.5}$$

does not explain the experimentally observed orientation relationships, cf. Sec. 2.2.3.

$$S = J\,\mathcal{B}$$

D — C   D — C   D — C

| Austenite | $\boldsymbol{P}$ → | Proved shape, unproved structure | $\boldsymbol{Q}$ → | Martensite (proved structure, unproved shape) |

A — B   A — B   A — B

Lattice invariant deformation

D — C   D — C

Twinned   Slipped

A — B   A — B

Proved shape, proved structure
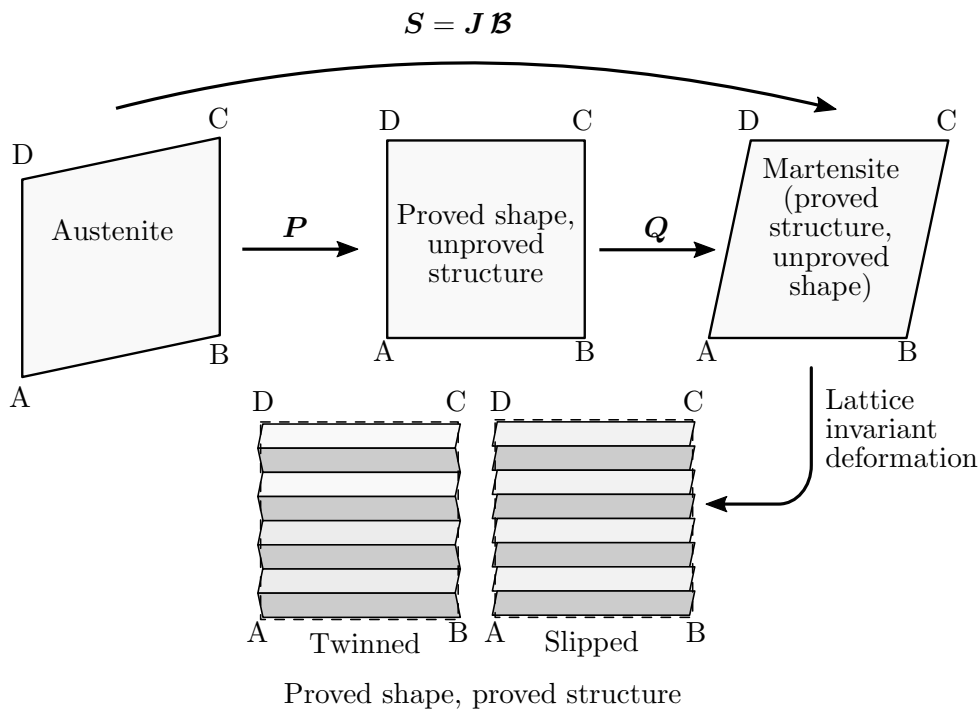
Figure 2.6: Illustration of the PTMC, based on the illustration by Bhadeshia (2001b)

2.3.2. Phenomenological Theory of Martensite Crystallography

The PTMC takes into account the Bain correspondence and at the same time approximates the observed orientation relations. An illustrative representation of the concept is given in Fig. 2.6. It shows that the Bain deformation $\mathcal{B}$ combined with an appropriate rigid body rotation $\boldsymbol{J}$ converts the atomistic structure of austenite (FCC) into martensite (BCC or BCT). However, the structure that results from the deformation $\boldsymbol{J}\mathcal{B}$ has a shape which is not observed in reality. According to the PTMC, an invariant plane deformation $\boldsymbol{P}$ converts the material into a shape that is experimentally observed. A second invariant plane deformation $\boldsymbol{Q}$ converts the material into a proven atomistic structure, since $\boldsymbol{J}\mathcal{B}$ is equal to the combination of the two invariant plane strain deformations $\boldsymbol{P}\,\boldsymbol{Q}$. In accordance with the previously described substructure in Sec. 2.2.2, the experimental proven shape is achieved by slipping or twinning.

Note that the PTMC only describes the correspondence of the crystal structure based on the atomic positions of the parent and product phases. The underlying mechanism that generates martensite is not described. Furthermore, an ideal situation without lattice imperfections is assumed. With the PTMC, it is possible to exactly predict the characteristics of thin plate martensite. However, variations may occur in other morphologies, which is reviewed, for example by Kelly (2012). Deviations are probably due to lattice defects or plastic effects. Kelly (1992) states that the PTMC explains all the crystallographic features of lath martensite. However, there has never been a reliably measuring of the shape strain, cf. Kelly (2012) and a large scattering of the habit plane in lath martensite is reported, cf. McDougall & Wayman (1992). Nevertheless, according to Kelly (2012), the PTMC can be considered as the best predictive theory of phase transformation in crystalline solids.

2.4. Mechanisms of the Transformation

As mentioned earlier, during martensite transformation, crystal lattice sites are rearranged purely by deformation to reduce the free energy of the system. Due to the deformation a martensitic transformation within a parent phase is associated with elastic strain. This requires high driving forces, which may be achieved by significant supercooling. This section deals with the transformation mechanisms that take place when the conditions for a martensite transformation are met.

2.4.1. Nucleation

The martensite transformation in steel is a first-order phase transformation and follows the nucleation-and-growth mechanism. This means that by exceeding an absolute instability temperature, the development of martensite involves formations and growth of nuclei. However, formation of a martensite embryo (local displacive heterogeneity) is accompanied with an increase in elastic strain energy and in contrast to transformations involving diffusion such embryos may not be formed by the thermo-nucleation mechanism. Instead such embryos are always present as crystal lattice defects in the parent phase, where they act as nuclei, see e.g. Olson & Cohen (1981) or as source of an elastic strain field supporting a martensite formation, see e.g. Magee (1970).

Many researchers proposed various lattice defects as possible microstructural nucleation sites. Accordingly, grain boundaries, twin boundaries, free surfaces and inclusion interfaces are possible nucleation sites, see e.g. Gaggero & Hull (1962); Dash & Brown (1966); Ferraglio & Mukherjee (1974); Krauss et al. (1989); Ueda et al. (2003). Furthermore, Olson & Cohen (1981), Suezawa & Cook (1980) and Kajiwara (1986) discuss the role of dislocations on martensite nucleation. Olson & Cohen (1981) proposed that the nucleation of martensite occurs due to dissociation of certain ordering of dislocations. The findings of Suezawa & Cook (1980) indicate that martensite nucleates at areas with high dislocation densities. Kajiwara (1986) states that dislocations themselves do not act as preferential nucleation sites. However, they may contribute to martensite transformation by serving plastic accommodation. A review of existing theories of the martensitic phase nucleation is given by Lobodyuk (2014). More recently, Song & De Cooman (2014) found that grain boundaries containing intrinsic grain boundary dislocations act as preferential nucleation sites.

When a critical size of the martensite embryo is exceeded, it starts to grow. The typical critical size in metal alloys corresponds to the crystal lattice spacing. In real structures, possible nucleation sites are distributed heterogeneously. After the first nucleation event has taken place, the martensite formation can have a strong autocatalytic character, which results from the stimulation of further nucleation events, whereby it is difficult to distinguish autocatalytic nucleation from spontaneous nucleation in the bulk. Autocatalytic nucleation can take place within a grain as well as across grain boundaries, cf. Rios & Guimarães (2008).

The following three mechanisms can contribute to autocatalytic nucleation (Olson & Cohen (1981), Lin et al. (1992)): stress-assisted, strain induced, and interfacial autocatalysis. The latter was proposed by Olson & Cohen (1976) and is a direct nucleation of new martensitic units by a dislocation-dissociation process in existing martensitic interfaces. However, this mechanism seems to be disregarded nowadays, c.f. Villa (2013). Strain-induced nucleation is accompanied with plastic deformation in the surrounding austenite,

which activates new embryos. This effect may be autocatalytic if the strengthening of the material and the resulting increase in the critical free energy difference does not prevent further martensite growth. Stress-assisted nucleation of pre-existing embryos results from the interaction of the stress field with the transformation strain (Maxwell et al. (1974)).

2.4.2. Formation Kinetics

Historically the macroscopic martensite transformation kinetics can be classified in athermal and isothermal transformations (Villa (2013)) introduced by Fisher et al. (1948). Sometimes the burst kinetics is also considered as a separate class, see e.g. Van Bohemen & Sietsma (2014). Under continuous cooling, athermal martensite transformation starts the transformation from austenite to martensite at a well-defined and cooling rate insensitive temperature T_{MS}. When the cooling process is stopped, the growth of martensite fraction in a macroscopic specimen stops and no further martensite transformation occurs with isothermal holding. The degree of athermal martensite transformations depends on the temperature (degree of undercooling) and is independent of time. This type of transformation can be observed in low-alloy steels, see Magee (1970). Isothermal martensite transformation is time-dependent and forms at a constant temperature below T_{MS}. Typically, isothermal martensite forms in Fe-based alloys with high Ni content at low temperatures. Villa (2013), concludes that the auto-nucleation dominates the martensite transformation in isothermal transformations, since the number of spontaneous nucleation events is too small to be compatible with macroscopic transformation in bulk materials.

By extrapolation of typical isothermal kinetics at low temperatures to temperatures comparable to $T_{\mathrm{MS}} \approx 250\,°\mathrm{C}$ of low-alloy steels, Entwisle (1971) argues that the observed athermal kinetics might be a result of rapid isothermal transformation with reaction times between 10^{-6} and $10^{-1}\,\mathrm{s}$. Such reaction times are too fast to be measured experimentally by classical methods, which makes the transformation appear athermal. In athermal transformations it is not immediately evident that autocatalysis takes place, however, it cannot be ruled out that this is a relevant mechanism on very small time scales (Van Bohemen & Sietsma (2014)).

The burst transformation can be regarded as an extreme form of autocatalysis (Raghaven (1992)), where a large part of the material is transformed in a unique quasi-instantaneous stress-assisted nucleation event. A burst transformation is recognizable by a pronounced zig-zag morphology.

Based on the review given by Ivanov & Kozlov (2002), the research group of Shastlivtsev conducted extensive investigations on the influence of cooling rates on the structure and phase state of iron and low-alloy carbon steels (Mirzaev et al. (1979, 1983); Mirzaev (1987); Schastlivtsev et al. (1994)). Accordingly, a fast isothermal martensitic transformation takes place in steels with low and medium carbon contents at moderate cooling rates. At high cooling rates, an athermal mechanism of martensitic transformation was observed. Regarding steels with carbon concentrations $\geq 0.7\,\mathrm{wt}\%$, an athermal mechanism of martensitic transformation was already observed at moderate cooling rates. The absence of an influence of the cooling rate on the kinetics of martensite formation was confirmed for plain carbon Fe-0.8 wt% (Van Bohemen & Sietsma (2014)) and FeNiCoMo alloy (Loewy et al. (2014)).

Despite past intensive research, the formation of lath martensite is still not fully understood, cf. Ping et al. (2018). Furuhara et al. (2010) describe the transformation process as

follows (Villa (2013)). The first nucleation event is triggered at a grain boundary, where the most favorite variant starts to grow. Thereafter, continuous strain-induced autocatalysis forms parallel laths within a block. After that, the growth is stopped and a further martensite growth requires either a reduction of the strain energy due to formation of a new variant of another block or an increase of the driving force obtained by an increasing undercooling. Thus, strain-induced autocatalysis is active on the lath level, while the autocatalytic formation of martensite blocks is of stress-assisted type.

3. Continuum Mechanics and Thermodynamics

To describe the physical phenomena considered in this work, a continuum approach is used. Therefore this section deals with two basic ingredients: the description of motion and deformation as well as the balance principles. The essential equations of these fields are introduced while the reader who is interested in further information is referred to Holzapfel (2000), Altenbach & Altenbach (1994) and Haupt (2013).

3.1. Kinematics

3.1.1. Configurations and Motion of Continuum Bodies

A material body, denoted by B, is considered as a continuous distribution of matter in space and time t, see Fig. 3.1. It is assumed that the material body is a composition of a continuous set of material points $\mathsf{P} \in \mathsf{B}$. In a three-dimensional Euclidean space $\mathcal{R}^3$ this set occupies a certain domain $\mathcal{B} \in \mathcal{R}^3$. The behavior of a particle P goes along with the collective behavior of all the molecules constituting that particle. By moving from one instant of time to another, the continuum body B occupies continuously a sequence of geometrical regions $\mathcal{B}_0, ..., \mathcal{B}_t$. The configuration at a reference or initial time $t = t_0$ is referred to as the reference configuration $\mathcal{B}_0$ and $\mathcal{B}_t$ represents the current configuration at a certain time $t > t_0$. With placement

$$\boldsymbol{\chi}_t : \begin{cases} \mathsf{B} \to \mathcal{B}_t \subset \mathcal{R}^3 \\ \mathsf{P} \mapsto \boldsymbol{x} = \boldsymbol{\chi}_t \left(\mathsf{P} \right) \end{cases} \tag{3.1}$$

the mapping of the matter into the Euclidean space is described. At a certain time t the placement $\boldsymbol{\chi}_t$ uniquely maps a material point P onto a coordinate triple $\boldsymbol{x} \in \mathcal{R}^3$. Concerning the reference configuration

$$\boldsymbol{\chi}_0 : \begin{cases} \mathsf{B} \to \mathcal{B}_0 \subset \mathcal{R}^3 \\ \mathsf{P} \mapsto \boldsymbol{X} = \boldsymbol{\chi}_0 \left(\mathsf{P} \right) \end{cases} \tag{3.2}$$

is defined. It is assumed that the mapping is a one-to-one correspondence between a particle $\mathsf{P} \in \mathsf{B}$ and $\boldsymbol{X} \in \mathcal{B}_0$, which is why $\boldsymbol{\chi}_0$ is invertible $(\boldsymbol{\chi}_0^{-1})$ and excludes inter-penetration of matter. By a composition of the mappings (3.1) and (3.2) a relative description of the body's motion is defined, which is the nonlinear deformation map

$$\boldsymbol{\phi} \left(\boldsymbol{X}, t \right) : \begin{cases} \mathcal{B}_0 \times \mathcal{T} \to \mathcal{B}_t \subset \mathcal{R}^3 \\ \left(\boldsymbol{X}, t \right) \mapsto \boldsymbol{x} = \boldsymbol{\phi} \left(\boldsymbol{X}, t \right) = \boldsymbol{\chi}_t \left[\boldsymbol{\chi}_0^{-1} \left(\boldsymbol{X} \right) \right] \end{cases}, t \in \mathcal{T} \subset \mathcal{R}_+ \tag{3.3}$$

In a time interval $\mathcal{T}$, the referential position $\boldsymbol{X} \in \mathcal{B}_0$ of a particle $\mathsf{P} \in \mathsf{B}$ is mapped to its deformed spatial position $\boldsymbol{x} = \boldsymbol{\phi} \left(\boldsymbol{X}, t \right) \in \mathcal{B}_t$ in current configuration. With (3.3) the entire motion of a deformed body is described, whereas with reference to the notation in (3.1) and (3.2) the configuration at a certain time t is defined with the mapping

$$\boldsymbol{\phi}_t \left(\boldsymbol{X} \right) : \begin{cases} \mathcal{B}_0 \to \mathcal{B}_t \subset \mathcal{R}^3 \\ \boldsymbol{X} \mapsto \boldsymbol{x} = \boldsymbol{\phi}_t \left(\boldsymbol{X} \right). \end{cases} \tag{3.4}$$

Analogous to (3.4), the path of particle P is denoted with $\boldsymbol{\phi}_{\boldsymbol{X}} \left(t \right)$.
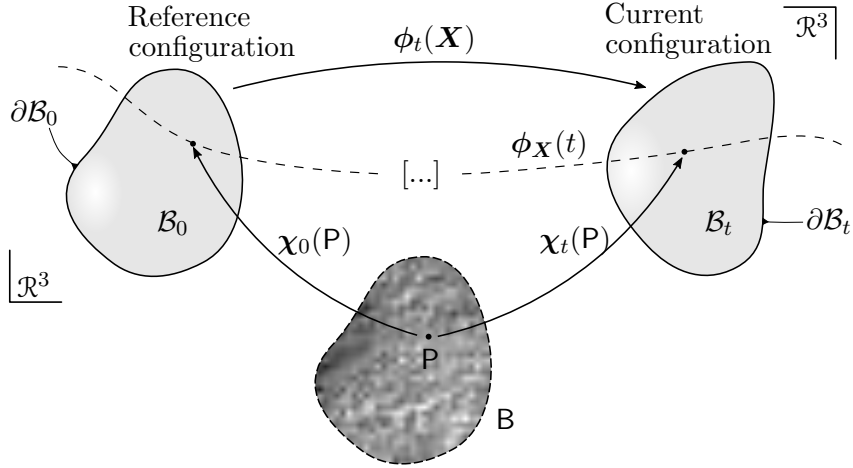
Figure 3.1: Configuration and motion of a continuum body B in the Euclidean space $\mathcal{R}^3$

3.1.2. Displacement, Velocity and Acceleration Fields

The considered fields refer to a reference frame of right-handed, rectangular coordinate axes at a fixed origin O with orthonormal basis vectors depicted in Fig. 3.2. The difference between position $\boldsymbol{X}$ in the undeformed configuration and position $\boldsymbol{x}$ in the deformed configuration gives the Lagrangian form of the displacement field

$$\boldsymbol{u}\left(\boldsymbol{X},t\right) = \boldsymbol{x}\left(\boldsymbol{X},t\right) - \boldsymbol{X}. \tag{3.5}$$

By deriving the entire motion $\boldsymbol{\phi}\left(\boldsymbol{X},t\right)$ with respect to the time t and holding $\boldsymbol{X}$ fixed, the velocity of a material point

$$\boldsymbol{v}(\boldsymbol{X},t) = \frac{\partial \boldsymbol{\phi}\left(\boldsymbol{X},t\right)}{\partial t} = \dot{\boldsymbol{x}} \tag{3.6}$$

is obtained and further derivation gives the material acceleration

$$\boldsymbol{a}(\boldsymbol{X},t) = \frac{\partial \boldsymbol{v}\left(\boldsymbol{X},t\right)}{\partial t} = \dot{\boldsymbol{v}} = \ddot{\boldsymbol{x}}. \tag{3.7}$$

The spatial acceleration $\boldsymbol{a}(\boldsymbol{x},t) = \boldsymbol{a}(\boldsymbol{X}(\boldsymbol{x},t),t)$ is classically given as the sum of a local and convective part and is thus obtained with

$$\boldsymbol{a} = \frac{d\boldsymbol{v}\left(\boldsymbol{x},t\right)}{dt} = \frac{\partial \boldsymbol{v}\left(\boldsymbol{x},t\right)}{\partial t} + \boldsymbol{\nabla}_{\boldsymbol{x}}\boldsymbol{v}\left(\boldsymbol{x},t\right)\frac{\partial \boldsymbol{x}\left(\boldsymbol{X},t\right)}{\partial t} = \frac{\partial \boldsymbol{v}}{\partial t} + \boldsymbol{L} \cdot \boldsymbol{v} \quad \text{with} \quad \boldsymbol{L} = \boldsymbol{\nabla}_{\boldsymbol{x}}\boldsymbol{v}\left(\boldsymbol{x},t\right), \tag{3.8}$$

where $\boldsymbol{\nabla}_{\boldsymbol{x}}\left(\cdot\right)$ denotes the gradient $\text{grad}\left(\cdot\right)$ with respect to the spatial coordinates $\boldsymbol{x}$. Furthermore, the spatial velocity gradient $\boldsymbol{L}$ can be identified.

3.1.3. Deformation Gradient and Small Strain Theory

In order to describe the strain kinematics it is usual to define the deformation gradient

$$\boldsymbol{F} = \boldsymbol{\nabla}_{\boldsymbol{X}}\,\boldsymbol{\phi}\left(\boldsymbol{X},t\right) = \frac{\partial \boldsymbol{\phi}\left(\boldsymbol{X},t\right)}{\partial \boldsymbol{X}} = \frac{\partial \boldsymbol{x}}{\partial \boldsymbol{X}}. \tag{3.9}$$
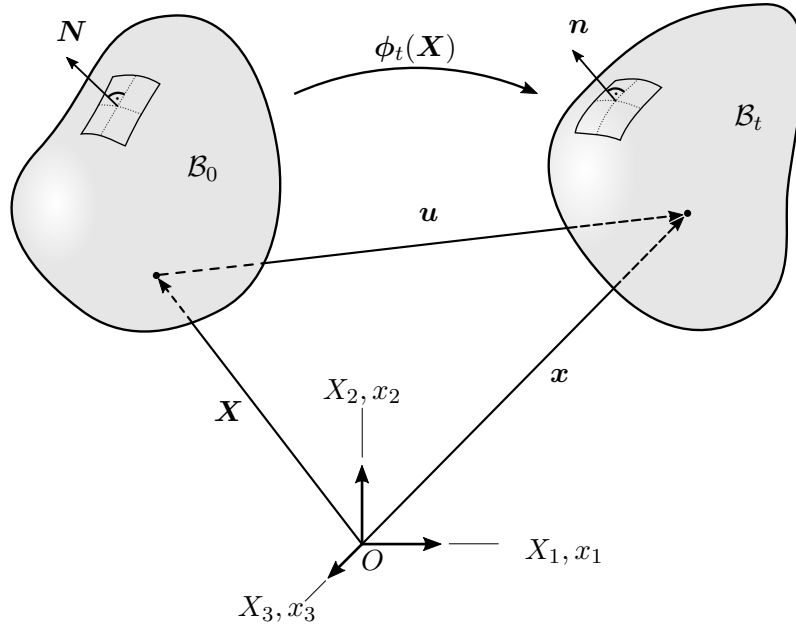
Figure 3.2: Material body $\mathcal{B}$

as gradient with respect to the reference positions $\boldsymbol{X} \in \mathcal{B}_0$ of the deformation map (3.3). The assumption that there is a one-to-one mapping between reference and current positions results in a non-vanishing determinant of the deformation gradient. By further excluding matter penetrations associated with negative values of the Jacobian $J = \det(\boldsymbol{F})$, the following condition is obtained:

$$\det(\boldsymbol{F}) > 0. \tag{3.10}$$

Therefore $\boldsymbol{F}$ is invertible and the former introduced velocity gradient may be formulated as

$$\boldsymbol{L} = \dot{\boldsymbol{F}} \boldsymbol{F}^{-1}. \tag{3.11}$$

Starting from Eq. (3.9) and splitting $\boldsymbol{x}$ into $\boldsymbol{X}$ and the displacement $\boldsymbol{u}$ according to (3.5) leads to

$$\boldsymbol{F} = \frac{\partial \boldsymbol{x}}{\partial \boldsymbol{X}} = \frac{\partial}{\partial \boldsymbol{X}} (\boldsymbol{X} + \boldsymbol{u}) = \boldsymbol{I} + \boldsymbol{\nabla}_{\boldsymbol{X}} \boldsymbol{u} = \boldsymbol{I} + \boldsymbol{H}, \tag{3.12}$$

where $\boldsymbol{I}$ denotes the second order identity tensor and $\boldsymbol{H} = \boldsymbol{\nabla}_{\boldsymbol{X}} \boldsymbol{u}$ the displacement gradient. The Green-Lagrange strain tensor is defined by

$$\boldsymbol{E} = \frac{1}{2} \left(\boldsymbol{F}^T \boldsymbol{F} - \boldsymbol{I} \right). \tag{3.13}$$

With the use of Eq. (3.12) the strain tensor $\boldsymbol{E}$ can be expressed as

$$\boldsymbol{E} = \frac{1}{2} \left(\boldsymbol{H} + \boldsymbol{H}^T + \boldsymbol{H}^T \boldsymbol{H} \right).$$

In this equation the third term may be neglected by assuming small strains $|\boldsymbol{H}| \ll 1$, which leads to the linearized strain tensor

$$\boldsymbol{\varepsilon} = \frac{1}{2}\left(\boldsymbol{H} + \boldsymbol{H}^T\right) = \frac{1}{2}\left(\boldsymbol{\nabla}_{\boldsymbol{X}}\,\boldsymbol{u} + (\boldsymbol{\nabla}_{\boldsymbol{X}}\,\boldsymbol{u})^T\right). \tag{3.14}$$

In the context of (geometrically) small strains no distinction of reference and current configuration is made which leads to following simplifications.

$$\mathcal{B} = \mathcal{B}_0 \approx \mathcal{B}_t, \quad \partial\mathcal{B} = \partial\mathcal{B}_0 \approx \partial\mathcal{B}_t, \quad \boldsymbol{X} \approx \boldsymbol{x}, \quad \frac{\partial(\cdot)}{\partial\boldsymbol{X}} \approx \frac{\partial(\cdot)}{\partial\boldsymbol{x}} \tag{3.15}$$

3.2. Balance Equations

To construct a general balance equation for a material field density ϑ in $\mathcal{B}$, the field quantity $\theta = \int_{\mathcal{B}} \vartheta\, dV$ is formulated. The time derivation of θ must be equal to a flux $\boldsymbol{f}_\theta$ over the boundary $\partial\mathcal{B}$, a production p_θ of ϑ in $\mathcal{B}$ and a supply s_θ of ϑ in $\mathcal{B}$. It follows the general structure of the balance equations

$$\frac{d}{dt}\int_{\mathcal{B}} \vartheta\, dV = \int_{\partial\mathcal{B}} \boldsymbol{f}_\theta \cdot \boldsymbol{n}\, dA + \int_{\mathcal{B}} p_\theta\, dV + \int_{\mathcal{B}} s_\theta\, dV, \tag{3.16}$$

where $\boldsymbol{n}$ is the outer normal along $\partial\mathcal{B}$, see Fig. 3.2. Note that within the small strain framework $\boldsymbol{N} \approx \boldsymbol{n}$ is valid. For easier transferability to the following mechanical and thermodynamic balance equations, a summary of the components of Eq. (3.16) is given below.

$$\begin{aligned}
\vartheta &\quad - \quad \text{field density in } \mathcal{B}, \\
p_\theta &\quad - \quad \text{production of } \theta \text{ in } \mathcal{B}, \\
s_\theta &\quad - \quad \text{supply of } \theta, \\
\boldsymbol{f}_\theta &\quad - \quad \text{flux of } \theta \text{ over } \partial\mathcal{B},
\end{aligned}$$

By applying the divergence theorem to the surface integral in Eq. (3.16) for any arbitrary $\mathcal{B}$ the local form of, the general balance equation

$$\frac{d\vartheta}{dt} + \vartheta\, \text{div}\,(\boldsymbol{v}) = \text{div}\,(\boldsymbol{f}_\theta) + p_\theta + s_\theta \tag{3.17}$$

is obtained, which must be fulfilled for each material point $\boldsymbol{x} \in \mathcal{B}$ at all times.

3.2.1. Mechanical Balance Principles

Conservation of Mass. The mass of a body is determined by the density field $\varrho = \frac{dm}{dV}$. In classical mechanical systems there is no production or supply of mass. Furthermore, in closed systems there is no flux over the surface, after which

$$\begin{aligned}
\vartheta = \varrho &\quad - \quad \text{density of mass } m \text{ in } \mathcal{B}, \\
p_{\mathrm{m}} = 0 &\quad - \quad \text{production of mass } m \text{ in } \mathcal{B}, \\
s_{\mathrm{m}} = 0 &\quad - \quad \text{supply of mass } m \text{ in } \mathcal{B}, \\
\boldsymbol{f}_{\mathrm{m}} = \boldsymbol{0} &\quad - \quad \text{flux of mass } m \text{ over } \partial\mathcal{B},
\end{aligned}$$

applies in summary. According to this,

$$\frac{d}{dt} \int_{\mathcal{B}} \varrho \, dV = 0 \tag{3.18}$$

is obtained for the global form of balance of mass. The local form then results in

$$\frac{d\varrho}{dt} + \varrho \, \text{div} \, (\boldsymbol{v}) = 0. \tag{3.19}$$

Accordingly, the mass balance can be used to rewrite expressions of the form $\frac{d}{dt} \left[\int_{\mathcal{B}} \varrho \, (\bullet) \, dV \right]$ as follows:

$$\frac{d}{dt} \left[\int_{\mathcal{B}} \varrho \, (\bullet) \, dV \right] = \int_{\mathcal{B}} \dot{\varrho} \, (\bullet) + \varrho \dot{(\bullet)} + \varrho \, (\bullet) \, \text{div} \, (\boldsymbol{v}) \, dV = \int_{\mathcal{B}} \varrho \dot{(\bullet)} \, dV. \tag{3.20}$$

Balance of Linear Momentum. The total linear momentum of a material domain is defined as

$$\boldsymbol{\mathfrak{J}} = \int_{\mathcal{B}} \varrho \, \boldsymbol{v} \, dV. \tag{3.21}$$

It is postulated by Newton's second law of motion that the temporal change of the linear momentum $\boldsymbol{\mathfrak{J}}$ of a region $\mathcal{B}$ is equal to the resulting external force acting on that region. Written as global balance it is

$$\frac{d}{dt} \int_{\mathcal{B}} \varrho \, \boldsymbol{v} \, dV = \int_{\partial \mathcal{B}} \boldsymbol{t} \, dA + \int_{\mathcal{B}} \varrho \, \boldsymbol{b}^* \, dV, \tag{3.22}$$

where $\boldsymbol{t}$ is the traction vector acting on the boundary $\partial \mathcal{B}$ and $\boldsymbol{b}^*$ the force density per unit mass of $\mathcal{B}$. The production term is equal to zero. Regarding the general balance Eq. (3.16) it is

$$\begin{aligned}
\vartheta &= \varrho \, \boldsymbol{v} & &- & &\text{density of linear momentum } \boldsymbol{\mathfrak{J}} \text{ in } \mathcal{B}, \\
p_{\boldsymbol{\mathfrak{J}}} &= \boldsymbol{0} & &- & &\text{production of linear momentum } \boldsymbol{\mathfrak{J}} \text{ in } \mathcal{B}, \\
s_{\boldsymbol{\mathfrak{J}}} &= \varrho \, \boldsymbol{b}^* & &- & &\text{supply of linear momentum } \boldsymbol{\mathfrak{J}} \text{ in } \mathcal{B}, \\
\boldsymbol{f}_{\boldsymbol{\mathfrak{J}}} \cdot \boldsymbol{n} &= \boldsymbol{t} & &- & &\text{flux of linear momentum } \boldsymbol{\mathfrak{J}} \text{ over } \partial \mathcal{B}.
\end{aligned}$$

In order to formulate the local form

$$\varrho \, \boldsymbol{a} = \text{div} \left(\boldsymbol{\sigma}^T \right) + \varrho \, \boldsymbol{b}^* \quad \text{with} \quad \boldsymbol{t} = \boldsymbol{\sigma}^T \, \boldsymbol{n} \tag{3.23}$$

Cauchy's theorem with the Cauchy stress tensor $\boldsymbol{\sigma}$ is used.

Balance of Angular Momentum. The balance of total angular momentum

$$\boldsymbol{\mathcal{L}} = \int_{\mathcal{B}} \boldsymbol{x} \times \varrho \, \boldsymbol{v} \, dV \tag{3.24}$$

postulates that the temporal change of the angular momentum with respect to a certain point of a fixed coordinate system is equal to the resultant external torque which acts on the considered region $\mathcal{B}$ with respect to the same point of reference. With the components

$$\begin{aligned}
\vartheta &= \boldsymbol{x} \times \varrho \, \boldsymbol{v} & &- & &\text{density of angular momentum } \boldsymbol{\mathcal{L}} \text{ in } \mathcal{B}, \\
p_{\boldsymbol{\mathcal{L}}} &= \boldsymbol{0} & &- & &\text{production of angular momentum } \boldsymbol{\mathcal{L}} \text{ in } \mathcal{B}, \\
s_{\boldsymbol{\mathcal{L}}} &= \boldsymbol{x} \times \varrho \, \boldsymbol{b}^* & &- & &\text{supply of angular momentum } \boldsymbol{\mathcal{L}} \text{ in } \mathcal{B}, \\
\boldsymbol{f}_{\boldsymbol{\mathcal{L}}} \cdot \boldsymbol{n} &= \boldsymbol{x} \times \boldsymbol{t} & &- & &\text{flux of angular momentum } \boldsymbol{\mathcal{L}} \text{ over } \partial \mathcal{B},
\end{aligned}$$

the global balance of angular momentum reads

$$\frac{d}{dt} \int_{\mathcal{B}} \boldsymbol{x} \times \varrho \, \boldsymbol{v} \, dV = \int_{\partial \mathcal{B}} \boldsymbol{x} \times \boldsymbol{t} \, dA + \int_{\mathcal{B}} \boldsymbol{x} \times \varrho \, \boldsymbol{b}^* dV. \tag{3.25}$$

The local form gives the well-known condition

$$\boldsymbol{\sigma} = \boldsymbol{\sigma}^T. \tag{3.26}$$

By considering the symmetry of the Cauchy tensor as well as assuming the acceleration $\boldsymbol{a}$ is zero and the absence of volume forces, Eq. (3.23) becomes the equilibrium condition

$$\mathrm{div}\,(\boldsymbol{\sigma}) = \boldsymbol{0}. \tag{3.27}$$

3.2.2. Thermodynamic Extensions

Balance of Energy. The balance of energy is the first law of thermodynamics, which postulates the equivalence between the temporal change of total energy $\mathcal{E}$ and the sum of external mechanical power $\mathcal{P}_{\mathrm{ext}}$ and thermal power $\mathcal{Q}_{\mathrm{ext}}$. Thereby, the total energy

$$\mathcal{E} = \int_{\mathcal{B}} \tfrac{1}{2} \, \varrho \, |\boldsymbol{v}|^2 \, dV + \int_{\mathcal{B}} \varrho \, w^* \, dV \tag{3.28}$$

consists of the kinetic energy $\int_{\mathcal{B}} \varrho \, \frac{|\boldsymbol{v}|^2}{2} \, dV$ and the internal energy $\int_{\mathcal{B}} \varrho \, w^* \, dV$, where w^* denotes the specific internal energy per unit mass. A change in this energy is associated with the energy supply from a mechanical part

$$\mathcal{P}_{\mathrm{ext}} = \int_{\partial \mathcal{B}} \boldsymbol{t} \cdot \boldsymbol{v} \, dA + \int_{\mathcal{B}} \varrho \, \boldsymbol{b}^* \cdot \boldsymbol{v} \, dV, \tag{3.29}$$

which is the power of the external forces and the heat supply

$$\mathcal{Q}_{\mathrm{ext}} = \int_{\mathcal{B}} \varrho \, r \, dV - \int_{\partial \mathcal{B}} \boldsymbol{q}_{\mathrm{th}} \cdot \boldsymbol{n} \, dA. \tag{3.30}$$

In Eq. (3.30) r denotes the scalar heat radiation and $\boldsymbol{q}_{\mathrm{th}}$ the heat flux. A positive heat flux corresponds to a heat supply across the boundary $\partial \mathcal{B}$. The balance of energy is then

$$\frac{d}{dt} \int_{\mathcal{B}} \left(\tfrac{1}{2} \, |\boldsymbol{v}|^2 + w^* \right) \varrho \, dV = \int_{\partial \mathcal{B}} ((\boldsymbol{\sigma} \, \boldsymbol{n}) \cdot \boldsymbol{v} - \boldsymbol{q}_{\mathrm{th}} \cdot \boldsymbol{n}) \, dA + \int_{\mathcal{B}} (\boldsymbol{b}^* \cdot \boldsymbol{v} + r) \, \varrho \, dV. \tag{3.31}$$

In comparison with the general balance Eq. (3.16) the following densities are identified.

$$
\begin{aligned}
\vartheta &= \varrho \, \tfrac{1}{2} \, |\boldsymbol{v}|^2 + \varrho \, w^* &&- && \text{density of energy } \mathcal{E} \text{ in } \mathcal{B}, \\
p_{\mathcal{E}} &= 0 &&- && \text{production of energy } \mathcal{E} \text{ in } \mathcal{B}, \\
s_{\mathcal{E}} &= \varrho \, \boldsymbol{b}^* \cdot \boldsymbol{v} + \varrho \, r &&- && \text{supply of energy } \mathcal{E} \text{ in } \mathcal{B}, \\
\boldsymbol{f}_{\mathcal{E}} \cdot \boldsymbol{n} &= (\boldsymbol{\sigma} \, \boldsymbol{n}) \cdot \boldsymbol{v} - \boldsymbol{q}_{\mathrm{th}} \cdot \boldsymbol{n} &&- && \text{flux of Energy } \mathcal{E} \text{ over } \partial \mathcal{B}.
\end{aligned}
$$

Since the energy is a conservation quantity no term of production occurs in Eq. (3.31). By using the above densities and taking Eqs. (3.19) and (3.27) into account, results in the local form of energy balance

$$\varrho \, \frac{dw^*}{dt} = -\,\mathrm{div}\,(\boldsymbol{q}_{\mathrm{th}}) + \boldsymbol{\sigma} : \boldsymbol{\nabla} \boldsymbol{v} + \varrho \, r. \tag{3.32}$$

Balance of Entropy. The balance of entropy is the second law of thermodynamics. It states that the temporal change of total entropy $\mathcal{H}$ is equal to the sum of the entropy supply an the entropy production. It is

$$\mathcal{H} = \int_{\mathcal{B}} s \, dV \quad \text{with} \quad s = \varrho \, s^*, \tag{3.33}$$

where s^* denotes the specific entropy per unit mass. The global balance of entropy reads

$$\frac{d}{dt} \int_{\mathcal{B}} s \, dV = - \int_{\partial \mathcal{B}} \frac{\boldsymbol{q}_{\text{th}} \cdot \boldsymbol{n}}{T} \, dA + \varrho \left(\int_{\mathcal{B}} p_{\text{s}^*} \, dV + \int_{\mathcal{B}} \frac{r}{T} \, dV \right), \tag{3.34}$$

where p_{s^*} is the specific production of entropy per unit mass and T the absolute temperature ($T > 0$). The supply, production and flux terms may be identified as

$$\begin{aligned}
\vartheta &= s & &- & &\text{density of entropy } \mathcal{H} \text{ in } \mathcal{B}, \\
p_{\mathcal{H}} &= \varrho \, p_{\text{s}^*} & &- & &\text{production of entropy } \mathcal{H} \text{ in } \mathcal{B}, \\
s_{\mathcal{H}} &= \varrho \, r \, / \, T & &- & &\text{supply of entropy } \mathcal{H} \text{ in } \mathcal{B}, \\
\boldsymbol{f}_{\mathcal{H}} &= -\boldsymbol{q}_{\text{th}} \, / \, T & &- & &\text{flux of Entropy } \mathcal{H} \text{ over } \partial \mathcal{B},
\end{aligned}$$

resulting in the local form

$$\varrho \frac{ds^*}{dt} = \varrho \left(p_{\text{s}^*} + \frac{r}{T} \right) - \text{div} \left(\frac{\boldsymbol{q}_{\text{th}}}{T} \right). \tag{3.35}$$

The second law of thermodynamics postulates that the entropy must always be greater than zero, which is why

$$p_{\text{s}^*} \geq 0 \tag{3.36}$$

applies to any material point $\boldsymbol{x} \in \mathcal{B}$ at any time t in every admissible thermodynamic process. Inserting Eq. (3.35) in (3.36) yields the Clausius-Duhem inequality

$$\varrho \frac{ds^*}{dt} + \text{div} \left(\frac{\boldsymbol{q}_{\text{th}}}{T} \right) - \varrho \frac{r}{T} = \varrho \, p_{\text{s}^*} \geq 0 \tag{3.37}$$

and the elimination of the supply term $\varrho \, r$ by Eq. (3.32) yields

$$\varrho \left(T \dot{s}^* - \dot{w}^* \right) - \frac{1}{T} \boldsymbol{\nabla} T \cdot \boldsymbol{q}_{\text{th}} + \boldsymbol{\sigma} : \boldsymbol{L} \geq 0. \tag{3.38}$$

Following Coleman & Noll (1963) and Coleman & Gurtin (1967) by introducing the local Helmholtz energy per unit mass

$$\psi^* = w^* - T \, s^* \quad \text{and} \quad \dot{\psi}^* = \dot{w}^* - \dot{T} \, s^* - T \, \dot{s}^*, \tag{3.39}$$

Eq. (3.38) may be formulated as

$$\boldsymbol{\sigma} : \dot{\boldsymbol{\varepsilon}} - \varrho \left(\dot{\psi}^* + s^* \dot{T} \right) - \frac{1}{T} \boldsymbol{q}_{\text{th}} \cdot \boldsymbol{\nabla} T \geq 0, \tag{3.40}$$

which is often referred to as the Clausius-Plank inequality. Note that in the small strain context $\boldsymbol{L} = \dot{\boldsymbol{\varepsilon}}$ is valid. Suppose $\psi = \varrho \, \psi^*$ is a function of strain $\boldsymbol{\varepsilon}$ and absolute Temperature T, the time derivate

$$\dot{\psi} = \frac{\partial \psi}{\partial \boldsymbol{\varepsilon}} : \dot{\boldsymbol{\varepsilon}} + \frac{\partial \psi}{\partial T} \dot{T} \tag{3.41}$$

gives by inserting in Eq. (3.40)

$$\left(\boldsymbol{\sigma} - \frac{\partial \psi}{\partial \boldsymbol{\varepsilon}}\right) : \dot{\boldsymbol{\varepsilon}} + \left(-\varrho\, s^* - \frac{\partial \psi}{\partial T}\right) \dot{T} - \frac{1}{T}\, \boldsymbol{q}_{\text{th}} \cdot \boldsymbol{\nabla} T \geq 0. \tag{3.42}$$

Eq. (3.42) has to be fulfilled for all rates of $\boldsymbol{\varepsilon}$ and T. This can be achieved by

$$\boldsymbol{\sigma} = \frac{\partial \psi}{\partial \boldsymbol{\varepsilon}} \quad \text{and} \quad -\varrho\, s^* = \frac{\partial \psi}{\partial T} \tag{3.43}$$

and the heat conduction inequality

$$\boldsymbol{q}_{\text{th}} \cdot \boldsymbol{\nabla} T \leq 0. \tag{3.44}$$

4. Experimental Investigations

This section deals with the experimental characterization of the exemplary investigated low-alloy steel 50CrMo4 (SAE 4150) with a special focus on martensite sizes. Parts of this section are already published by Graf et al. (2020).

4.1. Background and Motivation

The packet and block sizes can significantly affect the mechanical properties of the considered materials (Morito et al. (2006b); Swarr & Krauss (1976)), which can be explained by grain boundary strengthening according to the Hall–Petch strengthening mechanism (Hall (1951); Petch (1953)). As a consequence, there is an interest in quantifying such size effects in order to predict the structure–property relationships.

The resulting martensite sizes are determined by various factors. It has been observed that packet and block sizes decrease with increasing carbon content, see Morito et al. (2003). A correlation between the PAG size and the packet size as well as the block thickness is reported by Morito et al. (2005); Furuhara et al. (2008). With a finer austenite grain structure, a finer packet and block width is achieved. However, no significant correlation between the block width and the PAG size was found by Hanamura et al. (2013). Nevertheless, there seems to be some consensus on the lath sizes, which seem to be insensitive to changes in the PAG sizes, cf. Swarr & Krauss (1976); Morito et al. (2005); Hanamura et al. (2013). Furthermore, higher cooling rates can lead to finer packet and block structures, cf. Morito et al. (2010); Bardelcik et al. (2010); Tsuzaki & Maki (1981); Eggbauer et al. (2018); Loewy et al. (2015); Shtejnberg et al. (1977). No size effects with regard to the cooling rate were found by Villa et al. (2014). The effects of process parameters related to induction hardening on phase transformation including microstructure size effects were recently investigated by Vieweg et al. (2016, 2017c,b,a); Liu et al. (2018); Hu et al. (2018); Javaheri et al. (2019); Eggbauer et al. (2019); Vieweg et al. (2018).

With regard to the effect of the cooling rate on resulting size effects on the microstructure, several discussions can be found in the literature. In Loewy et al. (2015), a modulated martensite formation in a Fe-22 wt% Ni alloy was investigated. It was concluded that subsequent simultaneous block formation is influenced by thermally activated local stress relaxation. Based on Eggbauer et al. (2018), it can be argued that the quenching rate influences the volume fraction gradient concerning temperature. With shorter cooling times, more martensite is formed at lower temperatures, which means a higher resistance against lattice displacement, resulting in higher stresses. From an energetic point of view, it is therefore beneficial to minimize the stresses by forming a finer block structure. Another explanation was formulated by Hu et al. (2018). Thus, due to the higher cooling rate, the amount of dislocations increases. These lattice defects may act as nucleation sites for martensite. Additional higher driving forces lead to an increase in the growth rate of martensite.

In this work, the microstructure of different quenched specimens is evaluated by means of EBSD. Based on the orientations, the cross-sections of martensite blocks are reconstructed and analyzed. In addition to Eggbauer et al. (2018), the CPPs packets and PAGs are reconstructed based on the martensite orientation relationship. With this method, sections of the microstructure on the scale of representative volume elements can be evaluated,

resulting in a statistically significant amount of data. The findings serve as an essential basis for the development of the phase field simulation model describing the evolution of martensite on mesoscopic length scale in order to contribute to the understanding of martensite transformations.

4.2. Experimental Setup and Methodology

For the experimental investigations in this work, referring to previous studies, the material 50CrMo4 is used, cf. Schäfer et al. (2019a,c,b); Eggbauer et al. (2018). For the sake of completeness, mean values of the chemical composition are documented in Tab. 4.1. These values were determined by spark emission spectroscopy analysis, see Schäfer et al. (2019a). The initial material condition is pre-hardened.

Table 4.1: Chemical composition of the investigated material 50CrMo4 in wt.%; the remainder is Fe.

Material	Reference	C	Si	Mn	P	S	Cr	Mo
50CrMo4	Schäfer et al. (2019a)	0.52	0.26	0.74	0.014	0.008	1.31	0.18

Different types of cylindrical specimens are heat-treated in order to form a homogeneous and purely martensitic microstructure. In Fig. 4.1(a), the three types are depicted with their nominal dimensions. Types A and B are analyzed with regard to the morphology of their martensite structure. The reason for the hole in type B is that, due to the reduced mass, a higher quenching rate is achieved with the same quenching medium. Specimen type C only serves as an accompanying specimen to measure the temperature inside. The temperature is measured with a thermocouple (type K), which is inserted and fixed in the blind hole of specimen type C.

In order to achieve different quenching rates, two different heat treatment processes were used. The first was performed with the dilatometer DIL 805A from TA Instruments. Specimens of type A and B were heated by induction at a rate of $20.0 \, \mathrm{Ks}^{-1}$ to a temperature of $860 \, °C$. A vacuum in the chamber containing the specimen prevented the decarburization of the surface layer of the specimen. For supercooling, the chamber was flooded with nitrogen, where a linear temperature curve was specified. The temperature was measured with a type S thermocouple. With this experimental setup, the critical quenching rate necessary to obtain a fully martensitic microstructure was determined step by step with specimen type A. Furthermore, the highest cooling rate possible with this test configuration was tested with specimen types A and B.

As the quenching rate of the dilatometer was limited, a second experimental setup was used. With this setup, specimen types A and C were heated in a furnace and then quenched in a water bath. The temperature inside (①) and outside (②) the specimen was measured, see Fig. 4.1(a). With both experimental setups, a holding time of 30 min at high temperature was employed to guarantee full austenitization.

After heat treatment, the specimens were divided crosswise as depicted in Fig. 4.1(b). In order to check the homogeneity of the microstructure, hardness measurements were taken on the new surface highlighted in gray with the low-load Vickers hardness tester KB30 BVZ. Two runs of measurements were performed in each case. Before each run, the specimens were ground and polished (final polishing step: $3.0 \, \mu\mathrm{m}$ diamond suspension).
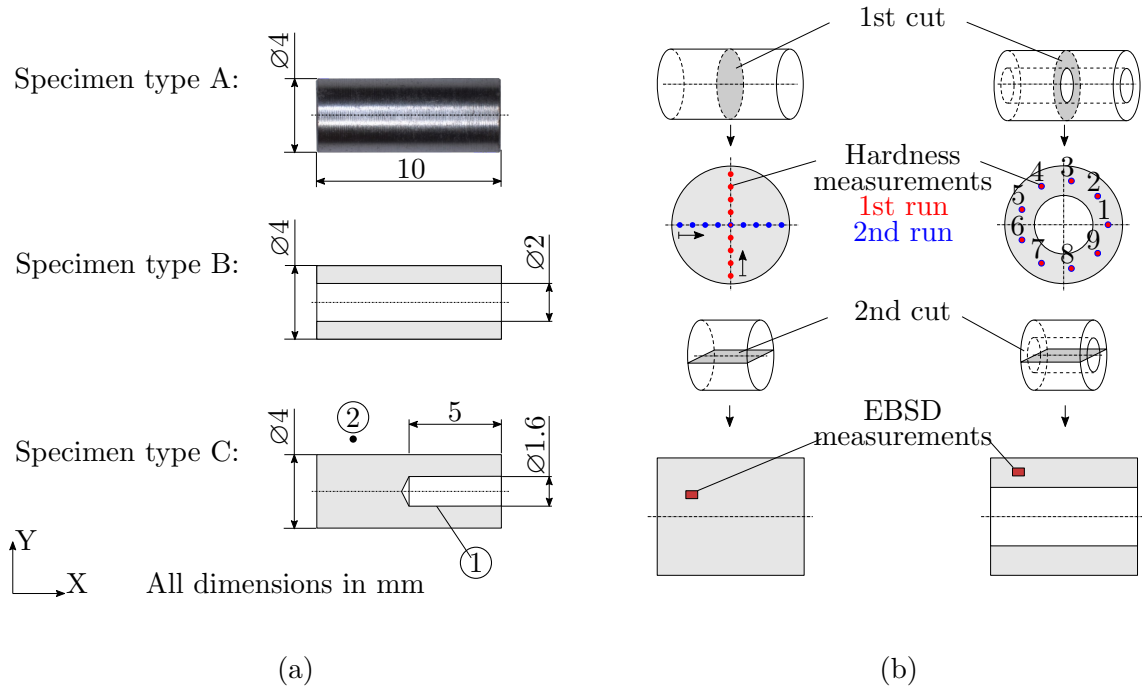
Figure 4.1: Specimen geometry and measurement methodology, (a) specimen types with nominal dimensions of material 50CrMo4, Specimen type C is only used for temperature measurement, (b) specimen handling after heat treatment

A second cut lengthwise exposed the surface on which the microstructure was characterized, see Fig. 4.1(b). For the EBSD analyses, the surface was ground with SiC sand paper with grades up to 4000 followed by diamond polishing with suspension sizes of $3.0\,\mu m$ and $1.0\,\mu m$. The final polish was performed with a $0.06\,\mu m$ aluminum suspension (Eposal). The EBSD measurements were performed with the scanning electron microscope Zeiss Supra 55 VP. Areas of $114\,\mu m \times 85\,\mu m$ with a step size of $0.15\,\mu m$ were measured. Only phases that could be assigned to martensite or retained austenite were indexed. After the analysis was performed at a suitable location, the surface was etched with 1% alcoholic HNO3 (Nital) in order to analyze the location with optical microscopes (Axioimager.M2m and Axioplan 2 Imaging) to check whether a completely martensitic structure was present.

In order to calculate the high-temperature austenite grains, the python tool ARPGE (version 2.4) was used (Cayron (2007)). The visualization, as well as the evaluation of the morphology, was performed with the Matlab toolbox MTEX 5.1.1 (Bachmann et al. (2010)).

4.3. Heat Treatment and Hardness

To differentiate different heat treatments, cooling times from $800\,°C$ to $500\,°C$ (t_{85}), from $800\,°C$ to $100\,°C$ (t_{81}) and from the martensite start temperature T_{MS} to $100\,°C$ ($t_{T_{MS}\to100\,°C}$) were used. Furthermore, the approximated quenching rates

$$\dot{T}_{85} = \frac{800\,°C - 500\,°C}{t_{85}}, \quad \dot{T}_{T_{MS}\to100\,°C} = \frac{T_{MS} - 100\,°C}{t_{T_{MS}\to100\,°C}} \quad \text{and} \quad \dot{T}_{81} = \frac{800\,°C - 100\,°C}{t_{81}} \tag{4.1}$$

were defined.
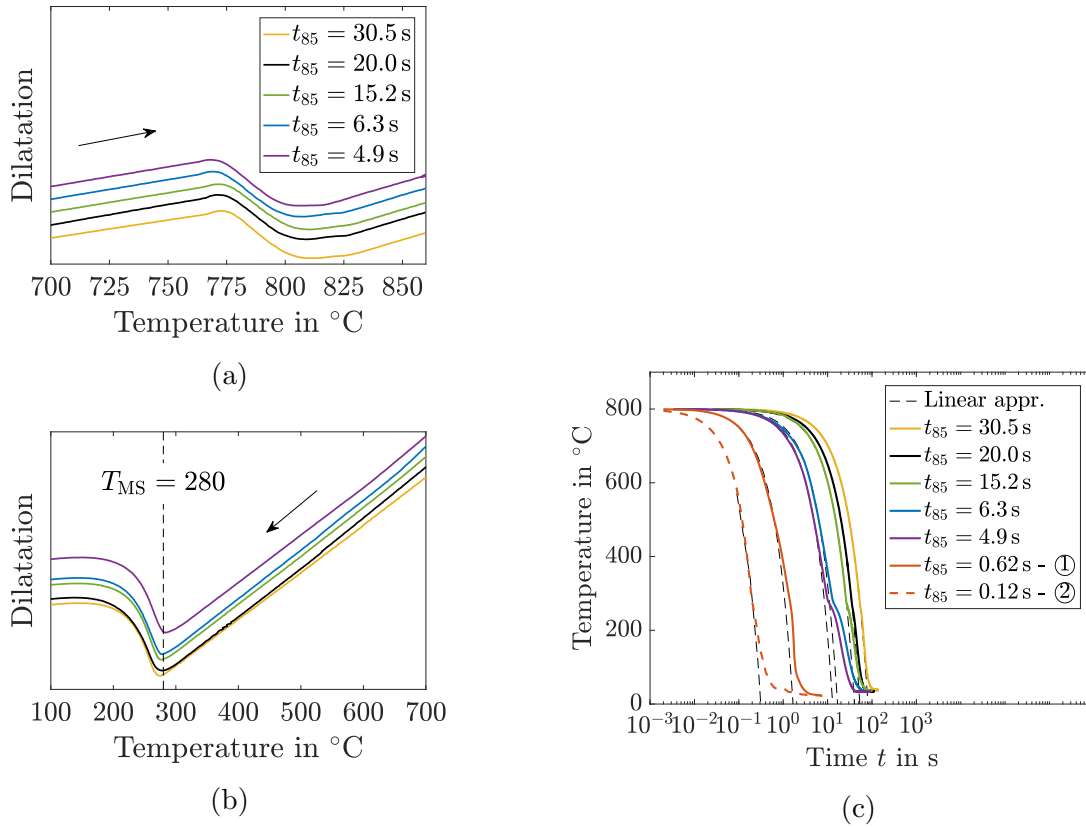
Figure 4.2: Heat treatment of the specimens, (a) dilatation curves of 50CrMo4 during heating, (b) dilatation curves of 50CrMo4 during cooling, (c) temperature profile during cooling, note that temperature curves are time-shifted so that $T(t=0) = 800°C$

In Fig. 4.2(a), the dilatation curves of the specimens during the heating are shown. The linear course of all curves from a temperature of 825 °C indicates that, for all specimens, full austenitization is achieved. Fig. 4.2(b) shows the corresponding dilatation curves during the quenching. Concerning the martensite start temperature, no significant influence of the quenching rate is observed. However, the yellow curve corresponding to $t_{85} = 30.5\,\text{s}$ has a different gradient, which indicates the formation of a non-martensitic phase at high temperature. All other curves show a parallel course. Thus, the critical time interval is $t_{85} = 20.0\,\text{s}$, corresponding to a quenching rate of $\dot{\tilde{T}}_{85} = 15.0\,°\text{Cs}^{-1}$.

The temperature curves with respect to time in Fig. 4.2(c) are extended by the temperature measurements during the water bath quenching. The reduction of the temperature rate at approximately the martensite start temperature is due to the exothermic austenite–martensite transformation. The black dashed lines indicate the corresponding ideal linear course. Based on this diagram, the parameters t_{85} and $\dot{\tilde{T}}$ can be determined. Accordingly, by using water as quenching medium, a time interval of $t_{85} = 0.62\,\text{s}$ corresponding to a quenching rate of $\dot{\tilde{T}}_{85} = 484\,°\text{Cs}^{-1}$ is achieved inside the sample.

Four heat treatments were selected for the next analysis step, which are summarized in Tab. 4.2 with their respective cooling times. The further investigated test runs corresponded to the lowest possible quenching rate to form a fully martensitic microstructure, the maximal possible quenching rate with specimen types A and B with the dilatometer
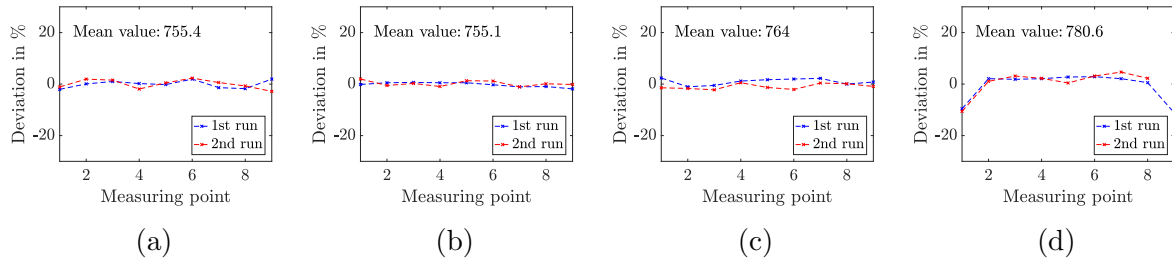
Figure 4.3: Variation of the hardness measurements by indicating the deviation from the mean value of the individual samples (a) A1, (b) A2, (c) A3, (d) A4

setup and the water bath quenching rate, which is the overall maximum rate investigated in this work. Note that the dilatometer with the chosen quenching medium could not keep the specified cooling rate below the martensite start temperature. As a result, the sample from analysis A2 experienced slower cooling below T_{MS}.

Table 4.2: Relevant measured quenching parameters and martensite start temperatures of EBSD-analyzed specimens; parameters for A4 refer to measuring point ①.

Analysis Specimen Type	A1 A	A2 A	A3 B	A4 A
T_{MS} in °C	279.3	277.1	286.8	-
t_{85} in s	20.0	6.3	4.9	0.62
$t_{T_{\mathrm{MS}} \to 100\,°\mathrm{C}}$ in s	18.1	20.1	15.3	0.47 *
t_{81} in s	52.8	33.5	25.0	1.9
$\dot{\tilde{T}}_{85}$ in °Cs^{-1}	15.0	47.6	61.2	484
$\dot{\tilde{T}}_{\mathrm{T_{MS}} \to 100\,°\mathrm{C}}$ in Ks^{-1}	9.9	8.8	12.2	383 *
$\dot{\tilde{T}}_{81}$ in °Cs^{-1}	13.3	20.9	28.0	368

* underlying assumption: $T_{\mathrm{MS}} = 280\,°\mathrm{C}$.

The results of the hardness measurements for each test run and specimen are depicted in Fig. 4.3. In these diagrams, the deviation from the overall mean per specimen is given depending on the position number. Hereby it is shown that with the chosen specimen geometry and the heat treatment with the first experimental setup, a homogeneous hardness course, and thus a homogeneous martensite structure, is obtained. Regarding the fourth specimen (Fig. 4.3(d)), decarburization took place at the edge of the specimen. Outside the surface layer zone, however, a homogeneous structure is achieved.

In Fig. 4.4, the correlation between the quenching rate and the hardness is shown. By increasing the cooling rate, a higher hardness is obtained.

4.4. Microstructure Characterization

The results of the EBSD analyses are shown as orientation maps in Fig. 4.5, where the inverse pole figure (IPF) color scheme is used for the illustration of the martensite orientations. Note that the raw data have been smoothed and filtered using the half-quadratic minimization of manifold-valued data (Bergmann et al. (2015)). Within the measuring
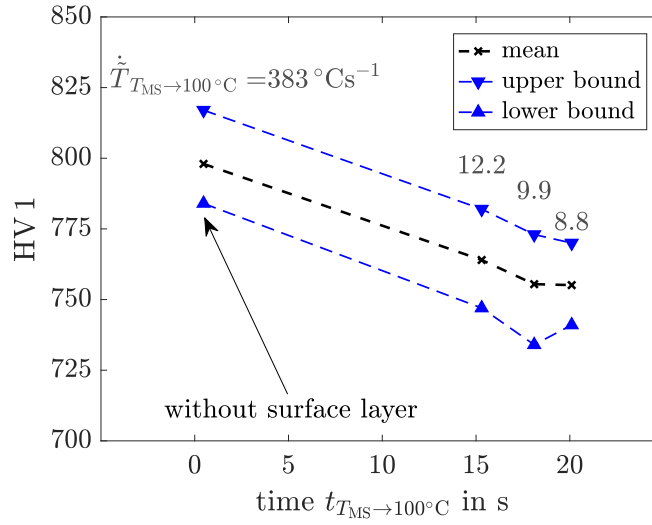
Figure 4.4: Correlation between measured hardness and cooling time, number above data points indicate cooling rates

accuracy, no retained austenite could be detected for all heat treatments. In accordance with Vieweg et al. (2017c), the present measured orientations confirm the KS orientation relationship. Based on this, PAG boundaries are automatically reconstructed and depicted as black lines in Fig. 4.5. White lines indicate recrystallization twin boundaries of PAGs, which are identified via their special orientation to each other. Contrary to expectations, in several cases, the (twin) boundaries follow somewhat jagged lines, which is a sign that some orientations have been misindexed. This can be attributed to the fact that austenite grains and their twins share equal martensite variants. A detailed discussion about this can be found, for example, in Nyyssönen et al. (2018). In the context of the statistical analyses in the present study, twins are considered as single PAGs.

Moreover, the CPP packets (in the following, these are referred to as packets) are calculated, which are shown in Fig. 4.6. For the grain reconstruction, the threshold misorientation angle indicating a grain boundary is defined with $\theta_{\text{crit}} = 5°$. Since the laths cannot be clearly identified in this purely orientation-based reconstruction, the reconstructed "martensite grain" is called a "block". As a reminder, in the martensite hierarchy, blocks are the superordinate structure of the laths and a block consists of several laths of the same or a very similar orientation. The cross-section areas of the structure recorded with the EBSD system are referred to as areas A^{2D}.

According to the heat treatment, no significant differences in the grain sizes of the PAGs are expected. In Fig. 4.7, this is checked by means of the median and mean equivalent grain diameter

$$d_{\text{eq}} = 2 \sqrt{\frac{A^{\text{2D}}}{\pi}}. \tag{4.2}$$

Reconstructed austenite grains which are intersected by the measurement boundary are excluded from the evaluation. Furthermore, here and in the following, grains and martensite blocks with a size smaller than $0.32 \, \mu\text{m}^2$ are not evaluated. The resulting number of evaluable grains is indicated above the corresponding bars. Experiments with a higher
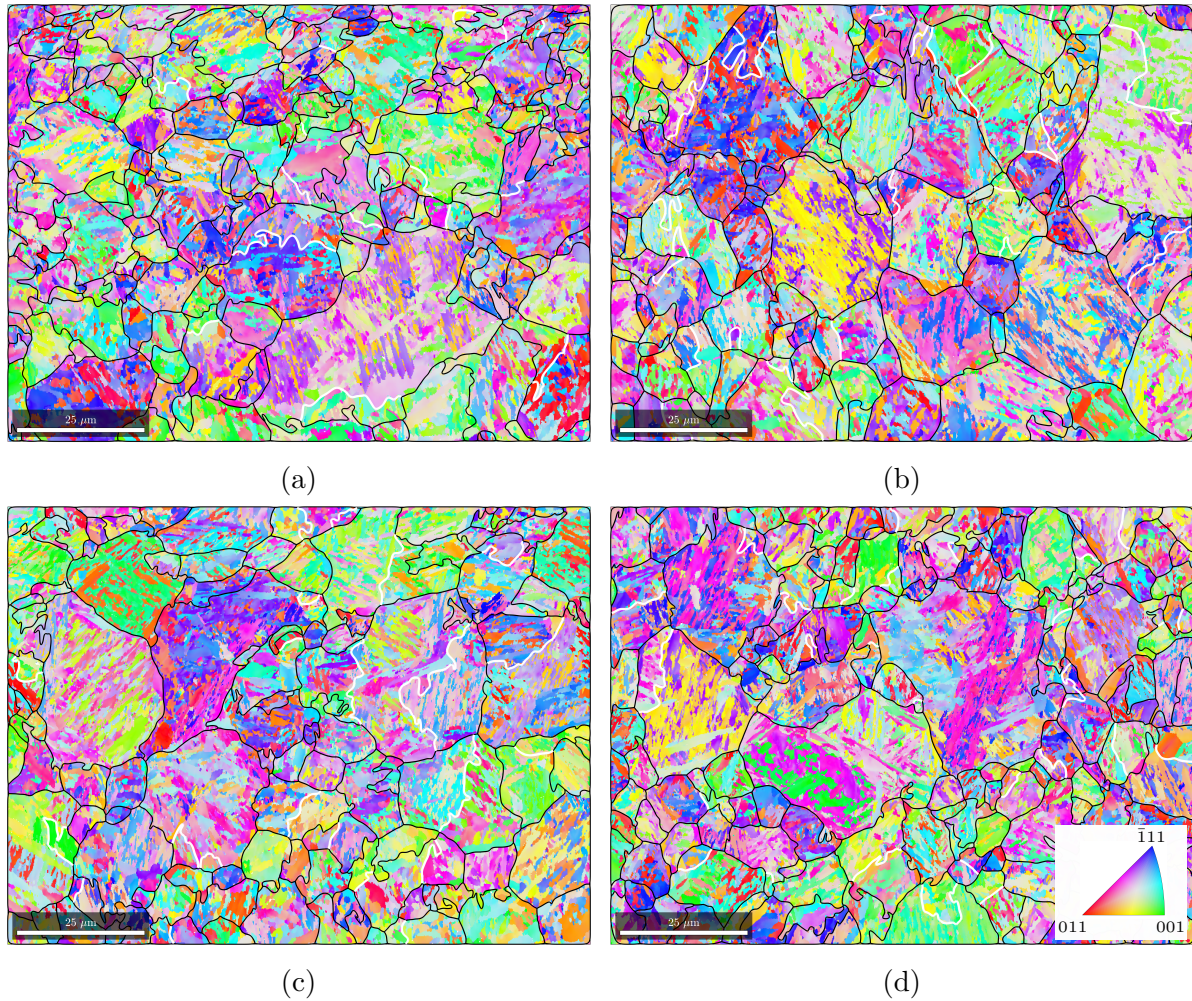
Figure 4.5: EBSD map in IPF color scheme with superimposed PAG boundaries (black) and recrystallization twin boundaries (white), (a) A1, (b) A2, (c) A3, (d) A4

amount of evaluable grains tend to have a smaller mean; however, a systematic influence from the heat treatment cannot be identified. Differences are therefore due to the size of the measurement section.

In Fig. 4.8 the empirical cumulative distribution function of the packet and martensite block areas – respectively, $A_{\text{CPP}}^{\text{2D}}$ and A_{B}^{2D} – are shown. Note the different scale of the abscissa in Fig. 4.8(b). No systematic correlation between the quenching rate and the packet areas as well as the martensite block areas can be derived.

The diagrams in Fig. 4.8 only represent a one-dimensional representation of the data, which is why the analyses are supplemented by a two-dimensional representation. Thus, Fig. 4.9 shows the packet areas $A_{\text{CPP}}^{\text{2D}}$ over the PAG areas $A_{\text{PAG}}^{\text{2D}}$. In Fig. 4.9(a), the complete data of the highest and lowest tested quenching rates are documented as an example. The black dashed line depicts the highest possible packet area $A_{\text{CPP}}^{\text{2D}}(A_{\text{PAG}}^{\text{2D}})^{-1} = 1$ in this diagram. A wide spread of packet areas is identified.

In order to evaluate whether the cooling rate has an influence on the distribution of packet sizes, an attempt is made to represent the holistic trend of the data. Based on the data

(a)

(b)

(c)

(d)
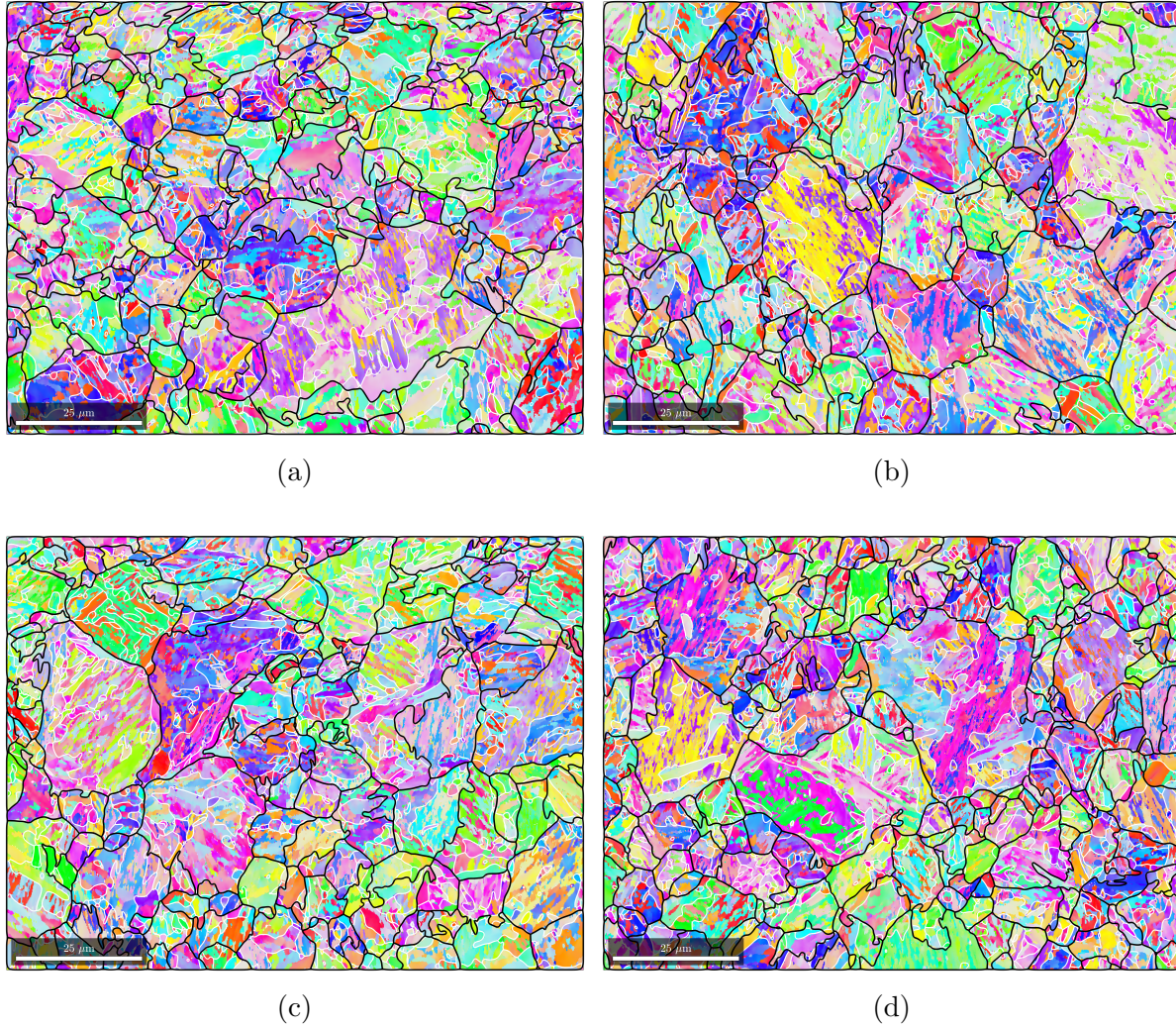
Figure 4.6: EBSD map in IPF color scheme with superimposed PAG boundaries, recrystallization twin boundaries (black) and CPP packets (white), (a) A1, (b) A2, (c) A3, (d) A4

recorded, as shown in Fig. 4.9(a), for each quenching rate, a curve of type

$$g(x) = c_1\, x^{c_2} + c_3 \tag{4.3}$$

with the fitting constants c_1, c_2 and c_3 is fitted with the nonlinear least squares method to represent the data. The resulting curves are shown in Fig. 4.9(b). Based on this, the packet size depends considerably on the PAG areas. Accordingly, a larger austenite grain tends to contain larger packets. However, a clear correlation of the quenching rate with the packet areas as a function of PAG areas is not identified. The same evaluation procedure is applied to the martensite block areas, see Fig. 4.11. The curves fitted in Fig. 4.11(b) show a lower dependency of the martensite block areas on their PAG area. However, again, no systematic influence of the cooling rate can be identified. The evaluation of the numbers of packets and blocks in each PAG leads to the same results, see Fig. 4.10.
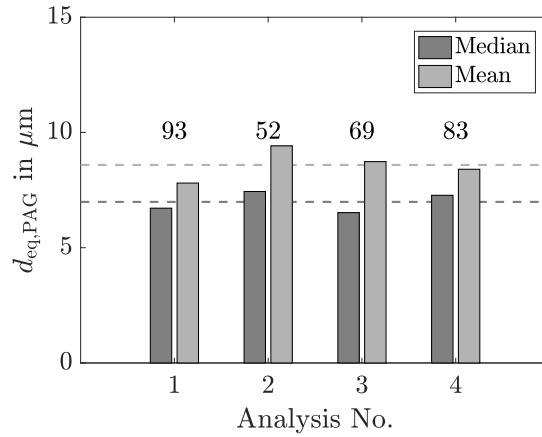
Figure 4.7: Comparison of mean and median of the equivalent diameter of the PAG cross-sections in the measured EBSD domain, number above bars indicates the number of evaluable grains in the domain
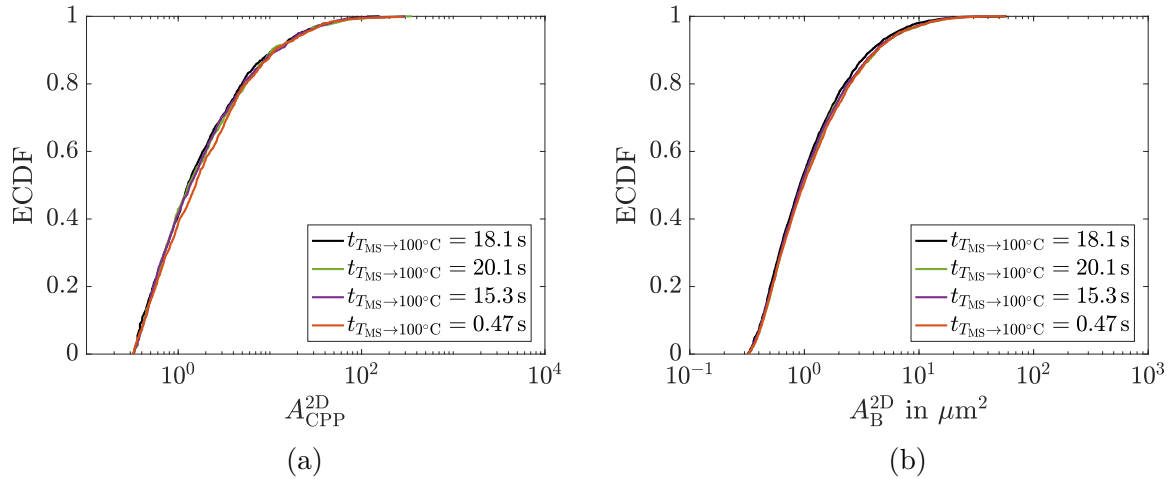

Figure 4.8: Empirical cumulative distribution function (ECDF), (a) normalized packet cross-section areas, (b) normalized block cross-section areas

4.5. Discussion

In the present investigation, specimens were heat-treated with comparable austenitization conditions but different quenching rates. A typical partitioning was omitted in order to isolate the quenching process, which is responsible for the formation of martensite. Hardness measurements were used to prove that a homogeneous microstructure was present. Accordingly, the specimens were chosen small enough to neglect influences of the temperature gradient. In accordance with the current state of knowledge, a higher hardness was achieved with a more intensive quenching, see Fig. 4.4.

Since microstructure size effects can contribute to an increase in hardness, it was investigated how the quenching intensity affects the microstructure scales. For the same material, an influence of the cooling rate on the resulting block size was determined by Eggbauer et al. (2018). However, with a comprehensive evaluation of the sizes of the hierarchical microstructure, no significant systematic influence of the cooling rate could
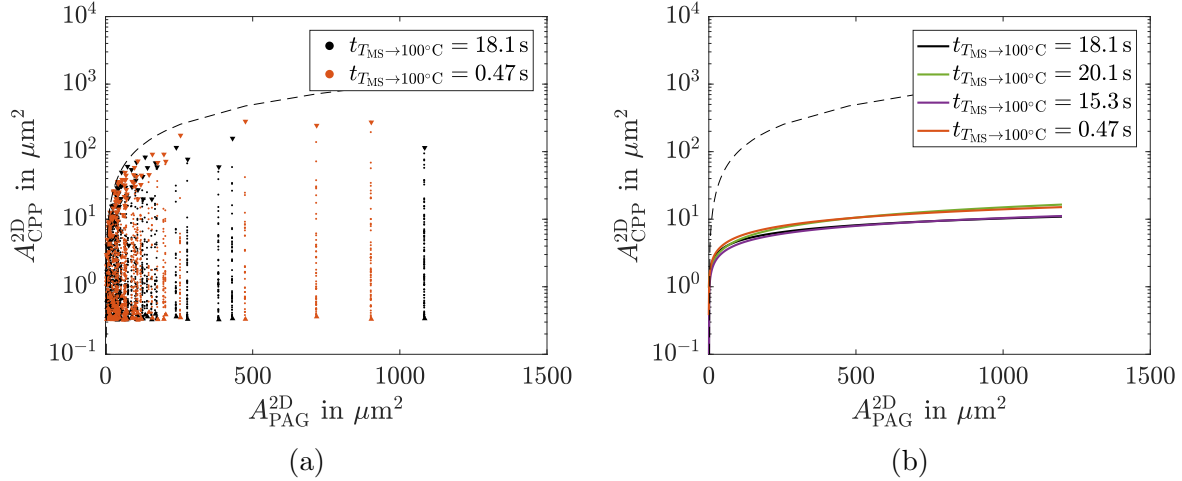
Figure 4.9: Packet cross-section area in dependence of PAG area, (a) measured data, (b) representation of measured data with fitted curves
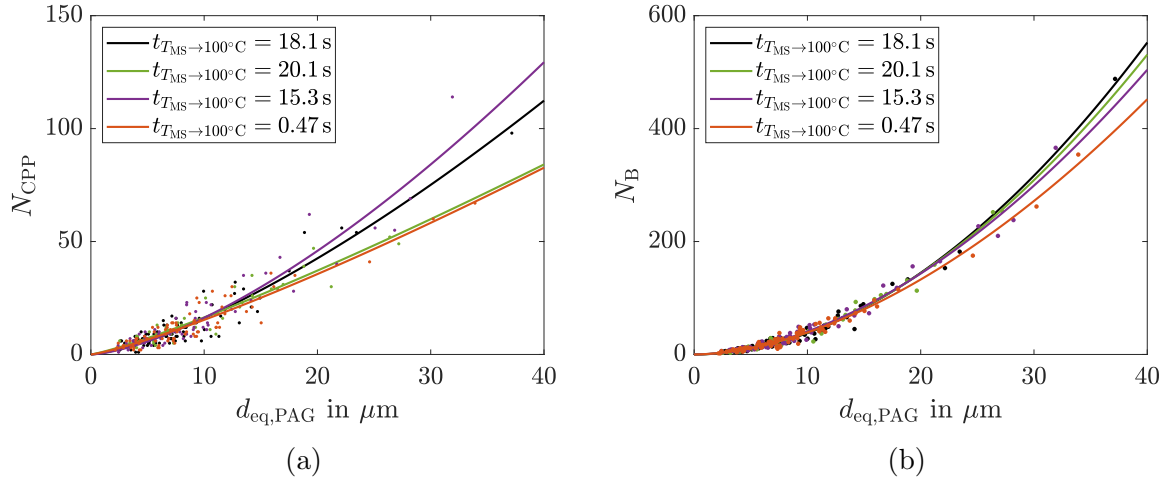

Figure 4.10: Number of blocks in (a), and packets in (b) depending on the PAG size

be identified. The difference could be due to the size of the measurement domain, which was chosen to be larger in the present investigation. Furthermore, Eggbauer et al. (2018) do not describe how the values that were considered representative for the block sizes were evaluated in detail.

Due to the comparable austenitization conditions, the PAGs were expected to have the same appearance in size and shape. In order to verify this, the mean and median values of the areas were analyzed. It was shown that the median values were very similar and the mean values differed. This was due to the size of the measurement domain. However, in this study, the focus was on martensite; a possible influence of the austenite grain size was considered by the presentation of the data in relation to the austenite grain cross-section areas, see Figs. 4.9 and 4.11. The following can be derived from these analyses.

The packet size as well as the number of packets is dependent on the austenite grain size. This is in agreement with the concept of pre-existing nuclei of martensite, representing crystal lattice defects in the parent austenite phase, cf. Olson & Cohen (1981). Assuming
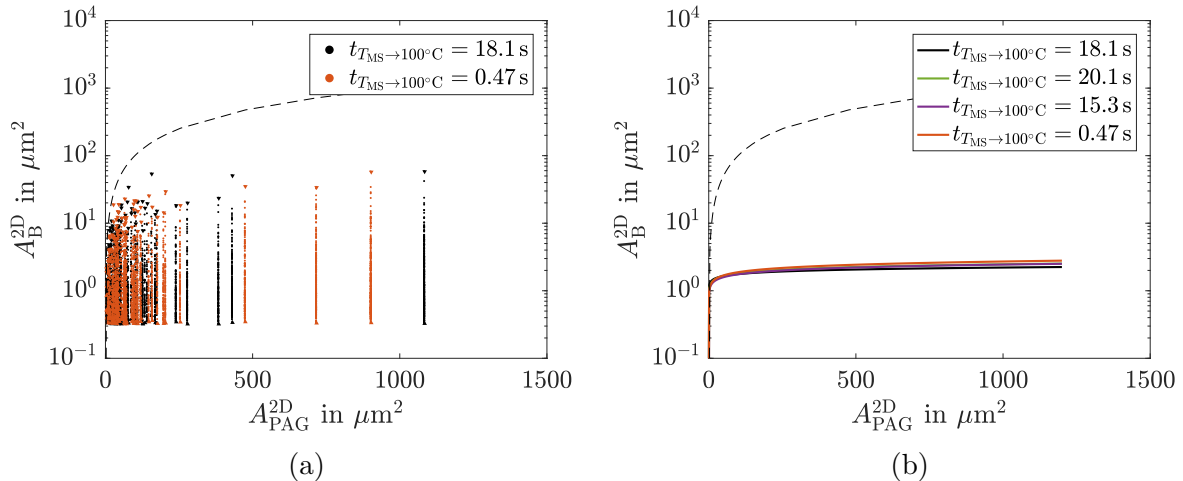
Figure 4.11: Martensite block cross-section area in dependence of PAG cross-section area, (a) measured data, (b) representation of measured data with fitted curves

that packets are generated from these kind of nucleation points, the probability of lattice defects increases with the size of the PAG. Considering fitting curves in order to evaluate the holistic trend of block sizes with regard to PAG sizes reveals a slight dependency, which decreases with increasing $A_{\mathrm{PAG}}^{\mathrm{2D}}$. This is consistent with the Hall–Petch concept of grain boundary strengthening, where a term of type $k_{\mathrm{HP}}\, d^{-0.5}$ is added to the initial yield strength. In this term, k_{HP} represents a material specific constant and d is the diameter of the grain. However, the geometric restriction of grain boundaries is most likely the dominant effect which leads to smaller blocks in smaller PAGs.

The observations of the size effect in this work are in contrast to the phenomenon observed in the majority of the literature, in which martensite sizes become smaller with increasing cooling rates (Morito et al. (2010); Bardelcik et al. (2010); Tsuzaki & Maki (1981); Eggbauer et al. (2018); Loewy et al. (2015); Shtejnberg et al. (1977)). This motivates a detailed discussion of the differences. For this purpose, relative differences of the equilibrium temperature and martensite start temperature $(T_0 - T_{\mathrm{MS}})/T_0$ as well as the chemical driving forces $\Delta G_{\mathrm{chem}}^{\mathrm{MS}}$ necessary to initiate the martensite transformation are calculated with Thermo-Calc TCFE 8 and compared. These values give an indication of the size of energy barrier, which must be overcome. The energy barrier is composed of an additional mechanical energy component due to the displacement of the atomic structure and an interface energy component.

For comparison, references were considered in which the influence of the quenching rate was systematically investigated, T_{MS} was specified and a size effect was verifiable via corresponding images. Investigations whose temperature profiles simulated induction hardening processes and thus did not have a corresponding holding time at austenitization temperature were not considered. The limited number of references with the corresponding values are documented in Tab. 4.3.

Table 4.3: Comparison of relative differences between the equilibrium temperature and martensite start temperature $\frac{T_0 - T_{MS}}{T_0}$, differences of Gibbs free energies at the martensite start temperature ΔG^{MS}_{chem} and size effects of several materials.

Material (name)	T_{MS} in °C	Obvious size effect	Reference	$\frac{T_0 - T_{MS}}{T_0}$	ΔG^{MS}_{chem} in Jmol^{-1}
				(Thermo-Calc TCFE 8)	
Fe-22 wt.% Ni	240	Yes	Loewy et al. (2015)	0.22	−416 *
Fe-24 wt.% Ni	187	Yes	Tsuzaki & Maki (1981)	0.29	−461 *
Fe-18 wt.% Ni	297	Yes	Tsuzaki & Maki (1981)	0.25	−615 *
18% Ni maraging steel	217	Yes	Tsuzaki & Maki (1981)	0.44	−1120
WHT1500HF	382	Yes	Hu et al. (2018)	0.45	−1718
50CrMo4	280	No	Graf et al. (2020)	0.52	−1875
AISI 630	140	No	Villa et al. (2014)	0.76	−2400

* a conservative value of 0.005 wt.% C is assumed.

In Loewy et al. (2015) (Fe-22 wt.% Ni), a subsequent block formation (simultaneous in all packets and PAGs) is stated. The size dependency is explained by a thermally activated relaxation of austenite in the direct vicinity of the new blocks. A faster cooling rate leads to less relaxation, which is accompanied with a higher amount of elastic energy being introduced by the transformation. A reduced size of the block at a single block formation event is the consequence of this. The subsequent block formation mechanism is consistent with the small energy barrier indicated by the relatively low values of $(T_0 - T_{\mathrm{MS}})/T_0$ in Table 4.3. With a small energy barrier, the induced stresses must be relatively small. Furthermore, the chemical driving force $\Delta G_{\mathrm{chem}}^{\mathrm{MS}}$ is relatively small. If the energy barrier is exceeded, only a small amount of material has to be converted due to the low chemical driving force. The simultaneously induced stresses are too low to cause a stress-assisted auto-nucleation of another block.

Another martensite formation mechanism is stated in Villa et al. (2014). An energy barrier crossing event is accompanied by the formation of martensite clusters consisting of several blocks and packets. These martensite clusters extend over several PAGs, which are significantly smaller than in Loewy et al. (2015). The plausibility of this fundamentally different formation mechanism can be explained by comparing $(T_0 - T_{\mathrm{MS}})/T_0$ and $\Delta G_{\mathrm{chem}}^{\mathrm{MS}}$ values with those of the material investigated by Loewy et al. (2015). The significantly larger ratio of $(T_0 - T_{\mathrm{MS}})/T_0$ indicates a higher energy barrier. A significantly higher chemical driving force is therefore necessary to overcome this barrier. Higher induced stresses lead to a stress-assisted auto-nucleation mechanism which is stopped when the total of the additional mechanical energy and interfacial energy equals the driving force for martensite formation (Villa et al. (2014)). Higher mechanical stresses during the transformation could be caused by elements such as C, which reduces T_{MS} and increases solid solution hardening, cf. Morito et al. (2003). Furthermore, smaller austenite grain sizes contribute to higher mechanical stresses due to grain boundary strengthening.

Based on the limited data available, the materials in Loewy et al. (2015) and Villa et al. (2014) seem to be extreme cases. As for the influence of the cooling rate, the first discussed mechanism of block formation shows a significant dependence on the cooling rate. The second mechanism is insensitive against the applied cooling rate. Indicators of which mechanism is present seem to be $(T_0 - T_{\mathrm{MS}})/T_0$ and $\Delta G_{\mathrm{chem}}^{\mathrm{MS}}$, see Tab. 4.3. It is assumed that there is a smooth – currently unclear – transition of one mechanism into the other. Based on the results in Sec. 4.4, and with regard to the influence of the cooling rate, the investigated 50CrMo4 is sorted into the group of the latter discussed martensite formation mechanism. It is assumed that the block formation is at least so fast that no significant size effects due to time-dependent relaxation of the austenite matrix is noticeable.

The lack of size effects raises the question of the origin of the increase in hardness. This can be explained by decreased carbon segregation to lattice defects with an increasing quenching rate, which results in a higher lattice distortion and therefore higher hardness. In addition, a reduced retained austenite ratio lead to higher hardness. With the chosen methods of analysis, both effects cannot be proven beyond doubt, but an experimental confirmation is given by Eggbauer et al. (2018). Furthermore, it should be noted that Mirzaev et al. (1979) observed a morphological transition from lath to $(225)_\gamma$-martensite by increasing the cooling rate. This morphological change could also increase the hardness without having an influence on T_{MS}.

5. Modeling of Multivariant Martensite Transformations

Despite intensive research, the formation of lath martensite in carbon steels is still not fully understood. This is due to the complexity and speed, which leads to limitations in experimental observation. In this work, therefore, some idealizations/simplifications as well as assumptions are made, which are based on the presented experimental findings (Sec. 2) as well as findings from the literature (Sec. 4):

- The martensite transformation is initiated at lattice defects, mainly on the PAG boundaries.

- Further martensite transformation is performed by sequentially forming of martensite clusters consisting of laths and blocks that form crystallographic packets by auto-nucleation. Such a transformation event is considered as a fast isothermal transformation.

- The carbon segregation, which was identified as the key factor of hardness increase is neglected. This is due to the fact that in the context of this work mainly the martensite morphology is of interest.

- The martensite transformation can be described with a continuum model in small strain context.

- The substructure is not resolved. The shape change and the resulting orientations on the size scale considered are estimated via the PTMC.

- The laths as well as the sub-blocks and their most likely strain-induced auto-nucleation are not resolved. Sub-blocks and laths are of less interest, since no crack initiation is expected at sub-block or lath boundaries due to the relatively small misorientation in a subsequent microstructure-based fatigue simulation.

- A maximum of twelve variants approximating the NW orientation relationship are considered. The NW orientation relationship is considered here as a simplified KS orientation relationship, cf. Koumatos & Muehlemann (2017), without a sub-block structure.

- The nucleation/formation of blocks within a crystallographic packet is of the stress-assisted auto-nucleation type. The auto-nucleation of blocks of another packet is inhibited, since the other variants are created on a different CPP.

- The phase boundary, which in general extends over few atomic lattice distances, is described as diffuse interface whose width is determined by the numerical (spatial) discretization.

Based on these points, the modeling methodology is described in this section in detail.

5.1. Phase Field Model

The phase field model used in this work and its numerical implementation was recently published by Graf et al. (2021c) and is an advancement based on the work of Müller (2016). Parts of this sections strongly follow these works. Another reference concerning the thermodynamics of the model and the numerical implementation was the work of Kuhn (2013).

In this work, the evolution of multivariant martensite phase transformation is described by a set of order parameters φ_i (with $i = 1, \ldots, n_{\mathrm{mart}}$), where $\varphi_i = 0$ represents the austenitic parent phase and $\varphi_i = 1$ the ith martensitic variant (product phase). Each order parameter has its separate evolution equation. For the sake of clarity, this evolution equation is derived for the monovariant case, without index i in Sec. 5.1.1. In Sec. 5.1.2, the multivariant free energy potential is presented. Together with the determined weighting factors in Sec. 5.1.3, the strong form of the model equations is then derived in Sec. 5.1.4.

5.1.1. Thermodynamics and Order Parameter Evolution

In order to derive an evolution equation concerning the order parameter φ a thermodynamic consistent continuum theory was proposed by Fried & Gurtin (1993, 1994) and Gurtin (1996). Accordingly, micro-forces are introduced whose working is accompanied with changes in φ. The micro-force system is described by a vector stress $\boldsymbol{\xi}$ as well as internal and external scalar body forces ϖ and ς, respectively. The following declarations are made (Gurtin (1996)):

- The micro-forces act as thermodynamic conjugate to the rate $\dot{\varphi}$. Concerning a control volume $\mathcal{B}$, the external power is thus

$$\mathcal{P}_{\mathrm{ext,mic}} = \int_{\partial\mathcal{B}} \boldsymbol{\xi} \cdot \boldsymbol{n}\,\dot{\varphi}\,dA + \int_{\mathcal{B}} \varsigma\dot{\varphi}\,dV. \tag{5.1}$$

- The micro-force system is consistent with the global micro-force balance

$$\int_{\partial\mathcal{B}} \boldsymbol{\xi} \cdot \boldsymbol{n}\,dA + \int_{\mathcal{B}} (\varsigma + \varpi)\,dV = 0 \tag{5.2}$$

  and the equivalent local form

$$\mathrm{div}\boldsymbol{\xi} + \varsigma + \varpi = 0. \tag{5.3}$$

The external power of the micro-force system (5.1) is added to the external mechanical power (3.29) resulting in a supplemented energy balance. Finally, with use of micro-force balance (5.3) and restriction to isothermal conditions, a modified version of the Clausius-Planck inequality (3.40) is obtained with

$$\boldsymbol{\sigma} : \dot{\boldsymbol{\varepsilon}} + \boldsymbol{\xi} \cdot \boldsymbol{\nabla}\dot{\varphi} - \varpi\,\dot{\varphi} - \dot{\psi} \geq 0. \tag{5.4}$$

The free energy density is now a function of the strain, the order parameter and its gradient: $\psi = \psi(\boldsymbol{\varepsilon}, \varphi, \boldsymbol{\nabla}\varphi)$. Accordingly, with

$$\dot{\psi} = \frac{\partial\psi}{\partial\boldsymbol{\varepsilon}} : \dot{\boldsymbol{\varepsilon}} + \frac{\partial\psi}{\partial\varphi}\dot{\varphi} + \frac{\partial\psi}{\partial\boldsymbol{\nabla}\varphi} \cdot \boldsymbol{\nabla}\dot{\varphi}. \tag{5.5}$$

the time derivate is calculated. Following the procedure in Sec. 3.2.2, Eq. (5.4) becomes

$$\left(\boldsymbol{\sigma} - \frac{\partial \psi}{\partial \boldsymbol{\varepsilon}}\right) : \dot{\boldsymbol{\varepsilon}} + \left(\boldsymbol{\xi} - \frac{\partial \psi}{\partial \boldsymbol{\nabla} \varphi}\right) \cdot \boldsymbol{\nabla} \dot{\varphi} - \left(\varpi + \frac{\partial \psi}{\partial \varphi}\right) \dot{\varphi} \geq 0. \tag{5.6}$$

by inserting Eq. (5.5). Eq. (5.6) is fulfilled with the constitutive relations

$$\boldsymbol{\sigma} = \frac{\partial \psi}{\partial \boldsymbol{\varepsilon}} \quad \text{and} \quad \boldsymbol{\xi} = \frac{\partial \psi}{\partial \boldsymbol{\nabla} \varphi}, \tag{5.7}$$

when the inequality

$$\varpi_{\text{dis}} \dot{\varphi} \leq 0 \quad \text{with} \quad \varpi_{\text{dis}} = \varpi + \frac{\partial \psi}{\partial \varphi} \tag{5.8}$$

is fulfilled. The most general form of ϖ_{dis}, which is consistent with Eq. (5.8) is given in the work of Gurtin (1996) and reads

$$\varpi_{\text{dis}} = -\beta \, \dot{\varphi} \quad \text{with} \quad \beta \geq 0, \tag{5.9}$$

where β is a constitutive modulus. Thus, the internal force

$$\varpi = -\beta \, \dot{\varphi} - \frac{\partial \psi}{\partial \varphi} \tag{5.10}$$

has a dissipative contribution (first term) and a contribution due to changes in the free energy. By choosing a constant mobility $M = 1/\beta$ and in absence of external forces $\varsigma = 0$ the time-dependent Ginzburg-Landau or Allen-Cahn equation

$$\dot{\varphi} = -M \left(\frac{\partial \psi}{\partial \varphi} - \text{div}\left(\frac{\partial \psi}{\partial \boldsymbol{\nabla} \varphi}\right)\right) = -M \frac{\delta \psi}{\delta \varphi} \tag{5.11}$$

can be derived by inserting Eq. (5.10) and the constitutive relation of $\boldsymbol{\xi}$ (Eq. 5.7) into the local micro-force balance (5.3). Accordingly, the rates of the order parameter are proportional to the variational derivate of ψ, the free energy density or phase field potential.

5.1.2. Free Energy Potential

With minimizing free energy $\int_\Omega \psi \, dV$ as driving force, the phase field approach computes the martensite evolution in a dissipative gradient-descent fashion. The potential ψ may be expressed in the spirit of Schrade et al. (2007) by three contributions

$$\psi = \psi^{\text{el}} + \psi^{\text{sep}} + \psi^{\text{grad}}, \tag{5.12}$$

where ψ^{el} represents the elastic energy density, ψ^{sep} the phase separation potential and ψ^{grad} the gradient potential. The elastic energy density is defined as

$$\psi^{\text{el}} = \frac{1}{2} \left(\boldsymbol{\varepsilon} - \boldsymbol{\varepsilon}^0\right) : \boldsymbol{\mathcal{C}} \left(\boldsymbol{\varepsilon} - \boldsymbol{\varepsilon}^0\right)$$
$$\text{with} \quad \boldsymbol{\varepsilon}^0 = \sum_{i=1}^{n_{\text{mart}}} h_i \tilde{\boldsymbol{\varepsilon}}_i, \quad \boldsymbol{\mathcal{C}} = \boldsymbol{\mathcal{C}}^\gamma + \sum_{i=1}^{n_{\text{mart}}} h_i \left(\boldsymbol{\mathcal{C}}_i^\alpha - \boldsymbol{\mathcal{C}}^\gamma\right). \tag{5.13}$$

In Eq. (5.13), $\boldsymbol{\varepsilon}^0$ considers the martensite strains $\tilde{\boldsymbol{\varepsilon}}_i$ due to the transformation of the ith martensite variant. The tensors $\boldsymbol{\mathcal{C}}^\gamma$ and $\boldsymbol{\mathcal{C}}_i^\alpha$ indicate the elasticity tensor with respect to

austenite (γ) and the martensite (α) variant, respectively. With the function $h_i = h_i(\varphi_i)$ the transformation strain and the elasticity matrix is interpolated between the parent and product phase. Eq. (5.13) is the generalization to n_{mart} martensitic variants of the formulation of Schmitt et al. (2013a, 2012), which is limited to two variants (Schmidt et al. (2017)).

Concerning the formulation of the phase separation potential, the Landau polynomial

$$\psi^{\text{sep}}(\varphi_i) = \frac{c_{\text{a}}}{2} \sum_{i=1}^{n_{\text{mart}}} \varphi_i^2 - \frac{c_{\text{b}}}{3} \sum_{i=1}^{n_{\text{mart}}} \varphi_i^3 + \frac{c_{\text{c}}}{4} \left(\sum_{i=1}^{n_{\text{mart}}} \varphi_i^2 \right)^2 \tag{5.14}$$

with the constants $c_{\{\text{a,b,c}\}}$ is utilized (Wang & Khachaturyan (1997); Yamanaka et al. (2008)). With this fourth-order polynomial the transition path from austenite to martensite can be described energetically as a function of temperature, cf. Engin & Urbassek (2008) and Schmidt et al. (2017).

Considering the simple case of one order parameter, the constants $c_{\{a,b,c\}}$ can be defined with $c_{\text{a}} = 32\,\tilde{g}$, $c_{\text{b}} = 3\,c_{\text{a}} - 12\,\Delta g$ and $c_{\text{c}} = 2\,c_{\text{a}} - 12\,\Delta g$, where $\tilde{g}$ is a parameter regarding the height of the chemical energy barrier and Δg defines the chemical energy difference between austenite and martensite, cf. Yeddu et al. (2012b). Following Yeddu et al. (2012b), the Landau polynomial in Eq. (5.14) can be reformulated as

$$\psi^{\text{sep}}(\varphi_i) = 16\,\tilde{g} \underbrace{\left(\sum_{i=1}^{n_{\text{mart}}} \varphi_i^2 - 2 \sum_{i=1}^{n_{\text{mart}}} \varphi_i^3 + \left(\sum_{i=1}^{n_{\text{mart}}} \varphi_i^2 \right)^2 \right)}_{=f^{\text{int}}}$$

$$+ \Delta g \underbrace{\left(4 \sum_{i=1}^{n_{\text{mart}}} \varphi_i^3 - 3 \left(\sum_{i=1}^{n_{\text{mart}}} \varphi_i^2 \right)^2 \right)}_{=f^{\text{bulk}}}, \tag{5.15}$$

where it is split into two parts. The first term is referred to as the interface part with the dimensionless polynomial f^{int}, the second as the bulk part with f^{bulk}. Using the case of a single order parameter, Fig. 5.1 illustrates the courses of interface and bulk part. With $n_{\text{mart}} = 1$, Eq. (5.15) simplifies to

$$\psi^{\text{sep}}(\varphi) = 16\,\tilde{g}\,\varphi^2 \left(1 - \varphi\right)^2 + \Delta g\,\varphi^3 \left(4 - 3\varphi\right). \tag{5.16}$$

The gradient potential ψ^{grad} is defined as

$$\psi^{\text{grad}} = \frac{1}{2}\,\beta^* \sum_{i=1}^{n_{\text{mart}}} |\boldsymbol{\nabla}\varphi_i|^2. \tag{5.17}$$

where the constant β^* is a scaling parameter of the gradient potential and $\boldsymbol{\nabla}\varphi_i$ denotes the gradient of φ_i.

In order to be able to control the width of the interface l without affecting overall energy, a further scaling factor α^* is introduced into the interface part of the separation potential. Thus, the phase field potential becomes

$$\psi = \psi^{\text{el}} + \Delta g f^{\text{bulk}} + \underbrace{16\,\tilde{g}\,\alpha^*\,f^{\text{int}} + \frac{1}{2}\beta^* \sum_{i=1}^{n_{\text{mart}}} |\boldsymbol{\nabla}\varphi_i|^2}_{\psi^{\text{int}}}, \tag{5.18}$$
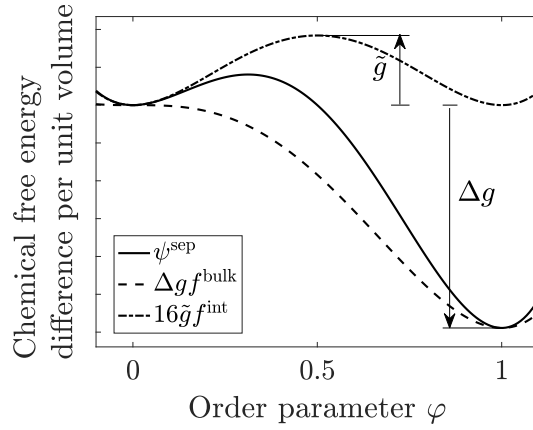
Figure 5.1: Landau polynomial for the simple case of a single order parameter

where the interface energy density ψ^{int} can be defined. The volume integral $\Psi^{\text{int}} = \int_\Omega \psi^{\text{int}} \, dV$ gives the interface energy of the model.

5.1.3. Determination of Weighting Factors

The basic idea for following procedure goes back to Cahn & Hilliard (1958). Consider the standard equilibrium case ($\Delta g = 0$) of an indefinitely extended one-dimensional continuum, which consists of two phases as depicted in Fig. 5.2. In equilibrium state, the order parameter function

$$\varphi = \frac{1}{2}\left[\tanh\left(\frac{2x}{l}\right) + 1\right] \tag{5.19}$$

solves the Euler-Lagrange equation

$$\frac{\partial \psi^{\text{int}}}{\partial \varphi} - \frac{d}{dx}\left[\frac{\partial \psi^{\text{int}}}{\varphi'}\right] = 0 \quad \text{with} \quad \varphi' = \frac{d\varphi}{dx} \tag{5.20}$$

of the variational problem

$$\Psi^{\text{int}} = \int_{-\infty}^{\infty} \psi^{\text{int}} \, dx. \tag{5.21}$$

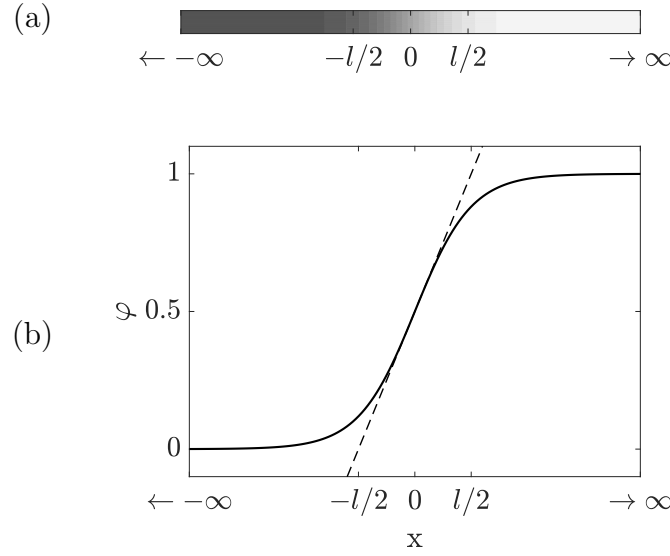Multiplying Eq. (5.20) with φ' and utilizing the identity

$$\frac{d}{dx}\left[\frac{\partial \psi^{\text{int}}}{\varphi'}\right]\frac{d\varphi}{dx} = \frac{d}{dx}\left[\frac{\partial \psi^{\text{int}}}{\varphi'}\frac{d\varphi}{dx}\right] - \frac{\partial \psi^{\text{int}}}{\varphi'}\frac{d^2\varphi}{dx^2} \tag{5.22}$$

leads to

$$\frac{d}{dx}\left[\psi^{\text{int}} - \frac{\partial \psi^{\text{int}}}{\partial \varphi'}\frac{d\varphi}{dx}\right] = 0. \tag{5.23}$$

From Eq. (5.23) follows

$$\psi^{\text{int}} - \frac{\partial \psi^{\text{int}}}{\partial \varphi'}\frac{d\varphi}{dx} = \text{const.} = c_{\text{d}}. \tag{5.24}$$

Figure 5.2: Indefinitely extended two phase continuum, one-dimensional with two phases (a) field plot, (b) profile plot of the order parameter

The constant c_d is found to be $c_\mathrm{d} = 0$ by evaluation of Eq. (5.24) regarding the specific order parameter $\varphi = 0$ with $\psi^\mathrm{int}(\varphi = 0) = 0$ and $\frac{d\varphi}{dx}\big|_{\varphi=0} = 0$. Analogously to Eq. (5.18) it is

$$\psi^\mathrm{int} = 16\,\tilde{g}\,\alpha^*f^\mathrm{int} + \frac{1}{2}\beta^*|\varphi'|^2,$$

$$\frac{\partial \psi^\mathrm{int}}{\partial \varphi'} = \beta^*\varphi'. \tag{5.25}$$

Inserting Eq. (5.25) in (5.24) leads to

$$dx = \sqrt{\frac{\beta^*}{32\,\alpha^*\tilde{g}f^\mathrm{int}}}\,d\varphi. \tag{5.26}$$

With Eq. (5.26), the integral with respect to x in Eq. (5.21) can be rewritten as an integral with respect to φ. Eventually,

$$\Psi^\mathrm{int} = \sqrt{32\,\alpha^*\beta^*\tilde{g}}\int_0^1 \sqrt{f^\mathrm{int}}\,d\varphi = \gamma \tag{5.27}$$

is obtained. Evaluation of the integral leads to

$$\frac{\sqrt{32\,\alpha^*\beta^*\tilde{g}}}{6} = \gamma \tag{5.28}$$

Furthermore, Eq. (5.26) can be used to derive

$$\frac{d\varphi}{dx}\bigg|_{x=0} = \sqrt{\frac{32\,\alpha^*\tilde{g}f^\mathrm{int}}{\beta^*}}\bigg|_{\varphi=\frac{1}{2}} = \sqrt{\frac{2\alpha^*\tilde{g}}{\beta^*}} = \frac{1}{l}. \tag{5.29}$$

By solving Eq. (5.28) and (5.29), the parameters α^* and β^* according to Eq. (5.30) are determined.

Considering a one-dimensional system, the constants

$$\alpha^* = \frac{3\gamma}{4\tilde{g}\,l} \quad \text{and} \quad \beta^* = \frac{3}{2}\gamma\,l \tag{5.30}$$

can be obtained, where γ is an interface energy parameter. The substitution of these parameters in Eq. (5.18) leads to

$$\psi = \psi^{\text{el}} + \Delta g\, f^{\text{bulk}} + 12\,\frac{\gamma}{l}f^{\text{int}} + \frac{3}{4}\gamma\,l\sum_{i=1}^{n_{\text{mart}}} |\boldsymbol{\nabla}\varphi_i|^2\,. \tag{5.31}$$

The pre-factors $12\,\gamma\,l^{-1}$ and $3/4\,\gamma\,l$ in Eq. (5.31) are the same as in Diewald et al. (2018). Remarkably, the energy barrier $\tilde{g}$ is canceled out, which follows from the parameter setting with γ and l.

5.1.4. Strong Form of Model Equations

By inserting Eq. (5.31) in Eq.(5.11) with respect to the ith phase field, the strong form

$$\frac{1}{M}\dot{\varphi}_i = -\frac{\partial \psi^{\text{el}}}{\partial \varphi_i} - \gamma\left(\frac{12}{l}\frac{\partial f^{\text{int}}}{\partial \varphi_i} - \frac{3}{2}l\,\underline{\Delta}\varphi_i\right) - \Delta g\,\frac{\partial f^{\text{bulk}}}{\partial \varphi_i} \quad \text{for} \quad i = 1, 2, \ldots, n_{\text{mart}}, \tag{5.32}$$

is obtained, where $\underline{\Delta}(\bullet)$ represents the Laplacian $\text{div}(\text{grad}(\bullet))$, respectively. The constitutive relation $(5.7)_2$ results in

$$\boldsymbol{\xi}_i = \frac{3}{2}\gamma\,l\boldsymbol{\nabla}\varphi_i \tag{5.33}$$

considering Eq. (5.31). The corresponding von Neumann and Dirichlet boundary conditions acting on the disjointed boundary surfaces are

$$\boldsymbol{\xi}_i \cdot \boldsymbol{n} = \underline{\xi}_i \quad \text{on} \quad \partial\mathcal{B}_\xi, \tag{5.34}$$

$$\varphi_i = \underline{\varphi}_i \quad \text{on} \quad \partial\mathcal{B}_{\varphi_i}, \tag{5.35}$$

$$\varphi_i|_{t=0} = \varphi_{0,i} \quad \text{in} \quad \mathcal{B}. \tag{5.36}$$

In order to achieve compatibility,

$$\underline{\varphi}_i\big|_{t=0} = \varphi_{0,i} \quad \text{on} \quad \partial\mathcal{B}_{\varphi_i}, \tag{5.37}$$

is additionally required. The mechanical quantities are coupled to the phase field via the elastic energy potential. According to Eq. (3.27), the mechanical stress $\boldsymbol{\sigma}$ has to satisfy

$$\text{div}\boldsymbol{\sigma} = \mathbf{0}$$

with the constitutive relation $(5.7)_1$

$$\boldsymbol{\sigma} = \frac{\partial \psi}{\partial \boldsymbol{\varepsilon}} = \boldsymbol{\mathcal{C}}\left(\boldsymbol{\varepsilon} - \boldsymbol{\varepsilon}^0\right).$$

Note that Eq. (3.27) is a simplification of Cauchy's first equation of motion (3.23), which neglects inertia effects and volume forces such as gravity. The corresponding von Neumann and Dirichlet boundary conditions are

$$\boldsymbol{t} = \boldsymbol{\sigma}\,\boldsymbol{n} = \underline{\boldsymbol{t}} \quad \text{on} \quad \partial\mathcal{B}_\sigma, \tag{5.38}$$

$$\boldsymbol{u} = \underline{\boldsymbol{u}} \quad \text{on} \quad \partial\mathcal{B}_{\boldsymbol{u}}, \tag{5.39}$$

respectively, where $\partial\mathcal{B}_\sigma$ and $\partial\mathcal{B}_{\boldsymbol{u}}$ are the disjointed boundary surfaces.

5.2. Finite Element Implementation

The finite element formulation is obtained by inserting shape functions into the weak forms of the mechanical force balance and the evolution equation for the phase field. After evaluating the integrals of the weak forms, a vector-matrix formulation is obtained, which can be solved with the help of computers. The explanations in this section are limited to the two-dimensional plane strain case, since three-dimensional implementation is straightforward. The spatial discretization is done with four noded quadrilateral elements. In addition, the time integration scheme is presented, which is required by the presence of transient term $\dot{\varphi}$.

5.2.1. Weak Forms and Spatial Discretization

In order to obtain the weak forms, the procedure of Galerkin is applied. Accordingly, the field Eqs. (5.32) and (3.27) are scalar multiplied by the corresponding virtual test function $\delta\varphi_i$ and $\delta\boldsymbol{u}$, respectively, and integrated over the domain $\mathcal{B}$. The application of partial integration, taking into account the respective boundary conditions, finally leads to the weak forms

$$\int_{\mathcal{B}} \delta\varphi_i \left(\frac{1}{M}\dot{\varphi}_i + \frac{\partial\psi^{\mathrm{el}}}{\partial\varphi_i} + 12\frac{\gamma}{l}\frac{\partial f^{\mathrm{int}}}{\partial\varphi_i} + \Delta g\frac{\partial f^{\mathrm{bulk}}}{\partial\varphi_i} \right)$$
$$+ \frac{3}{2}\gamma\, l\, (\boldsymbol{\nabla}\delta\varphi_i) \cdot (\boldsymbol{\nabla}\varphi_i)\ dV = \int_{\partial\mathcal{B}_\xi} \delta\varphi\,\underline{\xi}\, dA \qquad (5.40)$$

and

$$\int_{\mathcal{B}} (\boldsymbol{\nabla}\delta\boldsymbol{u})^T : \boldsymbol{\sigma}\, dV = \int_{\partial\mathcal{B}_\sigma} \delta\boldsymbol{u} \cdot \underline{\boldsymbol{t}}\, dA. \qquad (5.41)$$

In Eqs. (5.40) and (5.41), the left hand sides represent the first variation of internal potential and right hand sides the first variation of the external potential. In this work, only cases with $\underline{\boldsymbol{t}} = \boldsymbol{0}$ and $\underline{\xi} = 0$ are considered, which is why these terms are not considered further. With the symmetry of the Cauchy stress $\boldsymbol{\sigma}$ and the definition of the symmetrical linearized strain tensor $\boldsymbol{\varepsilon}$, the relation

$$(\boldsymbol{\nabla}\delta\boldsymbol{u})^T : \boldsymbol{\sigma} = \delta\boldsymbol{\varepsilon} : \boldsymbol{\sigma} \qquad (5.42)$$

holds.

The geometric region $\mathcal{B}$ is approximated by n_{fe} elements and the assembly of the system is described by

$$\mathcal{B} \approx \bigcup_{e=1}^{n_{\mathrm{fe}}} \mathcal{B}_e, \qquad (5.43)$$

where $\mathcal{B}_e$ occupies the element domain. Using the following equations, the displacement $\boldsymbol{u}$ as well as the order parameters φ_i and their rates $\dot{\varphi}_i$ are approximated element wise,

$$\boldsymbol{u} \approx \sum_{I=1}^{n_{\mathrm{n}}} N_I\hat{\boldsymbol{u}}_I, \qquad \varphi_i \approx \sum_{I=1}^{n_{\mathrm{n}}} N_I\hat{\varphi}_{i,I}, \qquad \dot{\varphi}_i \approx \sum_{I=1}^{n_{\mathrm{n}}} N_I\dot{\hat{\varphi}}_{i,I}. \qquad (5.44)$$

Here, N_I is the bilinear shape function at node I, which interpolates the nodal values and n_{n} is the total number of nodes per element. The superimposed hat $(\hat{\bullet})$ indicates nodal quantities.

Using the Voigt notation, denoted by $(\bullet)^{\mathrm{V}}$, the gradient quantities are approximated with the differential operator matrices

$$\boldsymbol{B}_I^{\boldsymbol{u}} = \begin{pmatrix} \frac{\partial N_I}{\partial x} & 0 \\ 0 & \frac{\partial N_I}{\partial y} \\ \frac{\partial N_I}{\partial y} & \frac{\partial N_I}{\partial x} \end{pmatrix} \quad \text{and} \quad \boldsymbol{B}_I^{\varphi_i} = \begin{pmatrix} \frac{\partial N_I}{\partial x} \\ \frac{\partial N_I}{\partial y} \end{pmatrix} \tag{5.45}$$

by

$$\boldsymbol{\varepsilon}^{\mathrm{V}} \approx \sum_{I=1}^{n_{\mathrm{n}}} \boldsymbol{B}_I^{\boldsymbol{u}} \hat{\boldsymbol{u}}_I \quad \text{and} \quad \boldsymbol{\nabla}\varphi_i \approx \sum_{I=1}^{n_{\mathrm{n}}} \boldsymbol{B}_I^{\varphi_i} \hat{\varphi}_{i,I}. \tag{5.46}$$

Analogously, the virtual field variables

$$\delta\varphi_i \approx \sum_{I=1}^{n_{\mathrm{n}}} N_I \hat{\delta\varphi}_{i,I}, \qquad \boldsymbol{\nabla}\delta\varphi_i \approx \sum_{I=1}^{n_{\mathrm{n}}} \boldsymbol{B}_I^{\varphi_i} \hat{\delta\varphi}_{i,I},$$

$$\delta\boldsymbol{\varepsilon}^{\mathrm{V}} \approx \sum_{I=1}^{n_{\mathrm{n}}} \boldsymbol{B}_I^{\boldsymbol{u}} \hat{\delta\boldsymbol{u}}_I \tag{5.47}$$

are approximated. Applying discretization to the weak forms by inserting Eqs. (5.44), (5.46) and (5.47) in Eqs. (5.40) and (5.41) yields the discrete forms

$$\bigcup_{e=1}^{n_{\mathrm{fe}}} \sum_{I=1}^{n_{\mathrm{n}}} \hat{\delta\varphi}_{i,I} R_{e,I}^{\varphi_i} = 0 \tag{5.48}$$

and

$$\bigcup_{e=1}^{n_{\mathrm{fe}}} \sum_{I=1}^{n_{\mathrm{n}}} (\hat{\delta\boldsymbol{u}}_I)^T \boldsymbol{R}_{e,I}^{\boldsymbol{u}} = 0 \tag{5.49}$$

with the nodal residuals

$$R_{e,I}^{\varphi_i} = -\int_{\mathcal{B}_e} \left[\frac{N_I}{M} \dot{\varphi}_i + N_I \left(\frac{\partial \psi^{\mathrm{el}}}{\partial \varphi_i} + 12\frac{\gamma}{l}\frac{\partial f^{\mathrm{int}}}{\partial \varphi_i} + \Delta g\frac{\partial f^{\mathrm{bulk}}}{\partial \varphi_i} \right) + (\boldsymbol{B}_I^{\varphi_i})^T \boldsymbol{\xi}_i \right] dV \tag{5.50}$$

and

$$\boldsymbol{R}_{e,I}^{\boldsymbol{u}} = -\int_{\mathcal{B}_e} (\boldsymbol{B}_I^{\boldsymbol{u}})^T \boldsymbol{\sigma}^{\mathrm{V}} \, dV. \tag{5.51}$$

According to the fundamental theorem of the calculus of variations, Eqs. (5.48) and (5.49) hold, if $\boldsymbol{R}_{e,I}^{\boldsymbol{u}} = \boldsymbol{0}$ and $R_{e,I}^{\varphi_i} = 0$.

In order to obtain the global residual vector $\boldsymbol{R}$, the nodal residuals are collected in the vector

$$\boldsymbol{R}_{e,I} = \left((\boldsymbol{R}_I^{\boldsymbol{u}})^T, \ R_I^{\varphi_i}, \ \cdots, \ R_I^{\varphi_{n_{\mathrm{mart}}}} \right)^T. \tag{5.52}$$

It depends on the nodal degrees of freedom

$$\hat{\boldsymbol{d}}_{e,I} = \left(\hat{\boldsymbol{u}}^T, \ \hat{\varphi}_i, \ \cdots, \ \hat{\varphi}_{n_{\mathrm{mart}}} \right)_{e,I}^T \tag{5.53}$$

and their rates. The residual vector for an element is then

$$\boldsymbol{R}_e = \left((\boldsymbol{R}_{e,I})^T, \;\; \cdots, \;\; (\boldsymbol{R}_{e,n_{\mathrm{n}}})^T \right)^T. \tag{5.54}$$

Assembling the element residuals yields the global residual vector

$$\boldsymbol{R}(\hat{\boldsymbol{d}}, \dot{\hat{\boldsymbol{d}}}) = \bigcup_{e=1}^{n_{\mathrm{fe}}} \boldsymbol{R}_e. \tag{5.55}$$

5.2.2. Temporal Discretization

In order to solve the time-dependent model numerically, the continuous course of time is evaluated at discrete time steps. Therefore, in each time step $t_n \to t_{n+1}$, the nonlinear system of equations

$$\boldsymbol{R}_{n+1} = \boldsymbol{0}, \tag{5.56}$$

needs to be solved, which is typically rewritten as

$$\boldsymbol{R}_{n+1} = \tilde{\boldsymbol{F}}_{n+1} - \tilde{\boldsymbol{P}}(\hat{\boldsymbol{d}}_{n+1}, \dot{\hat{\boldsymbol{d}}}_{n+1}) = \boldsymbol{0}, \tag{5.57}$$

where $\tilde{\boldsymbol{F}}_{n+1}$ represents the external (prescribed) force contributions and $\tilde{\boldsymbol{P}}$ represents the internal forces. Note that in Eqs. (5.50) and (5.50) only the internal force vector $\tilde{\boldsymbol{P}}$ is present, which is due to the choice of boundary conditions $\underline{\boldsymbol{t}} = \boldsymbol{0}$ and $\underline{\xi} = 0$. In order to solve Eq. (5.57), the fully implicit backward Euler scheme is applied. Accordingly, the time derivate of the nodal degrees of freedom $\dot{\hat{\boldsymbol{d}}}_{n+1}$ is approximated by

$$\dot{\hat{\boldsymbol{d}}}_{n+1} \approx \frac{\hat{\boldsymbol{d}}_{n+1} - \hat{\boldsymbol{d}}_n}{\Delta t_n}. \tag{5.58}$$

With this approximation, $\tilde{\boldsymbol{P}}$ is a function of the known degrees of freedom $\hat{\boldsymbol{d}}_n$ and the unknown degrees of freedom $\hat{\boldsymbol{d}}_{n+1}$, i.e. $\tilde{\boldsymbol{P}}(\hat{\boldsymbol{d}}_n, \hat{\boldsymbol{d}}_{n+1})$. The solution for $\hat{\boldsymbol{d}}_{n+1}$ is obtained iteratively by means of the Newton-Raphson method. With the initial guess $\hat{\boldsymbol{d}}_{n+1}^{(0)} = \hat{\boldsymbol{d}}_n$, the solution for the next iteration step is updated with

$$\hat{\boldsymbol{d}}_{n+1}^{(k+1)} = \hat{\boldsymbol{d}}_{n+1}^{(k)} + \Delta\hat{\boldsymbol{d}}_{n+1}^{(k)}, \tag{5.59}$$

where the superscript $(\bullet)^{(k)}$ denotes the iteration step. In Eq. (5.59), $\Delta\hat{\boldsymbol{d}}_{n+1}^{(k)}$ is determined by linearization of the residual equation

$$\boldsymbol{R}_{n+1}^{(k+1)} \approx \boldsymbol{R}_{n+1}^{(k)} - \tilde{\boldsymbol{S}}_{n+1}^{(k)}\Delta\hat{\boldsymbol{d}}_{n+1}^{(k)} = \boldsymbol{0} \quad \text{with} \quad \tilde{\boldsymbol{S}}_{n+1}^{(k)} = \frac{\partial\tilde{\boldsymbol{P}}(\hat{\boldsymbol{d}}_n, \hat{\boldsymbol{d}}_{n+1}^{(k)})}{\partial\hat{\boldsymbol{d}}_{n+1}^{(k)}}, \tag{5.60}$$

where $\tilde{\boldsymbol{S}}$ is the system matrix. If the residual (5.60) vanishes with a given precision, the solution is found. With reference to the approximation of transient terms, the system matrix can be determined by total derivation according to

$$\tilde{\boldsymbol{S}}_{n+1} = \frac{\partial\tilde{\boldsymbol{P}}(\hat{\boldsymbol{d}}_n, \hat{\boldsymbol{d}}_{n+1})}{\partial\hat{\boldsymbol{d}}_{n+1}} = \frac{d\tilde{\boldsymbol{P}}(\hat{\boldsymbol{d}}_{n+1}, \dot{\hat{\boldsymbol{d}}}_{n+1})}{d\hat{\boldsymbol{d}}_{n+1}} =$$
$$\frac{\partial\tilde{\boldsymbol{P}}(\hat{\boldsymbol{d}}_{n+1}, \dot{\hat{\boldsymbol{d}}}_{n+1})}{\partial\hat{\boldsymbol{d}}_{n+1}} + \frac{1}{\Delta t}\frac{\partial\tilde{\boldsymbol{P}}(\hat{\boldsymbol{d}}_{n+1}, \dot{\hat{\boldsymbol{d}}}_{n+1})}{\partial\dot{\hat{\boldsymbol{d}}}_{n+1}}. \tag{5.61}$$

With suppression of time step index, Eq. (5.61) can be rewritten in compact form

$$\tilde{S} = \tilde{K} + \frac{1}{\Delta t} \tilde{D} \tag{5.62}$$

with the global stiffness matrix

$$\tilde{K} = \frac{\partial \tilde{P}}{\partial \hat{d}} \tag{5.63}$$

and the global damping matrix

$$\tilde{D} = \frac{\partial \tilde{P}}{\partial \dot{\hat{d}}}. \tag{5.64}$$

As the residuals, these matrices are calculated on element level. Accordingly, the stiffness matrix $\tilde{K}_{e,IJ}$ is defined with

$$\tilde{K}_{e,IJ} = \begin{pmatrix} \tilde{K}^{uu} & \tilde{K}^{u\varphi_1} & \cdots & \tilde{K}^{u\varphi_i} & \cdots & \tilde{K}^{u\varphi_{n_{\mathrm{mart}}}} \\ \tilde{K}^{\varphi_1 u} & \tilde{K}^{\varphi_1\varphi_1} & \cdots & \tilde{K}^{\varphi_1\varphi_i} & \cdots & \tilde{K}^{\varphi_1\varphi_{n_{\mathrm{mart}}}} \\ \vdots & \vdots & \ddots & \vdots & \ddots & \vdots \\ \tilde{K}^{\varphi_i u} & \tilde{K}^{\varphi_i\varphi_1} & \cdots & \tilde{K}^{\varphi_i\varphi_i} & \cdots & \tilde{K}^{\varphi_i\varphi_{n_{\mathrm{mart}}}} \\ \vdots & \vdots & \ddots & \vdots & \ddots & \vdots \\ \tilde{K}^{\varphi_{n_{\mathrm{mart}}} u} & \tilde{K}^{\varphi_{n_{\mathrm{mart}}}\varphi_1} & \cdots & \tilde{K}^{\varphi_{n_{\mathrm{mart}}}\varphi_i} & \cdots & \tilde{K}^{\varphi_{n_{\mathrm{mart}}}\varphi_{n_{\mathrm{mart}}}} \end{pmatrix}_{e,IJ}, \tag{5.65}$$

where the matrix entries are given by the derivative of the internal forces at node I with respect to the nodal degrees of freedom at node J. With

$$\tilde{\sigma}_i = (\boldsymbol{C}_i^\alpha - \boldsymbol{C}^\gamma)(\boldsymbol{\varepsilon} - \boldsymbol{\varepsilon}^0) - \boldsymbol{C}\,\tilde{\boldsymbol{\varepsilon}}_i \tag{5.66}$$

the following matrix entries are found:

$$\tilde{K}^{uu}_{e,IJ} = \frac{\partial \tilde{P}^u_{e,I}}{\partial \hat{u}_J} = \int_{\mathcal{B}_e} (\boldsymbol{B}^u_I)^T \boldsymbol{C}^{\mathrm{V}} \boldsymbol{B}^u_J \, dV, \tag{5.67}$$

$$\tilde{K}^{u\varphi_i}_{e,IJ} = \frac{\partial \tilde{P}^u_{e,I}}{\partial \hat{\varphi}_{i,J}} = \int_{\mathcal{B}_e} (\boldsymbol{B}^u_I)^T \frac{\partial h_i}{\partial \varphi_i} \tilde{\sigma}^{\mathrm{V}}_i N_J \, dV \tag{5.68}$$

$$\tilde{K}^{\varphi_i u}_{e,IJ} = \left(\tilde{K}^{u\varphi_i}_{e,IJ} \right)^T, \tag{5.69}$$

$$\tilde{K}^{\varphi_i\varphi_i}_{e,IJ} = \frac{\partial \tilde{P}^{\varphi_i}_{e,I}}{\partial \hat{\varphi}_{i,J}} = \int_{\mathcal{B}_e} N_I \left(\frac{\partial^2 \psi^{\mathrm{el}}}{\partial \varphi_i^2} + 12 \frac{\gamma}{l} \frac{\partial^2 f^{\mathrm{int}}}{\partial \varphi_i^2} + \Delta g \frac{\partial^2 f^{\mathrm{bulk}}}{\partial \varphi_i^2} \right) N_J$$
$$+ \frac{3}{2} \gamma \, l \, (\boldsymbol{B}^{\varphi_i}_I)^T \boldsymbol{B}^{\varphi_i}_J \, dV, \tag{5.70}$$

$$\tilde{K}^{\varphi_i\varphi_j}_{e,IJ} = \frac{\partial \tilde{P}^{\varphi_i}_{e,I}}{\partial \hat{\varphi}_{j,J}} = \int_{\mathcal{B}_e} N_I \left(\frac{\partial^2 \psi^{\mathrm{el}}}{\partial \varphi_j \partial \varphi_i} + 12 \frac{\gamma}{l} \frac{\partial^2 f^{\mathrm{int}}}{\partial \varphi_j \partial \varphi_i} + \Delta g \frac{\partial^2 f^{\mathrm{bulk}}}{\partial \varphi_j \partial \varphi_i} \right) N_J \, dV, \tag{5.71}$$

$$\tilde{K}^{\varphi_j\varphi_i}_{e,IJ} = \tilde{K}^{\varphi_i\varphi_j}_{e,IJ}. \tag{5.72}$$

Note the symmetry of $\tilde{K}_{e,IJ}$. The corresponding damping matrix reads

$$\tilde{D}_{e,IJ} = \frac{\partial \tilde{P}_{e,I}}{\partial \dot{\hat{d}}_J} = \frac{1}{M} \int_{\mathcal{B}_e} N_I N_J \, dV \begin{pmatrix} \boldsymbol{0}^{(2\times 2)} & \boldsymbol{0}^{(2\times n_{\mathrm{mart}})} \\ \boldsymbol{0}^{(n_{\mathrm{mart}}\times 2)} & \boldsymbol{I}^{(n_{\mathrm{mart}}\times n_{\mathrm{mart}})} \end{pmatrix}. \tag{5.73}$$
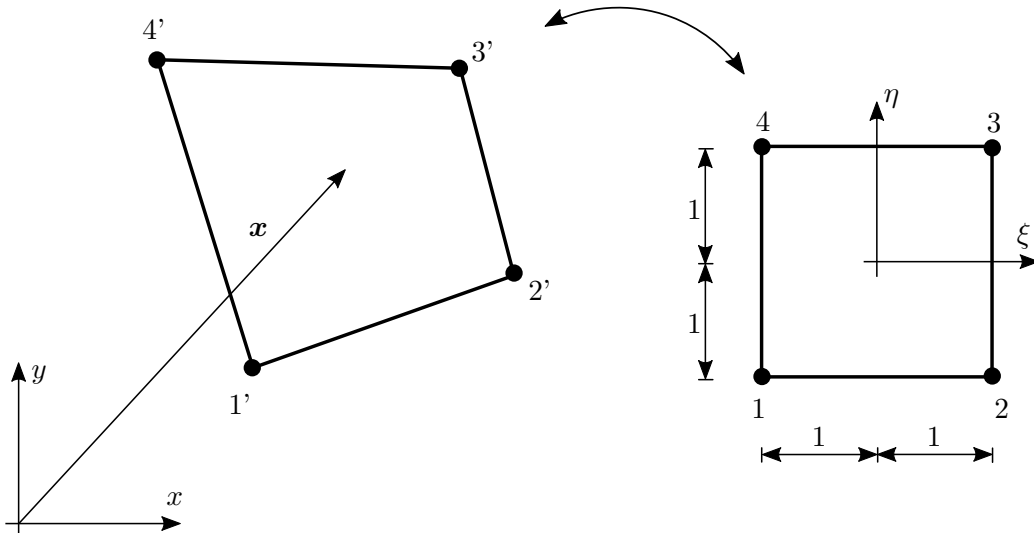
Figure 5.3: Isoparametric quadrilateral element with four nodes

5.2.3. Isoparametric Representation and Numerical Quadrature

In order to approximate an arbitrary geometry with quadrilateral elements, the isoparametric concept is used. The integrals are evaluated with Gauss quadrature. Both are established methods in the context of the finite element method. For the sake of completeness, they are nevertheless briefly described.

When applying the isoparametric concept, the same shape functions are used as for the degrees of freedom. For two-dimensional quadrilateral elements, the shape functions are defined element wise as function of natural coordinates ξ and η in the unit space $[-1, 1] \times [-1, 1]$ in order to simplify the numerical implementation, see Fig. 5.3. Accordingly, the bilinear Lagrangian shape functions are

$$N_I(\xi, \eta) = \frac{1}{4}(1 + \hat{\xi}_I\,\xi)(1 + \hat{\eta}_I\,\eta), \quad I = 1, \ldots, 4. \tag{5.74}$$

The physical coordinates within an element are approximated by the mapping

$$\boldsymbol{x} \approx \sum_{I=1}^{n_{\mathrm{n}}} N_I(\xi, \eta)\hat{\boldsymbol{x}}_I. \tag{5.75}$$

Thus, the spatial position within an element can be expressed using the natural coordinates. Applying the chain rule differentiation yields

$$\frac{\partial N_I}{\partial \xi} = \frac{\partial N_I}{\partial x}\frac{\partial x}{\partial \xi} + \frac{\partial N_I}{\partial y}\frac{\partial y}{\partial \xi}, \tag{5.76}$$

$$\frac{\partial N_I}{\partial \eta} = \frac{\partial N_I}{\partial x}\frac{\partial x}{\partial \eta} + \frac{\partial N_I}{\partial y}\frac{\partial y}{\partial \eta}, \tag{5.77}$$

which can be expressed in matrix notation

$$\begin{pmatrix} \frac{\partial N_I}{\partial \xi} \\ \frac{\partial N_I}{\partial \eta} \end{pmatrix} = \boldsymbol{J}\begin{pmatrix} \frac{\partial N_I}{\partial x} \\ \frac{\partial N_I}{\partial y} \end{pmatrix} \quad \text{with} \quad \boldsymbol{J} = \begin{pmatrix} \frac{\partial x}{\partial \xi} & \frac{\partial y}{\partial \xi} \\ \frac{\partial x}{\partial \eta} & \frac{\partial y}{\partial \eta} \end{pmatrix}, \tag{5.78}$$

where $\boldsymbol{J}$ is the Jacobian matrix, which links the derivatives with respect to natural coordinates and the derivatives with respect to the global physical coordinates. Using the approximation of the geometry (5.75), the Jacobian matrix can be determined with

$$\boldsymbol{J} = \sum_{I=1}^{n_{\mathrm{n}}} \begin{pmatrix} \frac{\partial N_I}{\partial \xi} \hat{x}_I & \frac{\partial N_I}{\partial \xi} \hat{y}_I \\ \frac{\partial N_I}{\partial \eta} \hat{x}_I & \frac{\partial N_I}{\partial \eta} \hat{y}_I \end{pmatrix}. \tag{5.79}$$

In the following, the integrals, which form the element residuals, the stiffness matrix as well as the damping matrix are represented by

$$\int_{\mathcal{B}_e} q(x, y) \, dV, \tag{5.80}$$

where $q(\xi, \eta)$ is a placeholder function. With regard to the reference element in natural coordinates, this integral must be transformed accordingly. In the isoparametric concept with the corresponding shape functions, this is done with

$$\int_{\mathcal{B}_e} q(x, y) \, dV = \int_{-1}^{1} \int_{-1}^{1} q(\xi, \eta) \, \det \boldsymbol{J}(\xi, \eta) \, d\xi \, d\eta. \tag{5.81}$$

The numerical evaluation using the Gauss quadrature is then computed with

$$\int_{-1}^{1} \int_{-1}^{1} q(\xi, \eta) \, \det \boldsymbol{J}(\xi, \eta) \, d\xi \, d\eta \approx \sum_{p=1}^{n_{\mathrm{int}}} q(\xi_p, \eta_p) \, \det \boldsymbol{J}(\xi_p, \eta_p) w_q, \tag{5.82}$$

where n_{int} is the total number of Gauss points, with their respective positions ξ_p and η_p and weights w_q. For the specific values, reference is made to Zienkiewicz et al. (2005). In this work, the Gauss quadrature is performed with 2×2 integration points.

5.2.4. Irreversibility of Martensite Transformation

When simulating martensite transformation, it may be of interest to suppress a transformation from one martensite variant to another. To implement this, a method presented by Kuhn (2013) is used, which introduces an irreversibility in the fashion of Dirichlet boundary conditions. The procedure adapted to the problem at hand is described in the following, whereby Kuhn (2013) is strongly followed.

Once a martensite variant is fully transformed, a constraint is imposed to prevent re-transformation. In the time-discretized setting, this leads to

$$\underline{\varphi}_{i,I,n+1} = 1 \quad \text{if} \quad \hat{\varphi}_{i,I,n} > 1 - \epsilon_{\mathrm{irr}}, \tag{5.83}$$

where ϵ_{irr} is a numerical tolerance. In order to fulfill this requirement, in each iteration step (k) the value of $\hat{\varphi}_{i,I,n+1}^{(k+1)}$ must be one, if $\hat{\varphi}_{i,I,n} > 1 - \epsilon_{\mathrm{irr}}$ is detected in the previous time step. This is achieved by modifying the element system matrix $\tilde{\boldsymbol{S}}_e$ and the residuals $\boldsymbol{R}_e$. The individual steps of the modification are described below, whereby these steps are carried out for each martensite variant.

1. The column $\tilde{\boldsymbol{S}}_e^{[:,\hat{\varphi}_{i,I}]}$ referring to $\hat{\varphi}_{i,I}$ is multiplied with difference $(1 - \hat{\varphi}_{i,I,n})$ and added to the residual:

$$\boldsymbol{R}_e \leftarrow \boldsymbol{R}_e + (1 - \hat{\varphi}_{i,I,n+1}^{(k)}) \tilde{\boldsymbol{S}}_e^{[:,\hat{\varphi}_{i,I}]}$$

2. The residual entry $\boldsymbol{R}_e^{[\hat{\varphi}_{i,I}]}$ referring to $\hat{\varphi}_{i,I}$ is overwritten with difference $(1 - \hat{\varphi}_{i,I,n+1}^{(k)})$:

$$\boldsymbol{R}_e^{[\hat{\varphi}_{i,I}]} = 1 - \hat{\varphi}_{i,I,n+1}^{(k)}$$

3. The row $\tilde{\boldsymbol{S}}_e^{[:,\hat{\varphi}_{i,I}]}$ and column $\tilde{\boldsymbol{S}}_e^{[\hat{\varphi}_{i,I},:]}$ are overwritten with zeros:

$$\tilde{\boldsymbol{S}}_e^{[:,\hat{\varphi}_{i,I}]} = 0$$
$$\tilde{\boldsymbol{S}}_e^{[\hat{\varphi}_{i,I},:]} = 0$$

4. The matrix entry $\tilde{\boldsymbol{S}}_e^{[\hat{\varphi}_{i,I},\hat{\varphi}_{i,I}]}$ is overwritten with one:

$$\tilde{\boldsymbol{S}}_e^{[\hat{\varphi}_{i,I},\hat{\varphi}_{i,I}]} = 1$$

Using this manipulation, the system of Eqs. (5.60) yield a solution $\Delta \hat{\boldsymbol{d}}_{I,n+1}^{(k)}$ with

$$\Delta \hat{\varphi}_{i,I,n+1}^{(k)} = 1 - \hat{\varphi}_{i,I,n+1}^{(k)}, \tag{5.84}$$

which means that for the update

$$\hat{\varphi}_{i,I,n+1}^{(k+1)} = \hat{\varphi}_{i,I,n+1}^{(k)} + \Delta \hat{\varphi}_{i,I,n+1}^{(k)} = 1 \tag{5.85}$$

the value one is obtained. Unless otherwise noted, irreversibility is deactivated in the following studies.

5.3. Generation of Prior Austenite Grain Structure

As the current work is concerned with the martensite transformation in an austenitic matrix, a necessary input quantity is the PAG structure. A physically reasonable way would be to use of a physically based model, which describes the austenitization process. Such a model would be computationally demanding and is outside the scope of this work. However, by means of the orientation relationship between austenite and martensite it is possible to reconstruct the austenitic structure based on the measured martensitic structure, see e.g. Nyyssönen et al. (2018) and Cayron (2007). The validity of such reconstructions can be seen in the work of Brandl et al. (2019), where the reconstruction shows good agreement with high temperature EBSD measurements in a PH 15-5 with austenite memory effect.

With reconstructed and present austenite structures, several options are conceivable to use the data as input to the simulation. The first option is a direct reproduction and discretization of the reconstructed austenite structure. In the martensite phase field context this was done by Graf et al. (2021a,c) and Schmidt et al. (2018). This approach has the limitation that microstructural features cannot be varied. The systematic influence of microstructural features such as austenite grain size is thus difficult to analyze. Furthermore, in this work only two-dimensional EBSD data is available, which limits the reproduction to two dimensions. In principle, three-dimensional measurements could be obtained by sequentially ablating and measuring the surface. However, this procedure is extremely elaborate and costly. Concerning martensite, only one paper is known in which three-dimensional data were generated (Morito et al. (2013)).

Table 5.1: Statistics of austenite grain structure in material 50CrMo4

Experiment No.,	Equivalent grain diameter d_{eq}		Circularity $1 - s^{2\mathrm{D}}$	
see Sec. 4	mean in μm	stdev in μm	mean	stdev
A1	7.8	5.1	0.16	0.084
A2	9.4	5.8	0.16	0.082
A3	8.7	6.3	0.17	0.099
A4	8.4	5.4	0.15	0.086
Average	8.6	5.7	0.16	0.088

With some loss of physical justification and geometric information, geometric models provide an efficient alternative. Such approaches use mathematical tessellation techniques to generate polycrystalline structures, which are used in this work to generate the austenitic structure. The basic principle of this generation is briefly described here, whereas for further details reference is made from Kuhn et al. (2020). The implementation of the synthetic generation in the script-based work-flow in this work was supported by Steinmetz (2020).

Focusing on convex grains, Voronoi tessellation is a popular technique, see e.g. Fritzen et al. (2009); Quey et al. (2011). Here, the tessellation of space is determined by a set of seed points. For each seed point, a corresponding cell is formed that encompasses all points that are closer to the seed point of the considered region than to any other seed point. This corresponds to a simple model for homogeneous and isotropic grain growth. However, it has been empirically shown that Voronoi structures are generally unsuitable to reproduce microstructures with realistic grain size distributions (Döbrich et al. (2004); Luther & Könke (2009)). Laguerre tessellations, on the other hand, satisfy the requirements by grain size distributions in microstructures. In this tessellation technique, a positive scalar weight is assigned to each seed point. With appropriate adjustment of the weights, the size distribution can be influenced. In combination with suitable optimization algorithms, structures are found that statistically represent the experimentally observed microstructure. In the recent work of Kuhn et al. (2020), various algorithms are presented and compared in this regard.

In this work the open-source software toolkit Neper (Quey et al. (2011); Quey & Renversade (2018); Quey (2019)) is used to generate PAG structures of the in Sec. 4 analyzed material 50CrMo4.

5.3.1. Statistical Description of Microstructures

Usually polycrystalline morphologies are described in terms of their average grain sizes and grain size distributions (Quey & Renversade (2018)). In addition, the grain shape may also be relevant. With regard to the grain size description, the equivalent grain diameter according to Eq. (4.2),

$$d_{\mathrm{eq}} = 2\sqrt{\frac{A^{2\mathrm{D}}}{\pi}},$$

is used. Empirical studies have shown that grains sizes d_{eq} of materials that underwent grain boundary migration by capillarity effect follow a log-normal distribution. The grain size distribution of the austenitic structure in 50CrMo4 also corresponds to a log-normal

$$1 - s^{2\text{D}} = 0.3614$$
(a)

$$1 - s^{2\text{D}} = 0.0885$$
(b)

$$1 - s^{2\text{D}} = 0.0745$$
(c)
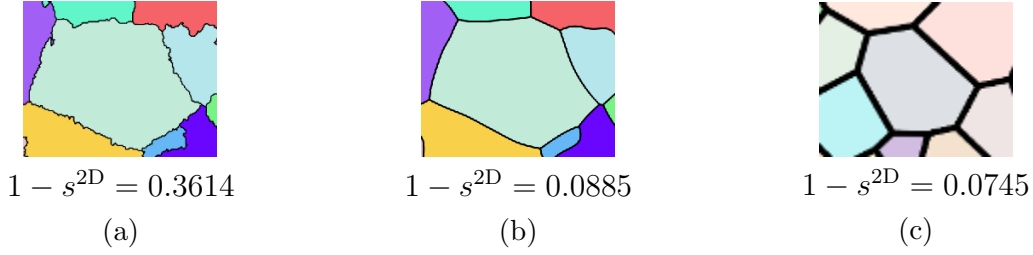
Figure 5.4: Comparison of exemplary form factors between (a) a raw data grain, (b) a smoothed grain, and (c) a synthetic grain

distribution.

The grain shape is described by form factor

$$s^{2\text{D}} = \frac{\pi \, d_{\text{eq}}}{p^{2\text{D}}}, \tag{5.86}$$

where $p^{2\text{D}}$ is the cross-section perimeter of the considered grain. The dimensionless form factor $s^{2\text{D}}$ is called circularity and lies between zero and one, where the value one represents a circular grain. From Spettl et al. (2014) and Quey & Renversade (2018) it is known that $1 - s^{2\text{D}}$ of experimental measured grains shapes follow a log-normal distribution. This is also a valid approximation of the distribution in the austenitic microstructure of 50CrMo4.

The probability density function of log-normal distribution of a generic quantity r is given by

$$f_{\text{r}}(r) = \frac{1}{r} \frac{1}{\sigma_{\text{r}} \sqrt{2 \, \pi}} \exp \left\{ -\frac{(\ln(r) - \mu_{\text{r}})^2}{2 \, \sigma_{\text{r}}} \right\}, \tag{5.87}$$

with logarithmic mean μ_{r} and logarithmic standard deviation σ_{r} as parameters. Mean and standard deviation are given by

$$\text{mean} = \exp \left\{ \mu_{\text{r}} + \tfrac{1}{2} \sigma_{\text{r}}^{\,2} \right\} \quad \text{and} \quad \text{stdev} = \exp \left\{ \mu_{\text{r}} + \tfrac{1}{2} \sigma_{\text{r}}^{\,2} \right\} \sqrt{\exp \left\{ \sigma_{\text{r}}^{\,2} \right\} - 1}. \tag{5.88}$$

5.3.2. Synthetic Austenite Grain Structure of Low-Alloy Steel 50CrMo4

The analysis of the microstructure generation parameters is performed based on the reconstructed austenitic microstructures of analyses A1-A4 in Sec. 4. Tab. 5.1 shows the determined statistical parameters. For the evaluation of circularity, a further intensive smoothing is performed. The reason for this can be seen from Fig. 5.4. This figure shows an example of a raw reconstructed grain, a smoothed grain and a synthetic grain with a similar shape and the respective shape factor. Due to the rough surface, the raw reconstructed grain has a significantly higher form factor compared to the synthetic grain. The rough surface of the grain is caused by measurement inaccuracies and the reconstruction. With smoothing of the rough surface, the circularity is reduced to a size in the order of the synthetic grain. Another effect is that the reconstructed grain structure approximates a convex grain structure, which is reproducible with the synthetic structure. The non-convexity of the reconstructed grains is mainly due to misindexing during reconstruction.
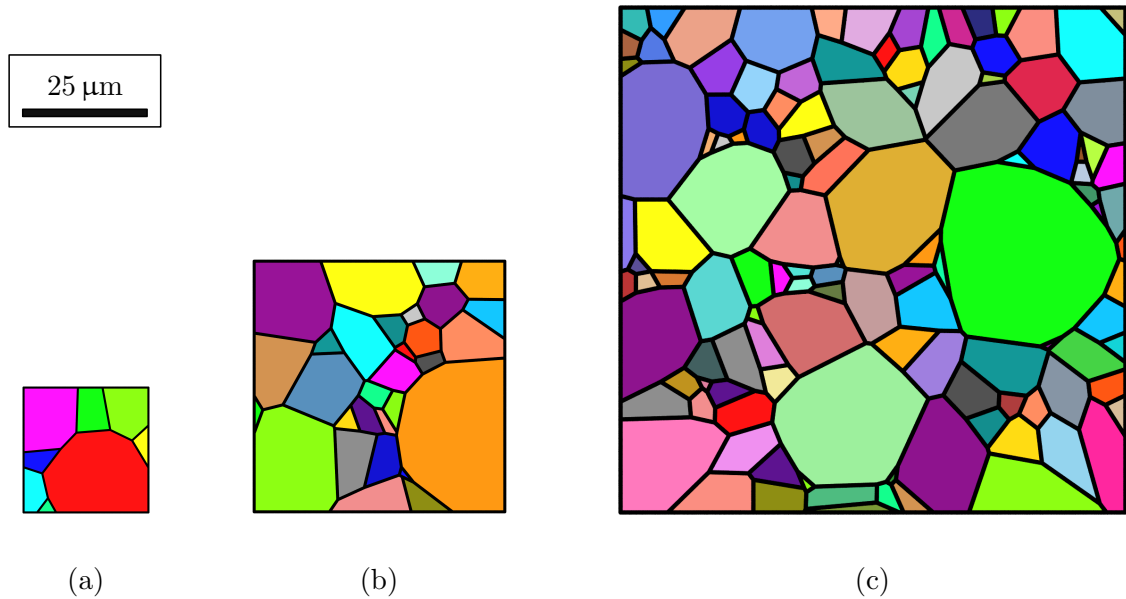
Figure 5.5: Synthetic microstructures of material 50CrMo4 with different sizes: (a) 25 μm, (b) 50 μm and (c) 100 μm
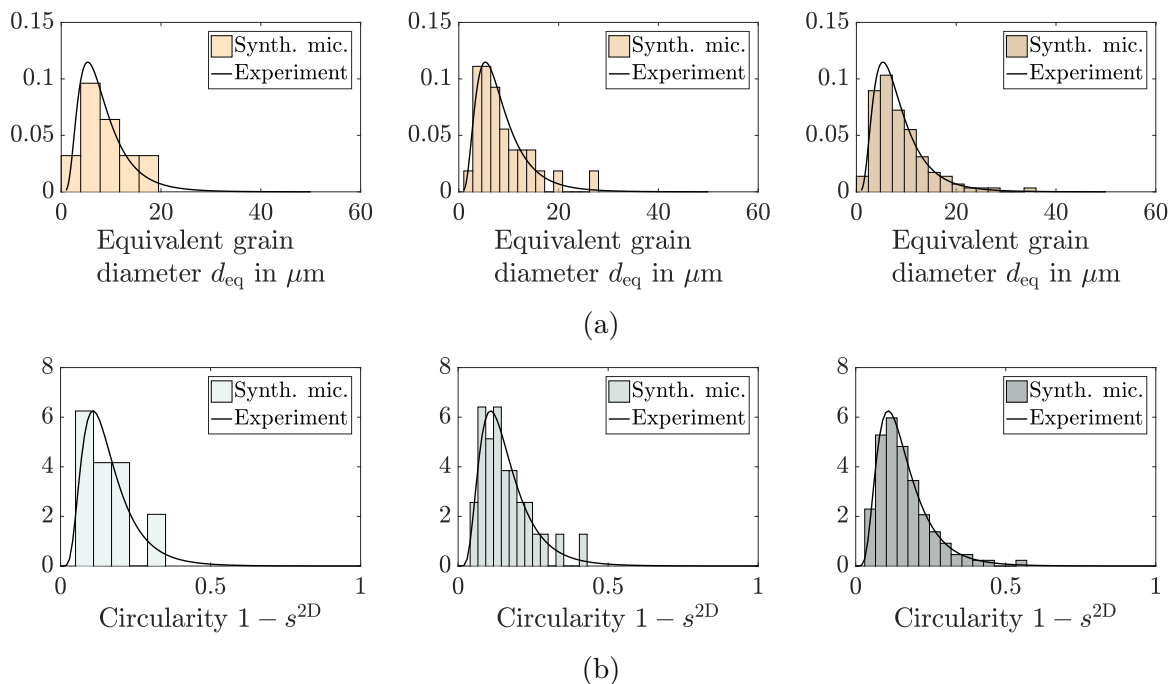
Figure 5.6: Statistics of synthetic microstructures in comparison with the experimental results, (a) probability density of equivalent grain diameter, (b) probability density of circularity

The average values in Tab. 5.1 of the four analyses are used to generate the synthetic microstructures. Fig. 5.5 shows exemplary morphologies with three different domain sizes: 25 μm, 50 μm and 100 μm. In Fig. 5.6 the histograms of the equivalent grain diameter and the circularity of the synthetic microstructures from Fig. 5.5 are shown. In addition, the probability density function of the experimental data is plotted. All microstructures

represent the experimental data. However, with larger domain size the data is reproduced more accurately. A disadvantage of the smallest domain size is that there is no complete grain in the bulk.

Another important criteria is the misorientation distribution. The misorientation between the grains results from the individual orientations of the grains. An analysis of the pole figures of the austenite structure reveals an isotropic distribution of the orientations present in the mircostructure. Accordingly, there is no texture and the orientations are randomly drawn from a uniform distribution.

5.3.3. Finite Element Meshing

In this work, a regular mesh is used to spatially discretize the tessellations generated above. This results in a pixelated representation of the austenite grain structure with loss of the smooth grain boundaries, which are approximated stepwise. The smaller the element size is chosen, the better the actual grain boundary is reproduced. The alternative would be an unstructured mesh where the grain boundaries could be represented as smooth boundary. With respect to the phase field martensite simulation, a detailed analysis of the influence of the meshing method is not known. From studies by Böhlke et al. (2010) and Zhang et al. (2015), however, it is known that the influence on the effective properties as well as the stress and strain distribution under mechanical load is negligible using a sufficient fine mesh. The meshes used here in the phase field context tend to be finer, so it is concluded that the use of structured meshes is permissible.
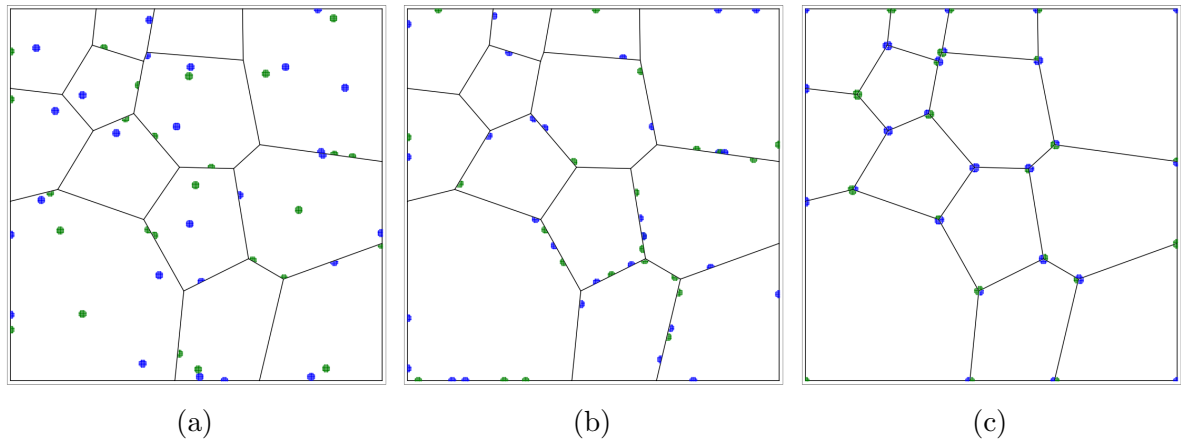
5.4. Nucleation Modeling

Regarding martensite nucleation, there seems to be a certain consensus that several types of defects or accompanying stress-fields promote martensite nucleation, see e.g. Sec. 2.4.2. However, the exact nature of martensite nucleation is not fully understood and is still the subject of current research, see e.g. Zhang et al. (2007), Song & De Cooman (2014), Wang et al. (2019). Within the phase field context, nucleation occurs when the system is locally brought out of the metastable state and the energetic barrier is overcome. All parameters, which influence the transformation path also have an impact on the nucleation behavior. For example, the required deviation from the metastable state increases with increasing interface energy parameter. In order to model the martensite nucleation in the current model, a distinction is made between two nucleation mechanisms: initial nucleation (Sec. 5.4.1), and auto-nucleation (Sec. 5.4.2). The implementation of the initial nucleation model in the script-based work-flow in this work was supported by Steinmetz (2020).

5.4.1. Initial Nucleation in Polycrystalline Structures

Assuming that pre-existing embryos of the product phase become super critical below T_{MS}, it could be shown empirically that martensite at T_{MS} occurs heterogeneously (Cech & Turnbull (1956); Kaufman & Cohen (1958); Löwy (2015)). Accordingly, the classical martensite nucleation theory describes a nucleus with the same structure as the fully transformed product, which increases in size due to a moving interface (Löwy (2015)). Regardless of the exact nature of nucleation, grain boundaries seem to play an important role in the initial martensite transformation in polycrystals, see e.g. Ueda et al. (2002, 2003); Furuhara et al. (2010); Song & De Cooman (2014).

Grain 1   Grain 2

— Geometric grain boundary
• Connecting nodes
○ Remaining nodes

— Geometric grain boundary
• Inner grain nodes
• Grain boundary nodes
• Triple junction nodes

(a)   (b)
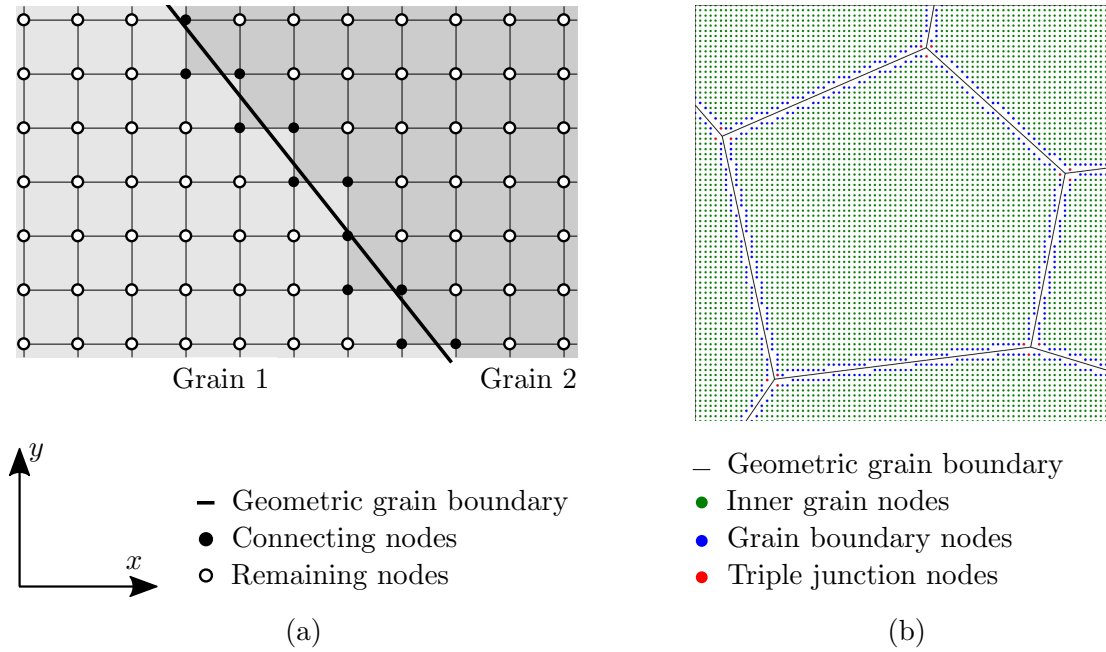
Figure 5.7: Mesh categorization, (a) connecting nodes (1) in a detailed view with element-wise grain assignment, (b) remaining categories (2-4) (without connecting nodes)

(a)   (b)   (c)

Figure 5.8: Example application of the two-dimensional nucleation model, nuclei radius to edge length ratio is 0.01, (a) 52 nucleation sides with about 50% at grain boundaries and 50% within grains, (b) 52 nucleation sides with 100% at grain boundaries, (c) full occupation of tripel junctions

In the context of martensite simulation using the phase field method, several methods are known to initiate martensite transformation. For example, Artemev et al. (2001) initiate the transformation by noising the order parameters in the initial time step, Yeddu et al. (2012b) define a pre-existing nucleus, and Zhang et al. (2007) define an initial dislocation loop. In addition, the martensite transformation can also be initiated by applying an external strain or stress, see e.g. Yeddu et al. (2013). With reference to the important role of grain boundaries in nucleation, a model was developed by Heo & Chen (2014) in which martensite transformation is initiated at grain boundaries. In this model, The austenite grain boundaries are described as a diffuse interface, which is coupled with

the martensite transformation strains. The martensite intrinsic strain are scaled down within the diffuse austenite-austenite boundaries, making the transformation in the grain boundaries more energetically favorable due to the lower strain energy. Initial nucleation is then triggered by noise and growth begins primarily at the grain boundaries. This model is applied, for example, in the works of Schoof et al. (2018a,b, 2019).

In this work, the initial nucleation is controlled by the order parameter by assigning a value $\varphi_i = 1$ (product phase) to nodes at individual heterogeneously distributed locations in the considered microstructure. For this purpose, the nodes of the generated mesh are assigned to three categories: (1) connecting nodes (2) inner grain nodes, (3) grain boundary nodes, (4) triple junction nodes. Connecting nodes are nodes which connect adjacent grains. These nodes are colored black in the exemplary illustration in Fig. 5.7(a) and are excluded from the assignment regarding the remaining categories, illustrated in Fig. 5.7(b). Inner grain nodes are all nodes within a grain, excluding the outermost nodes of each grain. Grain boundary nodes are the remaining outermost nodes of a grain, where the respective closest node to the geometric triple point is assigned to the triple point nodes.

The experimental investigations in this work indicate that the number of nucleation points within a grain or at grain boundaries of a grain correlate with the size of the corresponding grain. A predefined nominal total number of nucleation points is therefore distributed based on the number of nodes within the grains, which correlates with the grain size. Further weighting factors are used to influence with which distribution the nucleation points are assigned to the different categories (2-4). The subsequent positioning of the nucleation points is random within the respective category. For the initialization of a martensite embryo, all nodes of categories (2-4) within a predefined radius are allocated. This defines circular segments as nucleation sites, with martensite variants drawn randomly from a uniform distribution.

In Fig. 5.8 several examples of different nucleation configurations are shown. It should be noted that overlapping of nuclei may occur. Furthermore, grain boundary nucleation points can occur close to triple points, since no safety distance has been defined for this. A pronounced embryo formation at triple junctions, as shown in example (c), is not known from the literature.

Note that the interface energy can only be reproduced correctly with a fully developed diffuse interface, cf. Apel et al. (2009). With the initial definition of the nuclei, the presented method introduces a quasi-sharp interface between the nuclei and the austenitic matrix. This massively overestimates the interface energy until the diffuse interface has built up. If the nucleation points are defined as initial condition and a nucleation radius smaller than the interface width is chosen, the nuclei tend to shrink away rather then grow. Furthermore, induced mechanical stresses can promote initial shrinkage. To prevent possible shrinkage, the nuclei are often specified as Dirichlet boundary conditions in this work. This allows the interface to build up adequately and thus form a martensite embryo capable of growth.

5.4.2. Auto-Nucleation Mechanism

After the initial nucleation event is initiated, autocatalytic nucleation may occur during further transformation, see Sec. 2.4.2. This section describes how this effect can be modeled. For this purpose, reference is made to the interpolation function introduced in
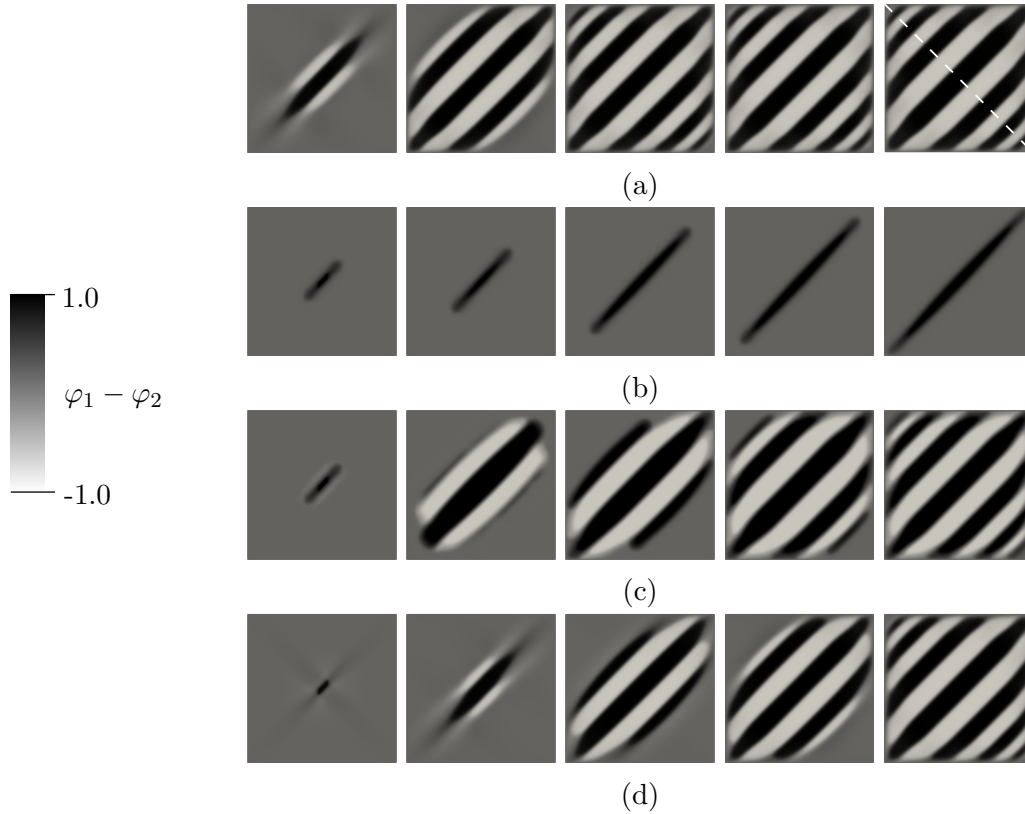
Figure 5.9: Evolution of martensite morphology in a clamped austenitic matrix with edge length of $6.25\,\mu\text{m}$ using (a) h_i^{p1}, (b) h_i^{p5}, (c) h_i^{p5} and additional injection of new martensite variants, (d) h_i^{p3}, the dashed line illustrates exemplary the path for further evaluations – model parameters are given in Appendix B

Sec. 5.1.2, which is relevant for modeling autocatalysis in the context of the martensite transformation. In addition, results of numerical simulations are anticipated to clarify or illustrate the effect of different modeling techniques. Since individual laths within a martensite block are not resolved in this work, the motivation is to describe stress-assisted autocatalytic martensite block formation.

In general, following types of interpolation functions are frequently used in phase field simulations, cf. Moelans et al. (2008):

$$h_i^{\text{p1}}(\varphi_i) = \varphi_i, \tag{5.89}$$
$$h_i^{\text{p5}}(\varphi_i) = \varphi_i^3 \left(6\varphi_i^2 - 15\varphi_i + 10\right). \tag{5.90}$$

In the context of this work, these functions are applied with respect to the interpolation h in the elastic energy potential (Eq. (5.13)). Fig. 5.9(a+b) shows the corresponding evolution of a pre-existing martensite lath in a clamped austenitic matrix, where two martensitic variants are considered. With Eq. (5.89) an autocatalytic formation of new blocks of alternating variants is obtained, whereas with Eq. (5.90) only one block of the pre-existing martensite variant is formed. The ability of Eq. (5.89) to autocatalytically form variants results from a shift in the local minima in the overall energy landscape. In interaction with the transformation strains induced by this, auto-nucleation becomes possible. By taking advantage of this effect, an additional noise term can be omitted. This was exploited, for example, in the works of Yamanaka et al. (2010), Yeddu et al.
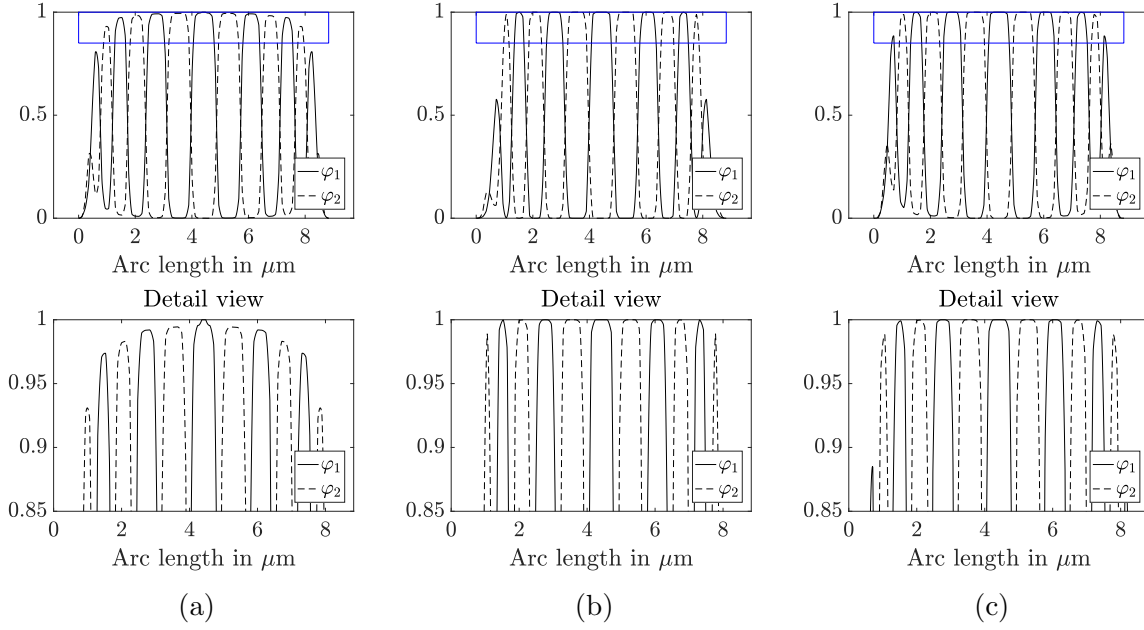
Figure 5.10: Path of order parameters along the diagonal, (a) $h_i^{\mathrm{p}1}$, (b) $h_i^{\mathrm{p}5}$ and additional injection of new martensite variants, (c) $h_i^{\mathrm{p}3}$

(2012b) and Malik et al. (2012). A diagonal line path (from the upper left corner to the lower right corner) of the order parameters illustrates the side effect of this minima shift, see Fig. 5.10(a). Within an apparently fully formed block, the order parameter takes values less than one. According to this, an unrestricted application of the irreversibility according to Sec. 5.2.4 would hardly be possible.

The auto-nucleation with Eq. (5.90) can be implemented with injection of an artificial noise. With reference to the martensite transformation this was done e.g. by Schoof et al. (2018b). Fig. 5.9(c) shows a result in which a disturbance was introduced with the respective other variant in the austenite-martensite interface by adding a corresponding order parameter field at equidistant time steps. These disturbances could represent lattice defects that promote martensite growth of another variant when this is energetically favorable. With some trials, a time interval and an amplitude can be found with which the final microstructure in Fig. 5.9 can be approximately reproduced. Since there is no shift in the energy minima with this function, the order parameter values zero and one are obtained within the martensite blocks, see Fig. 5.10(b). However, a choice must be made as to when and how strong the disturbance/noise is to be applied. Furthermore, with the chosen implicit time integration scheme, the abrupt disturbance can lead to convergence issues in more complex systems.

A pragmatic approach seems to be

$$h_i^{\mathrm{p}3}(\varphi_i) = -\frac{1}{2}\varphi_i^3 + \frac{3}{2}\varphi_i. \tag{5.91}$$

With this function, the minima of the austenitic state is slightly shifted and an auto-nucleation is possible, while the minima of the martensitic state remains at value one, see Fig. 5.9(d) and Fig. 5.10(c). Thus, the irreversibility according to Sec. 5.2.4 can be used without restrictions. It should be noted, however, that $\sum_i^{n_{\mathrm{mart}}} h_i > 1$ for $0 < \varphi < 1$ applies and due to the shift of the austenitic minima, values of $\sum_i^{n_{\mathrm{mart}}} \varphi_i > 1$ are obtained,

especially in the edge area of the simulation domain. A comparison of the morphologies with Eq. (5.91) and Eq. (5.89) indicates no relevant influence. In this work, Eq. (5.91) is used consistently, on the one hand to exploit the intrinsic auto-nucleation effect and on the other hand to keep the option of irreversibility open. The shift of the austenitic minima and the accompanying induction of the transformation strains could be considered as an effect of nucleation-supporting defects.

5.5. Extension to Viscoplastic Material Behavior

In the martensite transformation, the plastic deformation (of the austenite matrix in particular) seems to play an important role. On the one hand, the stress-assisted nucleation is affected by the reduction of these due to plastic relaxation. On the other hand, plastic effects can lead to strain-induced nucleation by creating new potent nucleating defects. According to the transformation process discussed in Sec. 2.4, the strain-induced nucleation creates new martensite laths within a martensite block. The martensite laths are not resolved with the simulation model, so the influence of plastic effects on stress-assisted block formation is of interest.

With regard to elasto-plastic phase field models for martensite transformations Yamanaka et al. (2008, 2010) combined the elastic phase field model by Wang & Khachaturyan (1997) (Khachaturyan model) with the evolution equation of plastic strain proposed by Guo et al. (2005). An elasto-plastic (rate-independent) phase field approach with finite element implementation is, for example, given by Schmitt et al. (2013b). More complex models which couple crystal plasticity and the phase field method with regard to microstructure evolutions are, for example, proposed by Yamanaka et al. (2009); Hildebrand & Miehe (2012a); Schmitt et al. (2014). To implement plasticity in the elastic model presented in Sec. 5.1, the first choice, for simplicity and numerical cost efficiency, is rate-dependent plasticity with linear isotropic hardening, knowing that on the size scale considered, crystal plasticity is closer to reality. The choice of a rate-dependent formulation in contrast to the rate-independent model of Schmitt et al. (2013b) is justified by the fact that with rate-independent plasticity, stress-assisted auto-nucleation is unlikely to occur because there is insufficient stress to motivate the formation of a compensatory variant, cf. Yeddu et al. (2012a).

The viscoplastic model implementation in this work is limited to isotropic material behavior. With this, basic effects of plasticity on the martensite transformation can be studied. In this section, the viscoplastic model is briefly described using the basic equations. For further details the reader is referred to Simo & Hughes (2006).

In order to consider plasticity the total strain is now

$$\boldsymbol{\varepsilon} = \boldsymbol{\varepsilon}^{\mathrm{el}} + \boldsymbol{\varepsilon}^{\mathrm{pl}} + \boldsymbol{\varepsilon}^{0}, \tag{5.92}$$

which leads to the adapted elastic energy potential

$$\psi^{\mathrm{el}} = \frac{1}{2} \left(\boldsymbol{\varepsilon} - \boldsymbol{\varepsilon}^{\mathrm{pl}} - \boldsymbol{\varepsilon}^{0} \right) : \boldsymbol{\mathcal{C}} \left(\boldsymbol{\varepsilon} - \boldsymbol{\varepsilon}^{\mathrm{pl}} - \boldsymbol{\varepsilon}^{0} \right) \tag{5.93}$$

and the constitutive relation

$$\boldsymbol{\sigma} = \frac{\partial \psi}{\partial \boldsymbol{\varepsilon}} = \boldsymbol{\mathcal{C}} \left(\boldsymbol{\varepsilon} - \boldsymbol{\varepsilon}^{\mathrm{pl}} - \boldsymbol{\varepsilon}^{0} \right). \tag{5.94}$$

The plasticity model is described by the following equations:

$$\text{deviatoric stress:} \quad \boldsymbol{s} \quad = \mathrm{dev}(\boldsymbol{\sigma}), \tag{5.95}$$

$$\text{yield condition:} \quad f_\mathrm{y} \quad = |\boldsymbol{s}| - \sqrt{\frac{2}{3}}\,(\sigma_\mathrm{y} + H\,e^\mathrm{pl}), \tag{5.96}$$

$$\text{flow rule:} \quad \dot{\boldsymbol{\varepsilon}}^\mathrm{pl} \quad = \gamma_\mathrm{c}\,\frac{\boldsymbol{s}}{|\boldsymbol{s}|}, \tag{5.97}$$

$$\text{isotropic hardening law:} \quad \dot{e}^\mathrm{pl} \quad = \gamma_\mathrm{c}\sqrt{\frac{2}{3}}, \tag{5.98}$$

$$\text{viscoplastic consistency:} \quad \gamma_\mathrm{c} \quad = \frac{\langle\!\langle f_\mathrm{y}\rangle\!\rangle}{\eta_\mathrm{v}}, \tag{5.99}$$

where $\langle\!\langle \bullet \rangle\!\rangle$ denotes the ramp function $\langle\!\langle \bullet \rangle\!\rangle = \frac{(\bullet) + |\bullet|}{2}$, $\mathrm{dev}(\bullet)$ determines the deviatoric part of $(\bullet)$, H is the hardening modulus, $\sigma_\mathrm{y} = \sigma_\mathrm{y}(\varphi_i)$ is the yield stress depending on the material condition, η_v is the viscosity of the material and e^pl is the equivalent plastic strain. According to other works, the internal variables are inherited from the parent phase to the product phase, cf. Yamanaka et al. (2008); Schoof et al. (2018a).

5.6. Choices of Boundary Conditions

The choice of boundary conditions at the simulation domain edges has a significant influence on the simulation result. At the same time, the boundary conditions on the considered meso-level in the bulk material are not unique, since only a segment of the microstructure is simulated. The behavior of the surrounding material is unknown and must be replaced by suitable boundary conditions.

Fig. 5.11 shows basic realizations of boundary conditions. With the boundary conditions in Fig. 5.11(a), no restriction is imposed except for the constraint on rigid body motions. With the Neumann boundary conditions in Fig. 5.11(b) external stresses are applied. With these boundary conditions, the material is free to expand during the shape-changing martensite transformation. However, imagine a virtual multiplication of the volume cutout in all spatial directions, creating a patchwork-like structure. Compatibility of all parts is not guaranteed under these conditions, as holes and overlaps may occur on the surfaces of the carpet parts. This circumstance can be overcome with Dirichlet boundary conditions, where the opposites surfaces undergo the same prescribed degrees of freedom. Fig. 5.11(c) shows a material segment, which is clamped by Dirichlet boundary conditions. In Fig. 5.11(d), the degrees of freedom of the opposite surfaces are linked, resulting in periodic boundary conditions. With both realizations, the relative difference between the opposite surfaces is zero and thus the piece of the patchwork is compatible with the adjacent (imaginary) pieces. A disadvantage is that these boundary conditions imply that the homogenized total strain is zero, which does not reflect the macroscopic volume expansion due to the martensite transformation.

Yeddu et al. (2012b) compared the three-dimensional evolution of a martensitic embryo in a cubic austenitic clamped and non-clamped matrix. In the non-clamped system the martensite embryo grows without auto-nucleation of other martensite variants, while in the clamped system auto-nucleation occurs and typical martensitic morphologies are formed. The same effect was observed in the context of this work. In order to generate microstructures with a martensitic appearance as well as a homogenized strain reflecting

(a)   (b)   (c)   (d)
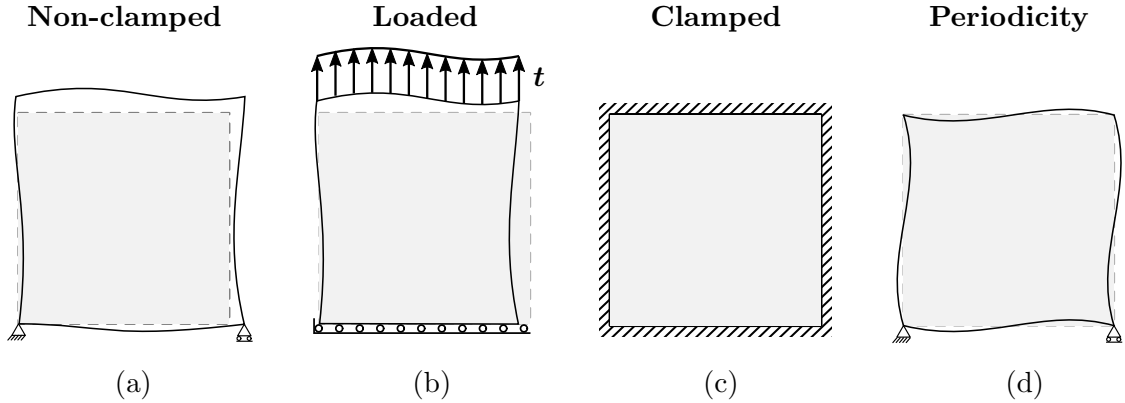
Figure 5.11: Four possible types of simulation edge boundary conditions for the simulation of martensite transformation on the mesoscale, (a) non-clamped, (b) loaded, (c) clamped, (d) periodic boundary conditions

the macroscopic strain, auto-nucleation could be simulated with a high number of pre-existing nuclei, cf. Graf et al. (2021c). However, clamped systems are typically used, cf. Yeddu (2018); Schoof et al. (2018b), or periodic boundary conditions, cf. Yamanaka et al. (2010); Ahluwalia et al. (2020). For the simulation of martensitic microstructures this work joins the publications which use clamped systems. It should be noted that with the used parallelized FEAP version 8.5 no periodic boundary conditions are usable. However, a parallelization is absolutely necessary for a large part of the simulations carried out in this work.

5.7. Transformation Strains and Variant Orientations

In this work, the martensite substructure is not resolved. Nevertheless, the martensite substructure should be somehow taken into account. Therefore, the PTMC is used to approximate the shape strains accompanying the martensite transformation and determine the resulting martensite crystal orientation due to internal slipping. This implies the assumption that the shape deformation $\boldsymbol{P}$ is decisive for the martensite morphology on the length scale considered here, cf. Fig. 2.6. The following describes how the PTMC is used to determine the corresponding input parameters for the simulation, using the work of Graf et al. (2021c) as a reference. An orthonormal system with the basis vectors $\mathbf{a}_1, \mathbf{a}_2, \mathbf{a}_3$ and $\mathbf{b}_1, \mathbf{b}_2, \mathbf{b}_3$ according to Fig. 2.5 is taken as a premise. Further explanations are given by Bhadeshia (2001a).

5.7.1. Lattice Deformation at Substructure Level

The transformation deformation is given by

$$\boldsymbol{S} = \boldsymbol{P}\boldsymbol{Q}, \tag{5.100}$$

where $\boldsymbol{P}$ and $\boldsymbol{Q}$ are invariant plane deformations, cf. Sec. 2.3.2, with the corresponding invariant line vectors $\boldsymbol{p}^{\mathrm{m}}$ and $\boldsymbol{q}^{\mathrm{m}}$ as well as invariant plane normals $\boldsymbol{p}^{\mathrm{n}}$ and $\boldsymbol{q}^{\mathrm{n}}$, respectively. The concatenation of these two deformations results in an invariant line shear described by $\boldsymbol{S}$ with the corresponding invariant line vector $\boldsymbol{s}^{\mathrm{m}}$. Furthermore, the normal denoted by $\boldsymbol{s}^{\mathrm{h}} = \boldsymbol{p}^{\mathrm{m}} \times \boldsymbol{q}^{\mathrm{m}}$ remains invariant. Note that the vector $\boldsymbol{p}^{\mathrm{n}}$ represents the habit plane normal.

In addition to the lattice constants, the invariant lines $\boldsymbol{q}^{\mathrm{m}}$ and normals $\boldsymbol{q}^{\mathrm{n}}$ of the lattice invariant shear $\boldsymbol{Q}$ are necessary input quantities of the theory. In Tab. 5.2 the assumed invariants are specified, cf. Bhadeshia (2001a). These invariants must be consistent with the invariants of the transformation strains $\boldsymbol{S}$. To ensure this for the invariant line, $\boldsymbol{s}^{\mathrm{m}}$ of $\boldsymbol{S}$,

$$\boldsymbol{s}^{\mathrm{m}} \cdot \boldsymbol{q}^{\mathrm{n}} = (s_j^{\mathrm{m}} \mathbf{a}_j) \cdot (q_i^{\mathrm{n}} \mathbf{a}_i) = s_i^{\mathrm{m}} q_i^{\mathrm{n}} = 0 \tag{5.101}$$

must be ensured. Furthermore, the vector $\boldsymbol{s}^{\mathrm{m}}$ should be of length one, which leads to

$$|\boldsymbol{s}^{\mathrm{m}}|^2 = (s_i^{\mathrm{m}} \mathbf{a}_i) \cdot (s_j^{\mathrm{m}} \mathbf{a}_j) = s_i^{\mathrm{m}} s_i^{\mathrm{m}} = 1. \tag{5.102}$$

The Bain transformation leads to a new vector $\bar{\boldsymbol{s}}^{\mathrm{m}} = \boldsymbol{\mathcal{B}} \boldsymbol{s}^{\mathrm{m}}$, which should have the same length

$$|\bar{\boldsymbol{s}}^{\mathrm{m}}|^2 = (\mathcal{B}_{ij} s_j^{\mathrm{m}} \mathbf{a}_i) \cdot (\mathcal{B}_{mn} s_n^{\mathrm{m}} \mathbf{a}_m) = 1. \tag{5.103}$$

With

$$\boldsymbol{\mathcal{B}}_{ij} = \begin{cases} i = j : \mathcal{B}_{ij} \neq 0 \\ i \neq j : \mathcal{B}_{ij} = 0 \end{cases}$$

and $|\bar{\boldsymbol{s}}^{\mathrm{m}}| = |\boldsymbol{s}^{\mathrm{m}}|$ the following equation can be derived:

$$(s_1^{\mathrm{m}})^2 + (s_2^{\mathrm{m}})^2 + (s_3^{\mathrm{m}})^2 = (\mathcal{B}_{11} s_1^{\mathrm{m}})^2 + (\mathcal{B}_{22} s_2^{\mathrm{m}})^2 + (\mathcal{B}_{33} s_3^{\mathrm{m}})^2. \tag{5.104}$$

The system of equations consisting of Eq. (5.101), Eq. (5.102) and Eq. (5.104) leads to two crystallographic relevant solutions for $\boldsymbol{s}^{\mathrm{m}}$. In a similar way, the equations

$$\boldsymbol{s}^{\mathrm{h}} \cdot \boldsymbol{q}^{\mathrm{m}} = 0, \tag{5.105}$$

$$|\boldsymbol{s}^{\mathrm{h}}|^2 = (s_i^{\mathrm{h}} \mathbf{a}_i) \cdot (s_j^{\mathrm{h}} \mathbf{a}_j) = s_i^{\mathrm{h}} s_i^{\mathrm{h}} = 1, \tag{5.106}$$

$$(s_1^{\mathrm{h}})^2 + (s_2^{\mathrm{h}})^2 + (s_3^{\mathrm{h}})^2 = \left(\frac{s_1^{\mathrm{h}}}{\mathcal{B}_{11}}\right)^2 + \left(\frac{s_2^{\mathrm{h}}}{\mathcal{B}_{22}}\right)^2 + \left(\frac{s_3^{\mathrm{h}}}{\mathcal{B}_{33}}\right)^2 \tag{5.107}$$

concerning the invariant normal $\boldsymbol{s}^{\mathrm{h}}$ can be obtained, where $\bar{\boldsymbol{s}}^{\mathrm{h}} = \boldsymbol{s}^{\mathrm{h}}(\boldsymbol{\mathcal{B}})^{-1}$ was used. Again two crystallographic relevant solutions for $\boldsymbol{s}^{\mathrm{h}}$ are computed. With

$$\boldsymbol{a} = \boldsymbol{s}^{\mathrm{m}} \times \boldsymbol{s}^{\mathrm{h}}, \tag{5.108}$$

$$\boldsymbol{b} = \bar{\boldsymbol{s}}^{\mathrm{m}} \times \bar{\boldsymbol{s}}^{\mathrm{h}}, \tag{5.109}$$

it is possible to set up the matrix equation

$$\begin{pmatrix} s_1^{\mathrm{m}} & s_1^{\mathrm{h}} & a_1 \\ s_2^{\mathrm{m}} & s_2^{\mathrm{h}} & a_2 \\ s_3^{\mathrm{m}} & s_3^{\mathrm{h}} & a_3 \end{pmatrix} = \boldsymbol{J} \begin{pmatrix} \bar{s}_1^{\mathrm{m}} & \bar{s}_1^{\mathrm{h}} & b_1 \\ \bar{s}_2^{\mathrm{m}} & \bar{s}_2^{\mathrm{h}} & b_2 \\ \bar{s}_3^{\mathrm{m}} & \bar{s}_3^{\mathrm{h}} & b_3 \end{pmatrix}. \tag{5.110}$$

By combining solutions for $\boldsymbol{s}^{\mathrm{m}}$ and $\boldsymbol{s}^{\mathrm{h}}$ in different ways, four solutions can be obtained for the matrix $\boldsymbol{J}$. Since there are three Bain variants, there is a total of twelve solutions for

$$\boldsymbol{S} = \boldsymbol{J} \boldsymbol{\mathcal{B}} \quad \text{or} \quad S_{ij} \mathbf{a}_i \otimes \mathbf{a}_j = J_{ik} \mathcal{B}_{kj} \mathbf{a}_i \otimes \mathbf{a}_j \tag{5.111}$$

per variant of $\boldsymbol{Q}$. With the six equivalent slip systems of $\boldsymbol{Q}$ in Tab. 5.2, 72 solutions can be computed, with some of them being identical.

Table 5.2: Shear systems of lattice invariant shear $\boldsymbol{Q}$, cf. Bhadeshia (2001a) and Graf et al. (2021c)

Name	Shear system $\boldsymbol{q}^{\mathrm{m}}$ $\boldsymbol{q}^{\mathrm{n}}$	Normalized direction and plane normal $\tilde{\boldsymbol{q}}^{\mathrm{m}}$	$\tilde{\boldsymbol{q}}^{\mathrm{n}}$
Q1	$[0\,\bar{1}\,1](0\,1\,1)$	$\left(\begin{array}{ccc} 0 & -\frac{1}{\sqrt{2}} & \frac{1}{\sqrt{2}} \end{array}\right)^{T}$	$\left(\begin{array}{ccc} 0 & \frac{1}{\sqrt{2}} & \frac{1}{\sqrt{2}} \end{array}\right)^{T}$
Q2	$[0\,1\,1](0\,1\,\bar{1})$	$\left(\begin{array}{ccc} 0 & \frac{1}{\sqrt{2}} & \frac{1}{\sqrt{2}} \end{array}\right)^{T}$	$\left(\begin{array}{ccc} 0 & \frac{1}{\sqrt{2}} & -\frac{1}{\sqrt{2}} \end{array}\right)^{T}$
Q3	$[1\,0\,\bar{1}](1\,0\,1)$	$\left(\begin{array}{ccc} \frac{1}{\sqrt{2}} & 0 & -\frac{1}{\sqrt{2}} \end{array}\right)^{T}$	$\left(\begin{array}{ccc} \frac{1}{\sqrt{2}} & 0 & \frac{1}{\sqrt{2}} \end{array}\right)^{T}$
Q4	$[1\,0\,1](\bar{1}\,0\,1)$	$\left(\begin{array}{ccc} \frac{1}{\sqrt{2}} & 0 & \frac{1}{\sqrt{2}} \end{array}\right)^{T}$	$\left(\begin{array}{ccc} -\frac{1}{\sqrt{2}} & 0 & \frac{1}{\sqrt{2}} \end{array}\right)^{T}$
Q5	$[1\,\bar{1}\,0](1\,1\,0)$	$\left(\begin{array}{ccc} \frac{1}{\sqrt{2}} & -\frac{1}{\sqrt{2}} & 0 \end{array}\right)^{T}$	$\left(\begin{array}{ccc} \frac{1}{\sqrt{2}} & \frac{1}{\sqrt{2}} & 0 \end{array}\right)^{T}$
Q6	$[1\,1\,0](1\,\bar{1}\,0)$	$\left(\begin{array}{ccc} \frac{1}{\sqrt{2}} & \frac{1}{\sqrt{2}} & 0 \end{array}\right)^{T}$	$\left(\begin{array}{ccc} \frac{1}{\sqrt{2}} & -\frac{1}{\sqrt{2}} & 0 \end{array}\right)^{T}$

5.7.2. Martensite Crystal Orientations

The coordinate transformation matrix $J_{ij}\mathbf{b}_i \otimes \mathbf{a}_j$ is identified in order to identify suitable solutions. For this, the respective Bain correspondence matrix with

$$\boldsymbol{\mathcal{T}}^{(1)} = \begin{pmatrix} 1 & \bar{1} & 0 \\ 1 & 1 & 0 \\ 0 & 0 & 1 \end{pmatrix}, \quad \boldsymbol{\mathcal{T}}^{(2)} = \begin{pmatrix} 0 & 1 & \bar{1} \\ 0 & 1 & 1 \\ 1 & 0 & 0 \end{pmatrix}, \quad \boldsymbol{\mathcal{T}}^{(3)} = \begin{pmatrix} \bar{1} & 0 & 1 \\ 1 & 0 & 1 \\ 0 & 1 & 0 \end{pmatrix}, \quad (5.112)$$

are used to solve the following equation:

$$\left(J_{ij}\mathbf{b}_i \otimes \mathbf{a}_j\right)\left(S_{kl}\mathbf{a}_k \otimes \mathbf{a}_l\right) = \mathcal{T}_{ij}\mathbf{b}_i \otimes \mathbf{a}_j. \quad (5.113)$$

The crystal orientations obtained with the transformation $J_{ij}\mathbf{b}_i \otimes \mathbf{a}_j$ can be represented in pole figures, as exemplary shown in Fig. 5.12. Here, the yellow and green bullets represent the orientations of possible martensite variants calculated by the PTMC. Furthermore, the orientations of the NW orientation relationship are depicted with black dots. For further consideration twelve NW near solutions are selected. These solutions are represented by the green numbered bullets in Fig. 5.12.

5.7.3. Shape Change and Mesoscopic Transformation Strain

With the previous considerations it is now possible to calculate the relevant deformations $\boldsymbol{P}$. As a reminder, the shape deformation is determined by Eq. (5.100), e.g.

$$\boldsymbol{S} = \boldsymbol{P}\boldsymbol{Q},$$

where the invariant plane deformations $\boldsymbol{P}$ and $\boldsymbol{Q}$ may be rewritten as

$$P_{ij}\,\mathbf{a}_i \otimes \mathbf{a}_j = \left(\delta_{ij} + \mathrm{m}\,\tilde{p}_i^{\mathrm{m}}\tilde{p}_j^{\mathrm{n}}\right)\mathbf{a}_i \otimes \mathbf{a}_j, \quad (5.114)$$

where $\tilde{\boldsymbol{p}}^{\mathrm{m}}$ and $\tilde{\boldsymbol{p}}^{\mathrm{n}}$ are the normalized invariant line and plane vectors of $\boldsymbol{P}$ and analogously

$$Q_{ij}\,\mathbf{a}_i \otimes \mathbf{a}_j = \left(\delta_{ij} + \mathrm{n}\,\tilde{q}_i^{\mathrm{m}}\tilde{q}_j^{\mathrm{n}}\right)\mathbf{a}_i \otimes \mathbf{a}_j. \quad (5.115)$$
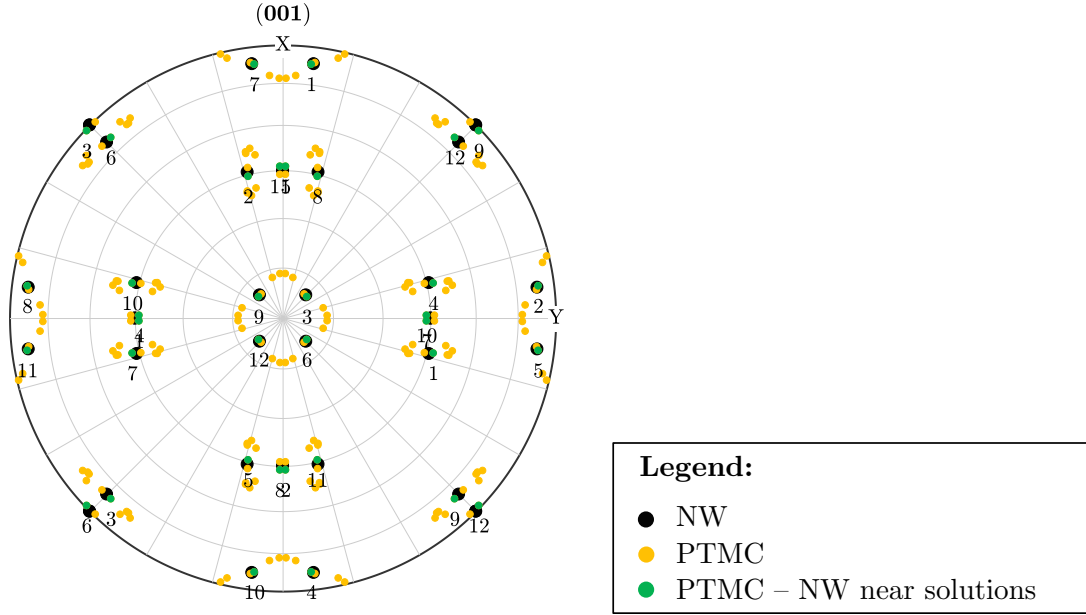
Figure 5.12: Pole figure of the orientations calculated by the PTMC with the lattice constants of pure iron as well as the NW orientation relationship, see Graf et al. (2021c)

The scalar quantities m and n represent the magnitude of the deformations. With the inverse $\boldsymbol{S}^{-1} = \boldsymbol{Q}^{-1}\boldsymbol{P}^{-1}$, the relation $(\tilde{\boldsymbol{q}}^{\mathrm{n}})^T (\tilde{\boldsymbol{q}}^{\mathrm{m}} (\tilde{\boldsymbol{q}}^{\mathrm{n}})^T) = \boldsymbol{0}$ and $\det \boldsymbol{Q} = 1$,

$$\tilde{\boldsymbol{p}}^{\mathrm{n}} = \frac{\tilde{\boldsymbol{q}}^{\mathrm{n}} - \tilde{\boldsymbol{q}}^{\mathrm{n}}\boldsymbol{S}^{-1}}{|\tilde{\boldsymbol{q}}^{\mathrm{n}} - \tilde{\boldsymbol{q}}^{\mathrm{n}}\boldsymbol{S}^{-1}|} \tag{5.116}$$

is derived and by multiplication of Eq. (5.100) with $\tilde{\boldsymbol{q}}^{\mathrm{m}}$ from the right hand side,

$$\tilde{\boldsymbol{p}}^{\mathrm{m}} = \frac{\boldsymbol{S}\tilde{\boldsymbol{q}}^{\mathrm{m}} - \tilde{\boldsymbol{q}}^{\mathrm{m}}}{|\boldsymbol{S}\tilde{\boldsymbol{q}}^{\mathrm{m}} - \tilde{\boldsymbol{q}}^{\mathrm{m}}|} \tag{5.117}$$

is obtained. Note that $(\tilde{\boldsymbol{q}}^{\mathrm{m}} (\tilde{\boldsymbol{q}}^{\mathrm{n}})^T)\tilde{\boldsymbol{q}}^{\mathrm{m}} = \boldsymbol{0}$ applies. With Eq. (5.116) and (5.117) the currently unknown magnitude can be calculated with

$$\mathrm{m} = \left| \frac{\boldsymbol{S}\tilde{\boldsymbol{q}}^{\mathrm{m}} - \tilde{\boldsymbol{q}}^{\mathrm{m}}}{\tilde{\boldsymbol{p}}^{\mathrm{n}} \cdot \tilde{\boldsymbol{q}}^{\mathrm{m}}} \right| . \tag{5.118}$$

Using Eq. (5.100) it is now possible to calculate the twelve different shape change matrices ($\boldsymbol{P}$) for the NW near variants selected in Sec. 5.7.2. The transformation strains introduced by the formation of martensite are obtained with

$$\tilde{\boldsymbol{\varepsilon}} = \frac{1}{2}\left(\boldsymbol{P}^T\boldsymbol{P} - \boldsymbol{I}\right). \tag{5.119}$$

With this method, twelve strain tensors (denoted by $\tilde{\boldsymbol{\varepsilon}}_i$ with $i = 1, \ldots, 12$) corresponding to twelve NW near martensite variants can be obtained. Four variants share the same Bain group, while each martensite variant results in a different orientation of the crystal.

6. Numerical Simulations of Martensite Transformations

The exemplarily investigated material 50CrMo4 is a low-alloy steel, which shows characteristics of an athermal martensite transformation. A major challenge in the holistic simulation of this martensite transformation are the different time scales that have to be considered. With reference to the macroscopic sample, the martensite transformation from 0 to 100% takes place in the order of 10^0 s. At the same time, the growth of a martensite needle takes place at very high velocities, which is in the order of magnitude of sound propagation. A simulation of the growth of a needle with a corresponding number of computational steps over the entire macroscopic cooling process seems to be impossible with the currently available computational capacities. In this work, the reasoning of Entwisle (1971) is followed, according to which the athermal martensite transformation should be considered as a rapid isothermal transformation. Accordingly, the numerical studies are carried out under isothermal conditions below T_{MS} and thus a small time slice of the macroscale transformation is considered at the mesoscale.

6.1. Analysis of Basic Model Behavior

In this section, the basic model behavior is analyzed. The findings of these investigations form an important basis for the interpretation of the results in the following sections. In a first step (Sec. 6.1.1), a quasi-one-dimensional problem is considered on which parameter studies are performed. Subsequently, the influence of the spatial discretization is investigated in Sec. 6.1.2.

6.1.1. Quasi One-Dimensional Austenite-Martensite Transformation

Based on a quasi one-dimensional example representing the one-dimensional consideration in Sec. 5.1.3, the influence of selected model parameters is investigated in detail. This is motivated by the fact that the derivation of the model parameters γ and l are derived from a state where the mechanical and the bulk potential is neglected ($\tilde{\boldsymbol{\varepsilon}}_i = \mathbf{0}$, $\Delta g = 0$). Thus, a deviation from this state influences the effective interface energy and interface width, which is evaluated with this study.

In a two-dimensional plane strain continuum with height l_y and length $l_x \gg l_y$ and two martensite variants, two phases representing austenite and martensite (variant 1) are initialized, where an initial non-diffuse interface is defined at $x = l_x/2$. At constant temperatures T corresponding to a constant chemical driving force $\Delta g < 0$, the relaxation behavior to the equilibrium state is observed. In order to avoid rigid body movements, the displacements of the node at $x = 0$ and $y = 0$ are fixed in horizontal and vertical direction, and furthermore the displacement of the node at $x = l_x$ and $y = 0$ is fixed in vertical direction. With $l_x = 7\,\mu\text{m}$ and $l_y = 1.5\,\mu\text{m}$, the spatial discretization is done with 84×18 elements. This results in an element edge length of $l_{el} = 1/12\,\mu\text{m}$.

In this study the influence of the interface width, the chemical driving force, the transformation strain in x-direction, and the interface energy parameter are of interest. Therefore, the parameters are systematically varied in the following intervals:

Interface width	l	$= \left[\frac{1}{6}; \frac{1}{2}\right]$	µm
Chemical driving force	Δg	$= [-600.0; 0.0]$	mJ(mm)$^{-3}$
Transformation strains	$\tilde{\boldsymbol{\varepsilon}}_1$	$= \begin{pmatrix} \tilde{\varepsilon}_{\mathrm{x}} & 0 \\ 0 & 0 \end{pmatrix}$ with $\tilde{\varepsilon}_{\mathrm{x}} = [0.02; 0.14]$	
	$\tilde{\boldsymbol{\varepsilon}}_2$	$= -\tilde{\boldsymbol{\varepsilon}}_1$	
Interface energy parameter	γ	$= [0.01; 0.03]$	mJ(mm)$^{-2}$

With these parameter settings, the smallest interface width value corresponds to two element lengths, and the biggest value corresponds to seven element lengths. The chemical driving force interval is chosen based on realistic free energy differences with regard to steels and represents values from free energy equilibrium at high temperature to energy differences at room temperature. With the transformation strain interval, realistic magnitudes calculated based on the Bain correspondence for steels are covered. For the sake of completeness, the transformation strain tensor of the second martensite variant is given. However, due to the boundary conditions, the second martensite variant is not formed in this example. The parameter interval of the interface energy parameter was defined retrospectively based on initial results of the parameter study. The mobility parameter scales the transformation kinetics and is chosen to be constant. The resulting velocity hereby varies within a similar order of magnitude as the velocity determined by Wang & Urbassek (2013) based on atomistic simulations for pure iron. For simplicity, an isotropic material behavior is assumed. Accordingly, the Young's modulus and the Poisson's ratio are defined as material parameters. In summary, the remaining parameters are selected as follows:

Young's modulus	E	$= 210\,000$	MPa
Poisson's ratio	ν	$= 0.3$	
Mobility	M	$= 50\,000$	mm^2(Ns)$^{-1}$

Influence on the Effective Interface Energy. First, the influence of the relevant input parameters on the effective interface energy $\tilde{\gamma}$ is investigated. A total of 625 simulations with five variations of each parameter are simulated and compared. For this purpose, the integral

$$\tilde{\gamma} = \frac{1}{l_{\mathrm{y}}} \int_{\Omega} \psi^{\mathrm{int}} dV \tag{6.1}$$

is evaluated numerically in each simulation at a time $t > 0$, at which a stationary diffuse interface has been formed. The results are shown in Figs. 6.1-6.3 as relative deviation to the interface energy parameter $(\tilde{\gamma} - \gamma)/\gamma$ in dependence of the variated parameters. Each of these figures contains the information of all simulations, with the results plotted differently to highlight the observed influences.

An increasing interface energy parameter leads to an increasing ratio of interface energy. The effective interface energy converges to the value of the interface energy parameter, see Fig. 6.1. An increasing negative magnitude of the chemical energy difference Δg increases the weight of minimizing the bulk energy. Thus, the effective interface energy tends to increase its deviation to the value of the interface energy parameter.

With focus on the influence of the interface width parameter l, Fig. 6.2 is provided. In a material with $\Delta g = 0$ an increasing interface width l leads to a convergence of the
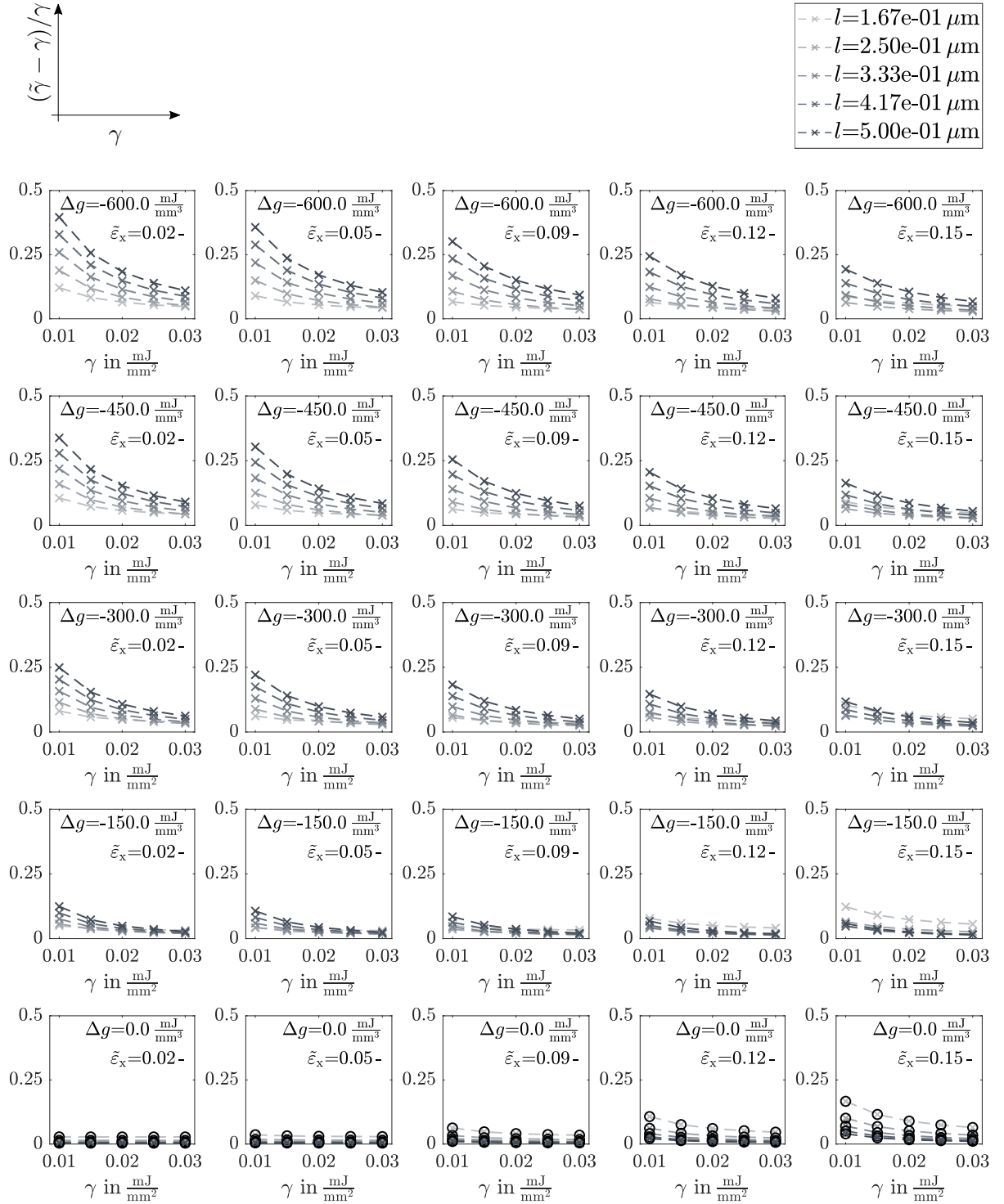
Figure 6.1: Influence of model parameters on the resulting interface energy with focus on the interface energy parameter γ and chemical energy difference Δg, the ordinate is the relative deviation to the interface energy parameter $(\tilde{\gamma} - \gamma)/\gamma$, black circles indicate simulations where no interface motion occurs, spatial discretization: 84×18 finite elements
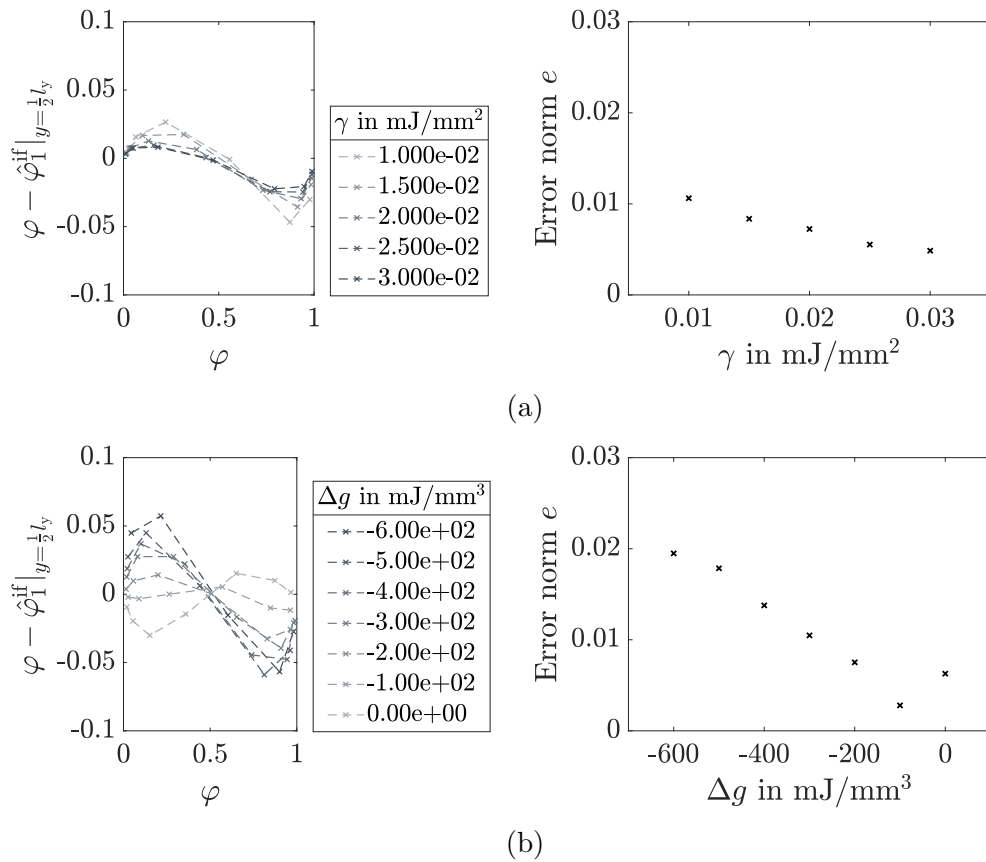
calculated interface energy to the value of the interface energy parameter γ. In highly undercooled materials ($\Delta g = -600\,\mathrm{mJ/mm^3}$), the increase of l leads to an increase of the

effective surface energy, resulting in increased deviations to γ. Regarding conditions with $-600 < \Delta g < 0 \,\mathrm{mJ/mm^3}$ a combination of these effects can be observed. Increasing l initially reduces the deviation, but the deviation increases again after a certain threshold value, depending on the other parameters.

A reversed effect is observed with regard to the variation of the transformation strains, see Fig. 6.3. With $\Delta g = 0$ an increasing transformation strain leads to an increasing deviation of the effective interface energy to the value of the interface energy parameter γ. Observations of undercooled systems predominantly show a decrease in deviation with increase in the transformation strain.

In order to understand and explain the observed effects, the formation of the interface is investigated in the following.
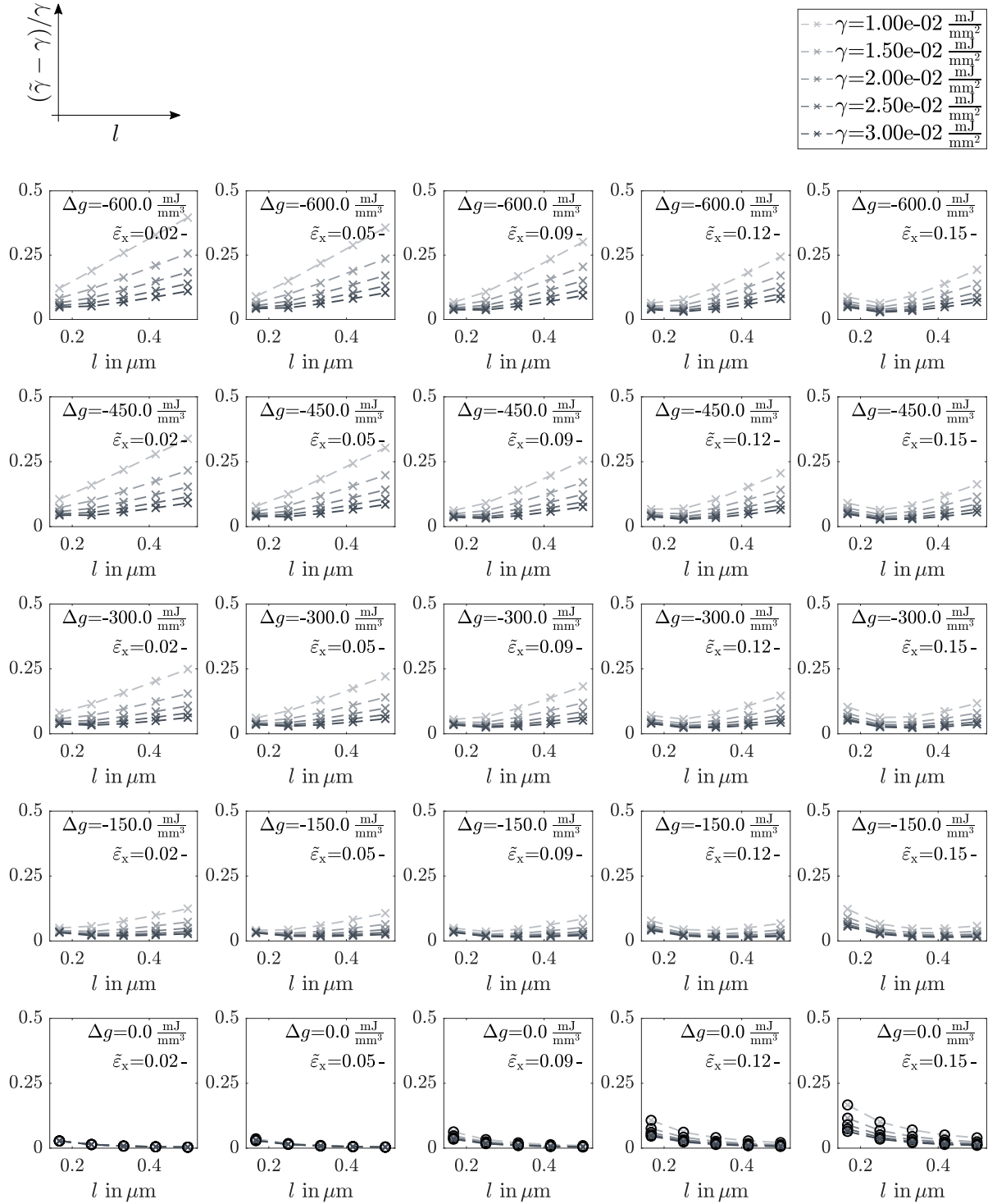
Figure 6.2: Influence of model parameters on the resulting interface energy with focus on the interface width l, the ordinate is the relative deviation to the interface energy parameter $(\tilde{\gamma} - \gamma)/\gamma$, black circles indicate simulations where no interface motion occurs, spatial discretization: 84×18 finite elements
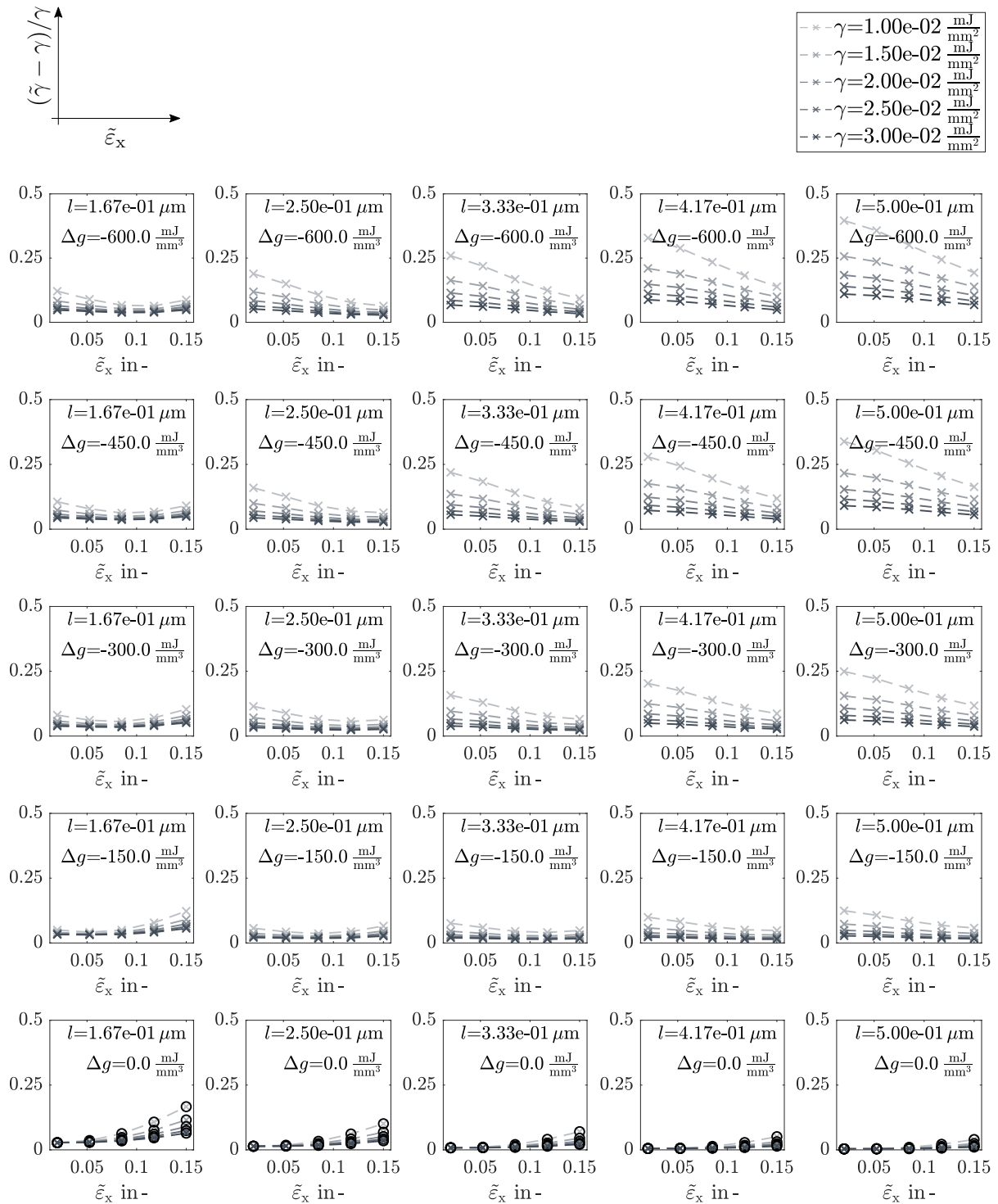
Figure 6.3: Influence of model parameters on the resulting interface energy with focus on the transformation strain $\tilde{\varepsilon}_{\mathrm{x}}$, the ordinate is the relative deviation to the interface energy parameter $(\tilde{\gamma} - \gamma)/\gamma$, black circles indicate simulations where no interface motion occurs, spatial discretization: 84×18 finite elements

Influence on the Interface Geometry. The influence of the relevant input parameters on the geometric formation of the interface is now investigated. The geometric formation of the interface is significant for the resulting interface energy and provides further insight into the effects observed in the previous section. For this purpose, a line path at $y = l_\mathrm{y}/2$ with respect to the field variable φ_1 is evaluated at time $t > 0$. For comparison, the stationary interfaces are shifted so that the interface position x_if of the linearly interpolated nodal solution $\hat\varphi_1 = 0.5$ is at $x = 0$. With focus on the solutions within the interface $\hat\varphi_1^\mathrm{if} = \{\hat\varphi_1 \,|\, 0.01 < \hat\varphi_1 < 0.99\}$, the difference to the one-dimensional smooth interpolation with Eq. (5.19) is shown in Fig. 6.4. With this definition, positive values of $\varphi - \hat\varphi_1^\mathrm{if}|_{y=0.5\,l_\mathrm{y}}$ for $\varphi < 0.5$ and negative values for $\varphi > 0.5$ correspond to an effective smaller interface width and vice versa. Furthermore, the error norm

$$ e = \frac{1}{n_\mathrm{if}} \left| \boldsymbol{d}_\varphi - \hat{\boldsymbol{d}}_\varphi \right| \tag{6.2} $$

is shown, where n_if is the number of nodes in the interface with the chosen line path, vector $\hat{\boldsymbol{d}}_\varphi$ contains the calculated order parameter solutions, and vector $\boldsymbol{d}_\varphi$ contains the corresponding solutions with Eq. (5.19).

As expected, the results in Fig. 6.4 show the same characteristics of the influences of the model parameters on the formation of the interface. The influence of the interface

Figure 6.4: Influence of model parameters on the diffuse interface in a two-phase beam with (a) $l = 0.25\,\mu\mathrm{m}$, $\tilde\varepsilon_\mathrm{x} = 0.1$, $\Delta g = -200\,\mathrm{mJ/mm^3}$ (b) $l = 0.25\,\mu\mathrm{m}$, $\gamma = 0.02\,\mathrm{mJ/mm^2}$, $\tilde\varepsilon_\mathrm{x} = 0.1$, (c) $\gamma = 0.02\,\mathrm{mJ/mm^2}$, $\tilde\varepsilon_\mathrm{x} = 0.1$, $\Delta g = -200\,\mathrm{mJ/mm^3}$, (d) $l = 0.25\,\mu\mathrm{m}$, $\gamma = 0.02\,\mathrm{mJ/mm^2}$, $\Delta g = -200\,\mathrm{mJ/mm^3}$, spatial discretization: 84×18 finite elements

(c)

(d)
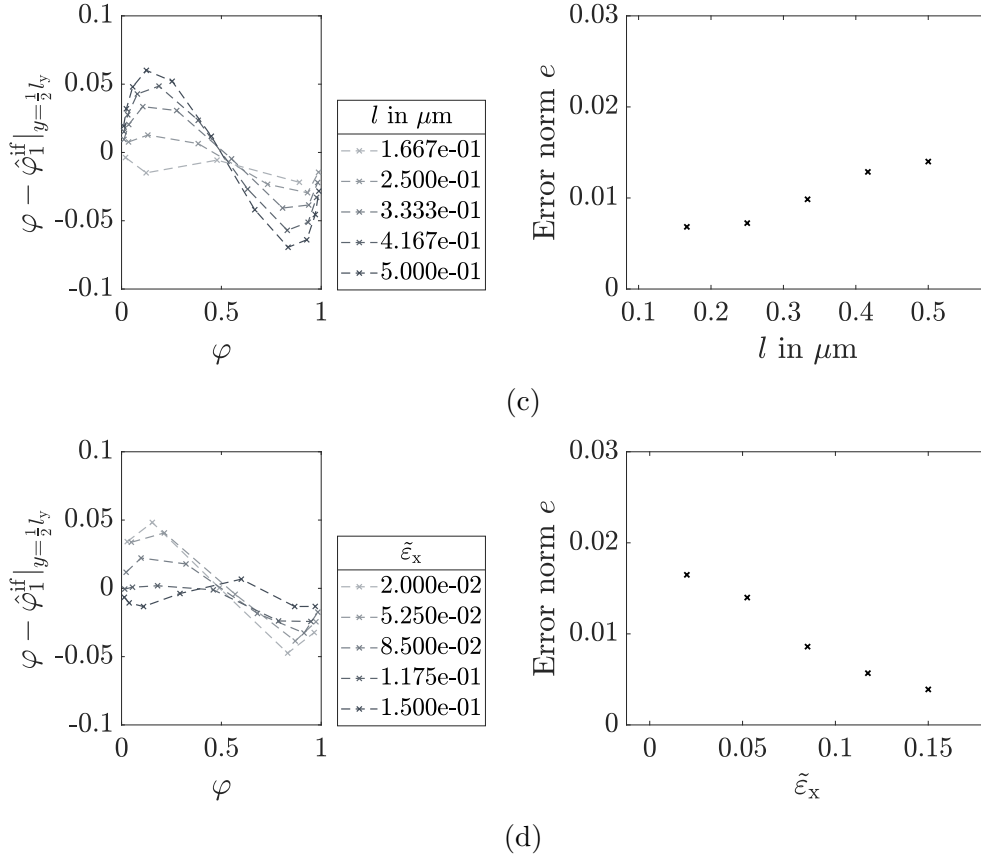
Figure 6.4: Influence of model parameters on the diffuse interface in a two-phase beam with (a) $l = 0.25\,\mu\text{m}$, $\tilde{\varepsilon}_\text{x} = 0.1$, $\Delta g = -200\,\text{mJ/mm}^3$ (b) $l = 0.25\,\mu\text{m}$, $\gamma = 0.02\,\text{mJ/mm}^2$, $\tilde{\varepsilon}_\text{x} = 0.1$, (c) $\gamma = 0.02\,\text{mJ/mm}^2$, $\tilde{\varepsilon}_\text{x} = 0.1$, $\Delta g = -200\,\text{mJ/mm}^3$, (d) $l = 0.25\,\mu\text{m}$, $\gamma = 0.02\,\text{mJ/mm}^2$, $\Delta g = -200\,\text{mJ/mm}^3$, spatial discretization: 84×18 finite elements (cont.)

energy parameter γ on the interface is shown in Fig. 6.4(a). An increase of γ leads to a convergence to the analytical solution. This results from the fact that with increasing γ the equation terms responsible for the formation of the interface according to Eq. (5.19) are strengthened against the dominant bulk part.

An increase in the chemical energy difference leads to a smaller effective interface width, see Fig. 6.4(b). The larger the negative magnitude of Δg, the larger the deviations to the idealized analytical interface. With $\Delta g = 0$ a wider interface is observed. In addition, the error norm e indicates an increased deviation to Eq. (5.19), which cannot be explained at first.

Basically, with an increasing interface width, the interface is described with more breakpoints, which leads to a more precise description of the interface. Concerning the variation of the interface width l with $\Delta g = -200\,\text{mJ(mm)}^{-3}$, the number of interface nodes along the line path at $y = l_\text{y}/2$ are evaluated in Tab. 6.1. However, a further increase of l increases the deviation to the idealized analytical solution, see Fig. 6.4(c). The reason for this is that an increased interface width l is contrary to the effect of $\Delta g < 0$ on the resulting interface width. Since the bulk portion is dominant in undercooled materials, the ideal interface cannot be formed with respect to interface regularization.

Table 6.1: Number of nodes in the diffuse interface with $\gamma = 0.02\,\text{mJ/mm}^2$, $\tilde{\varepsilon}_\text{x} = 0.1$, $\Delta g = -200\,\text{mJ/mm}^3$

l in µm	0.17	0.25	0.33	0.42	0.50
n_if	4	6	8	9	11

In an undercooled material, an increasing transformation strain up to a certain value leads to a convergence to the idealized analytical solution, which is accompanied with an increasing width of the resulting interface, see Fig. 6.4(d). If a certain threshold is reached, a wider interface results (compared to the analytical solution) and the deviation increases. The influence of the transformation strain $\tilde{\varepsilon}_\text{x}$ also explains the mentioned and yet unexplained increased deviation in Fig. 6.4(b) with $\Delta g = 0$. In this configuration, the strains in the interface lead to the increased deviation.

Influence on the Interface Formation and Kinetics. In order to further deepen the understanding of the model, the numerically solved contributions of the evolution Eq. (5.32),

$$\frac{1}{M}\dot{\varphi}_i = \underbrace{-\frac{\partial \psi^\text{el}}{\partial \varphi_i}}_{①} \underbrace{-\Delta g\, \frac{\partial f^\text{bulk}}{\partial \varphi_i}}_{②} \underbrace{-12\,\frac{\gamma}{l}\frac{\partial f^\text{int}}{\partial \varphi_i}}_{③} \underbrace{+\frac{3}{2}\,\gamma\, l \underline{\Delta}\varphi_i}_{④} \quad \text{for} \quad i = 1,2...N, \tag{6.3}$$

are analyzed. Note that with the chosen parameters, the gradient part ④ is factors smaller than the other contributions (① - ③) and is thus neglected in the following. The other relevant parts are illustrated exemplary in Fig. 6.5 as field plots. The mechanical part ① has a positive contribution to the interface mobility for $\varphi_1 < 0.5$ and a negative contribution for $\varphi_1 > 0.5$. This makes clear why the mechanical field widens the interface. However, the positive contribution is greater than the negative (and slowing) contribution. This course results mainly from the elastic strains that occur in the interface and the chosen interpolation function. The chemical bulk part has an exclusively positive contribution to the mobility in the interface, according to the course of $\frac{\partial f^\text{bulk}}{\partial \varphi_1}$ with its maximum at $\varphi_1 = 2/3$. This explains why an increased negative magnitude decreases the effective interface width. The contribution of the chemical interface part is negative for $\varphi_1 < 0.5$ and positive for $\varphi_1 > 0.5$ with approximately equal magnitudes. This course results from $\frac{\partial f^\text{int}}{\partial \varphi_1}$ with its extrema at $\varphi_1 = 1/2 \pm 1/(2\sqrt{3})$.

In Fig. 6.6, the homogenized martensite content

$$\langle \varphi \rangle = \sum_{i=1}^{n_\text{mart}} \langle \varphi_i \rangle \quad \text{with} \quad \langle \varphi_i \rangle = \frac{1}{V} \int_\mathcal{B} \varphi_i \, dV \tag{6.4}$$

in dependence of normalized time is shown with selected parameter configurations. Furthermore, the homogenized and normalized quantities of parts $\langle ① \rangle$ - $\langle ③ \rangle$ are depicted. Fig. 6.6(a) shows that in an undercooled material an increase of the interface energy parameter is accompanied with an increase in the interface velocity. While the mechanical part $\langle ① \rangle$ and the interface part $\langle ② \rangle$ seem to be constant, the chemical bulk part increases significantly compared to part $\langle ① \rangle$ and part $\langle ② \rangle$ and thus mainly increases the interface velocity. The increasing part $\langle ① \rangle$ can be explained by the fact that the bulk part density
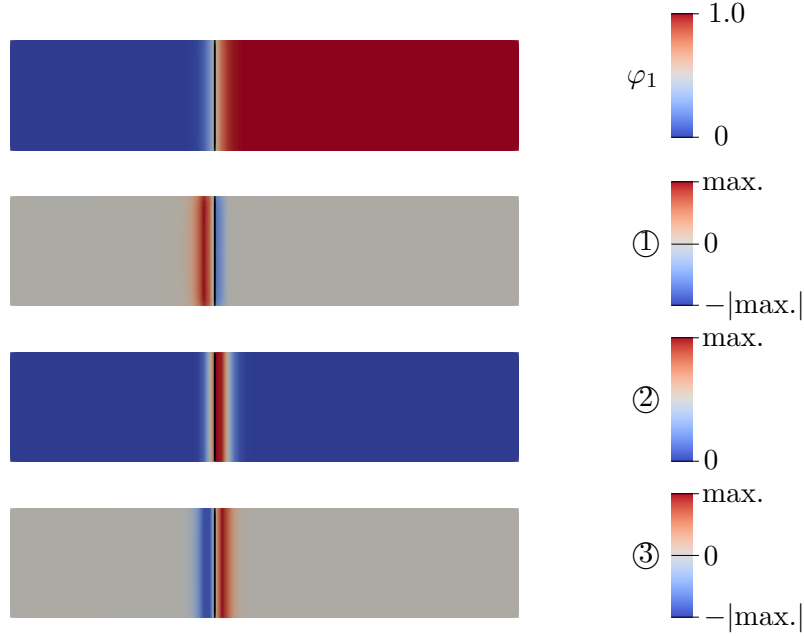
Figure 6.5: Illustration of interface mobility at a time $t > 0$, vertical black line represents the isoline with $\varphi_1 = 0.5$, parameter setting: $\gamma = 0.02\,\mathrm{mJ/mm^2}$, $\Delta g = -200\,\mathrm{mJ/mm^3}$, $l = 1/3\,\mathrm{\mu m}$, $\tilde{\varepsilon}_\mathrm{x} = 0.1$, spatial discretization: 84×18 finite elements

is distributed over an increasing effective interface width, which was demonstrated in the previous section.

With chemical phase equilibrium ($\Delta g = 0$), the diffuse interface forms but no significant interface motion occurs, which results in an apparently constant martensite ratio of $\langle \varphi \rangle = 0.5$, see Fig. 6.6(a). By decreasing Δg, the martensite becomes energetically more favorable, which initiates a significant interface motion until a full martensitic state is achieved. The interface velocity increases with decreasing Δg, which corresponds to a higher undercooling of the material. The higher interface velocity results from the increasing bulk part $\langle ② \rangle$, which is scaled by Δg.

In an undercooled material an increase of the interface width l increases the interface velocity, see Fig. 6.6(c). Again, this is a result of massive growth of the bulk part $\langle ② \rangle$ due to the distribution of its density over an increasing interface width. The mechanical part $\langle ① \rangle$ decreases slightly due to the decreasing elastic strains in the interface, which is accompanied with the increasing interface width. The slight increase of the interface part $\langle ③ \rangle$ is an effect of the increasing deviation of the interface geometry to the equilibrium solution with $\Delta g = 0$, which was demonstrated in the previous section.

The influence of the transformation strain $\tilde{\varepsilon}_\mathrm{x}$ is shown in Fig. 6.6(d). As demonstrated in the previous section, the transformation strain leads to a wider effective interface width and thus to a massive growth of the bulk part $\langle ② \rangle$. Furthermore, the increasing transformation strain increases the elastic strains in the interface and thus increases the mechanical part $\langle ① \rangle$. The increasing effective interface width leads to a decreasing interface part $\langle ③ \rangle$. In total, the mobility increases with increasing transformation strain. The same applies for the interface velocity.
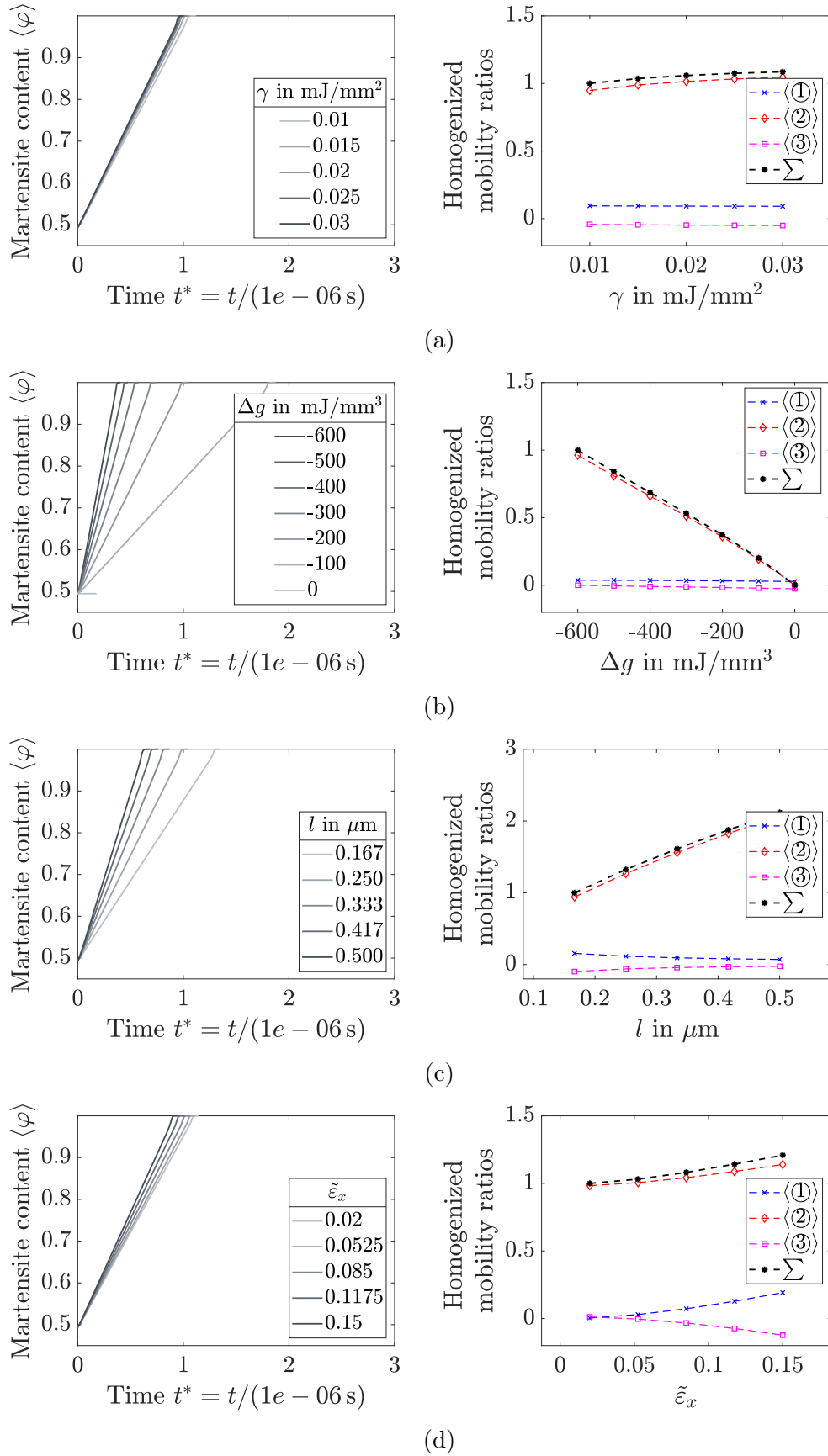
Figure 6.6: Influence of model parameters on the interface kinetics in a two-phase beam with (a) $l = 0.25\,\mu\text{m}$, $\tilde{\varepsilon}_\text{x} = 0.1$, $\Delta g = -200\,\text{mJ/mm}^3$, (b) $l = 0.25\,\mu\text{m}$, $\gamma = 0.02\,\text{mJ/mm}^2$, $\tilde{\varepsilon}_\text{x} = 0.1$, (c) $\gamma = 0.02\,\text{mJ/mm}^2$, $\tilde{\varepsilon}_\text{x} = 0.1$, $\Delta g = -200\,\text{mJ/mm}^3$, (d) $l = 0.25\,\mu\text{m}$, $\gamma = 0.02\,\text{mJ/mm}^2$, $\Delta g = -200\,\text{mJ/mm}^3$, spatial discretization: 84×18 finite elements

6.1.2. Influence of Spatial Discretization

The previous investigations took place based on a fixed discretization with 84×18 finite elements. The chosen discretization was motivated by published works in the field of phase field simulation of martensite transformations, where the interface is typically described with 3 to 4 elements resulting in about 6 to 8 interface breakpoints, cf. works of Schoof et al. (2018b) and Yeddu (2018). In order to evaluate the influence of the spatial discretization, in this study the interface width l is set analogous to the previous studies, while the number of elements is increased. In Fig. 6.7, the mobility parts of simulations with 336×72 finite elements corresponding to Fig. 6.6 are depicted. Furthermore, the local mobility parts in dependence of the order parameter are depicted in Fig. 6.8. The solid line represents the analytical solution.

Concerning the variation of the interface energy parameter, the chemical energy difference and the interface width, the same characteristic of the total mobility is observed. However, with increasing the number of elements, the influence of the transformation strain $\tilde{\varepsilon}_x$ is reduced. This is due to the fact that with the increased number of breakpoints in the interface, the elastic strains in the interface can be described more precisely and results effectively in lower elastic strains in the interface. These smaller strains are accompanied with smaller magnitudes of the mobility (part ①) within the interface and thus have less
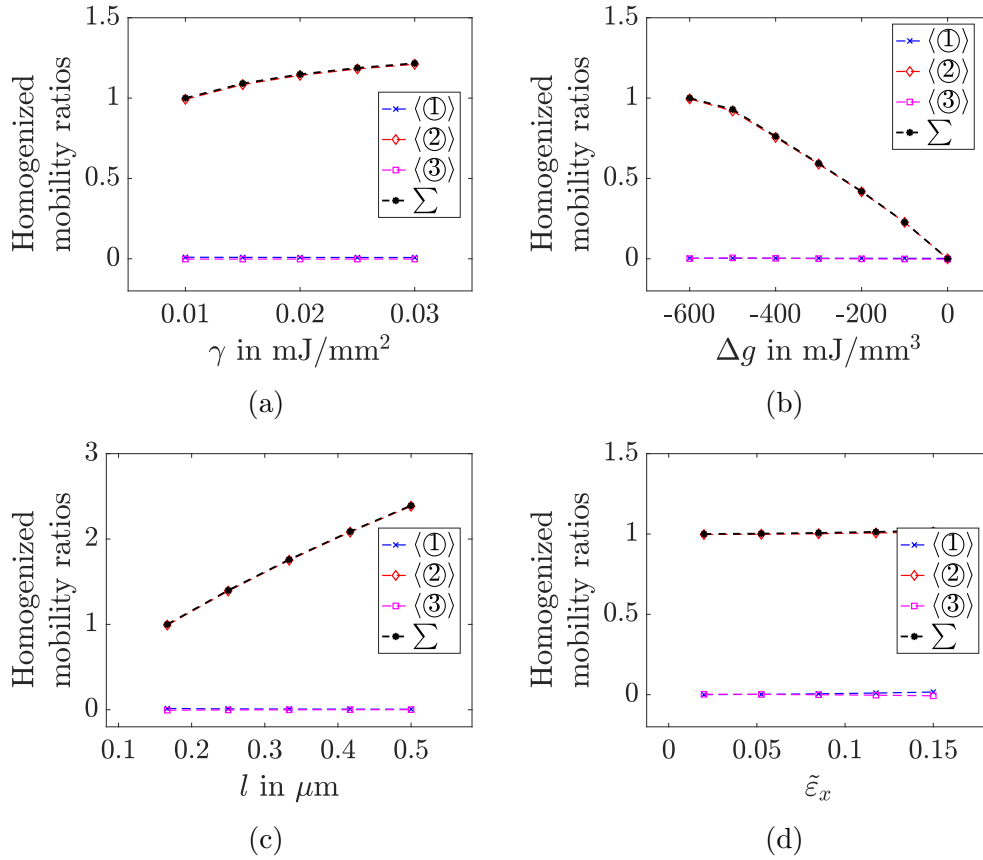
Figure 6.7: Influence of model parameters on the interface kinetics in a two-phase beam with (a) $l = 0.25\,\mu\text{m}$, $\tilde{\varepsilon}_x = 0.1$, $\Delta g = -200\,\text{mJ/mm}^3$ (b) $l = 0.25\,\mu\text{m}$, $\gamma = 0.02\,\text{mJ/mm}^2$, $\tilde{\varepsilon}_x = 0.1$, (c) $\gamma = 0.02\,\text{mJ/mm}^2$, $\tilde{\varepsilon}_x = 0.1$, $\Delta g = -200\,\text{mJ/mm}^3$, (d) $l = 0.25\,\mu\text{m}$, $\gamma = 0.02\,\text{mJ/mm}^2$, $\Delta g = -200\,\text{mJ/mm}^3$, spatial discretization: 336×72 finite elements

(a)

(b)
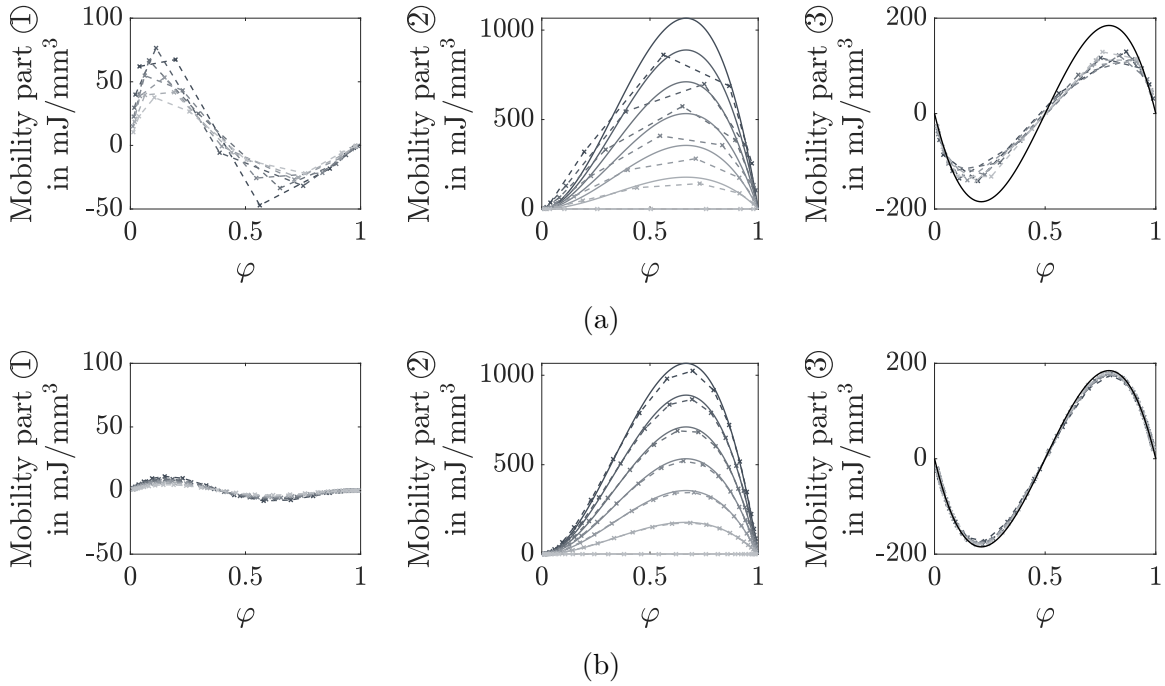
Figure 6.8: Comparison of numerical results of mobility parts in a two-phase beam with Δg analogous to Fig. 6.6(b), $l = 0.25\,\mu\text{m}$, $\gamma = 0.02\,\text{mJ/mm}^2$, $\tilde{\varepsilon}_\text{x} = 0.1$, solid line represents the analytical solution, spatial discretization: (a) 84×18 finite elements, (b) 336×72 finite elements

influence on the formation of the interface, cf. Fig. 6.8. Furthermore it is observed that with a finer mesh the homogenized mobility of part $\langle \text{①} \rangle$ and $\langle \text{③} \rangle$ reduce to approximately zero, since with a finer discretization the derived mobility parts can be described more precisely, cf. Fig. 6.7. Accordingly, the homogenized parts of $\langle \text{①} \rangle + \langle \text{③} \rangle \neq 0$ in Fig. 6.6 are a result of the discretization. This is why this effect is called retained mobility. However, the retained mobility is small compared to the actual mobility.

In order to assess the impact of spatial discretization on practical problems, a practical example is investigated. In a two-dimensional domain, a quadratic homogeneous field with two martensite variants is considered. The edge length of the quadratic domain is chosen to be $9\,\mu\text{m}$, motivated by the austenite grain sizes determined in Sec. 4. At the edges of the field, all degrees of freedom are set to zero using Dirichlet boundary conditions. In this field, the martensite transformation is initiated by a lath-like nucleus, where the order parameter of the first martensite variant is defined with $\varphi_1 = 1$, also with Dirichlet boundary conditions. The model and material parameters are defined comparable as in Sec. 6.1.1 with $l = 0.25\,\mu\text{m}$, $\Delta g = -500\,\text{mJ/mm}^3$, $\gamma = 0.02\,\text{mJ/mm}^2$. The transformation strains are defined with

$$\tilde{\varepsilon}_1 = \begin{pmatrix} \tilde{\varepsilon}_\text{x} & 0 \\ 0 & -\tilde{\varepsilon}_\text{x} \end{pmatrix}, \quad \tilde{\varepsilon}_2 = -\tilde{\varepsilon}_1$$

and material parameters remain the same. Five different mesh resolutions are investigated: 54×54, 108×108, 216×216, 432×432, 864×864. The 108×108 mesh corresponds to the element edge length of $l_\text{el} = 1/12\,\mu\text{m}$, which was chosen in Sec. 6.1.1.

Fig. 6.9 shows the martensite content of the first four mesh variants with respect to time. From t_0 to t_2, a slightly slower transformation takes place with the 108×108 discretization
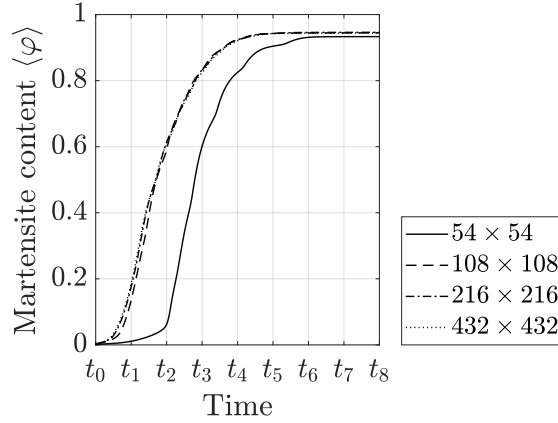
Figure 6.9: Homogenized martensite volume fraction with respect to time with four different spatial mesh resolutions, parameters: $l = 0.25\,\mu m$, $\Delta g = -500\,mJ/mm^3$, $\tilde{\varepsilon}_x = 0.1$, $\gamma = 0.02\,mJ/mm^2$, the 864×864-variant is not shown because it is indistinguishable with the 432×432-variant
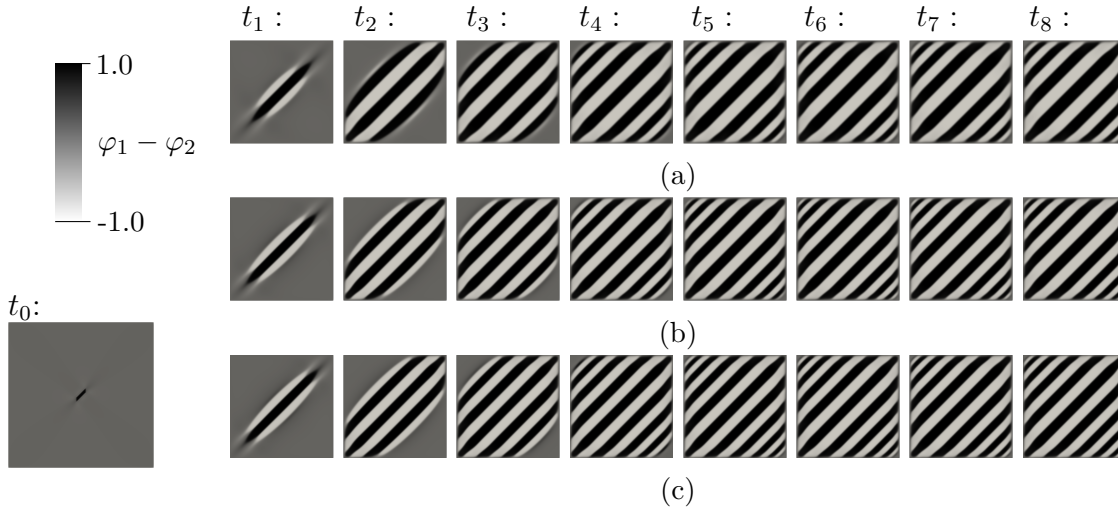

Figure 6.10: Evolution of martensite morphology with (a) 108×108, (b) 216×216, (c) 432×432 finite elements, parameters: $l = 0.25\,\mu m$, $\Delta g = -500\,mJ/mm^3$, $\tilde{\varepsilon}_x = 0.1$, $\gamma = 0.02\,mJ/mm^2$

compared to the finer meshes. However, from time t_2 no significant differences between the three mesh resolutions are observed. An almost constant martensite content is observed from time t_5 for the three finest variants in Fig. 6.9. With 54×54 elements a significant different transformation behavior is obtained.

For further analysis, the evolution of the martensite morphology is shown in Fig 6.10. With a similar homogenized martensite content over time a decreasing martensite block width is observed. It is concluded that the transformation induced stresses in the austenite-martensite interfaces as well as in new forming martensite-martensite interfaces are the reason for this. With a coarse mesh, the stresses in the interfaces are overestimated. This can be seen in Fig. 6.11, where exemplary the von Mises stress distribution of two mesh resolutions at time t_1 is shown. Due to the higher stresses in the interfaces, the self-accumulation of the two variants is delayed longer, resulting in a larger block width.
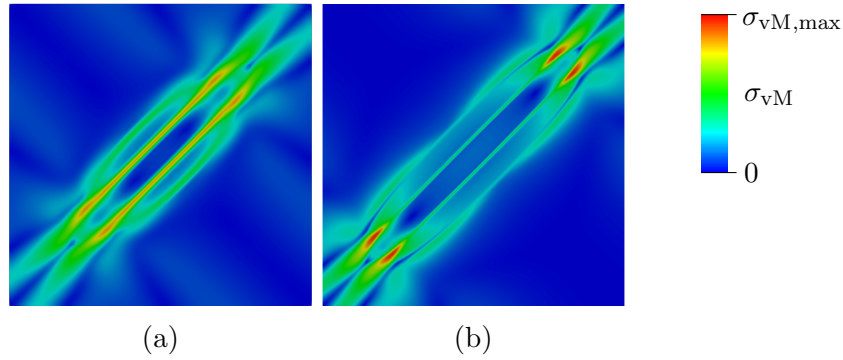
Figure 6.11: von Mises stress field at t_1 with (a) 108×108, (b) 432×432 finite elements, parameters: $l = 0.25\,\mu\text{m}$, $\Delta g = -500\,\text{mJ/mm}^3$, $\tilde{\varepsilon}_\text{x} = 0.1$, $\gamma = 0.02\,\text{mJ/mm}^2$
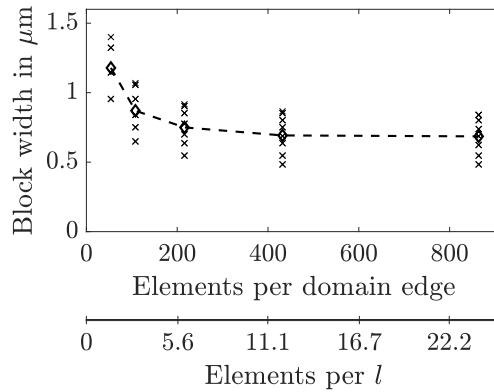
Figure 6.12: Block width dependency on the discretization with parameters $l = 0.25\,\mu\text{m}$, $\Delta g = -500\,\text{mJ/mm}^3$, $\tilde{\varepsilon}_\text{x} = 0.1$, $\gamma = 0.02\,\text{mJ/mm}^2$

The block width which occurs at time t_8 is quantified in Fig. 6.12. With increasing mesh resolution a smaller mean block width is obtained. Full convergence is achieved with 432×432 finite elements. Accordingly, the interface width l covers twelve finite elements.

6.1.3. Discussion and Conclusions for Further Simulations

For the phase equilibrium state with $\Delta g = 0$ in combination with $\tilde{\varepsilon}_\text{x} = 0$, the analytical solution is perfectly reproduced. The introduction of a transformation strain $\tilde{\varepsilon}_\text{x} > 0$ leads to a distortion of the interface. More precisely, the interface becomes wider. The introduction of a phase imbalance with $\Delta g < 0$ leads to a movement of the interface, whereby the width of the interface is narrowed. With a favorable ratio of the terms, which support the interface formation to the chemical bulk driving forces, satisfactory interface formations can be reproduced. However, the physical value of interface energy of austenite-martensite interfaces rather is $\gamma \approx 1.0 \times 10^{-3}\,\text{mJ/mm}^2$, cf. Wang et al. (2014), Yang & Johnson (1993), Murr (1975). Such a small value combined with the high magnitudes of Δg in martensite transformation results in excessive interface distortion. Furthermore, this may cause the interface being insufficiently resolved for a given discretization. In order to ensure a stable interface formation with precise kinetics and the

absence of transformation strains, the control condition

$$\frac{|\Delta g|\, l}{\gamma} \approx 1 \tag{6.5}$$

should be fulfilled, cf. Borukhovich (2016); Schoof (2020). However, with the stabilizing effect of transformation strains, a ratio greater than one can be chosen.

With regard to finite-difference implementations, several strategies to counteract excessive interface distortion due to an unfavorable ratio of interface supporting terms and chemical bulk driving forces are conceivable (Schoof (2020)):

- Local limitation of the driving forces when a certain threshold value is exceeded according to Borukhovich (2016).

- Increasing the interface-supporting terms by additional terms, which support the diffuse interface but do not contribute to curvature minimization according to Chen et al. (2014)

In addition, the interface supporting terms can be increased by decreasing the interface width while refining the mesh (Schoof (2020)). However, at the mesoscale considered here, this leads to computational costs that are not accessible within the scope of this work. For this reason, a sufficiently large interface energy parameter is selected in a simplified manner.

Regarding the spatial discretization, it was found that there is a mesh dependency that affects the block formation. This is most likely due to the high stress and strain gradients in the interface, which can only be poorly described with linear shape functions. With linear shape functions, derived quantities within an element can only be represented as constants. In order to nevertheless obtain comparable results with adequate computational effort, uniform element sizes as well as uniform interface widths are chosen in the following investigations. A threefold element width regarding the interface width parameter, e.g. $l = 3\, l_{\mathrm{el}}$, which results in about five nodes discribing the interface is in line with other works with similar model formulations, cf. Yeddu (2018).

The local incompatibility between the phases is accommodated by elastic strains, cf. Basak & Levitas (2018, 2017). This results in elastic stresses and strains within the austenite-martensite and martensite-martensite interfaces in the simulations. Furthermore, the chosen interpolation function $h_i^{\mathrm{p3}}(\varphi_i)$ with $\sum_i^{n_{\mathrm{mart}}} h_i > 1$ for $0 < \varphi < 1$ increases elastic strains within the martensite-martensite interface. Note that stresses in the martensite-martensite interface are also obtained with the other interpolation functions investigated in Sec. 5.4.2 and are also observed in other works, cf. Basak & Levitas (2018, 2017). Vanishing elastic strains may be of great importance in resolving internal martensitic twins on a lower length scale. Quantitative data of stresses in martensite block interfaces are not available within the scope of this thesis. Thus, the problem of interfacial stresses is not addressed further. For the limited number of advanced modeling techniques of solid-solid interfaces concerning the interfacial stresses/strains, the reader is referred to Basak & Levitas (2017, 2018) and Schneider et al. (2015).

6.2. Two-Dimensional Isotropic Elastic Monocrystal

In the following investigations in this section, the austenite-martensite transformation is analyzed based on isotropic elastic material behavior in a two-dimensional domain. Due to the two-dimensional restriction, two martensite variants are considered. At the simulation domain edges all degrees of freedom are set to zero via Dirichlet boundary conditions. According to Yeddu (2018), thus a clamped monocrystal is modeled in order to investigate the effect of austenite grain size on the martensite start temperature and the martensite block width. The motivation is to verify that the phase field model is basically capable of representing important phenomena known from the literature. However, the applied modeling technique implicitly considers a grain embedded in an infinitely stiff environment, resulting in an overestimation of the austenite grain size effect. Isothermal simulations at different quenching temperatures with different carbon contents are made. The initiation of the martensite transformation is done by a pre-existing martensite lath with a constant length of 0.6 μm and a constant width of 0.25 μm. The longitudinal axis is inclined 45° to the horizontal. The pre-existing lath is imposed as Dirichlet boundary condition. This allows the diffuse interface to build up without the nucleus disappearing first, cf. Sec. 5.4.1. With the shape of the initial lath, a uni-directional orientation of the martensitic plates is forced.

6.2.1. Parameter Identification

The determination of the model parameters is based on literature as well as on experimental investigations. This section describes successively how elastic constants, transformation strains, chemical driving force and the interface energy parameter are determined.

Elastic coefficients. In this investigation, isotropic material behavior defined by the Young's modulus E and the Poisson's ratio ν is considered. In general, both parameters are temperature dependent, cf. Spittel & Spittel (2009). However, the influence of temperature on Young's modulus is higher, which is why this work focuses on a temperature dependence of Young's modulus. A possible dependency on the chemical composition is neglected and regarding the material behavior of austenite and martensite the same temperature dependence is assumed. Laptev et al. (2012) investigated the temperature dependency of Young's modulus of five different steels. The mean of the results are reflected in Fig 6.13. Depending on the temperature, austenite and/or pearlite is present. For both material states, the Young's modulus decreases with increasing temperature. Based on the results of Laptev et al. (2012), a linear approximation of the Young's modulus is defined with

$$E(T) = -111.5 \, \frac{\text{MPa}}{{}^{\circ}\text{C}} \, T + 213\,340 \, \text{MPa}. \tag{6.6}$$

The graph of Eq. (6.6) is shown in Fig. 6.13 as red solid line.

Transformation strains. The transformation strains (mesoscopic shape change strains) are calculated via the procedure presented in Sec. 5.7. As input quantities the lattice constants regarding austenite and martensite are needed. In this work these parameters are identified via reverse engineering in order to reflect experimentally observed martensite dilatation, which is the measured dilatation in Sec. 4 minus the thermal dilatation. Nevertheless, care is taken to ensure that the determined values make physical sense by reviewing corresponding literature.
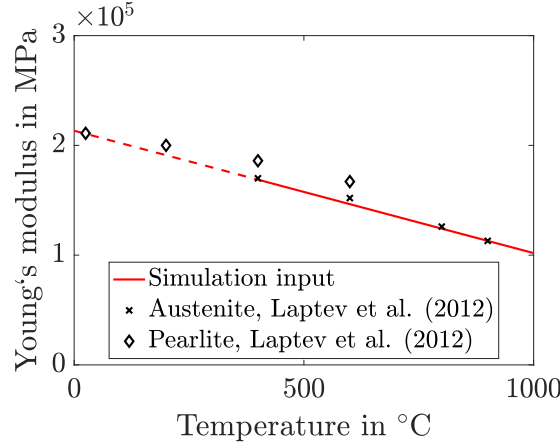
Figure 6.13: Temperature dependence of Young's modulus

With focus on Fe-C alloys the influence of carbon content on the austenite lattice parameters was investigated by Onink et al. (1993) using neutron diffraction. With increasing carbon content an increasing austenite lattice constant could be confirmed. Furthermore, the austenite lattice parameter was identified as a function of temperature. From these findings the lattice parameter of austenite is

$$
\begin{aligned}
a_\gamma{}^{\text{Onink}} &= \left(0.36306 + 7.83 \times 10^{-4} \times C_{\text{at.\%}}\right)\left(1 + \alpha_{\text{th},\gamma}\left(T - 1000\right)\right) \text{ in nm} \\
&\text{with} \quad \alpha_{\text{th},\gamma} = \left(24.9 - 0.5 \times C_{\text{at.\%}}\right) \times 10^{-6} \text{ in K}^{-1},
\end{aligned}
\tag{6.7}
$$

where $C_{\text{at.\%}}$ is the atomic percent of carbon and T the temperature in Kelvin. Lee et al. (2007) used Eq. (6.7) in a conversion model of transformation strains occurring during austenite decomposition to phase fractions concerning low-alloy steels with up to approximately 0.4 wt.% C. With data from Honda & Nishiyama (1932) (reflected by Nishiyama (2012)), the following equation can be extracted for carbon steels with 0.4 wt.% C to 1.6 wt.% C:

$$
a_\gamma{}^{\text{Honda}} = 0.005 \times C_{\text{wt.\%}} + 0.3545 \text{ in nm.}
\tag{6.8}
$$

Concerning the martensite lattice constants, Lee et al. (2007) developed temperature and carbon content dependent equations based on the work of Roberts (1953). Accordingly, the martensite lattice constants of low-alloy steel up to approximately 0.4 wt.% C are

$$
\begin{aligned}
c_\alpha{}^{\text{Lee}} &= \left(0.2861 + 0.0025855 \times C_{\text{at.\%}}\right)\left(1 + \alpha_{\text{th},\alpha}\left(T - 273\right)\right) \text{ in nm,} \\
a_\alpha{}^{\text{Lee}} &= \left(0.2861 + 0.0002898 \times C_{\text{at.\%}}\right)\left(1 + \alpha_{\text{th},\alpha}\left(T - 273\right)\right) \text{ in nm} \\
&\text{with} \quad \alpha_{\text{th},\alpha} = \left(14.9 - 1.9 \times C_{\text{at.\%}}\right) \times 10^{-6} \text{ in K}^{-1}.
\end{aligned}
\tag{6.9}
$$

Again, the data of Honda & Nishiyama (1932) is used to extract an equation for carbon steels with 0.4 wt.% C to 1.6 wt.% C:

$$
a_\alpha{}^{\text{Honda}} = 0.0125 \times C_{\text{wt.\%}} + 0.2855 \text{ in nm.}
\tag{6.10}
$$

The c_α/a_α ratio is given by Roberts (1953) and Roberts et al. (1953)

$$
\frac{c_\alpha{}^{\text{Honda}}}{a_\alpha{}^{\text{Honda}}} = 1 + 0.045 \times C_{\text{wt.\%}}.
\tag{6.11}
$$

Fig. 6.14 shows the graphs of the equations for the lattice constants known from the literature. Based on the equations from Lee et al. (2007) the lattice constants of two temperatures are depicted. It should be noted that with regard to Eqs. (6.7) and (6.9) the conversion from weight to atomic percent is based on a two-phase Fe-C system. The high temperature of $T = 720\,°C$ corresponds to the martensite start temperature of pure iron published by Morito et al. (2003). Furthermore, the lattice parameters of pure iron at martensite start temperature given by Morito et al. (2003) are depicted. The functions for c_α agree particularly well at room temperature, since they are based on the same data.
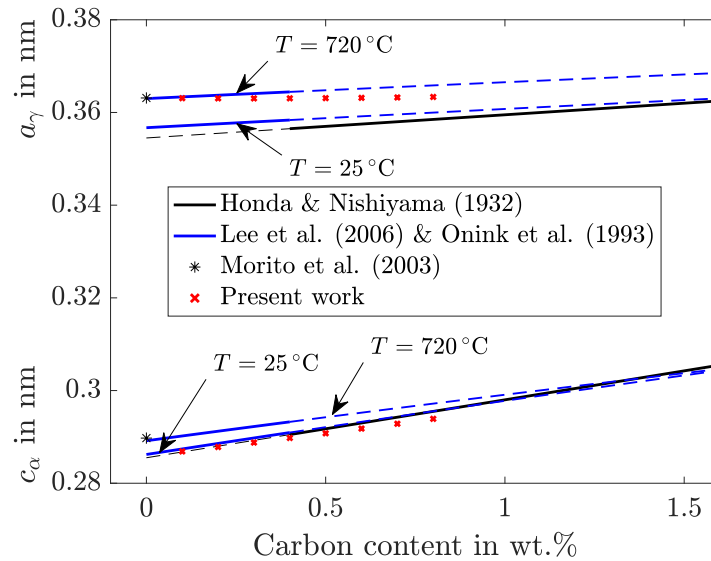
(a)
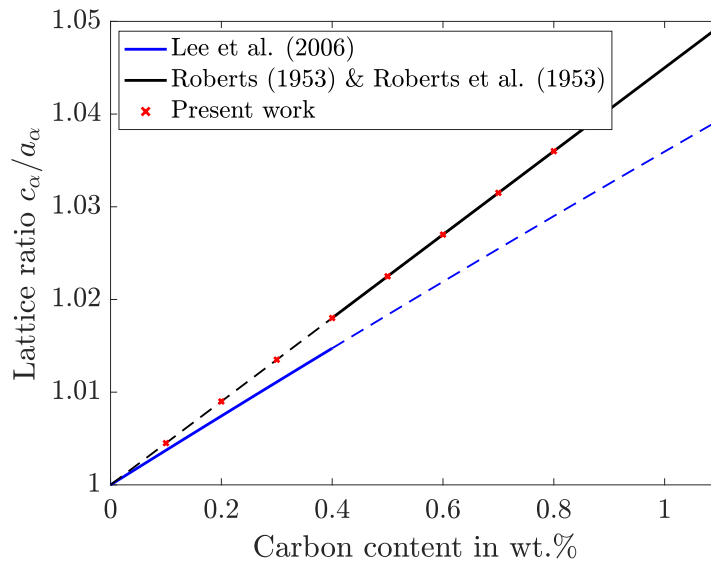
(b)

Figure 6.14: Lattice constants (a) a_γ and a_α, (c) c_α/a_α in dependence of carbon content

The aim is to identify transformation strains that reflect the experimentally evaluated macroscopic martensite dilatations. The macroscopic dilatation of the simulation can be determined by assuming a homogeneous distribution of all martensite variants. Thus, the

sum of the martensite transformation strains (shape change strains) calculated with the PTMC within a crystallographic (CPP) packet gives the macroscopic volumetric strain, which is identical in all three directions. The macroscopic dilatation determined in this way is fitted to experimentally determined data by adaption of the lattice constants. The martensite dilatation data of two materials are available in this work, which are shown in Fig. 6.15. In Fig. 6.15, the red curve represents the dilatation finally determined with the lattice parameters depicted in Fig. 6.14 as red crosses. The lattice constants thus determined are in plausible orders of magnitude compared to literature data. Based on the available data, an increasing dilation with increasing carbon content is obtained.
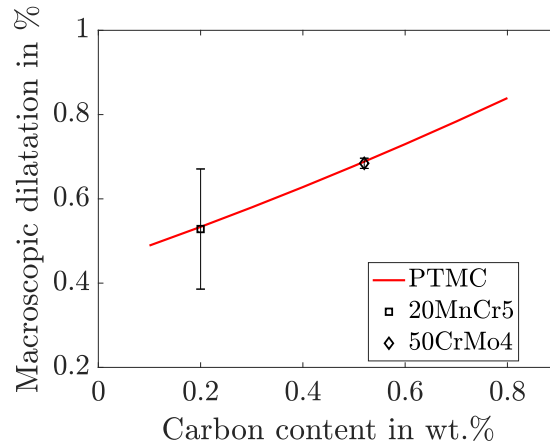
Figure 6.15: Macroscopic martensite dilatation in dependence of carbon content

Based on the PTMC, three-dimensional strain tensors in dependence of the carbon content are determined. These shape deformation strains are determined from invariant plane deformations. Thus, a principal axis transformation results in a tensor, where two entries of the main diagonal are occupied. The strain of the third direction is zero. The non-zero principals strains ϵ_I and ϵ_{II} are used to construct the martensite transformation strain tensors for the two-dimensional plane strain case

$$\tilde{\boldsymbol{\varepsilon}}_1 = \begin{pmatrix} \epsilon_I & 0 \\ 0 & \epsilon_{II} \end{pmatrix}, \quad \tilde{\boldsymbol{\varepsilon}}_2 = \begin{pmatrix} \epsilon_{II} & 0 \\ 0 & \epsilon_I \end{pmatrix}. \tag{6.12}$$

In contrast to Graf et al. (2021c), who simply set the components with respect to the third spatial direction to zero, the dilation of the three-dimensional case can be reproduced in this way. In Fig. 6.16, the determined strains are plotted against the carbon content. The magnitudes of the strain components decrease as carbon content increases, whereas the dilatation ($\epsilon_I + \epsilon_{II}$) increases.

With the chosen martensite transformation strains determined with the NW orientation relationship two martensite variants of two Bain groups are considered. One NW variant represents two KS variants of the same Bain group, cf. Koumatos & Muehlemann (2017). In the often observed lath morphology, a martensite block consists of laths that can be assigned to two KS variants of the same Bain group in the same crystallographic packet, cf. Kitahara et al. (2006) and Morito et al. (2003). Accordingly, simplified block structures consisting of two martensite variants are simulated with the variants selected here.
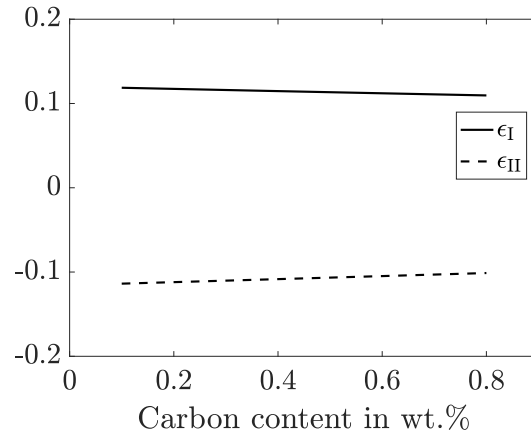
Figure 6.16: Martensite transformation strain for two-dimensional plane strain simulations

Chemical driving force. Here and in the rest of the work, isothermal temperatures $T \leq T_{\mathrm{MS}}$ are considered. With limitation to this regime, the parameter Δg is determined with Thermo-Calc (2020b) steels database version 8.1, which uses the CALPHAD methodology, see Andersson et al. (2002). Based on the material system 50CrMo4, the (Gibbs) free energy in J/m^3 is calculated for FCC and BCC material phase. In a temperature range from $0\,^\circ$C to $1000\,^\circ$C the difference of the energies are evaluated and used as temperature dependent model input parameter $\Delta g(T)$. Fig. 6.17 shows the energy density difference with different carbon contents. As carbon content increases, the austenitic phase is stabilized and the equilibrium temperature decreases. This leads to the fact that for a constant temperature $T \leq T_{\mathrm{MS}}$, the magnitude of chemical driving force decreases with increasing carbon content.
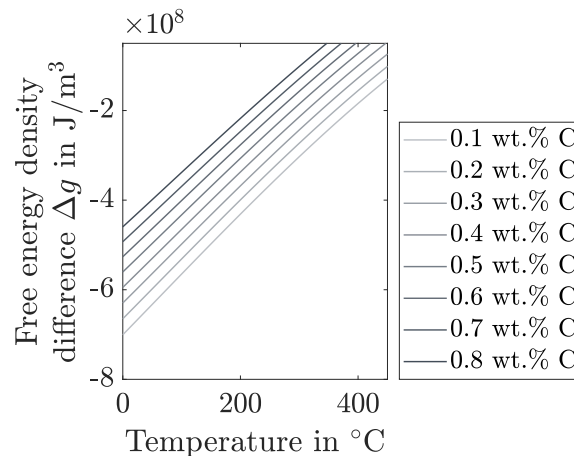
Figure 6.17: Free energy difference on basis of low-alloy steel 50CrMo4 with different carbon contents

Interface energy parameter. In this model, the interface energy parameter γ is a numerically driven parameter. With a given Δg, the interface energy parameter γ should be chosen large enough to form a stable interface, cf. Sec. 6.1.3. Therefore, for a given model setup with a critical Δg at martensite start temperature, the maximum value of γ is determined at which martensite embryo growth is still achieved.

In this section, γ is calibrated based on the two-dimensional clamped monocrystal with centered initial lath. Calibration is performed for a material system with carbon content of 0.4 wt.% (based on 50CrMo4). The material system with 0.4 wt.% corresponds approximately to the middle of the examined carbon variation (0.1 - 0.8 wt.%), with which the validity of the model can be examined in both directions. A simulation edge length of $l_\gamma = 9.0\,\mu\text{m}$ is chosen based on the measured austenite grain sizes of material 50CrMo4. The martensite start temperature is approximated with the relevant parts of the equation from Jäniche et al. (2013),

$$T_{\text{MS}}{}^{\text{Jaeniche}} = 0.495 \times T_{\text{MS}}{}^{\text{HJN}} + 0.00095 \times (T_{\text{MS}}{}^{\text{HJN}})^2 + 40 \text{ in } {}^\circ\text{C} \qquad (6.13)$$

with

$$T_{\text{MS}}{}^{\text{HJN}} = 550 - 350 \times \text{C}_{\text{wt.\%}} - 40 \times \text{Mn}_{\text{wt.\%}} - 20 \times \text{Cr}_{\text{wt.\%}} - 10 \times \text{Mo}_{\text{wt.\%}} \text{ in } {}^\circ\text{C} \quad (6.14)$$

by Hollomon et al. (1946). Eq. (6.13) represents a correction of Eq. (6.14) with respect to low-alloy steels, based on the data published by Wever et al. (1954) and Rose & Hougardy (1972). The measured T_{MS} of the actual 50CrMo4 agrees well with the martensite start temperature determined with Eq. (6.13). With simulating an isothermal state at $T_{\text{MS}}{}^{\text{Jaeniche}} = 332\,{}^\circ\text{C}$, the martensite starts to grow with a maximum interface energy parameter of $\gamma = 7.16 \times 10^{-3}$ mJ/mm^2. Despite the simplified model configuration, the determined value is remarkably in the order of magnitude of the natural interface energy with 1.0×10^{-3} mJ/mm^2.

6.2.2. Prediction of Martensite Start Temperature

The martensite start temperature with the current model is identified with a number of isothermal simulations at constant quenching temperatures T_{q} in relevant temperature ranges. The martensite start temperature is then the highest at which the pre-existing nucleus starts to grow. Using this method with the previously defined parameters, the prediction of the martensite start temperature with different carbon contents is possible. The results are shown in Fig. 6.18.

For validation, Fig. 6.18 shows the results of Eqs. (6.13) and (6.14), as well as the result of the model developed by Capdevila et al. (2002) with

$$\begin{aligned} T_{\text{MS}}{}^{\text{Capdevila}} = {} & 764.2 - 302.6 \times \text{C}_{\text{wt.\%}} - 30.6 \times \text{Mn}_{\text{wt.\%}} - 8.9 \times \text{Cr}_{\text{wt.\%}} \\ & + 2.4 \times \text{Mo}_{\text{wt.\%}} - 14.5 \times \text{Si}_{\text{wt.\%}} - 273.15 \text{ in } {}^\circ\text{C} \end{aligned} \qquad (6.15)$$

and the experimentally determined start temperature of material 50CrMo4. Compared with literature results, the martensite start temperature is underestimated for $\text{C}_{\text{wt.\%}} < 0.4$ and overestimated for $\text{C}_{\text{wt.\%}} > 0.4$. With reference to the result of Capdevila et al. (2002), the predicted martensite start temperature is about 4% lower with $\text{C}_{\text{wt.\%}} = 0.1$ and about 11% higher with $\text{C}_{\text{wt.\%}} = 0.8$. The discrepancies could be in the simplified assumption of a constant interface energy parameter. Additionally, the simplified assumption of a two-dimensional and fully clamped simulation with a constant size is probably the reason for deviations. For example, a smaller carbon content increases the required austenitization temperature, cf. Jäniche et al. (2013), while an increasing austenitization temperature can lead to enlarged austenite grains, cf. Yang & Bhadeshia (2009).

The influence of the austenite grain size on the martensite start temperature is investigated next. By means of phase field simulation, this has already been investigated recently by
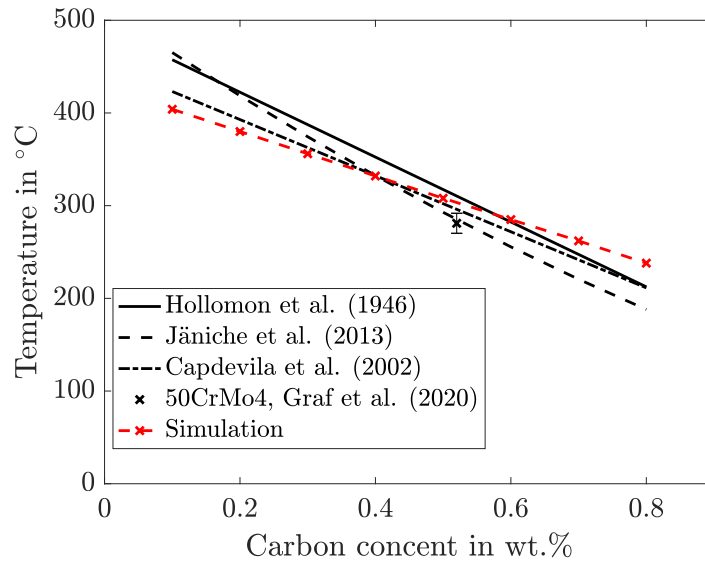
Figure 6.18: Martensite start temperature with different carbon contents on basis of low-alloy steel 50CrMo4

Yeddu (2018) with regard to stainless steels. In contrast to the work of Yeddu (2018), however, a temperature-dependent, purely elastic material behavior is assumed here. In this investigation, the size of the simulation domain is varied, keeping the discretization with a constant element length of $1/12\,\mu$m. Within the scope of this investigation, the simulation domain size l_γ is declared as austenite grain size.

Regarding the definition of the interface energy parameter, two variants are investigated. In the first variant, as before, the interface energy parameter is defined as constant $\gamma = 7.16 \times 10^{-3}$ mJ/mm². In the second variant, the ratio $\Delta g/\gamma$ is held constant. With increase of the negative magnitude of Δg, γ is linearly increased with

$$\gamma(\Delta g) = \frac{7.16 \times 10^{-3}}{\Delta g_{\mathrm{MS}}(\mathrm{C_{wt.\%}})}\Delta g(T)\,\mathrm{mJ/mm^2}, \tag{6.16}$$

where $\Delta g_{\mathrm{MS}}(\mathrm{C_{wt.\%}})$ is the critical Δg at T_{MS}. With this the ratio in Eq. (6.5) is held constant, which ensures the formation of the diffuse interface even with high negative magnitudes of Δg.

The results are shown in Fig. 6.19. With increasing austenite grain size, the martensite start temperature increases, whereas the slopes of the curves decrease with increasing austenite grain size. This is consistent with previous experimental observations, cf. Yang & Bhadeshia (2009). The reason for decreasing martensite start temperatures are increasing mechanical stresses (accompanied with the martensitic transformation) with decreasing austenite grain size. Compared to the slopes of the curves with $\gamma = $ const. in Fig. 6.19(a), the slopes of the curves with $\gamma/\Delta g = $ const. are larger, which is due to the Δg-dependence of the interface parameter. An increase of γ additionally inhibits the initial martensite formation, which is the case for $l_\gamma < 9\,\mu$m. With $l_\gamma > 9\,\mu$m a smaller energy parameter results, which leads to transformations at higher temperatures.
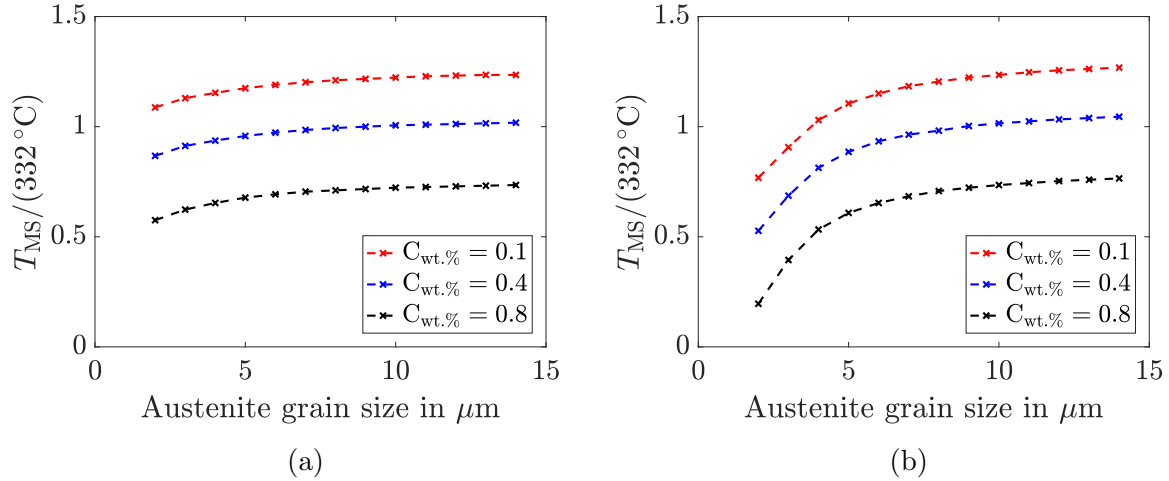
Figure 6.19: Martensite start temperature with different carbon contents and austenite grain sizes on basis of low-alloy steel 50CrMo4 with (a) $\gamma = $ const. and (b) $\gamma/\Delta g = $ const.

### 6.2.3. Martensite Size Effects and Retained Austenite

In order to evaluate martensite size effects and retained austenite, isothermal simulations at several quenching temperatures T_q are performed. The interface parameter is chosen analog to Eq. 6.16 in order to ensure smooth interfaces at low quenching temperatures. The evaluation is performed using the fully relaxed state. Size effects are quantified in terms of the block widths that occur and are shown in Fig. 6.20. Additionally, the number of fully formed blocks is evaluated and noted above the block widths in Fig. 6.20. Accordingly, a different number of martensite blocks is formed depending on the quenching temperature. At high temperatures it is energetically favorable to form nine blocks, while at low temperature eleven blocks are formed. As the carbon content increases, the temperature at which nine blocks are counted decreases. The jump from nine to eleven blocks leads to a shift in the average block width. With a constant number of blocks, the average block size increases as the quenching temperature decreases. At lower temperatures a higher final martensite fraction is obtained. With the same number of blocks this results in larger block widths.

In Fig. 6.21, the block widths of 50CrMo4 with different carbon contents at a constant quenching temperature of $T_q = 30\,°\text{C}$ are compared. With increasing carbon content a slightly decreasing block width is obtained. Based on experimental investigations, Morito et al. (2003) also identified decreasing blocks sizes with increasing carbon content. However, the effect seems to be much more significant in reality. Morito et al. (2003) state that a possible reason for this effect is that in low carbon alloys, laths in a large block are formed by autocatalysis and significant plastic accommodation might occur in the austenite matrix. According to Morito et al. (2003) it is further argued that in high carbon alloys the strain of martensitic transformation could not be easily relieved by plastic accommodation in the austenite matrix. The austenite is harder than in low carbon alloys due to solid solution hardening by carbon and lower martensite start temperatures. This effect cannot be described with the purely elastic model used here.

In the current modeling, the effect of increasing block widths with decreasing quenching temperature and the effect of decreasing block widths with increasing carbon content are
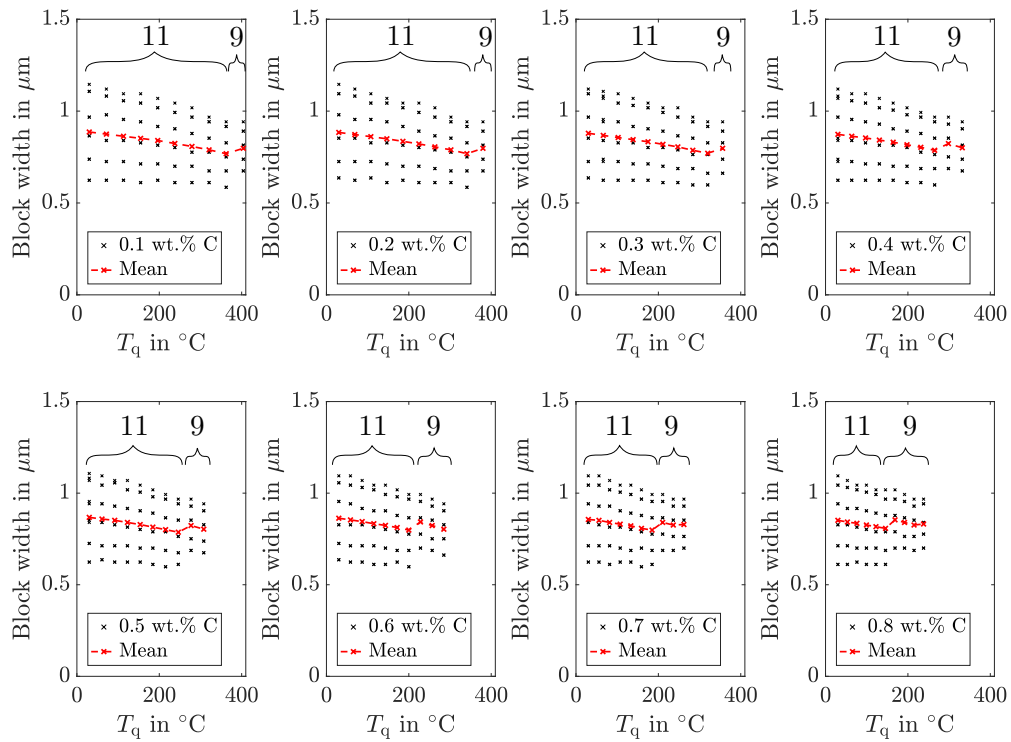
Figure 6.20: Martensite block widths with different carbon contents on basis of low-alloy steel 50CrMo4 at different quenching temperatures
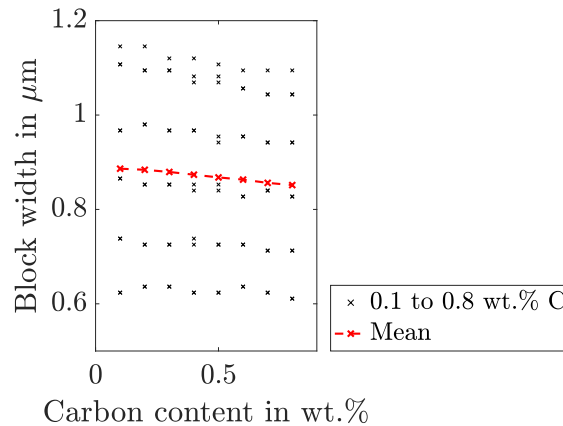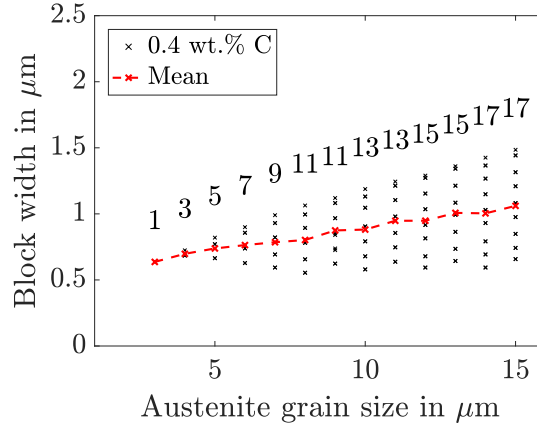

Figure 6.21: Martensite block widths with different carbon contents on basis of low-alloy steel 50CrMo4 at $T_{\mathrm{q}} = 30\,°\mathrm{C}$

a result of the chosen interface energy parameter with $\gamma/\Delta g = \mathrm{const}$. With decreasing quenching temperature, the magnitude of Δg increases, resulting in a higher γ. This is also the case at constant quenching temperature and decreasing carbon content. An increasing interface energy parameter inhibits the formation of martensite blocks during evolution, which results in a larger block width.

As the austenite grain size increases, the mean block width increases proportionally with

an increasing number of martensite blocks, cf. Fig. 6.22. Based on experiments, this effect has already been reported by Morito et al. (2005) regarding low-alloy steels with 0.2 wt.% C. In a Fe–0.1C–5Mn steel, however, no significant block width dependence on austenite grain size was found by Hanamura et al. (2013). It is assumed that an increased plastic relaxation rate in the austenite matrix with decreasing carbon content mitigates this effect.


Figure 6.22: Martensite block widths on basis of low-alloy steel 50CrMo4 with 0.4 wt.% C at $T_q = 25\,°C$ depending on austenite grain size

The retained austenite content $1 - \langle \varphi \rangle$ is evaluated with Eq. (6.4) at the fully relaxed state. Fig. 6.23 shows the result with different carbon contents in dependence of the constant quenching temperature. When the quenching temperature falls below the martensite start temperature, a large volume $> 70\%$ is suddenly transformed into martensite. With further decreasing quenching temperature, the retained austenite content decreases steadily to below 10% at $T_q = 30\,°C$. With increasing martensite content an increasing level of retained austenite is obtained. This effect is consistent with the literature, cf. Jäniche et al. (2013). Depending on the cooling rate, an amount of 5 - 7% retained austenite is experimentally detected in a quenched 50CrMo4 by Eggbauer et al. (2018), which is in good agreement with the results obtained here.
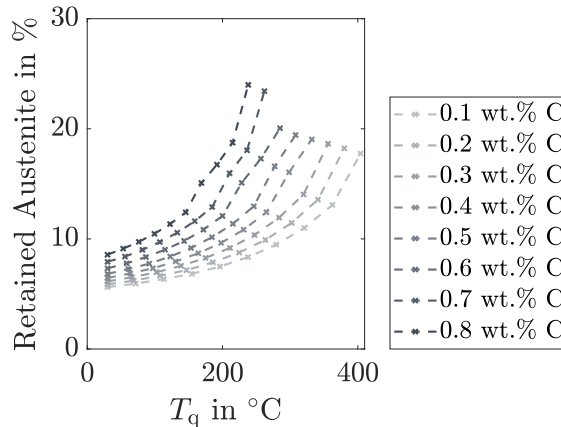
Figure 6.23: Retained austenite at different quenching temperatures on basis of low-alloy steel 50CrMo4 with different carbon contents
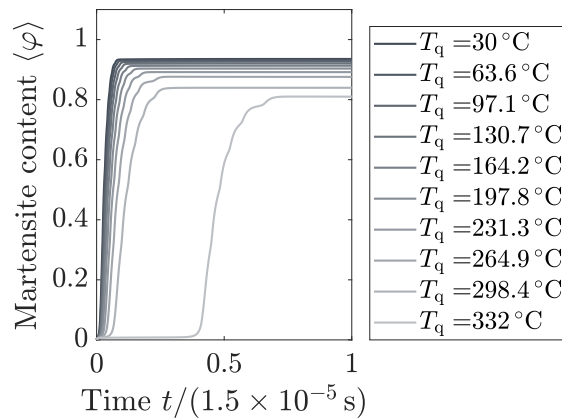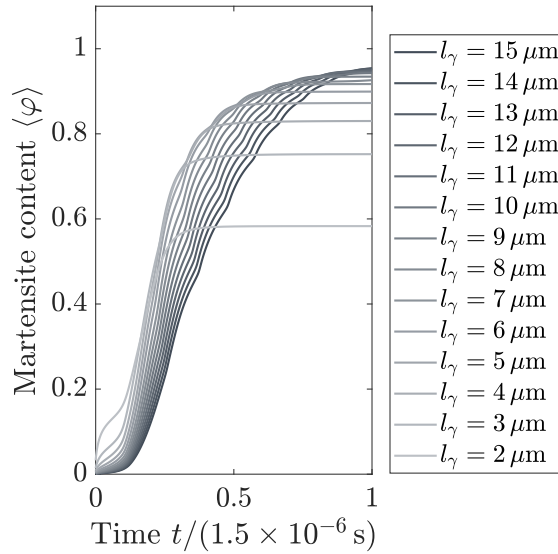
Figure 6.24: Martensite content over time of low-alloy steel 50CrMo4 with 0.4 wt.% C at different quenching temperatures

6.2.4. Transformation Kinetics

Based on the time course of the martensite volume fraction, the transformation kinetics are now investigated. Fig. 6.24 shows the martensite volume fraction of a steel with 0.4 wt.% C on basis of 50CrMo4. With decreasing quenching temperature, the final martensite content is reached earlier, whereby the final martensite content increases with decreasing quenching temperature. The slope of the martensite content over time increases with lower quenching temperature, which indicates an increased transformation velocity. The reason for this is the increasing chemical driving force.

The smaller the grain, the faster the final martensitic state is reached at a constant quenching temperature, see Fig. 6.25. Especially in the initial phase ($\langle \varphi \rangle < 0.2$), the transformation rate decreases with increasing austenite grain size. This is most likely due to the decreased stresses in systems with increasing austenite grain sizes. Based on experiments with continuous cooling an initially higher martensite transformation rate in microstructures with decreasing austenite grain size was observed by Van Bohemen & Sietsma (2014).

Figure 6.25: Martensite content over time of low-alloy steel 50CrMo4 with 0.4 wt.% C at $T_q = 25\,°\text{C}$ with different austenite grain sizes

6.3. Two-Dimensional Isotropic Viscoplastic Monocrystal

In Sec. 6.2.3 was found that martensite size effects with different carbon contents reported by experimental investigations in literature are not reflected by a purely elastic material behavior. Therefore, in this section the influence of plasticity on the martensite evolution is analyzed. The influence of plastic accommodation seems to be particularly relevant at low carbon contents. For this reason, the following investigation is based on the steel with 0.2 wt.% C studied in Sec. 6.2. Unless otherwise specified, the same model configuration as in Sec. 6.2 with $l_\gamma = 9.0\,\mu\text{m}$ and $\gamma/\Delta g = \text{const.}$ is used.

6.3.1. Influence of Interface Yield Stress Modeling

In general it is conceivable that the yield stress changes with transition from austenite to martensite. Thus, a yield stress regarding austenite $\sigma_{y,\gamma}$ and martensite $\sigma_{y,\alpha}$ is defined. By means of a function in dependence of the order parameter, the yield stress is interpolated between austenite and martensite. Various equations for calculating the effective yield stresses are known from the literature. As an example, consider the work of Schoof et al. (2018a), where the effective yield stress is weighted linearly. In other works a threshold is defined, see e.g. Yamanaka et al. (2008). In order to make a meaningful choice in this work, the following interpolation functions are investigated, where c_b and c_a are user constants:

$$h_{\sigma_y,1} = \begin{cases} \sigma_{y,\alpha} & \text{, if } \sum_{i=1}^{n_{\text{mart}}} \varphi_i > 0.5 \\ \sigma_{y,\gamma} & \text{, else} \end{cases} , \qquad (6.17)$$

$$h_{\sigma_y,2} = \sum_{i=1}^{n_{\text{mart}}} [\varphi_i^3(6\,\varphi_i^2 - 15\,\varphi_i + 10)]\,(\sigma_{y,\alpha} - \sigma_{y,\gamma}) + \sigma_{y,\gamma}, \qquad (6.18)$$

$$h_{\sigma_y,3} = \exp\left\{-\left(\frac{\sum_{i=1}^{n_{\text{mart}}} \varphi_i - 0.5}{c_a}\right)^2\right\} c_b + h_{\sigma_y,1}. \qquad (6.19)$$
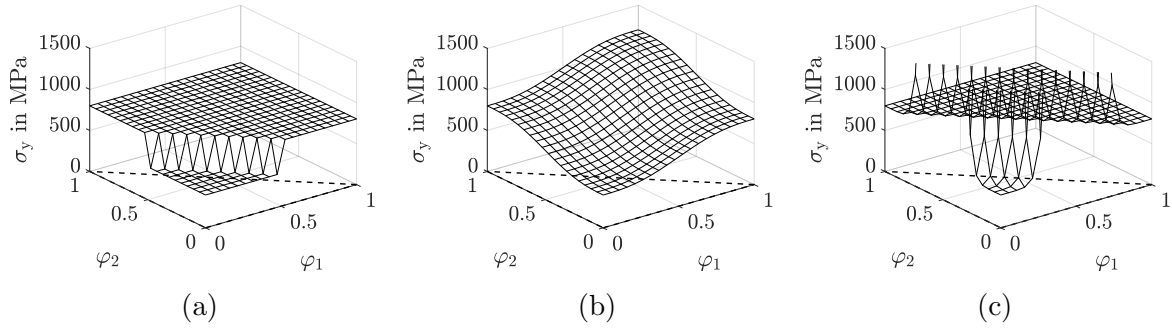
Figure 6.26: Graphs of yield stress in dependence of two order parameters with $\sigma_{\mathrm{y},\alpha} = 800\,\mathrm{MPa}$, $\sigma_{\mathrm{y},\gamma} = 400\,\mathrm{MPa}$ (a) $h_{\sigma_{\mathrm{y}},1}$ (b) $h_{\sigma_{\mathrm{y}},2}$ (c) $h_{\sigma_{\mathrm{y}},3}$, $c_{\mathrm{a}} = 1/8$, $c_{\mathrm{b}} = 20\,\mathrm{GPa}$, black dashed line encloses the relevant region

The graphs of Eqs. (6.17)-(6.19) are shown in Fig. 6.26 for the current case of two martensite variants. Eq. (6.17) describes an unsteady transition and is inspired by the work of Yamanaka et al. (2008). Eq. (6.18) is a smooth transition from austenite to martensite. The characteristic of Eq. (6.19) is that within the austenite-martensite interface the yield stress assumes such high values that no plastic deformation takes place within these interfaces. This is based on the assumption that the interface acts as a barrier to dislocation motion. With c_{a} the width of the barrier can be modified and c_{b} scales the height of the barrier.

Simulations with constant quenching temperature at $T_{\mathrm{q}} = 30\,^{\circ}\mathrm{C}$ are performed. Inspired by Yeddu (2018), the plasticity parameters are chosen to be

Viscosity	η_{v}	$= 0.006$	MPa s,
Yield stress (Austenite)	$\sigma_{\mathrm{y},\gamma}$	$= 500$	MPa,
Yield stress (Martensite)	$\sigma_{\mathrm{y},\alpha}$	$= 1000$	MPa,
Hardening modulus (Austenite and Martensite)	H	$= 700$	MPa.

Fig. 6.27 shows the martensite content and the resulting block widths of the corresponding simulations. Simulations with $h_{\sigma_{\mathrm{y}},1}$ and $h_{\sigma_{\mathrm{y}},2}$ do not show visible differences. At times $0 < t < 1 \times 10^{-6}\,\mathrm{s}$ with $h_{\sigma_{\mathrm{y}},3}$ a constant level of martensite content is achieved earlier, which can be explained by the increased elastic strains in the interface due to the high yield stress, cf. Sec. 6.1. From $t \approx 1 \times 10^{-6}\,\mathrm{s}$ a sightly lower final martensite content is observed, which is accompanied with a slightly smaller mean block width.

Fig. 6.28 shows the von Mises stress fields as well as the equivalent plastic strain fields with the final martensite structure. The martensite structure is similar with all yield stress functions and the choice of the function does not seem to have a significant influence on the stress and strain distribution inside the simulation domain for this model configuration. The cluster of plastic strain in the center is a result of the pre-existing martensite lath, which induces high stresses at the beginning of the simulation. At the edge of the simulation domain, higher stresses result with $h_{\sigma_{\mathrm{y}},3}$ due to lower plastic activity. Due to the high yield stresses between the martensitic phase and the boundary, where the transformation is restricted via Dirichlet boundary condition, the acting stresses cannot be relaxed here. This leads to the slightly lower final martensite content and the accompanying slightly thinner martensite blocks.
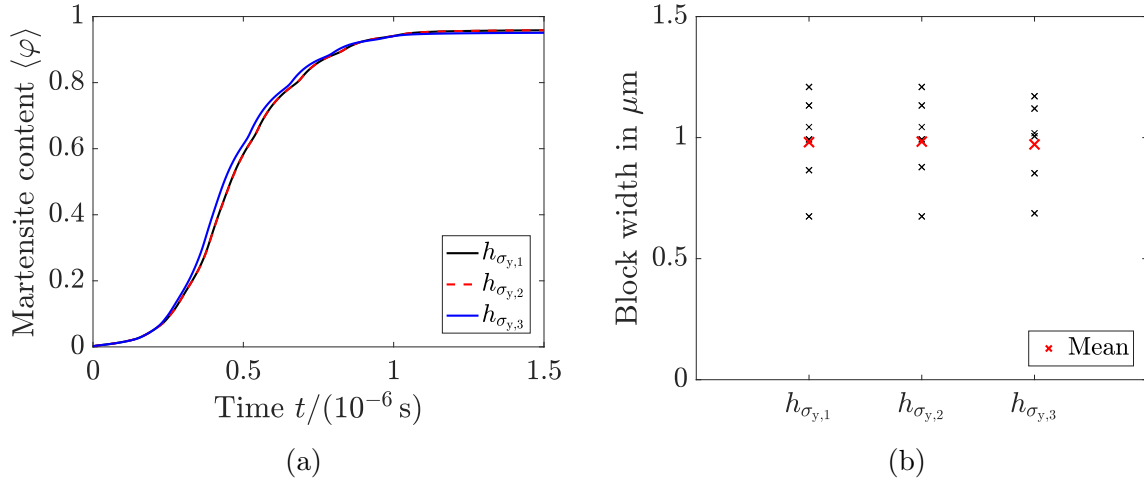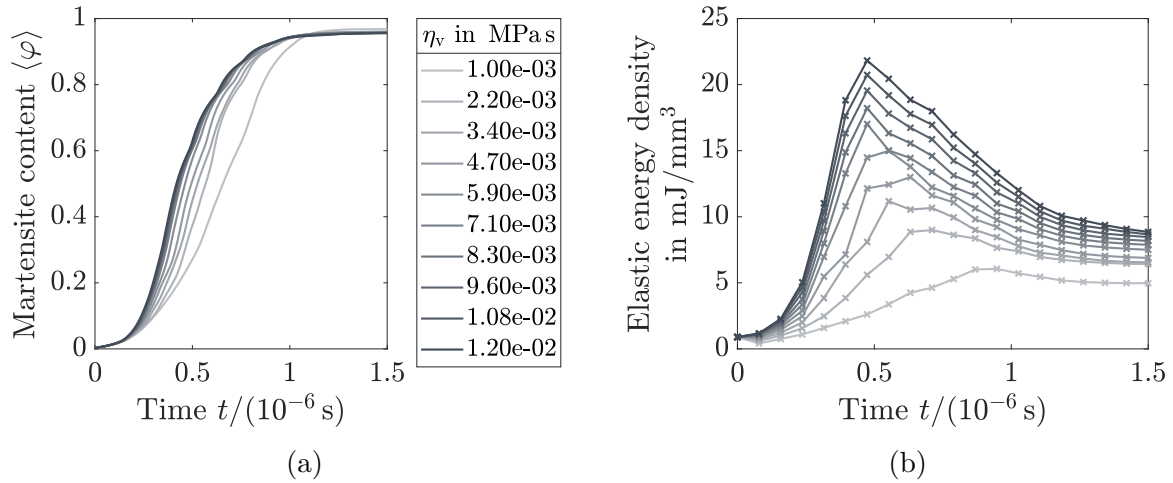
Figure 6.27: Martensite content in (a) and final block widths in (b) with different yield stress functions at $T_{\mathrm{q}} = 30\,^{\circ}\mathrm{C}$
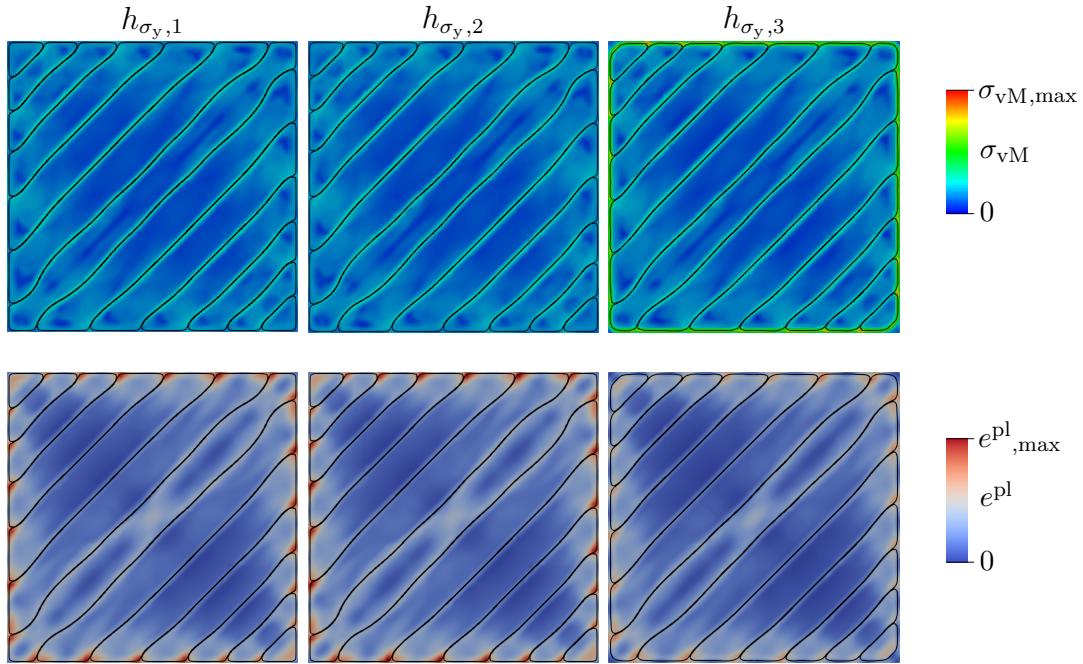
Figure 6.28: Final von Mises stress and equivalent plastic strain fields at $T_{\mathrm{q}} = 30\,^{\circ}\mathrm{C}$ with black isolines at $\varphi_i = 0.5$

6.3.2. Influence of Viscosity

It is known that the choice of the viscosity material parameter η_{v} influences the martensite evolution significantly, see e.g. Yeddu et al. (2012a) and Schoof et al. (2018a). Yeddu et al. (2012a) investigated the influence on the growth behavior of a spherical martensite embryo in an austenitic matrix at T_{MS}. In contrast to the numerical studies in this work, the martensitic embryo was initially set but not prevented from shrinking by boundary conditions. Thus, a critical value was found, which defines the limit with which a natural growth through sufficient relaxation is possible. With higher viscosity, the elastic driving force is too high and a reverse transformation takes place. With viscosities significant lower than the critical value a purely relaxation driven growth appear with no auto-nucleation of

Figure 6.29: Martensite content in (a) and elastic energy density in (b) with different viscosities at $T_q = 30\,°C$

other martensite variants. Moderate viscosities below the critical value allow martensite grow and the typical auto-nucleation of other variants is simulated. Based on these results, in several studies the relaxation rate or viscosity is calibrated to reflect the martensite start temperature (Yeddu (2018); Yeddu et al. (2012b); Malik et al. (2012)). Schoof et al. (2018a) note that the size of the initial martensite nucleus affects the critical value of viscosity and is thus not a classical material constant, but rather a problem dependent quantity. However, no other methodology is known from the literature.
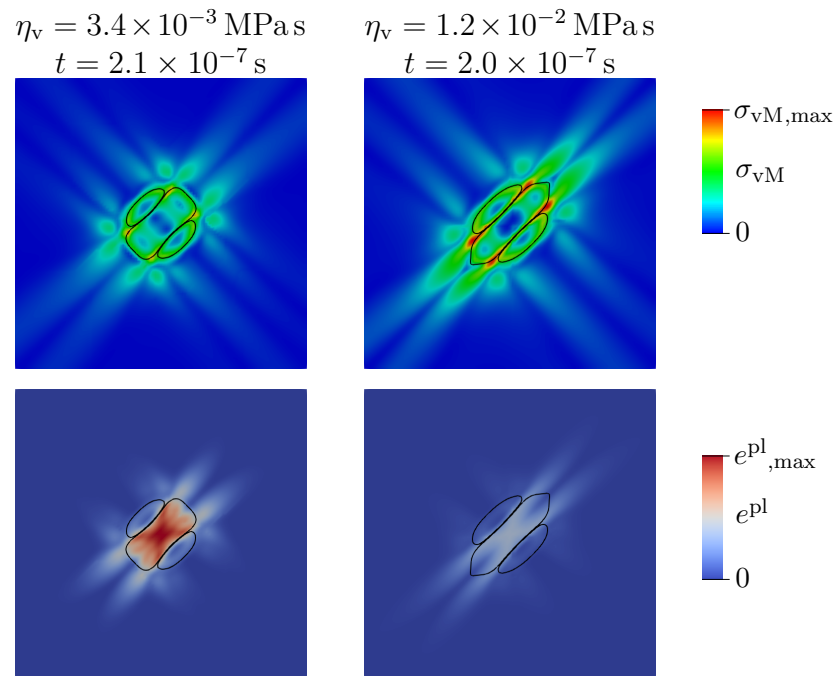
Figure 6.30: von Mises stress and equivalent plastic strain fields in the early transformation stage at $T_q = 30\,°C$ with black isolines at $\varphi_i = 0.5$

In this work, initial reverse transformation is prevent by boundary conditions and the numerical parameter γ is calibrated in order to reflect the martensite start temperature by
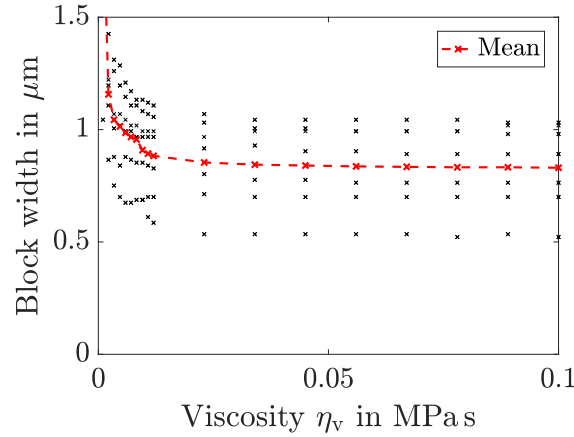
Figure 6.31: Block widths in dependence of viscosity at $T_q = 30\,°C$

taking stable interface formation into account. Accordingly, the conditions are different, which is why the influence of η_v is investigated in this model configuration based on isothermal simulations at $T_q = 30\,°C$. As interpolation function for the yield stress, $h_{\sigma_y,1}$ is chosen. Based on the previous results, this selection is not expected to have a significant impact on the resulting martensite structure. The plasticity parameters remain unchanged, while the viscosity is varied.

From the course of martensite content with respect to time in Fig. 6.29(a) a significant influence on the transformation behavior is detected. With increasing η_v the martensitic transformation occurs more rapidly. In the time interval $0 < t < 1 \times 10^{-6}\,$s a constant level of martensite content is achieved later with decreasing η_v. The final martensite content decreases with increasing viscosity. This is consistent with the results of Yamanaka et al. (2010). Fig. 6.29(b) shows that with increasing viscosity the mechanical stresses are relaxed more slowly. This results in a peak in the elastic energy density that becomes more pronounced with increasing viscosity.

In Fig. 6.30, the von Mises stress and equivalent plastic strain fields of two exemplary early transformation states is shown. With $\eta_v = 3.4 \times 10^{-3}\,$MPa s stresses are relaxed with more plastic accommodation compared to the simulation with $\eta_v = 1.2 \times 10^{-2}\,$MPa s. Due to the increased plastic accommodation, auto-nucleation takes place at larger block widths. Fig. 6.31 shows the block widths of the final structure in dependence of viscosity. As η_v increases, the block widths decrease. A significant reduction of the block width can be observed in the range $1.0 \times 10^{-3} < \eta_v < 1.2 \times 10^{-2}\,$MPa s. It should be noted that in the region around $1.0 \times 10^{-3}\,$MPa s no typical lath- or plate-like martensitic structure is formed due to the high degree of plastic accommodation.

In accordance with the discussion in Sec. 4.5, it can be concluded that a high level of elastic energy supports auto-nucleation and the martensite transformation can be designated as auto-nucleation driven. A low level of elastic energy accompanied by significant plastic accommodation inhibits auto-nucleation and the martensite growth can be designated as relaxation-driven.

6.3.3. Martensite Sizes at Different Quenching Temperatures

From the experimental investigation in this work it is known that there are martensitic steels, which block sizes seem to be unaffected from the corresponding cooling rates. With

other steels decreasing block sizes and/or widths with shorter cooling times are detected. Based on the investigation of modulated martensite transformation in Fe-Ni alloys, Loewy et al. (2015) conclude that the thermal activated mechanism behind that is the local stress/strain relaxation. Kim et al. (2012, 2011) compared the microstructural features of lath martensite isothermally formed at a temperature just below T_{MS} and athermally formed with continuous cooling to room temperature. In addition to a significant influence on the lath formation, a coarser and more complex block structure was observed with respect to the isothermally formed martensite at high temperature. In this section, the developed model is used to test whether this effect can be reproduced within the scope of fast isothermal martensite transformations, by consideration of plasticity.

With the currently chosen definition of the interface energy parameter according to Eq. (6.16) an increasing block width with decreasing quenching temperature is predicted. This effect counteracts the effect which is to be investigated here. Since no data is currently available to validate the martensite sizes at different quenching temperatures, an attempt is made to adjust γ in order to predict constant block widths for quenching temperatures $T_q < T_{MS}$ in an elastic material. This is achieved by the linear dependency

$$\gamma(\Delta g) = c_c \, \Delta g + c_d \tag{6.20}$$

with $c_c = -1.2030 \times 10^{-5}$ mm and $c_d = 6.3 \times 10^{-5}$ mJ/mm^2. The determined block widths with the adapted definition of γ are presented in Fig. 6.32(a). The viscosity and the yield stress of austenite are chosen to be temperature dependent with

$$\eta_v(T) = -2.29 \times 10^{-5} \, \frac{\text{MPa} \, \text{s}}{^\circ\text{C}} \, T + 9.6 \times 10^{-3} \, \text{MPa} \, \text{s} \tag{6.21}$$

based on the results in Sec. 6.3.2, and

$$\sigma_{y,\gamma}(T) = -1.7 \, \frac{\text{MPa}}{^\circ\text{C}} \, T + 851.4 \, \text{MPa}. \tag{6.22}$$

Using Eq. (6.21), the effective viscosity lies between $1.0 \times 10^{-3} < \eta_v < 9.0 \times 10^{-3}$ MPa s for the investigated temperatures $30\,^\circ\text{C} \leq T_q < T_{MS}$. The effective yield stress of austenite is in the range of $200 \leq \sigma_{y,\gamma} \leq 800$ MPa. Eq. (6.21) and (6.22) are strong simplifications of the temperature dependence that is probably present in reality. However, the focus is more on the basic representation of the thermally activated relaxation mechanism than on the exact simulation of a specific material.

Fig. 6.32 shows that taking visco-plasticity into account results in a larger block width at a higher quenching temperature. Based on the assumption that with higher quenching rates more martensite is produced at lower temperatures, the quenching rate dependence of the block width can be explained. It is also plausible that the viscosity increases with increasing carbon content. A higher viscosity leads to an auto-nucleation dominated transformation mechanism. This process is faster and the plastic relaxation is not sufficiently large to cause a rate-dependence of the block widths.

6.4. Two-Dimensional Polycrystalline Structures

In this section, martensite evolution in polycrystalline austenite structures is investigated. The investigation is carried out within the two-dimensional framework and is therefore limited to two martensite variants. In contrast to previous numerical studies in this
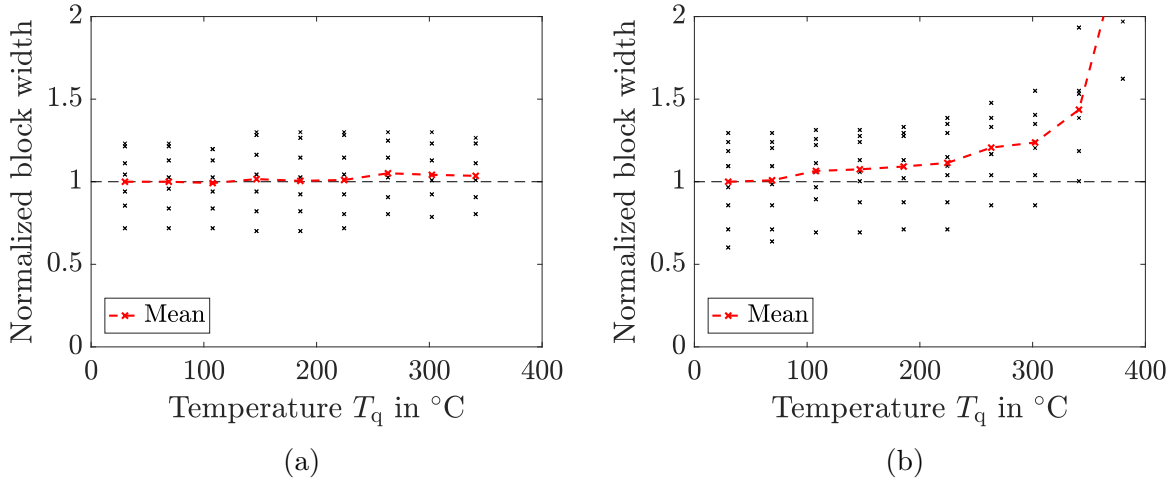
Figure 6.32: Block widths in dependence of quenching temperature T_q, (a) elastic material with interface parameter correction, (b) elasto-viscoplastic material behavior

work, anisotropic elasticity is considered here. In detail, an orthotropic symmetry of the elasticity tensor is assumed, see Vannucci (2018). With

$$(\boldsymbol{\mathcal{C}}^\gamma)^V = (\boldsymbol{\mathcal{C}}^{\alpha_i})^V = (\boldsymbol{\mathcal{C}}^*)^V = \begin{pmatrix} C_{11} & C_{12} & C_{12} & 0 & 0 & 0 \\ C_{12} & C_{11} & C_{12} & 0 & 0 & 0 \\ C_{12} & C_{12} & C_{11} & 0 & 0 & 0 \\ 0 & 0 & 0 & C_{44} & 0 & 0 \\ 0 & 0 & 0 & 0 & C_{44} & 0 \\ 0 & 0 & 0 & 0 & 0 & C_{44} \end{pmatrix} \tag{6.23}$$

the elastic crystals of austenite and martensite have identical properties along the three axis. In the polycrystal framework the elasticity tensors and the martensite strain tensor are rotated according to random angles around the axis perpendicular to the plane of display (z-axis). With the rotation matrix $\boldsymbol{\mathcal{R}}(\phi_1^{\mathrm{Eul}}, \Phi^{\mathrm{Eul}}, \phi_2^{\mathrm{Eul}})$ according to the chosen Euler angle convention, the elasticity tensor as well as the martensite strain tensors for a specific austenite grain are thus calculated in tensorial notation with

$$\mathcal{C}_{ijkl} = \mathcal{R}_{im}\mathcal{R}_{jn}\mathcal{R}_{ko}\mathcal{R}_{lp}\mathcal{C}^*_{mnop}, \tag{6.24}$$

and

$$\tilde{\varepsilon}_{i,kl} = \mathcal{R}_{km}\mathcal{R}_{ln}\tilde{\varepsilon}^*_{i,mn}, \tag{6.25}$$

respectively.

In Sec. 6.3 it was shown numerically that a block size dependency can result from a thermal activated plastic accommodation of the material. However, in Sec. 4 no systematic dependency of the martensite block sizes is observed within measuring accuracy and within technical relevant ranges of cooling rate. It is therefore concluded, that the martensite evolution is dominated by the auto-nucleation mechanism. In order to resolve the resulting morphology, a purely elastic material behavior seems to be sufficient. The corresponding simulation parameters of this study are summarized in Tab. 6.2. The martensite transformation is simulated under isothermal conditions at room temperature. Note that

Table 6.2: Simulation input parameters for martensite transformation in material 50CrMo4 with two spatial dimensions

Name	Symbol/Value	Remark
Material specific:		
Elastic constants:	$C_{11} = 253.1\,\mathrm{GPa}$ $C_{12} = 132.4\,\mathrm{GPa}$ $C_{44} = 75.8\,\mathrm{GPa}$	cf. Schäfer et al. (2019a); Xie et al. (2004)
Transformation strains:	$\epsilon_{\mathrm{I}} = 0.1134$ $\epsilon_{\mathrm{II}} = -0.1066$	Calculated with PTMC, cf. Sec 6.2.1
Free energy difference:	$\Delta g = -520\,\mathrm{mJ/m^3}$	Calculated with Thermo-Calc TCFE 8 (Andersson et al. (2002)), corresponds to difference at approximately room temperature, cf. Sec 6.2.1
Mobility constant:	$M = 50\,000\,\mathrm{mm^2(Ns)^{-1}}$	cf. Sec. 6.1.1
Numerically driven:		
Interface energy parameter:	$\gamma = 0.02\,\mathrm{mJ/mm^2}$	Large enough to ensure a smooth interface
Interface width:	$l = 0.25\,\mathrm{\mu m}$	Corresponds to edge length of three elements

with this configuration, the athermal history of the material is ignored. According to Sec. 6.2 the quadratic simulation domain is discretized with a constant edge length to element number ratio of $1/12\,\mathrm{\mu m}$. Similarly, at the edges of the simulation domain, all degrees of freedom are set to zero via Dirichlet boundary conditions.

6.4.1. Influence Prior Austenite Grain Boundary and Irreversibility

According to Schoof et al. (2018b) martensite phase field simulations in polycrystalline structures can be divided into two groups. The first group consists of models, where a continuous order parameter for each martensite variant is used, regardless of the austenitic parent grain. The works of Jin et al. (2001) and Yamanaka et al. (2010) are examples of this group. The second group consists of models, where a separate set of order parameters is used in each austenitic parent grain, see e.g. Heo & Chen (2014) and Shi et al. (2015). Typically, a grain shape function is introduced here, which is zero outside the parent grain and one inside. This defines the grain to be updated and prevents variant growing of one grain into an adjacent one. Schoof et al. (2018b) presented a model based on the multiphase field formulation of Steinbach et al. (1996), Steinbach & Pezzolla (1999) and Nestler et al. (2005), where additionally the interface energy between austenitic grains can be taken into account.

The polycrystalline model of this work is part of the first group, where the interface energy between the austenite grains is not taken into account. However, the influence of different austenite grain boundary modeling techniques on martensite evolution is investigated. The following three variants are examined:
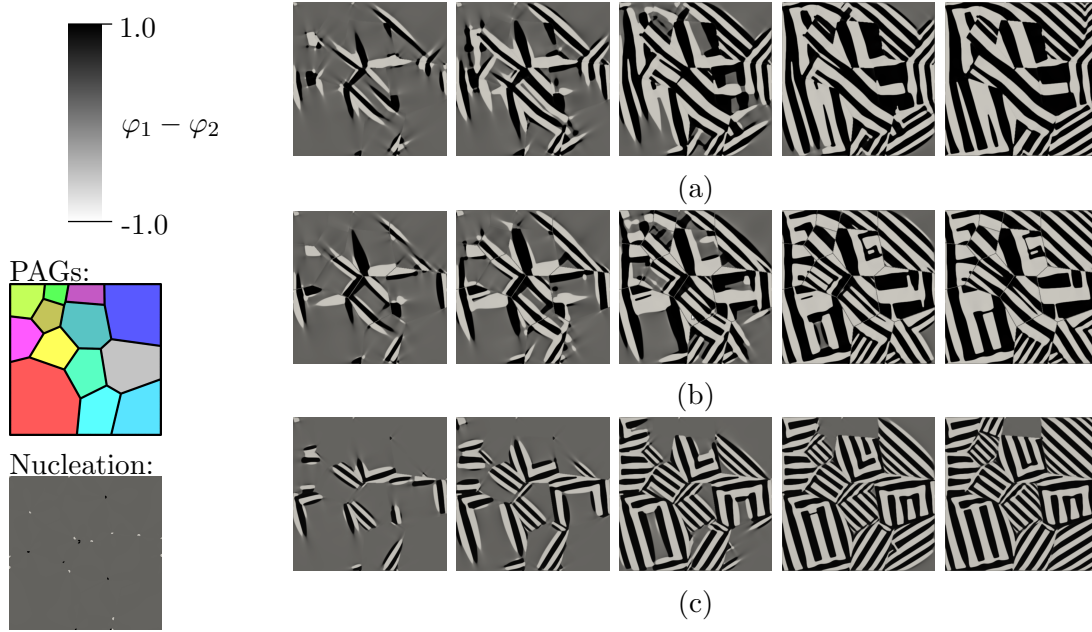
Figure 6.33: Evolution of martensitic structure with (a) variant A, (b) variant B, (c) variant C
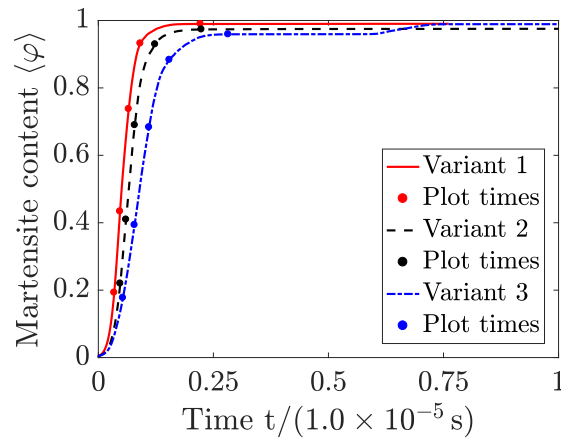
Figure 6.34: Martensite content over time with different boundary conditions at the PAG boundaries

Variant A No additional boundary conditions at the PAG boundaries.

Variant B Restriction of the order parameters via Dirichlet boundary conditions at PAG boundaries.

Variant C Restriction of displacements via Dirichlet boundary conditions at PAG boundaries.

With variant A there is an elastic incompatibility between the grain boundaries. Variant B additionally prevents the continuous growth of order parameters across grain boundaries and variant C corresponds to infinitely stiff grain boundaries.

A PAG structure is generated with Neper 3.5.3 grain growth parameters and 13 grains, see Quey (2019). With the method presented in Sec. 5.4.1, nucleation points are randomly
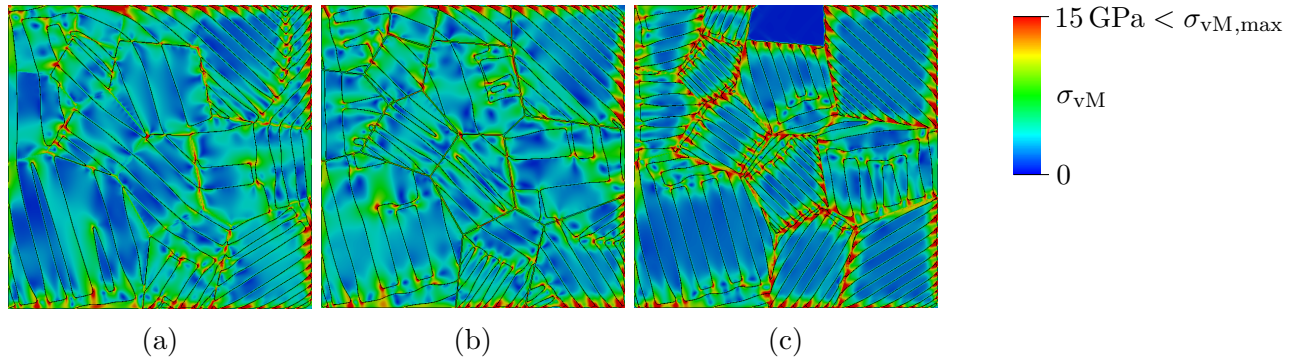
Figure 6.35: von Mises stress field in last snapshots in Fig. 6.33 with (a) variant A, (b) variant B, (c) variant C

distributed at triple junctions and grain boundaries. The corresponding PAG structure with edge length $37.5\,\mu m$, as well as the nucleation configuration are shown in Fig. 6.33. Nucleation sides represent pre-existing nuclei, which act as Dirichlet boundary conditions, where the order parameter of the corresponding variant is fixed at value one.

The resulting evolution of the overall martensite content in the exemplary PAG structure with identical nucleation sides is given in Fig. 6.34. With Variant A, a higher martensite content is obtained earlier compared to Variant B and C. The slowest development occurs with variant C, where additionally a stagnation of the martensite content starting at about $0.25 \times 10^{-5}\,s$ is observed. Between seconds 0.5×10^{-5} and 0.75×10^{-5}, there is another slight increase in the martensite content. The final martensite content is about the same level as with variant A. Variant B predicts the lowest final martensite content, which is due to the order parameter restriction at the grain boundaries.

The evolution of the morphology is illustrated in Fig. 6.33(a-c) with several snapshots. The times of these snapshots are marked as dots in Fig. 6.34. With all variants, the typical plate-like structure is achieved, although the structures differ in detail. With variant A continuous growth of martensite of one grain into an adjacent grain takes place especially at grain boundaries with low misorientation. In some places, a martensite needle of one variant triggers a martensite needle of the other variant in the adjacent grain. With variant B, there are clear boundaries between the grains. The mechanical interaction between the grains can nevertheless trigger a growth of a martensite needle in the neighboring grain. With the restriction of the displacements at the grain boundary (variant C), a finer block structure is obtained. It is remarkable that there is a clear correlation between grain size and block width, which was already determined in Sec. 6.2.3. This is not observed in variant A and B. The stagnation of the martensite content in variant C can clearly be attributed to the unfilled grain. After a certain time, however, the grain boundary is crossed and the last grain is filled with martensite.

The von Mises stress fields of the respective last snapshots in Fig. 6.33 are shown in Fig. 6.35. For illustration, the iso-lines with $\varphi_i = 0.5$ are overlaid as black lines. Due to the elastic incompatibility between the grains, stress peaks at PAG boundaries are predicted with variant A and B. Furthermore, stress peaks can be detected at the block ends, as well as at the edges of the simulation domain. With variant B, stress peaks with the same characteristics at the edges of the simulation domain are obtained at the PAG boundaries. Despite the high stresses, a continuous martensitic transition occurs without
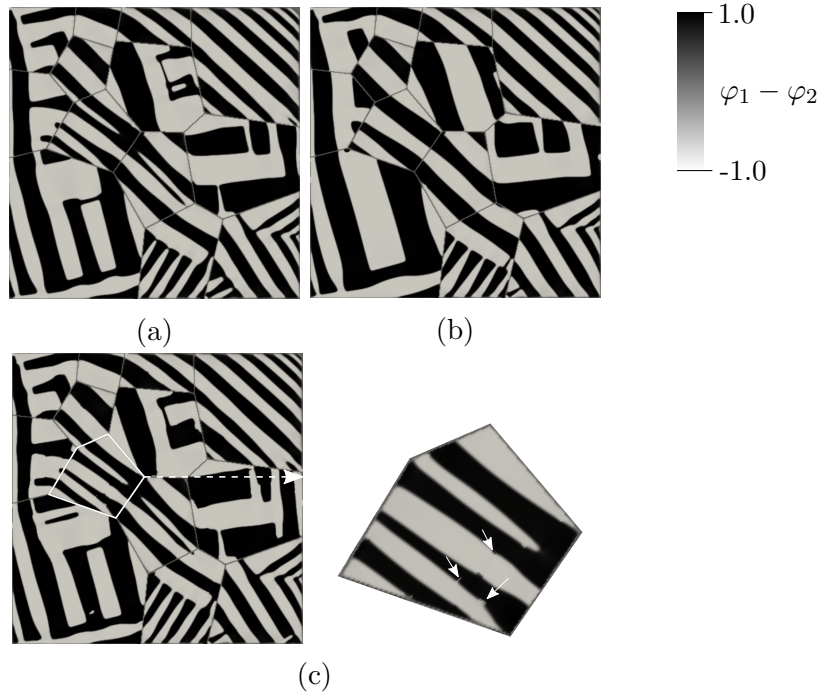
Figure 6.36: Illustration of martensite structure (a) at $t = 0.23 \times 10^{-5}$ s (b) at $t = 1.63 \times 10^{-5}$ s (c) fully relaxed microstructure with irreversibility

residual austenite at the grain boundaries.

In lath martensite, Mao et al. (2021) observed that localized stress is indirectly introduced into adjacent PAGs and can initiate a block growth. Thus some martensite blocks have special connectivity features. Accordingly, it is concluded that Variant B is the most realistic choice of boundary conditions at the PAG boundaries in the current model. Thus, a mechanical interaction between the grains is possible, while the evolution of the order parameter is stopped at the PAG boundaries. Therefore, Variant B is generally selected in the following.

The last snapshots shown in Fig. 6.33 correspond to a point in time at which the homogenized martensite content apparently does not change further. However, with almost constant martensite content, the martensite structure continues to change. This is shown in Fig. 6.36(a+b), which additionally shows a snapshot from a later point in time. At this point, re-transformations of one martensite variant into the other have dissolved individual block structures. One reason for this could be the overestimated interface energy due to the chosen interface energy parameter, which is factors higher than calculated with atomistic studies, cf. Wang & Urbassek (2013). A higher interface energy results in higher driving forces, which reduce the number of interfaces. Another reason may be the overestimated mechanical stresses, due to the purely elastic material behavior. Changes in the martensitic structure may be accompanied by load rearrangements, which may further cause changes in the structure. With plasticity taken into account, these high stresses would be relieved, cf. Sec. 6.3.

In a further simulation, the irreversibility presented in Sec. 5.2.4 is used in order to suppress a re-transformation. Hereby, the order parameter is fixed as soon as it reaches a threshold value $1 - \epsilon_{irr}$ with $\epsilon_{irr} = 1 \times 10^{-8}$. Fig. 6.36(c) shows the corresponding

fully relaxed martensitic structure. This reveals a disadvantage of the irreversibility. At some martensite-martensite boundaries a disrupted interface of the order parameters occur. This is exemplary demonstrated using a detailed view of a specific grain. The highlighted artifacts result from the fixed order parameters. However, comparison of the structures in Fig. 6.36(a) and (b) shows that essential features of the relaxed structure with irreversibility can be reproduced with the configuration without irreversibility by stopping the simulation at a time when there is no significant increase of the overall martensite content.

6.4.2. Influence of Austenite Grain Sizes and Nucleation

The influence of austenite grain structure as well as the number of nucleation sides is investigated in this section. For this purpose, microstructures with different numbers of nucleation points and PAG grain numbers are generated. The resulting average equivalent grain diameters are $d_{\mathrm{eq}} = 16.9, 11.2, 9.4$ in µm. Fig. 6.37 shows the microstructures of

Increasing number of nucleation points
$\longmapsto$

Increasing mean d_{eq}
$\uparrow$

Figure 6.37: Resulting martensite morphologies in different PAG structures and nucleation configurations
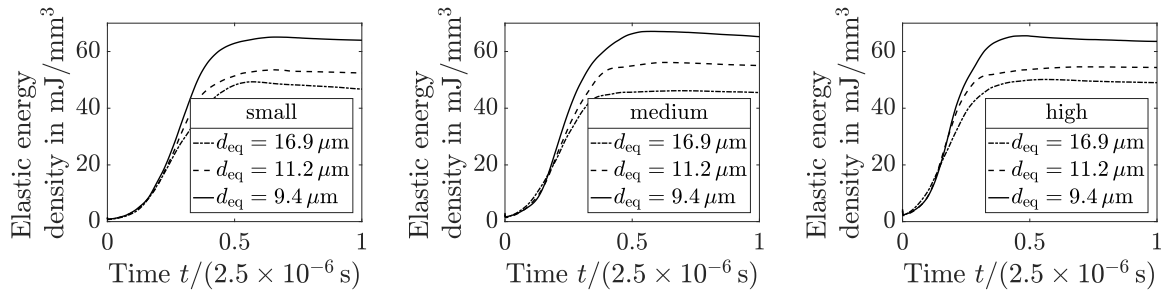
(a)

(b)
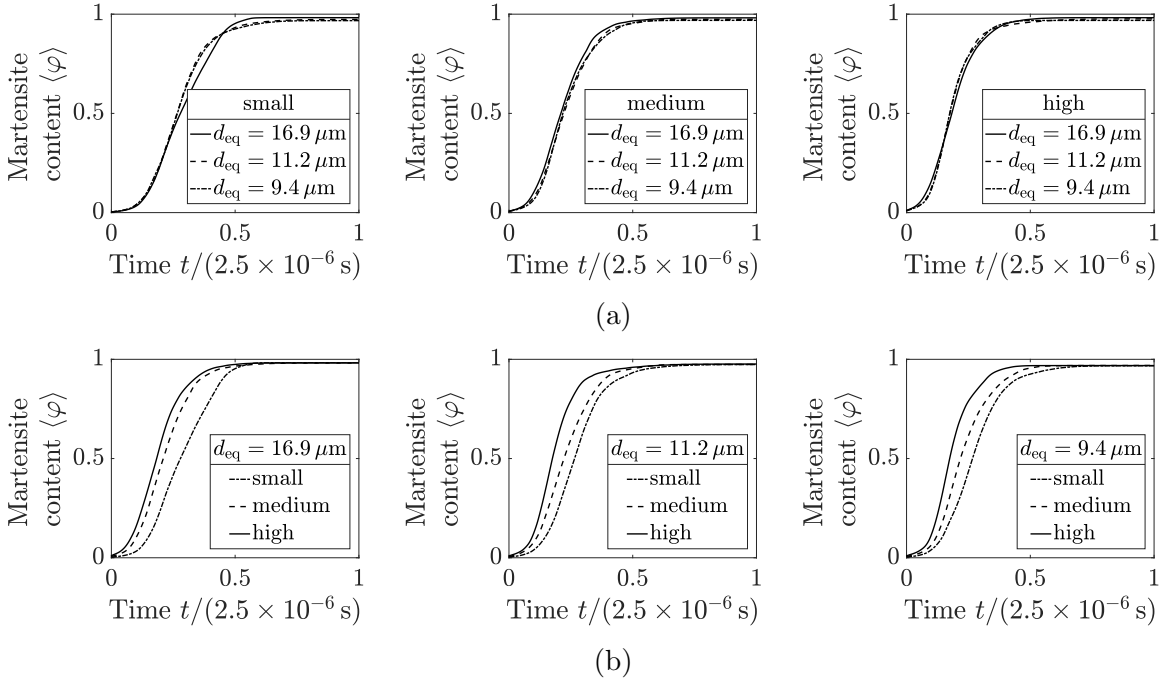
Figure 6.38: Martensite content evolution with respect to time in microstructures with different average austenite grains sizes ($9.4/11.2/16.9\,\mu$m) and different numbers of nucleation points (small/medium/high), comparison regarding (a) austenite grain sizes, (b) nucleation point numbers

these different configurations. According to the previous section, the snapshots show the microstructure of the point in time, where no further significant increase of the overall martensite content takes place. The nucleation sides are marked in red.

With the used PAG boundary modeling, a smaller austenite grain size leads to reduced lengths of blocks. Some grains with smaller grain sizes consist of blocks with smaller block widths. As an example, the lower left grain of the microstructures with the lowest number of nucleation points can be pointed out. However, a clear correlation between block width and PAG size cannot be identified. In the current modeling, the block width seems to be significantly influenced by the neighboring grains. Since direct coupling of the phase fields of adjacent grains is prevented by boundary conditions, this must result from mechanical interaction.

In the two-dimensional case with two martensite variants, those areas which have the same block orientation are considered as one packet. Focusing on the lower left PAG in the microstructures of the first row, shows that an increasing number of nucleation points can lead to an increasing number of packets. However, this is not universal, which is due to the fact that there are only two energetically favorable alignments of the block boundaries per grain in the two-dimensional environment. Thus, the martensite needles of different nucleation points often merge into one packet.

Fig. 6.38 shows the martensite content evolution regarding the different PAG and nucleation configurations. The comparison of the martensite content evolution with different average grain sizes in Fig. 6.38(a) shows no significant systematic influence of the grain size on the homogenized transformation behavior. The exception is the final martensite

Figure 6.39: Elastic energy density with respect to time in microstructures with different average austenite grains sizes $(9.4/11.2/16.9\,\mu m)$ and different numbers of nucleation points (small/medium/high), comparison regarding austenite grain sizes

content, which decreases with increasing PAG number, resulting from the higher PAG boundary density. From Fig. 6.38(b) it can be concluded that with an increasing number of total nucleation points, the considered domain is filled faster with martensite. With increasing number of PAGs (decreasing average equivalent diameter), a higher level of mechanical stresses is induced due to the martensitic transformation, cf. Fig. 6.39. This is most likely a result of the higher elastic incompatibility density, due to the higher density of PAG boundaries.

6.4.3. Martensite Transformation in 50CrMo4 Austenitic Microstructures

In this section, the martensitic transformation in austenitic structures, which represent the PAG structure of 50CrMo4 is simulated, see Sec. 5.3. The simulation domain edge length is chosen to be $50\,\mu m$. The initial martensite transformation event is stimulated by definition of pre-existing nuclei with the nucleation modeling presented in Sec. 5.4.1. Based on the assumed transformation process in Sec. 5 it can be concluded that the main number of packets result from single nucleation points at grain boundaries. According to Fig. 4.10 about twelve packets are counted in PAGs with $d_{eq} \approx 8.5\,\mu m$. Note that inevitably, packets that grew from a nucleation point outside the cutting plane were also counted. For this reason, a simplified average of four nuclei per grain is assumed in this two-dimensional simulation. Accordingly, 120 nucleation points are specified with the total number of 30 PAGs.

Fig. 6.40 illustrates the evolution of martensite in a 50CrMo4 austenitic microstructure. Starting from the initial nucleation, individual martensite blocks grow, and further ones are triggered by stress-assisted auto-nucleation. The overall martensite content with respect to time is shown in Fig. 6.41 in five microstructures with different PAG structures
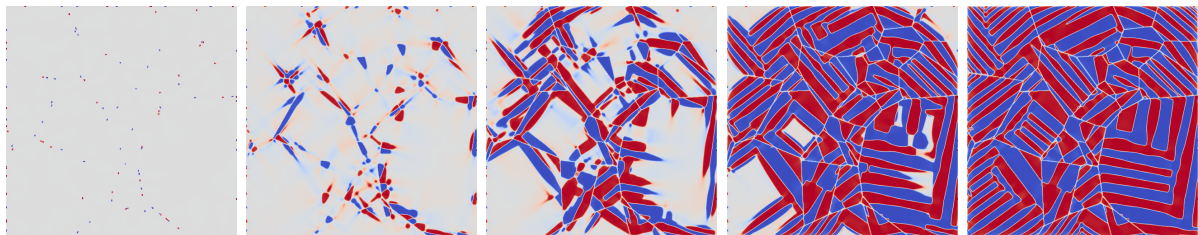
Figure 6.40: Simulated evolution of martensite (blue and red) in a 50CrMo4 austenitic structure, austenite is gray
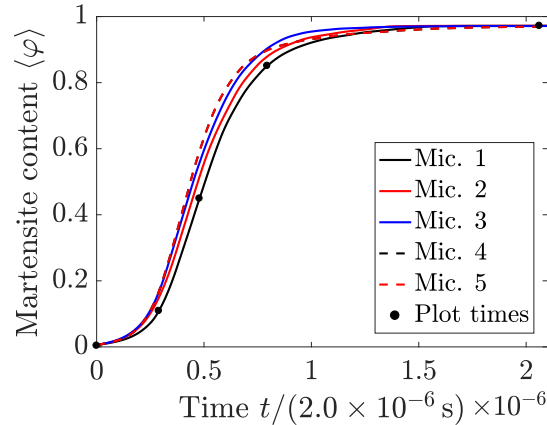
Figure 6.41: Martensite content with respect to time in different 50CrMo4 austenitic microstructures and plot times of snapshots in Fig. 6.40
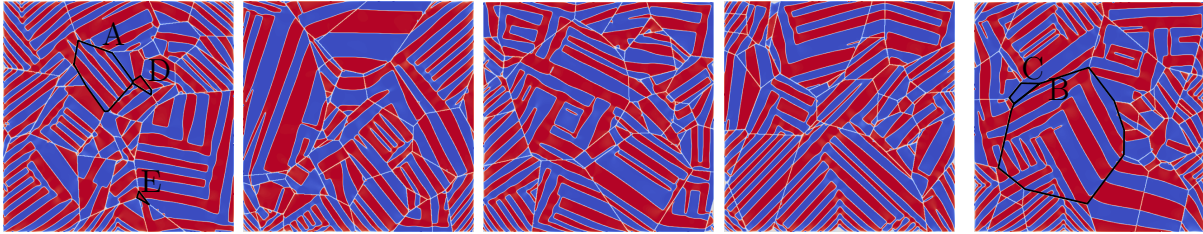
Figure 6.42: Simulated martensitic microstructures (blue and red) in different 50CrMo4 austenitic structures, austenite is gray

corresponding to the experimentally determined statistics. Fig. 6.42 shows the analogous resulting martensitic microstructures.

The final structures have a typical martensitic appearance with parallel blocks. Since the blocks in this two-dimensional view are aligned only in two directions within a PAG, the block structures of individual nucleation points unite. Consequently, the final structure does not represent the number of packets according to the number of nucleation points. In some large grains, a larger block width compared to other smaller grains can be observed, compare PAG A and B in Fig. 6.42. This effect could result from the stresses due to the elastic incompatibility at the grain boundaries. This can magnify the auto-nucleation within small grains. However, a strict correlation cannot be observed, since the block widths within a PAG are strongly influenced by the neighboring PAGs. With the identification of parallel blocks of one direction as a packet, it can be observed that, according to the experiment, larger PAGs tend to produce a higher number of packets, compare PAG A and B. In even smaller grains (PAGs C-E), sometimes only one block is formed. Such a characteristic is also documented in the literature, cf. Hanamura et al. (2013).

The simulations in two dimensions give a much more plate-like structure than observed in the experiment. This is partly due to the fact that the experimental observation is a two-dimensional cross-section of an actual three-dimensional problem. In the two-dimensional problem considered here, the variants can accumulate perfectly in the plane under consideration, resulting in an idealized martensite image. Therefore, a quantitative size comparison of the two-dimensional simulation with the experiments performed in this work is omitted.

6.5. Three-Dimensional Simulations with Twelve Martensite Variants

Regarding martensite in steels, a dominant amount of published phase field models so far simulate two martensite variants based on the Bain correspondence in two spatial dimensions or three martensite variants in three spatial dimensions. Such models can be used to simulate idealized martensitic microstructures. Basically, martensite evolution in steel is a three-dimensional problem and in order to simulate the hierarchical structure of lath or plate martensite in the future, it is necessary to consider the frequently experimentally observed twelve or twenty-four martensite variants. As for the lath martensite, Du (2017) and Shchyglo et al. (2019) were the first to consider the full set of twenty-four martensite variants according to the KS orientation relationship. Here, athermal martensite formation was simulated with randomly distributed pre-existing nuclei with different sizes. Monocrystaline simulation domain sizes up to $25.6^3 \, \mu m^3$ corresponding to austenite grain sizes were considered. Ahluwalia et al. (2020) investigated the effect of (rate-independent) plasticity under isothermal conditions, where monocrystaline simulation domain sizes of $64^3 \, nm^3$ were considered. Based on the mesoscopic shape changes determined with the PTMC, Graf et al. (2021c) considered twelve martensite variants similar to the NW orientation relationship in a monocrystal with a size of $6.25^3 \, \mu m^3$ motivated by experimentally observed austenite grain sizes. The martensite transformation was initiated by randomly placed pre-existing nuclei.

In this section, three-dimensional simulations with twelve martensite variants according to the NW orientation relationship are carried out. The material parameters are taken from Tab. 6.2, whereby the corresponding three-dimensional transformation strains are used. Furthermore, the crystal elasticity tensors of the martensitic states are rotated according to the orientation determined with the PTMC. In contrast to Graf et al. (2021c) an advanced interpolation concerning the elastic energy potential is used to reflect the in Sec. 5 assumed transformation mechanism. At the element level, at each time step it is checked which order parameter had the maximum value in the previous time step. The CPP packet of the corresponding variant is declared as active. For all variants within the active packet, an interpolation with h^{p3} is used. For all variants within the non-active packets an interpolation with h^{p5}:

$$h_i = \begin{cases} h^{p3} & \text{, for all variants } i \text{ in active packet} \\ h^{p5} & \text{, for all variants } i \text{ in non-active packets} \end{cases}. \qquad (6.26)$$

With this, the auto-nucleation of variants in the same packet is supported, while the auto-nucleation of variants from other packets is suppressed. The functionality of this principle is verified in Sec. 6.5.1. In Sec. 6.5.2, the model is applied to polycrystalline structures.

6.5.1. Clamped Monocrystal

To test whether auto-nucleation works as desired, a test scenario is set up. For this purpose, clamped austenitic monocrystals with different sizes are considered (4.25^3, 6.25^3, 8.25^3, $10.25^3 \, \mu m^3$). In the initial time step, nucleation points are set in the respective centers of the cube, which is mentally divided into eight equal partial volumes. The size of the nucleation points is chosen so that natural growth can occur in the smallest austenite grain considered after the corresponding shrinkage due to curvature minimization and the
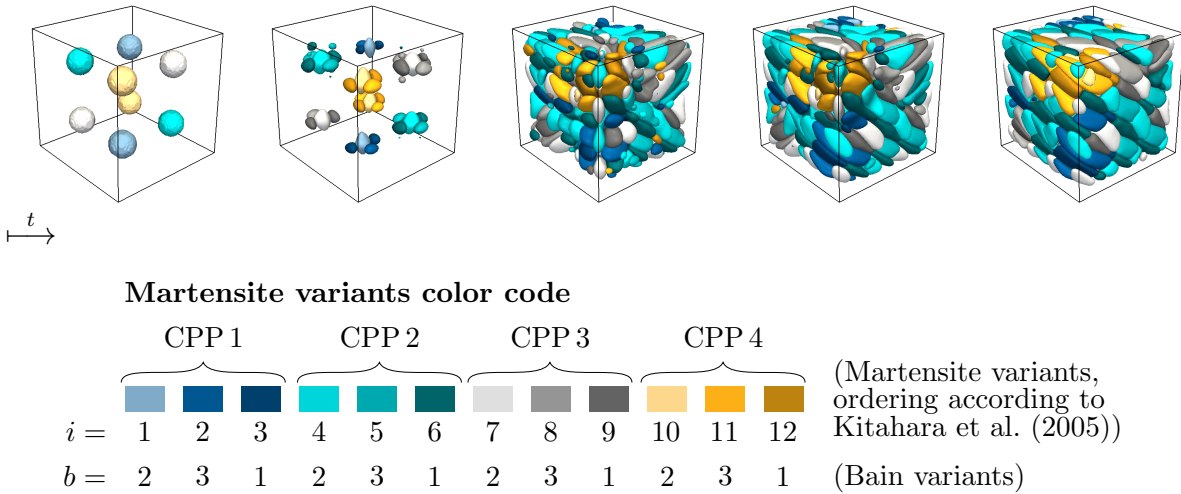
Figure 6.43: Martensite variant evolution in a clamped austenitic matrix with size $8.25^3\,\mu m^3$ with iso-surfaces at $\varphi_i = 0.5$

induced stresses. The first variant of each of the four crystallographic packets is assigned to the nucleation points lying on the respective spatial diagonal, cf. Fig. 6.43. The simulation is stopped as soon as the overall martensite content stagnates.

Fig. 6.43 shows the evolution of the martensite variants within the clamped austenite matrix with a size of $8.25^3\mu m^3$. From the second snapshot can be seen that martensite variants of corresponding packets are created autocatalytically in order to reduce the induced stresses by variants from different Bain groups. As time progresses, the initially differently oriented blocks align themselves along primarily one spatial diagonal. The final packet formations regarding different sizes are shown in Fig. 6.44. In these examples, the variants of packet CPP 2 combine into one large package. In larger simulation domains, more packets are created consisting of one block. The number of separate packets consisting of several blocks also increases with larger simulation domains, cf. Tab. 6.3. According to this, auto-nucleation is not completely suppressed by blocks of another packet. The formation of one dominant packet and the increased packet number is due to the fact that in the current formulation each material point at each time step has an active packet. The dominant formation of one packet then has numerical reasons. If this is undesirable, it can be suppressed by defining all packets as inactive when the maximum order parameter is approximately zero. Due to the more complex structure, in Tab. 6.3, the respective exemplary block widths of the block along the spatial diagonal is documented. As with the two-dimensional simulation, the block width increases with a larger simulation domain. However, as the simulation domain increases, the influence of the clamped boundary condition decreases and converges to a width of $1.1\,mm$.

6.5.2. Polycrystalline Structure

The simulation of three-dimensional polycrystalline structures with simulation domain edge length sizes of about $50\,\mu m$ according to Sec. 6.4.3 would be a computational demanding task. Currently, no work is known in which a three-dimensional simulation has been performed with twelve or more martensite variants in the order of representative

(a)

(b)

(c)

(d)
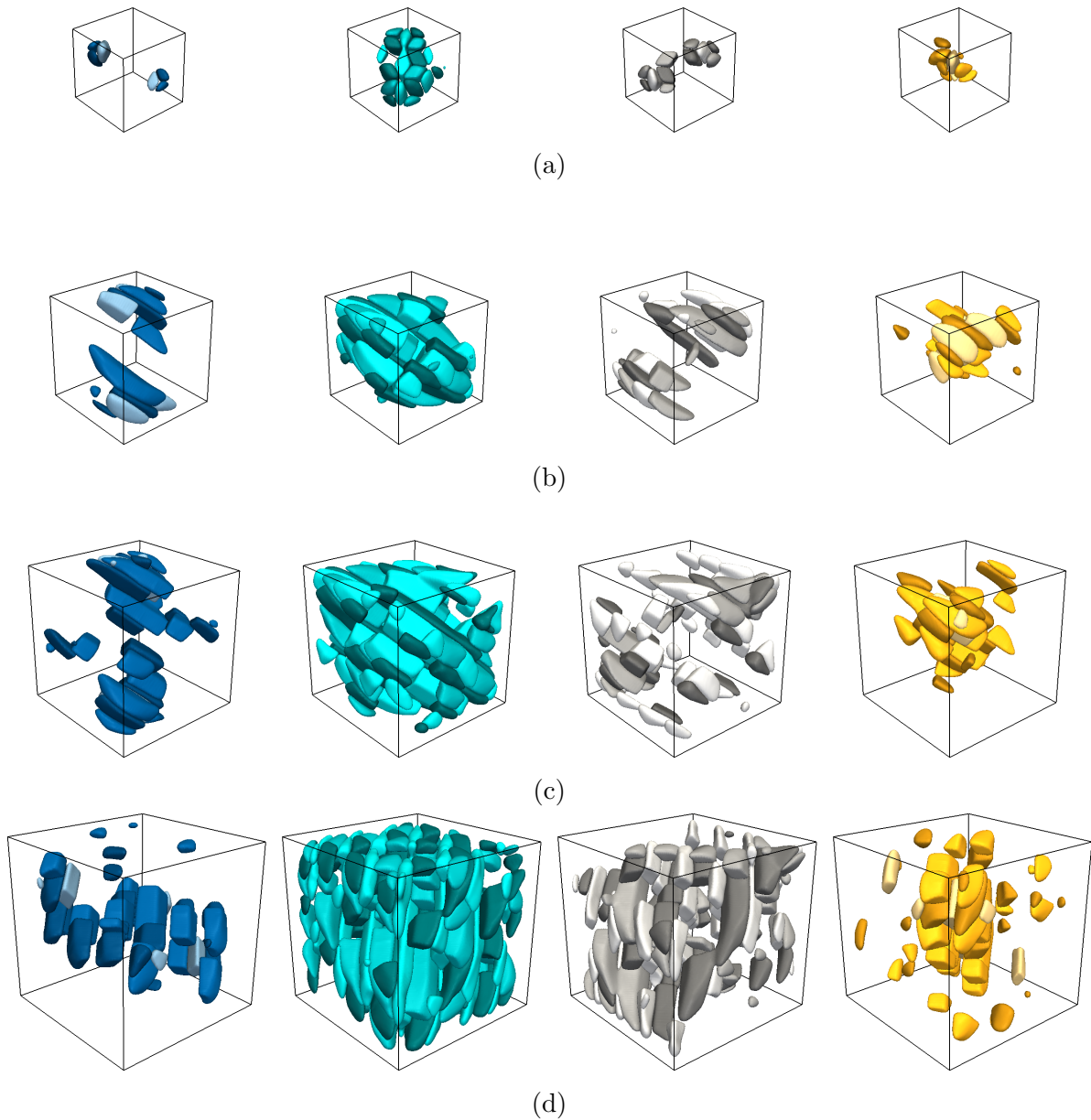
Figure 6.44: Final CPP packet formation in a clamped austenitic matrix with sizes (a) $4.25^3 \, \mu m^3$, (b) $6.25^3 \, \mu m^3$, (c) $8.25^3 \, \mu m^3$, (d) $10.25^3 \, \mu m^3$, iso-surfaces at $\varphi_i = 0.5$, color code according to Fig. 6.43

(polycrystalline) volume elements. In this section, an attempt is made to represent the character of a polycrystalline structure in a simplified way by placing a complete grain in the center of the simulation domain. This grain is surrounded by further grains, whereby these are cut by the cube-shaped simulation domain, cf. Fig. 6.45. Random orientations are assigned to the grains. Martensite transformation is initiated by a total of 68 nuclei randomly placed at the PAG boundary surfaces. With a simulation domain edge length of $10.25 \, \mu m$ an equivalent diameter of $d_{eq} = 8.6 \, \mu m$ of the centered PAG is obtained. This is

Table 6.3: Number of CPP packets consisting of more than one block and block widths of blocks along the spatial diagonal

PAG size in μm^3	Block width in μm	Number of CPP packets
4.25^3	0.7	7
6.25^3	1.06	10
8.25^3	1.1	13
10.25^3	1.1	20
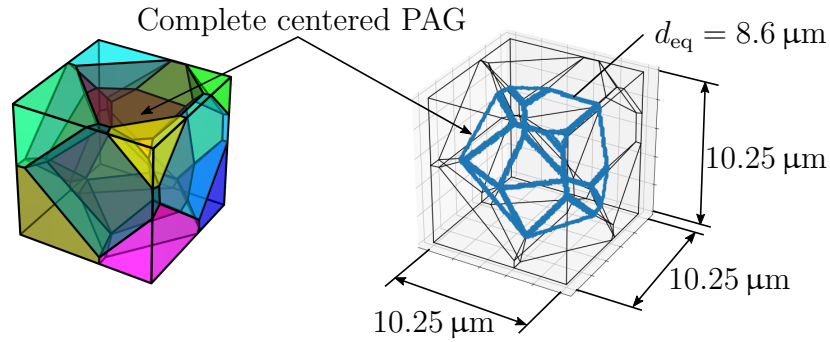
Figure 6.45: PAG structure with a complete PAG in the center, surrounded by parts of other PAGs.
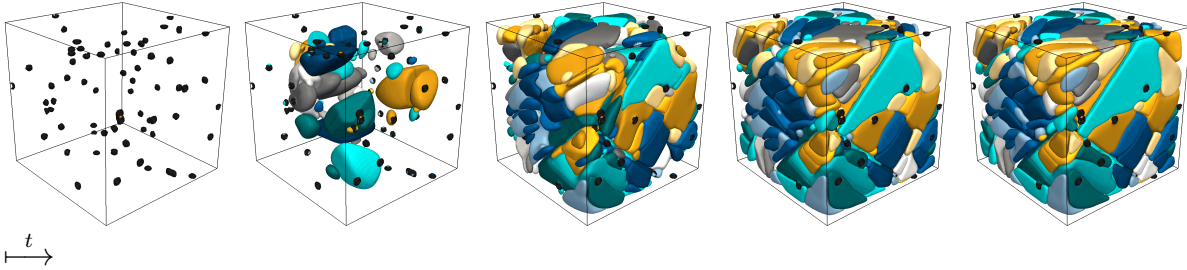
Figure 6.46: Martensite variant evolution in a clamped austenitic matrix with size $8.25^3 \, \mu m^3$ with iso-surfaces at $\varphi_i = 0.5$, color code according to Fig. 6.43

in good agreement with the mean equivalent diameter of the 50CrMo4 microstructure, cf. Sec. 4. The time-dependent simulation is stopped as soon as there is no further significant increase in the total martensite content, cf. Sec. 6.4.

The time-dependent martensite block evolution is shown in Fig. 6.46. At the beginning, martensite growth mainly takes place at the nucleation sites remote from the simulation domain surface. At the surface of the simulation area, the transformation-related and very high mechanical stresses due to the boundary conditions prevent martensite growth. Nevertheless, supported by stress-assisted auto-nucleation, martensite development progresses. The final simulated structure shows a typical martensitic appearance, in which a clear grouping of martensite blocks into martensite packets can be seen.

In Fig. 6.47, the focus is on the central grain, by showing the individual packets with the corresponding martensite blocks. Since no three-dimensional data are available from

CPP 1:   CPP 2:   CPP 3:   CPP 4:
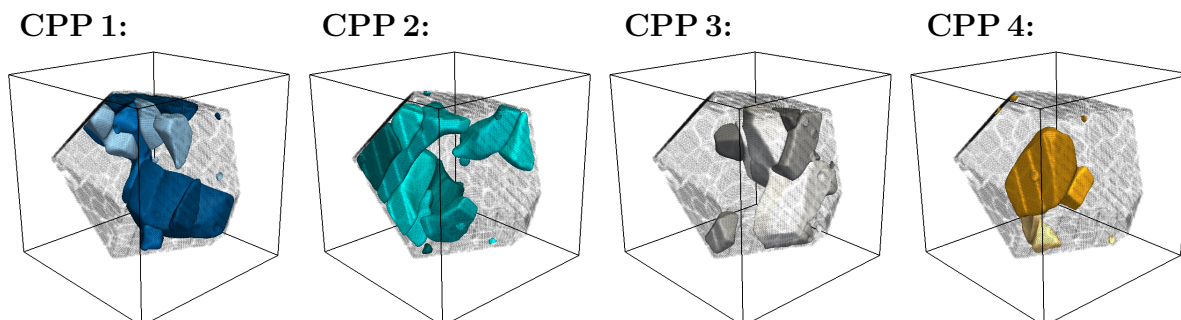
Figure 6.47: Martensite CPP formation inside the centered PAG, color code according to Fig. 6.43

Cross-sections of simulation:
(color code according to Fig. 6.43)
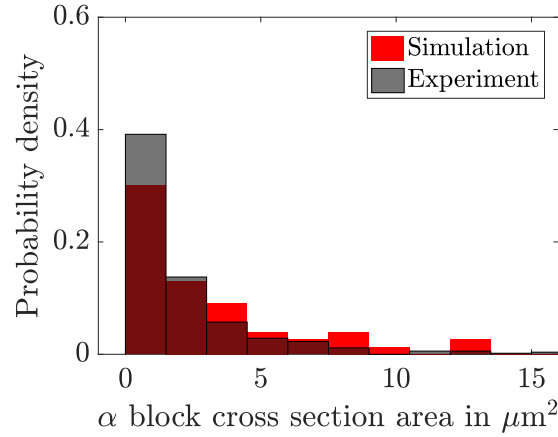
Experiment:
(IPF color code)
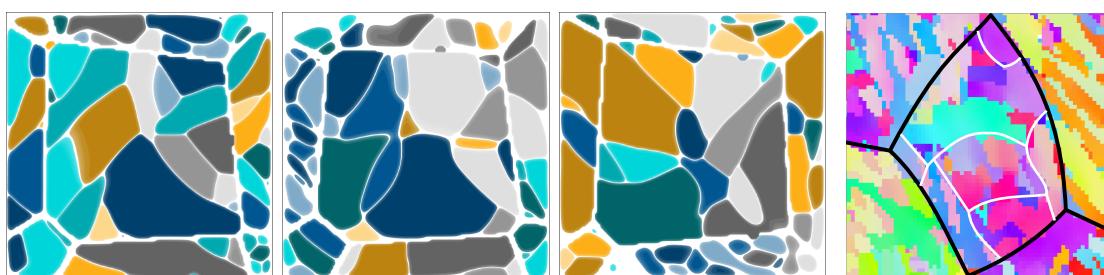
Figure 6.48: Cross-sections of 50CrMo4 martensite microstructures – cross-sections of the simulation are through the domain center along the three spatial directions, cross-section of experiment shows a PAG (black boundaries) with its CPP packets (white boundaries) with similar size, block boundaries are not highlighted in the experimental microstructure, same size scale for all images, color code according to Fig. 6.43

the experiment, a direct comparison is not possible. However, in the work of Morito et al. (2013), a three-dimensional quantitative measurement of a martensitic material with similar carbon content and lath morphology was performed. The austenite grain size of the material studied by Morito et al. (2013) is considerably larger, although the basic shape of the blocks and packets is remarkably similar.

In order to compare the results with the present experimental measurements, cross-sections through the simulation center are generated in the direction of the three spatial directions, cf. Fig. 6.48. Fig. 6.48 also shows the measured martensitic structure of a PAG with comparable size. The quantitative comparison of the block sizes is shown in Fig. 6.49, where the simulated cross-section areas of the centered PAG are evaluated. The experimental database are the block sizes within the PAGs of similar size from the microstructures in Sec. 4. From this follows that in this simplified polycrystalline structure, the simulation tends to predict larger block sizes.

Based on the findings of the investigations in the previous sections, it can be concluded that the following aspects lead to a coarser martensite block structure and most likely explain the deviations to the experiment. Firstly, due to the high chemical driving force in the supercooled material, the interface formation is stabilized by the choice of a corresponding interface energy parameter. With this, the interface energy is most likely higher than it is expected from reality. A higher interface energy leads to a coarser block

Figure 6.49: Probability density of martensite block cross-section areas of experiment within the reconstructed PAG cross-section areas with $A_{\mathrm{PAG}}^{\mathrm{2D}} \approx 58\,\mu\mathrm{m}^2 \mp 10\%$ and simulation, data basis are the experimental results presented in Sec. 4 with $\theta_{\mathrm{crit}} = 12\,^\circ$ since no sub-blocks are considered in the simulation

structure. Furthermore, a compromise had to be made regarding spatial discretization and interfacial stress precision. The higher the number of elements in the interface the lower are the interface stresses. High stresses in the interface counteract the stress-assisted auto-nucleation and thus also lead to coarser structures.

7. Conclusion and Outlook

The martensitic microstructure is of great relevance for highly loaded components. However, despite decades of intensive research, the complex mechanism of martensite transformation is still not fully understood. In order to increase the understanding of martensite transformation, experimental results and a simulation model capable of resolving microstructural martensite transformation (on the mesoscale) were presented in this work. The investigations were carried with focus on a technically relevant low-alloy steel. Sec. 7.1 summarizes the present work and Sec. 7.2 provides an outlook.

7.1. Conclusion

First, this work gives an overview of the current knowledge about martensite transformation in steels, focusing on lath martensite. The characteristics of the martensite morphology and the formation mechanisms form an important basis with regard to the modeling strategy. The continuum mechanics form the second fundamental part of this work. In this regard, assuming small deformations, the kinematic relations, equilibrium equations, and important fundamental notations of continuum mechanics were introduced.

In order to gain an understanding of the martensite transformation in the low-alloy steel 50CrMo4, different heat treatment routes were performed experimentally. The focus here was to systematically investigate the influence of the cooling rate on the resulting martensite. It was found that the cooling rate influences the hardness of the as-quenched martensite. A detailed analysis of block and packet sizes reveals no significant dependence on the rate of cooling. It is therefore concluded that the increase of hardness is an effect of reduced carbon segregation and reduced retained austenite.

No significant dependency of the martensite start temperature on the cooling rate was observed. This is consistent with an athermal initial nucleation mechanism. The number of initial nucleation points seems to depend largely on the size of the PAG: the larger the grain, the greater the probability of defects that can serve as martensite nucleation points. The block size – and thus also the packet size – is influenced by the grain size of the PAG due to the limitation of the grain boundary and grain boundary strengthening effects.

The invariance of the resulting martensite sizes against the cooling rate seems to be a consequence of fast isothermal formation of martensite clusters consisting of self-accommodating martensite blocks in order to reduce the transformation-induced stresses. Under these conditions, thermally activated and time-dependent processes during the martensite growth such as plastic relaxation do not influence the block and packet sizes in the considered technical relevant cooling rate regimes. Other publications with other materials have reported an effect of cooling rate on the resulting martensite sizes. The results of this work have been discussed in detail against this background. Based on this, the values of the relative difference between the equilibrium temperature and the chemical driving force at the martensite start temperature are proposed as first indicators to estimate whether the block and packets sizes are related to the cooling rate.

In order to be able to describe the martensite transformation in a model developed within the framework of this work, the evolution of the martensite transformation was idealized. With these idealizations at hand, a phase field model was developed and its numerical implementation based on the finite element method was presented in detail. This

model is capable of using synthetic PAG structures that statistically represent measured structures as input. Furthermore, according to the current state of knowledge, the PAG boundaries can be considered in the initial martensite nucleation event. Further, stress-assisted auto-nucleation is enabled via a suitable choice of the interpolation function in the elastic energy potential. In addition, a simplified plasticity model was implemented to investigate the basic effect of plastic relaxation on martensite transformation. Particular emphasis was placed on determining the transformation strains for the model. In contrast to previous phase field models for martensite transformation, the transformation strains are determined with the PTMC and correspond to the mesoscopic shape change. Thus, the substructure of the martensite is taken into account in this model. A complex material model, which takes into account a slipping according to the CPPs, can thus be dispensed with.

Numerous numerical studies have been performed to analyze the basic model behavior. With an increasing magnitude of the chemical driving force, the effective interface width decreases, while an increasing transformation strain increases the effective interface width. Due to the high chemical driving forces in the martensite transformation, the interface energy parameter must be chosen large enough to form an adequately diffuse interface with an practicable spatial discretization. Accordingly, the interface energy parameter represented a numerically driven quantity.

Considering a two-dimensional clamped elastic monocrystal with a temperature dependent Young's modulus, transformation strain dependent on carbon content, and chemical driving forces dependent on temperature and chemical composition, the model is able to predict the martensite start temperature of materials with different carbon contents. In qualitative and quantitative agreement with the literature, carbon stabilizes austenite, from which it follows that a decrease in martensite start temperature is predicted with increasing carbon content. It is also possible to consider the influence of the PAG size. Regarding the residual austenite content below T_{MS}, the model reflects findings from the literature. With higher supercooling, the model predicts less retained austenite and with higher carbon content a higher amount of retained austenite is predicted.

With the choice of a constant ratio between chemical energy difference and the interface energy parameter (to keep the interface stable), an increasing block width with higher supercooling is predicted. Since there is no experimental evidence for this effect, in the next step, the interface energy parameter was chosen in order to predict a constant block width at each level of undercooling. Thus, with the viscoplastic extension it could be shown that the time-dependent relaxation has an influence on the stress-assisted auto-nucleation. With faster relaxation, a wider block width is obtained. The influence of relaxation explains the martensite block size sensitivity to the cooling rate, which is observed in some materials.

In addition, polycrystalline structures were considered in the plane strain case. With this enhancement, a martensite evolution could be simulated, which reflects key features of natural martensite. Martensite crystals nucleate at crystal defects at the grain boundaries. Further growth of martensite is accompanied with stress-assisted nucleation of accommodating variants from the corresponding other Bain group. A higher number of nucleation points in larger grains can lead to a higher number of packets. In relatively small PAGs mainly only one martensite block is formed.

A major step forward in the simulation of martensite transformation with the phase

field method was the three-dimensional extension with twelve martensite variants. The model supports auto-nucleation of variants from the same crystallographic packet. Thus, the three-dimensional model can be used to simulate the hierarchical structure of the lath martensite. Hence, a quantitative comparison of the block sizes with the experiment is also possible in a meaningful way. With the simulation slightly larger block sizes are predicted compared to the experiment, which could be explained by the numerical driven interface energy parameter and by the resource-limited fineness of the spatial discretization.

The presented model describes an idealized form of the transformation mechanism, which cannot be used to answer all questions regarding variant selection, especially for high-carbon steels with a rather random variant selection within a crystallographic packet. However, with a minimum of model parameters, realistic (three-dimensional) martensitic microstructures can be simulated. Thus, the presented model in this work is a step forward to a holistic simulation of martensite transformation and leads to an understanding of the three dimensional formation of martensite, which can be approximated with the NW orientation relationship. The simulated martensitic microstructures may serve as input for e.g. microstructural based fatigue simulations according to Schäfer et al. (2019a).

7.2. Outlook

A major limiting factor of the presented model are the required computing resources. Therefore, in this work, a compromise between computational accuracy and discretization had to be chosen. In order to obtain comparable results, the influence of the mesh was quantified. Based on the results a consistent spatial discretization was used, which is in line with other publications. In fact, the model offers potential to increase numerical efficiency. For example, a sequential solution of the physical fields could lead to an increase in efficiency. Furthermore, the use of an adaptive mesh represents an improvement possibility. With a more efficient model, the interface width could be reduced to the point where the interface energy parameter can be chosen in a physically motivated manner. In addition, complex material models could be used, also for three-dimensional simulations.

So far, only isothermal conditions have been considered in this work. With PAG structures in the size of a representative volume element, the full martensite evolution from T_{MS} to the martensite finish temperature could be considered. For this, temperature-dependent material parameters should be taken into account. With more complex boundary conditions, such a model could also reproduce the macroscopic martensite dilatation. With a fixed aspect ratio for the mechanical boundary conditions, Shchyglo et al. (2019) achieved promising results. In their simulations, the simulation domain is allowed to expand or contract to its equilibrium volume by relaxing the hydrostatic pressure in the simulation domain while keeping the ratio between the side lengths of the simulation domain the same. This would most likely also make it possible to obtain realistic stress values in the final microstructure.

With the presented model it is also possible to investigate the Hall-Petch effect in a polycrystalline microstructure. To the best of the author's knowledge, the Hall-Petch effect has so far only been studied in the clamped single crystal, cf. Yeddu (2018).

With the interface part in the phase field potential (5.31), the (chemical) energetics of an austenite-martensite interface is well defined by the model parameters γ and l. However, the (chemical) energetics of martensite-martensite interfaces cannot be defined separately.
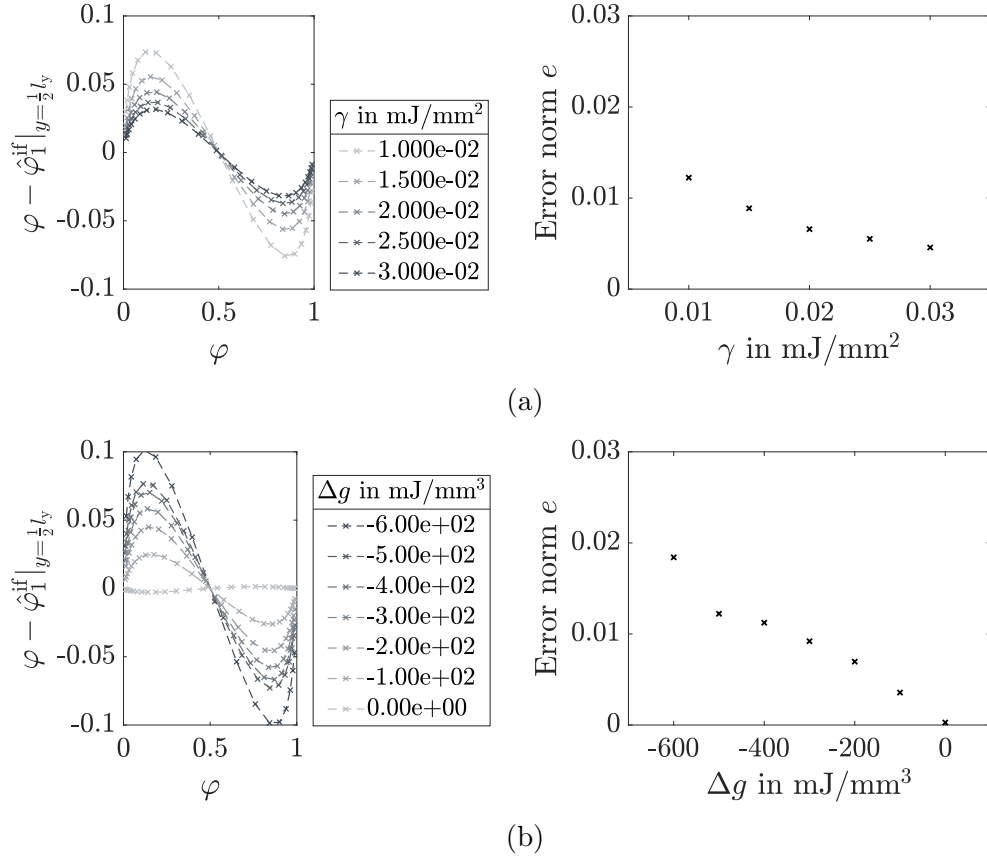
With the chosen model formulation, the martensite interfaces result from the overlapping of austenite-martensite interfaces. However, different and anisotropic interface energies could play an important role in the formation of the hierarchical lath martensite. Such a distinction could be addressed with the multiphase formulation according to Steinbach et al. (1996), Steinbach & Pezzolla (1999) and Nestler et al. (2005). Implementations of this formulation with respect to the martensite transformation have already been made in several works, cf. Du (2017); Schoof et al. (2018b); Shchyglo et al. (2019); Rezaee-Hajidehi & Stupkiewicz (2020). Nevertheless, with exception of Rezaee-Hajidehi & Stupkiewicz (2020), constant isotropic interface energies for all occurring interfaces were assumed.

In the diffuse interface of the phase field, local incompatibilities between the phases are compensated by elastic strains. Thus, elastic stresses and strains within the austenite-martensite and martensite-martensite interfaces are present, which influence the stress-assisted auto-nucleation. As in many publications on phase field simulation of martensite transformation, this fact has been neglected in this work, but cannot be further ignored in the future. Important works, which addresses this topic have been published by Basak & Levitas (2017, 2018) and Schneider et al. (2015). These approaches should also be considered for this model.

In this work, little effort was made with respect to the choice of the mobility constant. The mobility constant scales the velocity of interfaces. The interface velocity is strongly related to the martensite substructure. In the literature, velocities in the order of 10^3 m/s are reported for a martensite growth with internal twins, whereas for a dislocation substructure, velocities from 10^{-6} m/s to 10^{-1} m/s are reported (same order as dislocation velocities). The mechanism controlling the interface velocity in the intermediate regime is not yet clear, cf. Villa (2013). Typically, lath martensite has dislocations as substructure. However, it should also be noted that recent results indicate that internal twins can also be observed in the final lath martensite, cf. Ping et al. (2018). According to Ping et al. (2018), the twinning substructure is the initial product of the martensite transformation, whereas these substructure is resolved by detwinning in the auto-tempering process. These findings should be considered in the further development of the simulation model.

Appendix

A. Geometric Formation of the Interface with Fine Meshing

(a)

(b)

Figure A.1: Influence of model parameters on the diffuse interface in a two-phase beam with (a) $l = 0.25\,\mu\text{m}$, $\tilde{\varepsilon}_\text{x} = 0.1$, $\Delta g = -200\,\text{mJ/mm}^3$ (b) $l = 0.25\,\mu\text{m}$, $\gamma = 0.02\,\text{mJ/mm}^2$, $\tilde{\varepsilon}_\text{x} = 0.1$, (c) $\gamma = 0.02\,\text{mJ/mm}^2$, $\tilde{\varepsilon}_\text{x} = 0.1$, $\Delta g = -200\,\text{mJ/mm}^3$, (d) $l = 0.25\,\mu\text{m}$, $\gamma = 0.02\,\text{mJ/mm}^2$, $\Delta g = -200\,\text{mJ/mm}^3$, spatial discretization: 336×72 finite elements

(c)

(d)
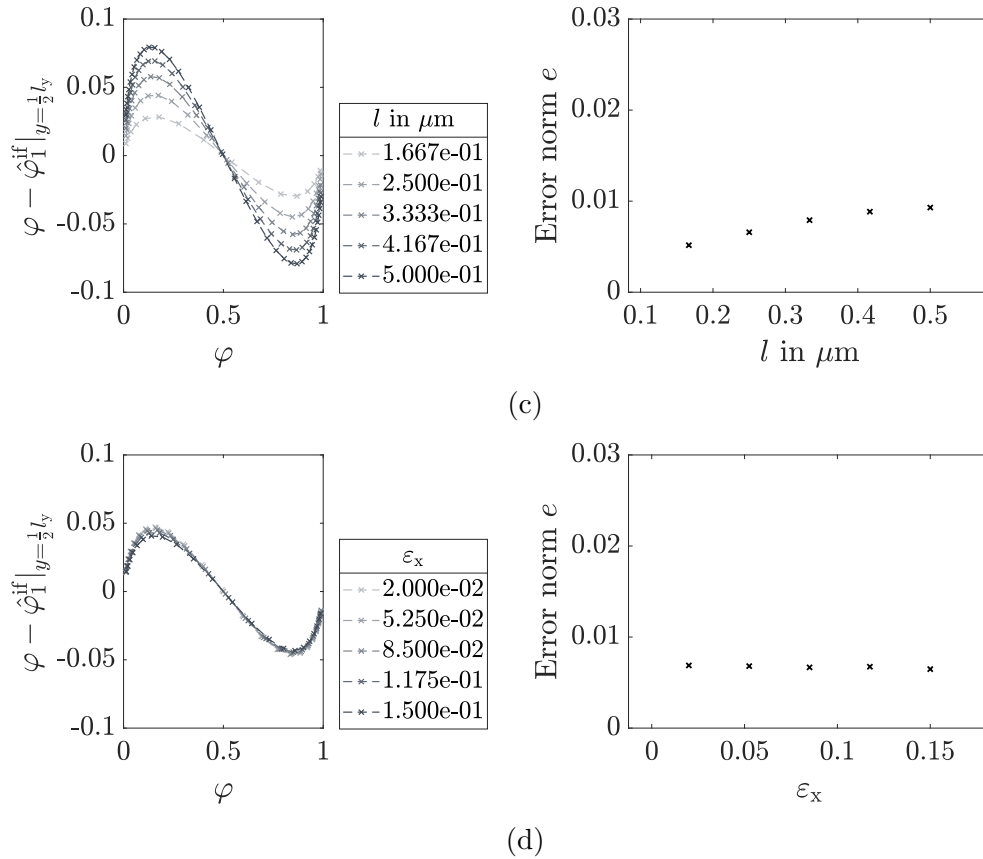
Figure A.1: Influence of model parameters on the diffuse interface in a two-phase beam with (a) $l = 0.25\,\mu$m, $\tilde{\varepsilon}_\mathrm{x} = 0.1$, $\Delta g = -200\,$mJ/mm^3 (b) $l = 0.25\,\mu$m, $\gamma = 0.02\,$mJ/mm^2, $\tilde{\varepsilon}_\mathrm{x} = 0.1$, (c) $\gamma = 0.02\,$mJ/mm^2, $\tilde{\varepsilon}_\mathrm{x} = 0.1$, $\Delta g = -200\,$mJ/mm^3, (d) $l = 0.25\,\mu$m, $\gamma = 0.02\,$mJ/mm^2, $\Delta g = -200\,$mJ/mm^3, spatial discretization: 336×72 finite elements (cont.)

B. Model input parameters

Table B.1: Simulation input parameters of the simulations in Sec. 5.4.2

Name	Symbol/Value
Material specific:	
Elastic constants:	$C_{11} = 253.1\,\text{GPa}$
	$C_{12} = 132.4\,\text{GPa}$
	$C_{44} = 75.8\,\text{GPa}$
Transformation strains:	$\epsilon_\text{I} = 0.1143$
	$\epsilon_\text{II} = -0.1048$
Free energy difference:	$\Delta g = -500\,\text{mJ/m}^3$
Mobility constant:	$M = 50\,000\,\text{mm}^2(\text{Ns})^{-1}$
Numerically driven:	
Interface energy parameter:	$\gamma = 0.015\,\text{mJ/mm}^2$
Interface width:	$l = 1/3\,\upmu\text{m}$

References

Abeyaratne, R. & Knowles, J. K. (1990). On the driving traction acting on a surface of strain discontinuity in a continuum. *Journal of the Mechanics and Physics of Solids*, 38(3), 345–360.

Abeyaratne, R. & Knowles, J. K. (2006). *Evolution of phase transitions: a continuum theory*. Cambridge University Press.

Ahluwalia, R., Lookman, T., Saxena, A., & Albers, R. C. (2004). Landau theory for shape memory polycrystals. *Acta Materialia*, 52(1), 209–218.

Ahluwalia, R., Mikula, J., Laskowski, R., & Quek, S. S. (2020). Phase field simulation of martensitic-transformation-induced plasticity in steel. *Physical Review Materials*, 4(10), 103607.

Ahluwalia, R., Quek, S. S., & Wu, D. T. (2015). Simulation of grain size effects in nanocrystalline shape memory alloys. *Journal of Applied Physics*, 117(24), 244305.

Alber, H.-D. & Zhu, P. (2008). Solutions to a model for interface motion by interface diffusion. *Proceedings of the Royal Society of Edinburgh Section A: Mathematics*, 138(5), 923–955.

Altenbach, J. & Altenbach, H. (1994). *Einführung in die Kontinuumsmechanik*. Teubner.

Amos, P. G. K., Schoof, E., Streichan, N., Schneider, D., & Nestler, B. (2019). Phase-field analysis of quenching and partitioning in a polycrystalline Fe-C system under constrained-carbon equilibrium condition. *Computational Materials Science*, 159, 281–296.

Andersson, J.-O., Helander, T., Höglund, L., Shi, P., & Sundman, B. (2002). Thermo-calc & dictra, computational tools for materials science. *Calphad*, 26(2), 273–312.

Apel, M., Benke, S., & Steinbach, I. (2009). Virtual dilatometer curves and effective Young's modulus of a 3D multiphase structure calculated by the phase-field method. *Computational materials science*, 45(3), 589–592.

Artemev, A., Jin, Y. M., & Khachaturyan, A. G. K. (2001). Three-dimensional phase field model of proper martensitic transformation. *Acta materialia*, 49(7), 1165–1177.

Artemev, A., Wang, Y., & Khachaturyan, A. G. (2000). Three-dimensional phase field model and simulation of martensitic transformation in multilayer systems under applied stresses. *Acta materialia*, 48(10), 2503–2518.

Aubry, S., Fago, M., & Ortiz, M. (2003). A constrained sequential-lamination algorithm for the simulation of sub-grid microstructure in martensitic materials. *Computer Methods in Applied Mechanics and Engineering*, 192(26-27), 2823–2843.

Bachmann, F., Hielscher, R., & Schaeben, H. (2010). Texture analysis with MTEX – free and open source software toolbox. In *Solid State Phenomena*, volume 160 (pp. 63–68).: Trans Tech Publ.

Bain, E. C. & Dunkirk, N. Y. (1924). The nature of martensite. *Trans. AIME*, 70(1), 25–47.

Bardelcik, A., Salisbury, C. P., Winkler, S., Wells, M. A., & Worswick, M. J. (2010). Effect of cooling rate on the high strain rate properties of boron steel. *International Journal of Impact Engineering*, 37(6), 694–702.

Bartel, T. (2009). *Multiskalenmodellierung martensitischer Phasentransformationen in Formgedächtnislegierungen unter Verwendung relaxierter Energiepotenziale*. PhD thesis, Ruhr University Bochum.

Bartel, T. & Hackl, K. (2008). A novel approach to the modelling of single-crystalline materials undergoing martensitic phase-transformations. *Materials Science and Engineering: A*, 481, 371–375.

Bartel, T. & Hackl, K. (2009). A micromechanical model for martensitic phase-transformations in shape-memory alloys based on energy-relaxation. *ZAMM-Journal of Applied Mathematics and Mechanics/Zeitschrift für Angewandte Mathematik und Mechanik: Applied Mathematics and Mechanics*, 89(10), 792–809.

Bartel, T., Menzel, A., & Svendsen, B. (2011). Thermodynamic and relaxation-based modeling of the interaction between martensitic phase transformations and plasticity. *Journal of the Mechanics and Physics of Solids*, 59(5), 1004–1019.

Basak, A. & Levitas, V. I. (2017). Interfacial stresses within boundary between martensitic variants: Analytical and numerical finite strain solutions for three phase field models. *Acta Materialia*, 139, 174–187.

Basak, A. & Levitas, V. I. (2018). Nanoscale multiphase phase field approach for stress- and temperature-induced martensitic phase transformations with interfacial stresses at finite strains. *Journal of the Mechanics and Physics of Solids*, 113, 162–196.

Bergmann, R., Chan, R. H., Hielscher, R., Persch, J., & Steidl, G. (2015). Restoration of manifold-valued images by half-quadratic minimization. *arXiv preprint arXiv:1505.07029*.

Bhadeshia, H. K. D. H. (2001a). Geometry of crystals. *Institute of Materials, London*.

Bhadeshia, H. K. D. H. (2001b). Martensite transformation. In *Encyclopedia of materials: science and technology* (pp. 5203–5206). Elsevier.

Bhattacharya, K. et al. (2003). *Microstructure of martensite: why it forms and how it gives rise to the shape-memory effect*, volume 2. Oxford University Press.

Böhlke, T., Jöchen, K., Kraft, O., Löhe, D., & Schulze, V. (2010). Elastic properties of polycrystalline microcomponents. *Mechanics of Materials*, 42(1), 11–23.

Borukhovich, E. (2016). *Consistent coupling of geometrically non-linear finite deformation with alloy chemistry and diffusion within the phase-field framework*. PhD thesis, Ruhr-Universität Bochum.

Bowles, J. S. & Mackenzie, J. K. (1954). The crystallography of martensite transformations I. *Acta Metallurgica*, 2(1), 129–137.

Brandl, D., Lukas, M., Stockinger, M., Ploberger, S., & Ressel, G. (2019). Evidence of austenite memory in PH 15-5 and assessment of its formation mechanism. *Materials & Design*, 176, 107841.

Cahn, J. W. & Hilliard, J. E. (1958). Free energy of a nonuniform system. i. interfacial free energy. *The Journal of chemical physics*, 28(2), 258–267.

Capdevila, C., F. G., C., & De Andrés, C. G. (2002). Determination of Ms temperature in steels: A Bayesian neural network model. *ISIJ international*, 42(8), 894–902.

Carr, M., Strife, J., & Ansell, G. (1978). An investigation of the effects of austenite strength and austenite stacking fault energy on the morphology of martensite in fe-ni-cr-0.3 c alloys. *Metallurgical Transactions A*, 9(6), 857–864.

Cayron, C. (2007). ARPGE: A computer program to automatically reconstruct the parent grains from electron backscatter diffraction data. *Journal of applied crystallography*, 40(6), 1183–1188.

Cech, R. E. & Turnbull, D. (1956). Heterogeneous nucleation of the martensite transformation. *The Journal of The Minerals, Metals & Materials Society*, 8(2), 124–132.

Chen, C. C., Lin, H. K., & Lan, C. W. (2014). Phase field modeling with large interface thickness and undercooling. *Journal of Crystal Growth*, 385, 121–126.

Chen, L.-Q. & Khachaturyan, A. G. (1991). Computer simulation of structural transformations during precipitation of an ordered intermetallic phase. *Acta metallurgica et materialia*, 39(11), 2533–2551.

Chen, L.-Q., Wang, Y., & Khachaturyan, A. G. (1992). Kinetics of tweed and twin formation during an ordering transition in a substitutional solid solution. *Philosophical magazine letters*, 65(1), 15–23.

Christian, J. (1976). O-lattice, surface dislocation and elastic theories of martensite crystallography and martensitic nuclei. *New Aspects of Martensitic Transformation. Japan Institute of Metals, Tokyo. 1976, 21-33.*

Coleman, B. D. & Gurtin, M. E. (1967). Thermodynamics with internal state variables. *The Journal of Chemical Physics*, 47(2), 597–613.

Coleman, B. D. & Noll, W. (1963). The thermodynamics of elastic materials with heat conduction and viscosity. *Archive for rational mechanics and analysis*, 13(1), 167–178.

Cui, S., Cui, Y., Wan, J., Rong, Y., & Zhang, J. (2016). Grain size dependence of the martensite morphology–a phase-field study. *Computational Materials Science*, 121, 131–142.

Cui, S., Wan, J., Rong, Y., & Zhang, J. (2017). Phase-field simulations of thermomechanical behavior of MnNi shape memory alloys using finite element method. *Computational Materials Science*, 139, 285–294.

Cui, S., Wan, J., Zhang, J., Chen, N., & Rong, Y. (2018). Phase-field study of microstructure and plasticity in polycrystalline MnNi shape memory alloys. *Metallurgical and Materials Transactions A*, 49(12), 5936–5941.

Dash, S. & Brown, N. (1966). Nucleation and growth of martensite in Fe-32.3% Ni alloy. *Acta Metallurgica*, 14(5), 595–603.

Davies, R. G. & Magee, C. L. (1971). Influence of austenite and martensite strength on martensite morphology. *Metallurgical Transactions*, 2(7), 1939–1947.

Diewald, F. (2020). *Phase field modeling of static and dynamic wetting*. PhD thesis, Technische Universität Kaiserslautern.

Diewald, F., Kuhn, C., Heier, M., Langenbach, K., Horsch, M., Hasse, H., & Müller, R. (2018). Investigating the stability of the phase field solution of equilibrium droplet configurations by eigenvalues and eigenvectors. *Computational Materials Science*, 141, 185–192.

Döbrich, K. M., Rau, C., & Krill, C. E. (2004). Quantitative characterization of the three-dimensional microstructure of polycrystalline Al-Sn using X-ray microtomography. *Metallurgical and Materials Transactions A*, 35(7), 1953–1961.

Du, G. (2017). *Phase-field simulation of lath martensite in low-carbon steel*. PhD thesis, Ruhr University Bochum.

Eggbauer, A., Lukas, M., Ressel, G., Prevedel, P., Mendez-Martin, F., Keckes, J., Stark, A., & Ebner, R. (2019). In situ analysis of the effect of high heating rates and initial microstructure on the formation and homogeneity of austenite. *Journal of materials science*, 54(12), 9197–9212.

Eggbauer, A., Ressel, G., Gruber, M., Prevedel, P., Marsoner, S., Stark, A., & Ebner, R. (2018). Different cooling rates and their effect on morphology and transformation kinetics of martensite. In *Proceedings of the International Conference on Martensitic Transformations: Chicago* (pp. 35–40).: Springer.

Engin, C. & Urbassek, H. M. (2008). Molecular-dynamics investigation of the fcc → bcc phase transformation in Fe. *Computational Materials Science*, 41(3), 297–304.

Entel, P., Meyer, R., & Kadau, K. (2000). Molecular dynamics simulations of martensitic transitions. *Philosophical Magazine B*, 80(2), 183–194.

Entwisle, A. R. (1971). The kinetics of martensite formation in steel. *Metallurgical transactions*, 2(9), 2395–2407.

Eshelby, J. D. (1957). The determination of the elastic field of an ellipsoidal inclusion, and related problems. *Proceedings of the Royal Society of London. Series A. Mathematical and Physical Sciences*, 241(1226), 376–396.

Ferraglio, P. L. & Mukherjee, K. (1974). The dynamics of nucleation and growth of a thermoelastic martensite in a splat quenched Au-47.5 at.% Cd alloy. *Acta Metallurgica*, 22(7), 835–845.

Fisher, J. C., Hollomon, J. H., & Turnbull, D. (1948). Nucleation. *Journal of Applied Physics*, 19(8), 775–784.

Fried, E. & Grach, G. (1997). An order-parameter-based theory as a regularization of a sharp-interface theory for solid-solid phase transitions. *Archive for Rational Mechanics and Analysis*, 138(4), 355–404.

Fried, E. & Gurtin, M. E. (1993). Continuum theory of thermally induced phase transitions based on an order parameter. *Physica D: Nonlinear Phenomena*, 68(3-4), 326–343.

Fried, E. & Gurtin, M. E. (1994). Dynamic solid-solid transitions with phase characterized by an order parameter. *Physica D: Nonlinear Phenomena*, 72(4), 287–308.

Fritzen, F., Böhlke, T., & Schnack, E. (2009). Periodic three-dimensional mesh generation for crystalline aggregates based on Voronoi tessellations. *Computational Mechanics*, 43(5), 701–713.

Furuhara, T., Kikumoto, K., Saito, H., Sekine, T., Ogawa, T., Morito, S., & Maki, T. (2008). Phase transformation from fine-grained austenite. *ISIJ international*, 48(8), 1038–1045.

Furuhara, T., Takayama, N., & Miyamoto, G. (2010). Key factors in grain refinement of martensite and bainite. In *Materials Science Forum*, volume 638 (pp. 3044–3049).: Trans Tech Publ.

Gaggero, J. & Hull, D. (1962). On the nucleation of martensite. *Acta Metallurgica*, 10(10), 995–998.

Garcke, H. (2000). On mathematical models for phase separation in elastically stressed solids. Habilitation thesis.

Graf, M., Kuntz, M., Autenrieth, H., Diewald, F., & Müller, R. (2021a). Phase field modeling and simulation of the evolution of twelve crystallographic martensite variants in austenitic parent grains. *PAMM*, 20(1), e202000121.

Graf, M., Kuntz, M., Autenrieth, H., Diewald, F., & Müller, R. (2021b). Phase field modeling and simulation of the evolution of twelve crystallographic martensite variants in austenitic parent grains–three-dimensional simulations. *PAMM*, 21(1), e202100161.

Graf, M., Kuntz, M., Autenrieth, H., Diewald, F., & Müller, R. (2021c). Simulation of martensitic microstructures in a low-alloy steel. *Archive of Applied Mechanics*, 91(4), 1641–1668.

Graf, M., Kuntz, M., Autenrieth, H., & Müller, R. (2020). Investigation of size effects due to different cooling rates of as-quenched martensite microstructures in a low-alloy steel. *Applied Sciences*, 10(15), 5395.

Greninger, A. B. & Troiano, A. R. (1949). The mechanism of martensite formation. *Trans AIME*, 1(9), 590–598.

Guo, X. H., Shi, S.-Q., & Ma, X. Q. (2005). Elastoplastic phase field model for microstructure evolution. *Applied Physics Letters*, 87(22), 221910.

Gurtin, M. E. (1996). Generalized Ginzburg-Landau and Cahn-Hilliard equations based on a microforce balance. *Physica D: Nonlinear Phenomena*, 92(3-4), 178–192.

Hall, E. O. (1951). The deformation and ageing of mild steel: III discussion of results. *Proceedings of the Physical Society. Section B*, 64(9), 747.

Hanamura, T., Torizuka, S., Tamura, S., Enokida, S., & Takechi, H. (2013). Effect of austenite grain size on transformation behavior, microstructure and mechanical properties of 0.1 C–5Mn martensitic steel. *ISIJ international*, 53(12), 2218–2225.

Haupt, P. (2013). *Continuum mechanics and theory of materials*. Springer Science & Business Media.

Heo, T. W. & Chen, L.-Q. (2014). Phase-field modeling of displacive phase transformations in elastically anisotropic and inhomogeneous polycrystals. *Acta Materialia*, 76, 68–81.

Hildebrand, F. & Miehe, C. (2010). A regularized sharp interface model for phase transformation accounting for prescribed sharp interface kinetics. *PAMM*, 10(1), 673–676.

Hildebrand, F. & Miehe, C. (2012a). Variational phase field modeling of laminate deformation microstructure in finite gradient crystal plasticity. *PAMM*, 12(1), 37–40.

Hildebrand, F. E. (2013). *Variational multifield modeling of the formation and evolution of laminate microstructure*. PhD thesis, University of Stuttgart.

Hildebrand, F. E. & Miehe, C. (2012b). A phase field model for the formation and evolution of martensitic laminate microstructure at finite strains. *Philosophical Magazine*, 92(34), 4250–4290.

Hollomon, J. H., Jaffe, L. D., & Norton, M. R. (1946). Anisothermal Decomposition of Austenite. *Trans. AIME*, 167, 419–441.

Holzapfel, A. G. (2000). *Nonlinear Solid Mechanics: A Continuum Approach for Engineering*. John Wiley & Sons, Inc.

Honda, K. & Nishiyama, Z. (1932). Science Reports, Tohoku Imperial Univ. *Trans. Am. Soc. Metals*, 21.

Hu, K., Zhou, G., & Liu, J. (2018). Effects of austenitizing and quenching parameters on microstructures and mechanical properties of press hardened wht1500hf steel. *Materials Performance and Characterization*, 7(1), 316–326.

Huiping, L., Guoqun, Z., Shanting, N., & Chuanzhen, H. (2007). FEM simulation of quenching process and experimental verification of simulation results. *Materials Science and Engineering: A*, 452, 705–714.

Ivanov, Y. F. & Kozlov, E. V. (2002). Bulk and surface quenching of structural steel: Morphological analysis of the structure. *Russian physics journal*, 45(3), 209–231.

Jäniche, W., Dahl, W., Klärner, H.-F., Pitsch, W., Schauwinhold, D., Schlüter, W., & Schmitz, H. (2013). *Werkstoffkunde Stahl: Band 1: Grundlagen*. Springer-Verlag.

Javaheri, V., Kolli, S., Grande, B., & Porter, D. (2019). Insight into the induction hardening behavior of a new 0.40% C microalloyed steel: Effects of initial microstructure and thermal cycles. *Materials Characterization*, 149, 165–183.

Javanbakht, M. & Levitas, V. I. (2015). Interaction between phase transformations and dislocations at the nanoscale. part 2: Phase field simulation examples. *Journal of the Mechanics and Physics of Solids*, 82, 164–185.

Ji, H., Chopp, D., & Dolbow, J. E. (2002). A hybrid extended finite element/level set method for modeling phase transformations. *International Journal for Numerical Methods in Engineering*, 54(8), 1209–1233.

Jin, Y. M., Artemev, A., & Khachaturyan, A. G. (2001). Three-dimensional phase field model of low-symmetry martensitic transformation in polycrystal: simulation of ζ'2 martensite in AuCd alloys. *Acta materialia*, 49(12), 2309–2320.

Kajiwara, S. (1986). Roles of dislocations and grain boundaries in martensite nucleation. *Metallurgical and Materials Transactions A*, 17(10), 1693–1702.

Kaufman, L. & Cohen, M. (1958). Thermodynamics and kinetics of martensitic transformations. *Progress in Metal Physics*, 7, 165–246.

Kelly, P., Jostsons, A., & Blake, R. (1990). The orientation relationship between lath martensite and austenite in low carbon, low alloy steels. *Acta Metallurgica et Materialia*, 38(6), 1075–1081.

Kelly, P. M. (1992). Crystallography of lath martensite in steels. *Materials Transactions, JIM*, 33(3), 235–242.

Kelly, P. M. (2012). Crystallography of martensite transformations in steels. In *Phase Transformations in Steels* (pp. 3–33). Elsevier.

Khachaturyan, A. G. (2013). *Theory of structural transformations in solids.* Courier Corporation.

Khachaturyan, A. G. & Shatalov, G. A. (1969). Theory of macroscopic periodicity for a phase transition in the solid state. *Soviet Phys. JETP*, 29(3), 557–561.

Kim, D., Lee, S.-J., & De Cooman, B. C. (2012). Microstructure of low C steel isothermally transformed in the M_s to M_f temperature range. *Metallurgical and Materials Transactions A*, 43(13), 4967–4983.

Kim, D., Speer, J. G., & De Cooman, B. C. (2011). Isothermal transformation of a CMnSi steel below the M_S temperature. *Metallurgical and Materials Transactions A*, 42(6), 1575–1585.

Kitahara, H., Ueji, R., Tsuji, N., & Minamino, Y. (2006). Crystallographic features of lath martensite in low-carbon steel. *Acta Materialia*, 54(5), 1279–1288.

Kitahara, H., Ueji, R., Ueda, M., Tsuji, N., & Minamino, Y. (2005). Crystallographic analysis of plate martensite in Fe-28.5 at.% Ni by FE-SEM/EBSD. *Materials Characterization*, 54(4-5), 378–386.

Klostermann, J. A. (1972). The concept of the habit plane and the phenomenological theories of the martensite transformation. *Journal of the Less Common Metals*, 28(1), 75–94.

Kochmann, J., Wulfinghoff, S., Reese, S., Mianroodi, J. R., & Svendsen, B. (2016). Two-scale FE-FFT- and phase-field-based computational modeling of bulk microstructural evolution and macroscopic material behavior. *Computer Methods in Applied Mechanics and Engineering*, 305, 89–110.

Koistinen, D. P. & Marburger, R. E. (1959). A general equation prescribing the extent of the austenite-martensite transformation in pure iron-carbon alloys and plain carbon steels. *Acta Metallurgica*, 7(1), 59 – 60.

Koumatos, K. & Muehlemann, A. (2017). A theoretical investigation of orientation relationships and transformation strains in steels. *Acta Crystallographica Section A: Foundations and Advances*, 73(2), 115–123.

Krauss, G. (1990). Steels: heat treatment and processing principles. *ASM International, 1990,*, (pp. 497).

Krauss, G. & Marder, A. R. (1971). The morphology of martensite in iron alloys. *Metallurgical Transactions*, 2(9), 2343.

Krauss, W., Pabi, S. K., & Gleiter, H. (1989). On the mechanism of martensite nucleation. *Acta Metallurgica*, 37(1), 25–30.

Kružík, M., Mielke, A., & Roubíček, T. (2005). Modelling of microstructure and its evolution in shape-memory-alloy single-crystals, in particular in CuAlNi. *Meccanica*, 40(4-6), 389–418.

Kuhn, C. (2013). *Numerical and Analytical Investigation of a Phase Field Model for Fracture.* doctoralthesis, Technische Universität Kaiserslautern.

Kuhn, J., Schneider, M., Sonnweber-Ribic, P., & Böhlke, T. (2020). Fast methods for computing centroidal Laguerre tessellations for prescribed volume fractions with applications to microstructure generation of polycrystalline materials. *Computer Methods in Applied Mechanics and Engineering*, 369, 113175.

Kundin, J., Raabe, D., & Emmerich, H. (2011). A phase-field model for incoherent martensitic transformations including plastic accommodation processes in the austenite. *Journal of the Mechanics and Physics of Solids*, 59(10), 2082–2102.

Kurdjumov, G. & Sachs, G. (1930). Over the mechanisms of steel hardening. *Z. Phys*, 64(325–343).

Laptev, A., Baufeld, B., Swarnakar, A. K., Zakharchuk, S., & Van der Biest, O. (2012). High temperature thermal expansion and elastic modulus of steels used in mill rolls. *Journal of materials engineering and performance*, 21(2), 271–279.

Lee, S.-J., Lusk, M. T., & Lee, Y.-K. (2007). Conversional model of transformation strain to phase fraction in low alloy steels. *Acta Materialia*, 55(3), 875–882.

Levitas, V. I. & Javanbakht, M. (2015). Interaction between phase transformations and dislocations at the nanoscale. Part 1. General phase field approach. *Journal of the Mechanics and Physics of Solids*, 82, 287–319.

Levitas, V. I., Lee, D.-W., & Preston, D. L. (2010). Interface propagation and microstructure evolution in phase field models of stress-induced martensitic phase transformations. *International Journal of Plasticity*, 26(3), 395–422.

Levitas, V. I., Roy, A. M., & Preston, D. L. (2013). Multiple twinning and variant-variant transformations in martensite: Phase-field approach. *Physical Review B*, 88(5), 054113.

Lin, M., Olson, G. B., & Cohen, M. (1992). Distributed-activation kinetics of heterogeneous martensitic nucleation. *Metallurgical Transactions A*, 23(11), 2987–2998.

Liu, H., Li, H., Li, Z., & He, L. (2018). Effects of heating and quenching processing parameters on phase transformation of 55CrMo steel. *Journal of Materials Engineering and Performance*, 27(10), 5254–5270.

Lobodyuk, V. A. (2014). Nucleation and martensitic transformation in subjects of small dimensions. *Advances in Metal Physics*.

Loewy, S., Rheingans, B., Meka, S. R., & Mittemeijer, E. J. (2014). Unusual martensite-formation kinetics in steels: Observation of discontinuous transformation rates. *Acta materialia*, 64, 93–99.

Loewy, S., Rheingans, B., Meka, S. R., & Mittemeijer, E. J. (2015). Modulated martensite formation behavior in Fe–Ni-based alloys; athermal and thermally activated mechanisms. *Journal Materials Research*, 30(13), 2101–2107.

Löwy, S. (2015). *Formation of lath martensite*. PhD thesis, University of Stuttgart.

Luskin, M. (1996). On the computation of crystalline microstructure. *Acta numerica*, 5, 191–257.

Luther, T. & Könke, C. (2009). Polycrystal models for the analysis of intergranular crack growth in metallic materials. *Engineering Fracture Mechanics*, 76(15), 2332–2343.

Magee, C. L. (1970). Phase transformations. *ASM, Metals Park, Ohio (1)*, (pp. 15–156).

Maki, T. (1990). Microstructure and mechanical behaviour of ferrous martensite. In *Materials Science Forum*, volume 56 (pp. 157–168).: Trans Tech Publ.

Maki, T. (2012). Morphology and substructure of martensite in steels. In *Phase Transformations in Steels* (pp. 34–58). Elsevier.

Maki, T., Shimooka, S., Umemoto, M., & Tamura, I. (1972). The morphology of strain-induced martensite and thermally transformed martensite in Fe-Ni-C alloys. *Transactions of the Japan Institute of Metals*, 13(6), 400–407.

Malik, A., Amberg, G., Borgenstam, A., & Ågren, J. (2013). Phase-field modelling of martensitic transformation: the effects of grain and twin boundaries. *Modelling and Simulation in Materials Science and Engineering*, 21(8), 085003.

Malik, A., Yeddu, H. K., Amberg, G., Borgenstam, A., & Ågren, J. (2012). Three dimensional elasto-plastic phase field simulation of martensitic transformation in polycrystal. *Materials Science and Engineering: A*, 556, 221–232.

Mamivand, M., Zaeem, M. A., & El Kadiri, H. (2013). A review on phase field modeling of martensitic phase transformation. *Computational Materials Science*, 77, 304–311.

Mao, C., Liu, C., Yu, L., Li, H., & Liu, Y. (2021). Discontinuous lath martensite transformation and its relationship with annealing twin of parent austenite and cooling rate in low carbon RAFM steel. *Materials & Design*, 197, 109252.

Maxwell, P. C., Goldberg, A., & Shyne, J. C. (1974). Stress-assisted and strain-induced martensites in Fe-Ni-C alloys. *Metallurgical Transactions*, 5(6), 1305–1318.

McDougall, P. G. & Wayman, C. M. (1992). The crystallography and morphology of ferrous martensites. *ASM International, Martensite(USA), 1992,*, (pp. 59–95).

Mecozzi, M. G., Eiken, J., Santofimia, M. J., & Sietsma, J. (2016). Phase field modelling of microstructural evolution during the quenching and partitioning treatment in low-alloy steels. *Computational Materials Science*, 112, 245–256.

Mirzaev, D. (1987). Martensite Points in Fe–C Alloys. *Fiz. Met. Metalloved.*, 63(4), 764–767.

Mirzaev, D. A., Korzunov, S. E., Schastlivtsev, V. M., & Yakovleva, I. L. (1983). The influence of cooling rate in hardening on the quantity of residual austenite and the hardness of carbon steels. *Fiz. Met. Metalloved.*, 56, 1033–1035.

Mirzaev, D. A., Shtejnberg, M. M., Ponomareaa, T. N., & Schastlivtsev, V. M. (1979). Effect of cooling rate on martensite point position. Carbon steels. *Fizika Metallov i Metallovedenie*, 47(1), 125–135.

Moelans, N., Blanpain, B., & Wollants, P. (2008). An introduction to phase-field modeling of microstructure evolution. *Computer Coupling of Phase Diagrams and Thermochemistry*, 32(2), 268–294.

Morito, S., Edamatsu, Y., Ichinotani, K., Ohba, T., Hayashi, T., Adachi, Y., Furuhara, T., Miyamoto, G., & Takayama, N. (2013). Quantitative analysis of three-dimensional morphology of martensite packets and blocks in iron-carbon-manganese steels. *Journal of Alloys and Compounds*, 577, S587–S592.

Morito, S., Huang, X., Furuhara, T., Maki, T., & Hansen, N. (2006a). The morphology and crystallography of lath martensite in alloy steels. *Acta Materialia*, 54(19), 5323–5331.

Morito, S., Igarashi, R., Kamiya, K., Ohba, T., & Maki, T. (2010). Effect of cooling rate on morphology and crystallography of lath martensite in Fe-Ni alloys. In *Materials Science Forum*, volume 638 (pp. 1459–1463).: Trans Tech Publ.

Morito, S., Saito, H., Ogawa, T., Furuhara, T., & Maki, T. (2005). Effect of austenite grain size on the morphology and crystallography of lath martensite in low carbon steels. *ISIJ international*, 45(1), 91–94.

Morito, S., Tanaka, H., Konishi, R., Furuhara, T., & Maki, T. (2003). The morphology and crystallography of lath martensite in Fe-C alloys. *Acta materialia*, 51(6), 1789–1799.

Morito, S., Yoshida, H., Maki, T., & Huang, X. (2006b). Effect of block size on the strength of lath martensite in low carbon steels. *Materials Science and Engineering: A*, 438, 237–240.

Müller, R. (2016). *A phase field model for the evolution of martensite microstructures in metastable austenites*. PhD thesis, University of Kaiserslautern.

Murr, L. E. (1975). Interfacial phenomena in metals and alloys.

Nestler, B., Garcke, H., & Stinner, B. (2005). Multicomponent alloy solidification: phase-field modeling and simulations. *Physical Review E*, 71(4), 041609.

Nishiyama, Z. (1934). X-ray investigation of the mechanism of the transformation from face centered cubic lattice to body centered cubic. *Sci. Rep. Tohoku Univ.*, 23, 637.

Nishiyama, Z. (2012). *Martensitic transformation*. Elsevier.

Nyyssönen, T., Peura, P., & Kuokkala, V.-T. (2018). Crystallography, morphology, and martensite transformation of prior austenite in intercritically annealed high-aluminum steel. *Metallurgical and Materials Transactions A*, 49(12), 6426–6441.

Olson, G. & Cohen, M. (1981). A perspective on martensitic nucleation. *Annual Review of Materials Science*, 11(1), 1–32.

Olson, G. B. & Cohen, M. (1976). A general mechanism of martensitic nucleation: Part II. FCC → BCC and other martensitic transformations. *Metallurgical transactions A*, 7(12), 1905–1914.

Onink, M., Brakman, C. M., Tichelaar, F. D., Mittemeijer, E. J., Zwaag, S., Root, J. H., & Konyer, N. B. (1993). The lattice parameters of austenite and ferrite in Fe-C alloys as functions of carbon concentration and temperature. *Scripta Metallurgica et Materialia;(United States)*, 29(8).

Ou, X. (2017). Molecular dynamics simulations of fcc-to-bcc transformation in pure iron: a review. *Materials Science and Technology*, 33(7), 822–835.

Pereloma, E. & Edmonds, D. V. (2012). *Phase transformations in steels: Diffusionless transformations, high strength steels, modelling and advanced analytical techniques*. Elsevier.

Petch, N. J. (1953). The cleavage strength of polycrystals. *Journal of the Iron and Steel Institute*, 174, 25–28.

Petryk, H. & Stupkiewicz, S. (2010). Interfacial energy and dissipation in martensitic phase transformations. Part I: Theory. *Journal of the Mechanics and Physics of Solids*, 58(3), 390–408.

Petryk, H., Stupkiewicz, S., & Maciejewski, G. (2010). Interfacial energy and dissipation in martensitic phase transformations. Part II: Size effects in pseudoelasticity. *Journal of the Mechanics and Physics of Solids*, 58(3), 373–389.

Ping, D. H., Guo, S. Q., Imura, M., Liu, X., Ohmura, T., Ohnuma, M., Lu, X., Abe, T., & Onodera, H. (2018). Lath formation mechanisms and twinning as lath martensite substructures in an ultra low-carbon iron alloy. *Scientific reports*, 8(1), 1–11.

Quey, R. (2019). Neper reference manual. *neper.info*.

Quey, R., Dawson, P. R., & Barbe, F. (2011). Large-scale 3D random polycrystals for the finite element method: Generation, meshing and remeshing. *Computer Methods in Applied Mechanics and Engineering*, 200(17-20), 1729–1745.

Quey, R. & Renversade, L. (2018). Optimal polyhedral description of 3D polycrystals: Method and application to statistical and synchrotron X-ray diffraction data. *Computer Methods in Applied Mechanics and Engineering*, 330, 308–333.

Raghaven, V. (1992). Martensite: A tribute to morris cohen. *AMS International, Materials Park*.

Rezaee-Hajidehi, M. & Stupkiewicz, S. (2020). Phase-field modeling of multivariant martensitic microstructures and size effects in nano-indentation. *Mechanics of Materials*, 141, 103267.

Rios, P. R. & Guimarães, J. R. C. (2008). Formal analysis of isothermal martensite spread. *Materials Research*, 11(1), 103–108.

Roberts, C. S. (1953). Effect of carbon on the volume fractions and lattice parameters of retained austenite and martensite. *JOM*, 5(2), 203–204.

Roberts, C. S., Averbach, B. L., & Cohen, M. (1953). The mechanism and kinetics of the 1st stage of tempering. *Transactions of the American Society for Metals*, 45, 576–604.

Rose, A. & Hougardy, H. P. (1972). *Atlas zur Wärmebehandlung der Stähle. Band 2*. Verlag Stahleisen, Max-Planck-Institute for Iron Research in collaboration with the Technical University of Berlin and the Steel Institute VDEh.

Roumi, F. (2010). *Shape changing transformations: interactions with plasticity and electrochemical processes*. PhD thesis, California Institute of Technology.

Rubini, S. & Ballone, P. (1993). Quasiharmonic and molecular-dynamics study of the martensitic transformation in Ni-Al alloys. *Physical Review B*, 48(1), 99.

Rubini, S. & Ballone, P. (1994). Erratum: Quasiharmonic and molecular-dynamics study of the martensitic transformation in Ni-Al alloys. *Physical Review B*, 49(21), 15428.

Sandoval, L. & Urbassek, H. M. (2009). Transformation pathways in the solid-solid phase transitions of iron nanowires. *Applied Physics Letters*, 95(19), 191909.

Schäfer, B. J., Song, X., Sonnweber-Ribic, P., Hartmaier, A., et al. (2019a). Micromechanical modelling of the cyclic deformation behavior of martensitic SAE 4150 – A comparison of different kinematic hardening models. *Metals*, 9(3), 368.

Schäfer, B. J., Sonnweber-Ribic, P., Hartmaier, A., et al. (2019b). Micromechanical Modeling of Fatigue Crack Nucleation around Non-Metallic Inclusions in Martensitic High-Strength Steels. *Metals*, 9(12), 1258.

Schäfer, B. J., Sonnweber-Ribic, P., Hartmaier, A., et al. (2019c). Micromechanical Modelling of the Influence of Strain Ratio on Fatigue Crack Initiation in a Martensitic Steel-A Comparison of Different Fatigue Indicator Parameters. *Materials*, 12(18), 2852.

Schänzel, M., Shakirov, D., Ilin, A., & Ploshikhin, V. (2019). Coupled thermo-mechanical process simulation method for selective laser melting considering phase transformation steels. *Computers & Mathematics with Applications*.

Schastlivtsev, V. M., Mirzaev, D. A., & Yakovleva, I. L. (1994). Structure of Heat Treated Steel. *Metallurgiya Publ., Moscow*.

Schmidt, S., Dornisch, W., & Müller, R. (2017). A phase field model for martensitic transformation coupled with the heat equation. *GAMM-Mitteilungen*, 40(2), 138–153.

Schmidt, S., Klein, M. W., Boemke, A., Smaga, M., Beck, T., & Müller, R. (2018). Investigation of austenitic TRIP steels by means of a phase field model. *PAMM*, 18(1), e201800369.

Schmidt, S. & Müller, R. (2017). Heat conduction in a phase field model for martensitic transformation. *PAMM*, 17(1), 561–562.

Schmitt, R., Kuhn, C., & Müller, R. (2017). On a phase field approach for martensitic transformations in a crystal plastic material at a loaded surface. *Continuum Mechanics and Thermodynamics*, 29(4), 957–968.

Schmitt, R., Kuhn, C., Müller, R., & Bhattacharya, K. (2014). Crystal plasticity and martensitic transformations – a phase field approach. *Technische Mechanik*, 34(1), 23–38.

Schmitt, R., Kuhn, C., Skorupski, R., Smaga, M., Eifler, D., & Müller, R. (2015). A combined phase field approach for martensitic transformations and damage. *Archive of Applied Mechanics*, 85(9-10), 1459–1468.

Schmitt, R., Müller, R., & Kuhn, C. (2012). A phase field model for martensitic transformations. *PAMM*, 12(1), 261–262.

Schmitt, R., Müller, R., Kuhn, C., & Urbassek, H. M. (2013a). A phase field approach for multivariant martensitic transformations of stable and metastable phases. *Archive of Applied Mechanics*, 83(6), 849–859.

Schmitt, R., Müller, R., Skorupski, R., Smaga, M., & Eifler, D. (2013b). A phase field approach for martensitic transformations in elastoplastic materials. *PAMM*, 13(1), 213–214.

Schmitt, R., Wang, B., Urbassek, H. M., & Müller, R. (2013c). Modeling of martensitic transformations in pure iron by a phase field approach using information from atomistic simulation. *Technische Mechanik*, 33, 119–130.

Schneider, D., Tschukin, O., Choudhury, A., Selzer, M., Böhlke, T., & Nestler, B. (2015). Phase-field elasticity model based on mechanical jump conditions. *Computational Mechanics*, 55(5), 887–901.

Schoof, E. (2020). *Chemomechanische Modellierung der Wärmebehandlung von Stählen mit der Phasenfeldmethode.* PhD thesis, Karlsruher Institut für Technologie (KIT).

Schoof, E., Herrmann, C., Schneider, D., Hötzer, J., & Nestler, B. (2019). Multiphase-Field Modeling and Simulation of Martensitic Phase Transformation in Heterogeneous Materials. In *High Performance Computing in Science and Engineering'18* (pp. 475–488). Springer.

Schoof, E., Herrmann, C., Streichhan, N., Selzer, M., Schneider, D., & Nestler, B. (2018a). On the multiphase-field modeling of martensitic phase transformation in dual-phase steel using J_2-viscoplasticity. *Modelling and Simulation in Materials Science and Engineering*.

Schoof, E., Schneider, D., Streichhan, N., Mittnacht, T., Selzer, M., & Nestler, B. (2018b). Multiphase-field modeling of martensitic phase transformation in a dual-phase microstructure. *International Journal of Solids and Structures*, 134, 181–194.

Schrade, D., Mueller, R., Xu, B. X., & Gross, D. (2007). Domain evolution in ferroelectric materials: A continuum phase field model and finite element implementation. *Computer methods in applied mechanics and engineering*, 196(41-44), 4365–4374.

Schwenk, M. (2014). *Numerische Modellierung der induktiven Ein-und Zweifrequenzrandschichthärtung.* PhD thesis, Karlsruhe Institute of Technology.

Shchyglo, O., Du, G., Engels, J. K., & Steinbach, I. (2019). Phase-field simulation of martensite microstructure in low-carbon steel. *Acta Materialia*.

Shi, R., Zhou, N., Niezgoda, S. R., & Wang, Y. (2015). Microstructure and transformation texture evolution during α precipitation in polycrystalline α/β titanium alloys–a simulation study. *Acta Materialia*, 94, 224–243.

Shtejnberg, M. M., Mirzaev, D. A., & Ponomareva, T. N. (1977). Gamma $\rightarrow$ alpha transformation during cooling of Fe-Mn alloys. *Fizika Metallov i Metallovedenie*, 43(1), 166–172.

Simo, J. C. & Hughes, T. J. R. (2006). *Computational inelasticity*, volume 7. Springer Science & Business Media.

Sinha, A. K. (2003). *Physical metallurgy handbook.* McGraw-Hill Professional Publishing.

Song, T. & De Cooman, B. C. (2014). Martensite nucleation at grain boundaries containing intrinsic grain boundary dislocations. *ISIJ International*, 54(10), 2394–2403.

Spettl, A., Werz, T., Krill, C. E., & Schmidt, V. (2014). Parametric representation of 3D grain ensembles in polycrystalline microstructures. *Journal of Statistical Physics*, 154(4), 913–928.

Spittel, M. & Spittel, T. (2009). Materials: metal forming data of ferrous alloys – deformation behavior, Landolt Börnstein, group VII advanced materials and technologies 2C1: AISI 4140 715-718.

Steinbach, I. & Pezzolla, F. (1999). A generalized field method for multiphase transformations using interface fields. *Physica D: Nonlinear Phenomena*, 134(4), 385–393.

Steinbach, I., Pezzolla, F., Nestler, B., Seeßelberg, M., Prieler, R., Schmitz, G. J., & Rezende, J. L. L. (1996). A phase field concept for multiphase systems. *Physica D: Nonlinear Phenomena*, 94(3), 135–147.

Steinmetz, F. (2020). Simulation of martensite transformation using the phase field method. Bachelor thesis. Technische Universität Kaiserslautern.

Suezawa, M. & Cook, H. E. (1980). On the nucleation of martensite. *Acta Metallurgica*, 28(4), 423–432.

Suikkanen, P. P., Cayron, C., DeArdo, A. J., & Karjalainen, L. P. (2011). Crystallographic analysis of martensite in 0.2 C-2.0 Mn-1.5 Si-0.6 Cr steel using EBSD. *Journal of Materials Science & Technology*, 27(10), 920–930.

Swarr, T. & Krauss, G. (1976). The effect of structure on the deformation of as-quenched and tempered martensite in an Fe-0.2 pct C alloy. *Metallurgical Transactions A*, 7(1), 41–48.

Tsuzaki, K. & Maki, T. (1981). Effect of cooling rate on the morphology of lath martensite in Fe-Ni alloys. *Nippon Kinzoku Gakkaishi/Journal of the Japan Institute of Metals*, 45(2), 126–134.

Ueda, M., Yasuda, H., & Umakoshi, Y. (2002). Effect of grain boundary on martensite transformation behaviour in Fe–32 at.% Ni bicrystals. *Science and Technology of Advanced Materials*, 3(2), 171–179.

Ueda, M., Yasuda, H. Y., & Umakoshi, Y. (2003). Controlling factor for nucleation of martensite at grain boundary in Fe-Ni bicrystals. *Acta materialia*, 51(4), 1007–1017.

Urbassek, H. M. & Sandoval, L. (2012). Molecular dynamics modeling of martensitic transformations in steels. In *Phase transformations in steels* (pp. 433–463). Elsevier.

Van Bohemen, S. M. C. & Sietsma, J. (2014). Kinetics of martensite formation in plain carbon steels: critical assessment of possible influence of austenite grain boundaries and autocatalysis. *Materials Science and Technology*, 30(9), 1024–1033.

Vannucci, P. (2018). General anisotropic elasticity. In *Anisotropic Elasticity* (pp. 19–73). Springer.

Vieweg, A., Povoden-Karadeniz, E., Ressel, G., Prevedel, P., Wojcik, T., Mendez-Martin, F., Stark, A., Keckes, J., & Kozeschnik, E. (2017a). Phase evolution and carbon redistribution during continuous tempering of martensite studied with high resolution techniques. *Materials & Design*, 136, 214–222.

Vieweg, A., Raninger, P., Prevedel, P., Ressel, G., Ecker, W., Marsoner, S., & Ebner, R. (2017b). Experimentelle und numerische Untersuchung des induktiven Anlassens eines Vergütungsstahles. *HTM Journal of Heat Treatment and Materials*, 72(4), 199–204.

Vieweg, A., Ressel, G., Prevedel, P., Marsoner, S., & Ebner, R. (2017c). Effects of the inductive hardening process on the martensitic structure of a 50CrMo4 steel. *HTM Journal of Heat Treatment and Materials*, 72(1), 3–9.

Vieweg, A., Ressel, G., Prevedel, P., Raninger, P., Panzenböck, M., Marsoner, S., & Ebner, R. (2016). Induction hardening: Differences to a conventional heat treatment process and optimization of its parameters. In *IOP Conference Series: Materials Science and Engineering*, volume 119 (pp. 012019).

Vieweg, A. E., Ressel, G., Raninger, P., Prevedel, P., Marsoner, S., & Ebner, R. (2018). Comparing fast inductive tempering and conventional tempering: Effects on microstructure and mechanical properties. *Metallurgical Research & Technology*, 115(4), 407.

Villa, M. (2013). *Isothermal martensite formation*. PhD thesis, The Technical University of Denmark Lyngby, Denmark.

Villa, M., Pantleon, K., Reich, M., Kessler, O., & Somers, M. A. J. (2014). Kinetics of anomalous multi-step formation of lath martensite in steel. *Acta materialia*, 80, 468–477.

Wang, B., Sak-Saracino, E., Gunkelmann, N., & Urbassek, H. M. (2014). Molecular-dynamics study of the $\alpha \leftrightarrow \gamma$ phase transition in Fe-C. *Computational Materials Science*, 82, 399–404.

Wang, B. & Urbassek, H. M. (2013). Phase transitions in an Fe system containing a bcc/fcc phase boundary: An atomistic study. *Physical Review B*, 87(10), 104108.

Wang, J., Xi, X., Li, Y., Wang, C., & Xu, W. (2019). New insights on nucleation and transformation process in temperature-induced martensitic transformation. *Materials Characterization*, 151, 267–272.

Wang, Y. & Khachaturyan, A. G. (1997). Three-dimensional field model and computer modeling of martensitic transformations. *Acta materialia*, 45(2), 759–773.

Wassermann, G. (1935). *Über den Mechanismus der α-γ-Umwandlung des Eisens*. Verlag Stahleisen.

Wayman, C. M. & Bhadeshia, H. K. D. H. (1996). Phase transformations, nondiffusive. In *Physical Metallurgy* (pp. 1507–1554). Elsevier.

Wechsler, M. S., Lieberman, D. S., & Read, T. A. (1953). On the theory of the formation of martensite. *Trans. AIME*, 197, 1503–1515.

Welschinger, F., Köbler, J., Andrä, H., Müller, R., Schneider, M., & Staub, S. (2019). Efficient Multiscale Methods for Viscoelasticity and Fatigue of Short Fiber-Reinforced Polymers. In *Key Engineering Materials*, volume 809 (pp. 473–479).: Trans Tech Publ.

Wever, F., Rose, A., Peter, W., Strassburg, W., & Rademacher, L. (1954). *Atlas zur Wärmebehandlung der Stähle. Band 1*. Verlag Stahleisen, Max-Planck-Institute for Iron Research in collaboration with the Technical University of Berlin and the Steel Institute VDEh.

Xie, C. L., Ghosh, S., & Groeber, M. (2004). Modeling cyclic deformation of HSLA steels using crystal plasticity. *Journal of engineering materials and technology*, 126(4), 339–352.

Yamanaka, A., Takaki, T., & Tomita, Y. (2008). Elastoplastic phase-field simulation of self-and plastic accommodations in cubic $\rightarrow$ tetragonal martensitic transformation. *Materials Science and Engineering: A*, 491(1-2), 378–384.

Yamanaka, A., Takaki, T., & Tomita, Y. (2010). Elastoplastic phase-field simulation of martensitic transformation with plastic deformation in polycrystal. *International journal of mechanical sciences*, 52(2), 245–250.

Yamanaka, A., Takaki, T., Tomita, Y., & Yoshino, M. (2009). Crystal plasticity phase-field simulation of deformation behavior and microstructure evolution in polycrystalline material. In *X International Conference on Computional Plasticity)*, volume 462 (pp. 1–4).

Yang, H.-S. & Bhadeshia, H. K. D. H. (2009). Austenite grain size and the martensite-start temperature. *Scripta materialia*, 60(7), 493–495.

Yang, Z. & Johnson, R. A. (1993). An EAM simulation of the alpha-gamma iron interface. *Modelling and Simulation in Materials Science and Engineering*, 1(5), 707.

Yeddu, H. K. (2018). Phase-field modeling of austenite grain size effect on martensitic transformation in stainless steels. *Computational Materials Science*, 154, 75–83.

Yeddu, H. K., Borgenstam, A., Hedström, P., & Ågren, J. (2012a). A phase-field study of the physical concepts of martensitic transformations in steels. *Materials Science and Engineering: A*, 538, 173–181.

Yeddu, H. K., Lookman, T., & Saxena, A. (2013). Strain-induced martensitic transformation in stainless steels: a three-dimensional phase-field study. *Acta materialia*, 61(18), 6972–6982.

Yeddu, H. K., Malik, A., Ågren, J., Amberg, G., & Borgenstam, A. (2012b). Three-dimensional phase-field modeling of martensitic microstructure evolution in steels. *Acta Materialia*, 60(4), 1538–1547.

Zhang, K.-S., Ju, J. W., Li, Z., Bai, Y.-L., & Brocks, W. (2015). Micromechanics based fatigue life prediction of a polycrystalline metal applying crystal plasticity. *Mechanics of Materials*, 85, 16–37.

Zhang, M.-X. & Kelly, P. M. (2009). Crystallographic features of phase transformations in solids. *Progress in Materials Science*, 54(8), 1101–1170.

Zhang, W., Jin, Y. M., & Khachaturyan, A. G. (2007). Phase field microelasticity modeling of heterogeneous nucleation and growth in martensitic alloys. *Acta Materialia*, 55(2), 565–574.

Zhang, X., Shen, G., Li, C., & Gu, J. (2019). Analysis of interface migration and isothermal martensite formation for quenching and partitioning process in a low-carbon steel by phase field modeling. *Modelling and Simulation in Materials Science and Engineering*, 27(7), 075011.

Zhong, Y. & Zhu, T. (2014). Phase-field modeling of martensitic microstructure in NiTi shape memory alloys. *Acta Materialia*, 75, 337–347.

Zienkiewicz, O. C., Taylor, R. L., & Zhu, J. Z. (2005). *The finite element method: its basis and fundamentals.* Elsevier.

Curriculum Vitae

Persönliche Daten

Name	Marius Graf
Geburtsdatum	15.04.1993
Geburtsort	Ostfildern/Ruit
Staatsangehörigkeit	deutsch

Schulbildung

1999–2000	Lindachschule Stetten, Leinfelden Echterdingen
2000–2003	Würmtalschule Merklingen, Weil der Stadt
2003–2009	Realschule Weil der Stadt, Weil der Stadt
2009–2012	Gottlieb-Daimler-Schule 1, Sindelfingen
2012	Fachhochschulreife

Hochschulbildung

2012–2015	Studium Luft- und Raumfahrttechnik, Duale Hochschule Baden-Württemberg
2015	Bachelor of Engineering
2015–2018	Studium Luft- und Raumfahrttechnik, Universität Stuttgart
2018	Master of Science

Betriebliche Ausbildung und berufliche Tätigkeit

2009–2012	Ausbildung Technischer Produktdesigner, Bertrandt Technikum GmbH, Ehningen
2012	Technischer Produktdesigner, Bertrandt Technikum GmbH, Ehningen
2012–2015	Duales Studium, Bertrandt Technikum GmbH, Ehningen
2015–2018	Mitarbeiter im Technischen Dienst, Deutsches Zentrum für Luft- und Raumfahrt e.V., Stuttgart
2018–2021	Doktorand, Robert Bosch GmbH, Renningen
seit 2021	Entwicklungsingenieur, Robert Bosch GmbH, Schwieberdingen

Liste der betreuten studentischen Arbeiten mit Bezug zur Dissertation

Steinmetz, Felix (2020). *Simulation of martensite transformation using the phase field method.* Bachelorarbeit. Technische Universität Kaiserslautern.